GEOPHYSICAL FINGERPRINTS OF EXHUMED SERPENTINIZED MANTLE DOMAINS AT THE ULTRASLOW-SPREADING SOUTHWEST INDIAN RIDGE

by

Ana Corbalán Castejón

Submitted in partial fulfilment of the requirements
for the degree of Doctor of Philosophy

at

Dalhousie University
Halifax, Nova Scotia
July 2023

For Javi – for all the tears and laughs shared over the course of this work

&

For Lara – for all the joy and happiness you have brought into my life

Table of Contents

List of Tables

List of Figures

Abstract

Ultraslow-spreading oceanic ridges (< 20 mm/yr) comprise ~35% of the global mid-ocean ridge system, yet their lithospheric structure and accretionary process are still little understood. At these ridges, the interplay between plate- and mantle-driven processes results in large along-axis variations in the accreted lithosphere and complex relationships between intermittent volcanic seafloor and extensive nonvolcanic seafloor domains. Geological and geophysical observations acquired at exhumed mantle domains indicate a subsurface structure that differs greatly from the traditional 3-layer crystalline crust topping the uppermost mantle formed at faster-spreading rates. At the eastern Southwest Indian Ridge (<14 mm/yr; SWIR), continuous emplacement of mantle-derived peridotites at the seafloor creates the widest nonvolcanic oceanic floor documented thus far. Extensive geological sampling in this area indicates that the peridotites are variably serpentinized (hydrothermally altered) and only a very minor component of crustal rocks derived from mantle melting are present.

The SISMO-SMOOTH survey collected coincident wide-angle ocean bottom seismometer (OBS) and multichannel seismic (MCS) data along two long (~150 km) orthogonal profiles across (NS profile) and along (EW profile) of the SWIR axis. This thesis discusses results based on these datasets and provides unique insights into the mantle exhumation dynamics in the subsurface and the evolution of the tectonically accreted topmost lithosphere. P-wave first arrivals recorded by OBSs are used to perform traveltime tomography and produce the first detailed 2D regional velocity models across and along an ultraslow-spreading SWIR amagmatic segment. I suggest that changes in velocity with depth are related to changes in the degree of serpentinization and interpret the subsurface structure to be composed of highly fractured and fully serpentinized peridotites at the top with a gradual decrease in pore space and serpentinization to unaltered peridotites at depth. Furthermore, a complex system of successive and alternating polarity detachment faults across-axis is imaged in the subsurface and constrained by the velocity structure for the first time in this thesis. A prestack depth migrated reflection section of the NS profile provides additional constraints on the detachment faults and serpentinization gradients. A detailed analysis of the velocity changes with time on the NS profile provides the first-ever seismic constraints on the evolution of the tectonically accreted topmost lithosphere. Comparing my results with the much better-studied magmatically accreted lithosphere, I find that the tectonically accreted lithosphere evolves much faster and in a fundamentally different way, with significant implications for continental crust genesis and geohazards associated with future subduction of tectonically accreted oceanic lithosphere.

Ultimately, the results shown in this thesis are applicable to other mid-ocean ridges and other plate boundaries. Tectonically accreted lithosphere has increasingly been reported at segment ends of slow-spreading ridges (Oceanic Core Complexes) and variably serpentinized peridotites have also been inferred worldwide in the oceanic crust adjacent to magma-poor rifted margins. Here, the lack of a clear understanding of the geophysical fingerprints of these domains challenges their unequivocal identification below thick post-rift sedimentary packages. For example, the results from this thesis may allow a reevaluation of existing seismic velocity models offshore eastern Canada and may assist in further detailing their identification and characterization.

List of Abbreviations Used

AAA ..... Anomalous Amplitude Attenuation
AD ..... Adaptive Deghosting
Adj. R-sq ..... Adjusted R-squared
AMC ..... Axial Magma Chamber
AML ..... Axial Magma Lens
B ..... Breakaways
b ..... intercept of the linear regression
BP ..... Band Pass Filter
CDP ..... Common Depth Point
CIR ..... Central Indian Ridge
CMP ..... Common Mid-Point
COMFI ..... Compact Fourier Interpolation
COT ..... Continent-Ocean Transition
CVS ..... Constant-Velocity Stacks
dbsf ..... depth below the seafloor
DWS ..... Derivative Weight Sum
E ..... Emergence
ECMA ..... East Coast Magnetic Anomaly
EW ..... East-West
FD ..... Finite-Difference
FTCS ..... Forward Time Centered Space
FWI ..... Full Waveform Inversion
GNDRs ..... Gently north dipping reflections
GSDRs ..... Gently south dipping reflections
HP ..... High Pass Filter
ID ..... Layer Identification
IL ..... Inline
IODP ..... International Ocean Discovery Program
KDM ..... Kirchhoff depth migration
KTM ..... Kirchhoff Time Migration
LP ..... Low Pass Filter
m ..... slope of the linear regression
Ma ..... Mega Annum (geological chronology)
MAR ..... Mid-Atlantic Ridge
mbsf ..... meters below sea floor
MCS ..... Multichannel Seismic
NOAA ..... National Oceanic and Atmospheric Administration
MOR ..... Mid-Ocean Ridge
MVFZ ..... Melville Fracture Zone
Myr ..... Million year (time duration)
NDPRs ..... North dipping sub-vertical reflections
NMO ..... Normal Moveout
NS ..... North-South

NU ..... Not Used
NUCNS ..... Non-Uniform Coherent Noise Suppression
OBS ..... Ocean Bottom Seismometer
OCC ..... Oceanic Core Complex
P ..... compressional wave
Pg ..... refracted crustal first arrivals
Pn ..... refracted mantle first arrivals
PmP ..... Moho reflection arivals
PSDM ..... Pre-Stack Depth Migration
pValue ..... p-value
QC ..... Quality Check
REE ..... Rare Earth Elements
RMBA ..... Residual Mantle Bouguer Anomaly
RMS ..... Root Mean Square
RMSE ..... Root Mean Squared Error
R-sq ..... R-squared
RTJ ..... Rodriguez Triple Junction
S ..... shear wave
S/N ..... Signal-To-Noise Ratio
SCAC ..... Surface-Consistent Amplitude Compensation
SD ..... Standard Deviation
SDPRs ..... South dipping sub-vertical reflections
SDRs ..... Seaward-Dipping Reflections
SE ..... Standard error
SHRs ..... Sub-horizontal reflections
SRME ..... Surface Related Multiple Elimination
SSE ..... Sum of Squares Errors
SWIR ..... Southwest Indian Ridge
T ..... Temperature
Tp ..... P-wave travel times
tStat ..... t-statistic
TWT ..... Two-Way Traveltime
Vp ..... P-wave velocity
Vs ..... S-wave velocity
γ ..... Gamma ratio
Ψ ..... Young's modulus
μ ..... Poisson's ratio
ρ ..... density
ρ_0 ..... density at standard pressure

Acknowledgments

I am very grateful to my thesis supervisor, Mladen Nedimović, for the opportunity, his support and guidance. I have learned from his skills in writing, science communication and big-picture thinking and I plan to use these learnings in future projects. He and his family made my family feel welcome and cared for on numerous occasions, and for that, I am most grateful. His support, empathy and understanding during my pregnancy and early motherhood will always be remembered. I would like to thank Keith Louden next for his advice, guidance and support. I wish that our professional timelines could have overlapped for a longer time.

I am thankful to my examining committee (Andy Calvert, Keith Louden, Djordje Grujic and Mladen Nedimović) for their appreciation and enthusiasm for my thesis and for their careful review and insightful comments. Thanks to Fundación La Caixa for generously funding the first two years of my studies and to the Transatlantic Ocean System Science & Technology Graduate Program for not only providing funding for the following two years but also providing unique interdisciplinary opportunities and bringing together a fantastic group of marine science students.

Thanks to all of my former and current lab-mates at the Dalhousie Seismic Imaging Laboratory. Harold Kuehn and Masoud Aali, thank you for your friendship and support. Helen Lau, Hanchao Jian, and Louise Watremez, thank you for sharing your expertise on seismic refraction studies. Pinar Gürün and Fernando Córdoba Ramírez, thank you for the support at very stressful times toward the end of my studies. I am grateful to José Miguel Castillo Castellanos for all of the help with the MCS data processing and for sharing invaluable knowledge of Omega Software. John Thibodeau, thank you for all the technical support provided during these years. I am also thankful to all of my Dalhousie Earth Sciences and interdepartmental friends. You know who you are, and I am grateful for the great moments that we shared and the times that you have listened to me when I needed someone to talk to. A special mention from this group goes to Sean Kelly, for all the stimulating conversations, and for his priceless help in building the thermal evolution models. Thanks to Daniel Salas González and Vanessa Linares Cabrera for sharing with me and Javier the wonders and challenges of raising a child while living far away from home and for becoming our family in Halifax.

I am wholeheartedly thankful to my parents, Kika Castejón Amenedo and Juan Corbalán Portillo, who gave me many happy childhood memories that were the strength I needed to face the challenges of adulthood. Thank you for all of your love, support, enthusiasm and all of your summer visits. They were some of my happiest moments during my studies. I want to thank my sister, Reyes Corbalán Castejón, for keeping me connected to Spain and its cultural wonders, the virtual laughs, your visits and your sisterhood. Thanks to my uncle José Castejón Amenedo and my aunt Keren Ellis for being my references and inspiration. Thank you for giving me the little push I needed to start this academic adventure.

Last but most important, I am immensely grateful to my partner, Javier Marquina Majadas, for his courage to come together with me to Canada, his patience, and his flexibility to accommodate my Ph.D. work often at inconvenient times, all with unmeasurable support. Above all, I am most grateful for the adventure we have started together raising our amazing little human, Lara.

Chapter 1

Introduction

1.1 Mid-ocean ridges

The global mid-ocean ridge (MOR) system (Fig. 1.1.1), the Earth's largest volcanic chain, stretches for nearly 65,000 km and shows a complex interplay of tectonic, magmatic, and hydrothermal processes (e.g., Berann et al., 1977). These volcanic ridges are divergent plate boundaries or places where two oceanic plates move away from each other, thus representing a fundamental piece of the Plate Tectonics Theory (e.g., Pitman and Heirtzler, 1966; Le Pichon, 1968; Morgan, 1968; Wilson, 1965). Oceanic lithosphere, which covers over two-thirds of the globe, has been and continues to be produced at the MORs. The speed at which the plates spread, or spreading rates, vary with location by more than an order of magnitude (e.g., Ito and Dunn, 2009). As plates drift away from the ridge, the oceanic lithosphere cools, thickens, and becomes denser until it is recycled back into the asthenosphere at subduction zones.

The MORs were first discovered in the 1950s after sonar development during World War II and by Marie Tharp's historic ocean floor maps (e.g., Heezen et al., 1959; Berann et al., 1977). Seafloor spreading, the process by which the newly created oceanic lithosphere moves away from the ridge, was first introduced by Dietz (1961) and Hess (1962) and later corroborated by samples from the International Ocean Discovery Program (IODP) Deep Sea Drilling Project Leg 3 (1968-1969) and by the studies of Heirtzler et al. (1968) and Pitman et al. (1966; 1968). The earlier studies found older ages in sedimentary and upper crustal samples collected away from the ridges than in samples taken at the ridge. The latter studies showed an alternating pattern of positive-negative magnetic anomalies that formed parallel to the spreading centers. These anomalies are relatable to the geomagnetic time scale and showed older age of the oceanic crust at a greater distance from the ridge and youngest crust at the ridge valley.

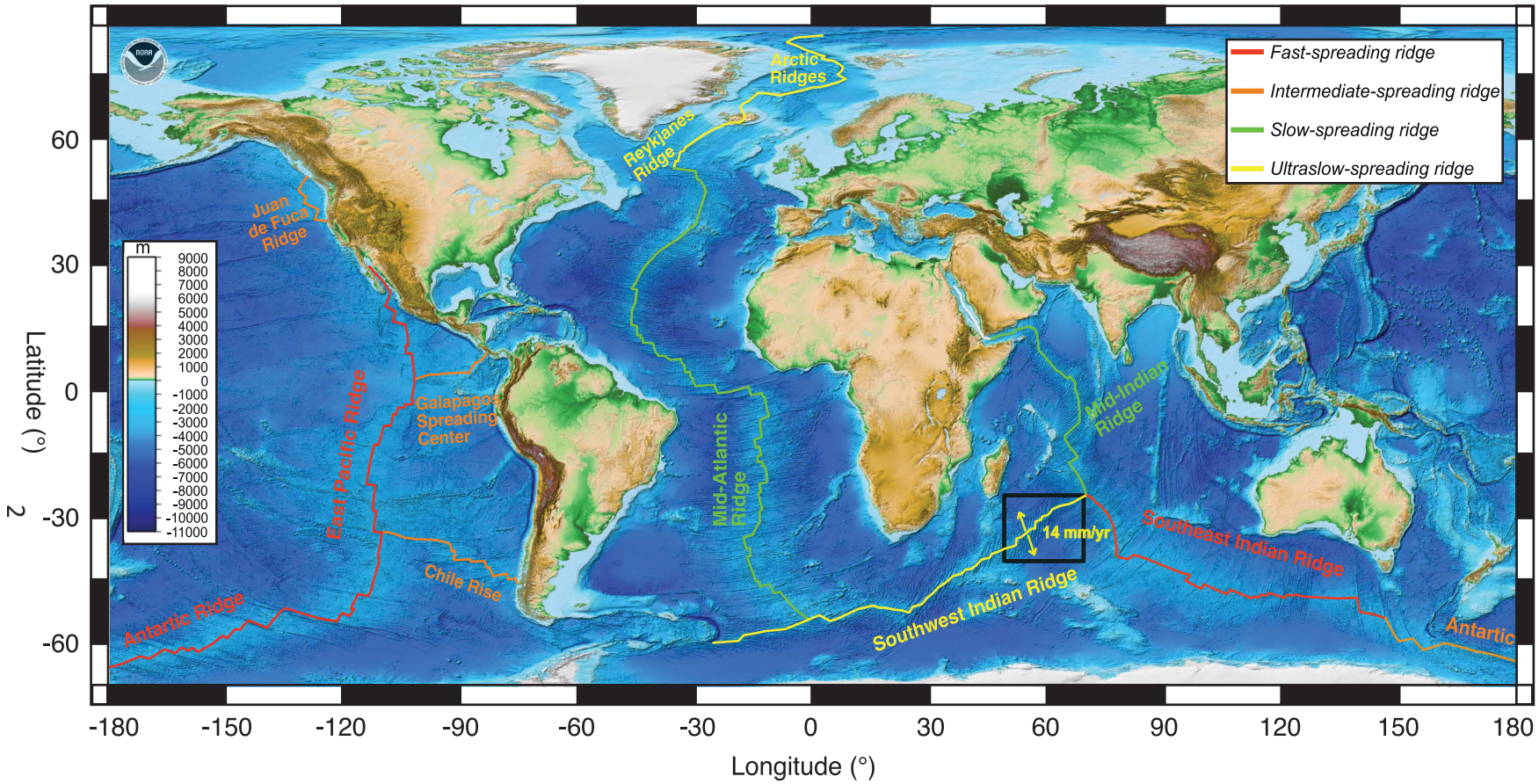

Figure 1.1.1. A worldwide map of the global mid-ocean ridge (MOR) system. Solid lines show the location of the MORs. These lines are colour-coded according to the MOR classification based on the spreading velocity: fast- (~80–180 mm/year) in red, intermediate- (~55–70 mm/year) in orange, slow- (20–55 mm/year) in green, and ultraslow-spreading (<~20 mm/year) in yellow (Dick et al., 2003). The Southwest Indian Ridge (SWIR) is the topic of this thesis. The study area is shown with a black rectangle, where the spreading velocity is 14 mm/yr (Kreemer et al., 2014). ETOPO1 one arc-minute resolution global relief model, shown in the background, is from the National Oceanic and Atmospheric Administration (NOAA).

Geological observations gathered across the MOR system throughout the 1980s and early 1990s revealed that MORs are partitioned into segments bounded by discontinuities (e.g., Macdonald et al., 1991). Fracture zones are major discontinuities defining the first-order segments and transform faults are their seismically and tectonically active portions (e.g., Fox & Gallo, 1984; Hekinian, 2014; Macdonald et al., 1991) and a type of plate boundary (Wilson, 1965). An example of second-order discontinuity is a non-transform discontinuity. The higher the order of the segmentation, the shorter length and shorter-lived the segments are, and segments at fast-spreading ridges are longer than segments at slow-spreading ridges (Macdonald et al., 1991).

The MOR system is heterogenous and shows remarkable differences in the axial morphology (e.g., Carbotte et al., 2016), the modes of seafloor accretion between different ridges and ridge segments (e.g., Cannat et al., 2006) and the spreading rate, which ranges from about 180 mm/yr at the East Pacific Rise (DeMets et al., 2010) to less than 14 mm/yr at the Gakkel (Arctic) and Southwest Indian ridges (Cochran et al., 2003; Kreemer et al., 2014) (Fig. 1.1.1). For example, the oceanic crust formed at faster-spreading ridges shows, in general, relatively gentle seafloor topography and a roughly dome-shaped rise (up to 400 m high) at the spreading axis, while the crust formed at slower-spreading ridges generally presents a more rugged topography and a sharp and well-developed axial rift valley (1-3 km deep) (e.g., Bach & Früh-Green, 2010; Carbotte et al., 2016; Heezen, 1960; Buck et al., 2005). Figure 1.1.2 shows the contrasting bathymetry for faster-spreading and slower-spreading ridges.

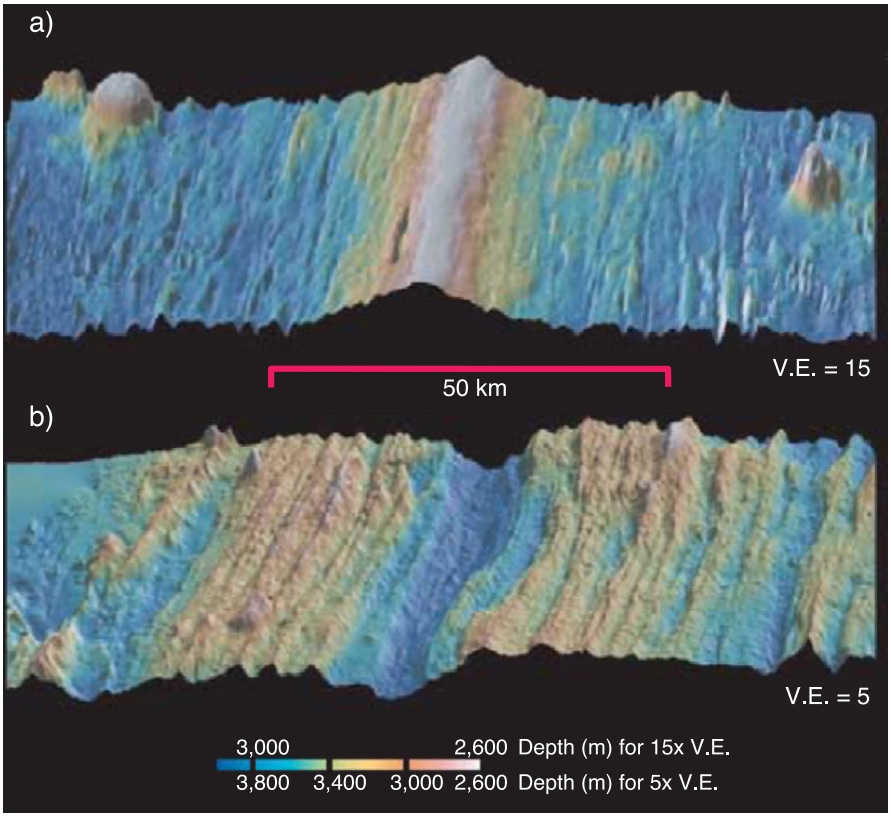

Figure 1.1.2. A comparison of seafloor topographic features characteristic of fast-spreading ridges in contrast to the typical features of intermediate- and slow-spreading ridges, after Buck et al. (2005). Bathymetric map of an axial high at the East Pacific Rise at 9°37'N (a) shows abyssal hill relief of ~50 m. The same structures of an axial valley at the Southeast Indian Ridge at 115°E (b) show much greater relief including a prominent rift valley. Note differences in the vertical scale: 15 in (a) and 5 in (b).

An axial summit trough, a volcanically modified graben at the crest of magmatically robust MORs, such as the fast-spreading East Pacific Rise, is normally 50 m deep and less than 500 m wide (Soule and Perfit, 2015), while fault-bounded axial valleys are normally 2 km deep and up to 10–15 km wide and characteristic of slow-spreading ridges (e.g., Needham and Francheteau, 1974; Sempéré et al., 1990), such as the Mid-Atlantic Ridge (MAR). These MOR characteristics are a consequence of the style of seafloor accretion and, ultimately, the spreading velocity. At faster-spreading ridges, the accretion is dominated by volcanic eruptions and lava flows while tectonic processes have greater control over seafloor accretion and spreading at slower-spreading ridges.

Oceanic crust structure and lithology

The oceanic crust is the uppermost layer of the oceanic lithosphere, and it is formed at the MORs. The type of oceanic structure and associated lithologies depend primarily on the spreading velocity. Oceanic crust accreted at fast (~80-180 mm/yr) and intermediate (~55-70 mm/yr) spreading centers, as well as at the magmatically robust segment centers of slow (~20-55 mm/yr) spreading ridges, exhibits common characteristics that are generally described to as the layered Penrose model. Oceanic crust accreted at ultraslow (<~20 mm/yr) spreading ridges and magma-poor segment ends (fracture zones and transform faults) of slow spreading ridges shows remarkably more complex structure.

1.1.1 The Penrose model

Early geophysical studies investigated the seismic structure of the oceanic crust and inferred a simple model with layers, 1, 2 and 3 (e.g., Hill, 1957; Raitt, 1963; Christensen 1970) defined by velocities of primary seismic waves (P waves). IODP early Deep Sea Drilling Projects showed that Layer 1 comprises unconsolidated or semi-consolidated sediments and is generally less than 1 km thick (e.g., Christensen and Salisbury 1975). Layers 2 and 3, with a variable thickness of 1–2.5 and 3.4–6.3 km, respectively, were proposed based on ophiolite studies and the available marine geophysical and dredging data (e.g., Vine and Moores 1972; Christensen and Salisbury 1975). In the Penrose model (Fig. 1.2.1.1), the uppermost mantle composed of ultramafic igneous rocks, peridotites, is separated from the crust by the Mohorovičić discontinuity or Moho. The oceanic crust topping the mantle is composed of, from bottom to top: low velocity gradient Layer 3, the lower crust, with layered gabbros at the base and isotropic gabbros at the top; and high velocity gradient Layer 2, the upper crust, which consists of basaltic pillow lavas overlying sheeted diabase dikes (e.g., Houtz and Ewing, 1976; Ewing and Houtz, 1979; White et al., 1992). Layer 2 is typically further divided into layers 2A and 2B, and they are typically interpreted as a high-porosity basaltic lava layer and lower-porosity sheeted diabase dike complex, respectively (e.g., Christeson et al., 1992; Toomey et al., 1990). Recent studies have debated whether the layer 2A/2B boundary may not always

correspond to a change in lithology, particularly as the crust ages (e.g., Christeson et al., 2007, 2010), but there still is a consensus that layer 2A/2B boundary is a result of a decrease in crustal porosity.

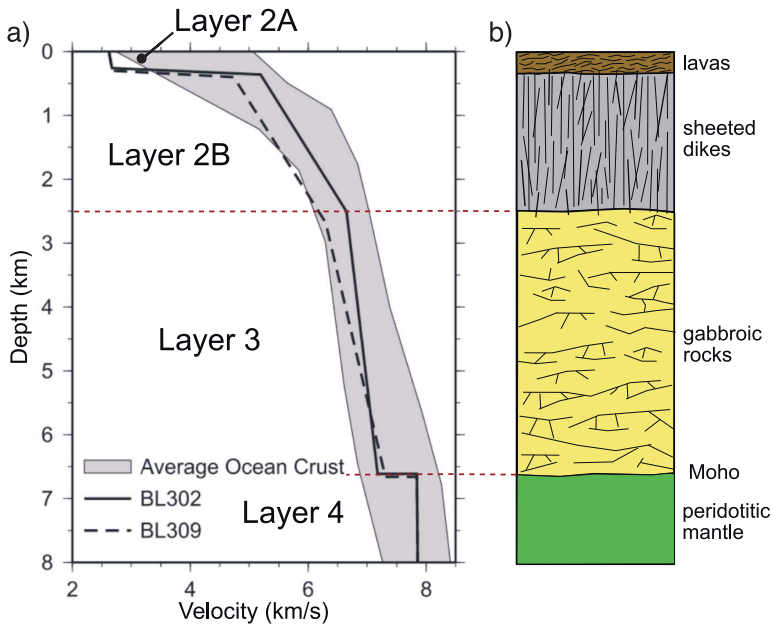

Figure 1.2.1.1. Vp and oceanic crust lithology relationship. (a) Vp-depth profiles for seismic refraction profiles BL302 and BL309 in the Blanco Transform Fault zone (modified from Christeson et al., 2010). The grey area comprises the average structure of young Pacific oceanic crust (White et al., 1992). Changes in the vertical velocity gradient guide division of structure into layers 2A, 2B, 3 and 4. (b) Schematic illustration of the "normal" oceanic crust generally interpreted from the Vp-depth profiles such as shown in (a) following the Penrose model.

Overall, the igneous crust is well characterized in terms of the average range of seismic velocities associated with each layer and the average thickness and vertical velocity gradients (Fig. 1.2.1.2) (e.g., Christeson et al., 2019; White et al., 1992), especially at intermediate- to fast-spreading ridges, where many of the early surveys were carried out. At these spreading rates, the crustal structure and lithology show significantly less variation between and along the ridge segments than at the slow- to ultraslow-spreading ridges. Thus, the overall understanding of intermediate- to fast-spreading ridges is much greater compared to our understanding of ultraslow-spreading ridges and segment ends at slow-spreading ridges. In these settings of limited melt budget, the Penrose model often does not apply, as marine geological and geophysical observations have evidenced broad outcrops of exposed mantle-derived rocks, peridotites, on the seafloor (e.g., Blackman et

al., 2002; Cannat et al., 2006; Dick et al., 2008; Ildefonse et al., 2007). Figure 1.2.1.2 shows a comparison of the expected crustal architecture formed at the two-end members: a fast-spreading ridge (a) and an ultraslow-spreading ridge (b). The lower and upper crustal layers at the melt-poor segments of ultraslow-spreading ridges, such as the SW Indian Ridge, are not present or extremely diminished (e.g., Cannat et al., 2006; Corbalán et al., 2021; Sauter et al., 2013); hence, it is more appropriate to further detail the lithospheric structure in these settings.

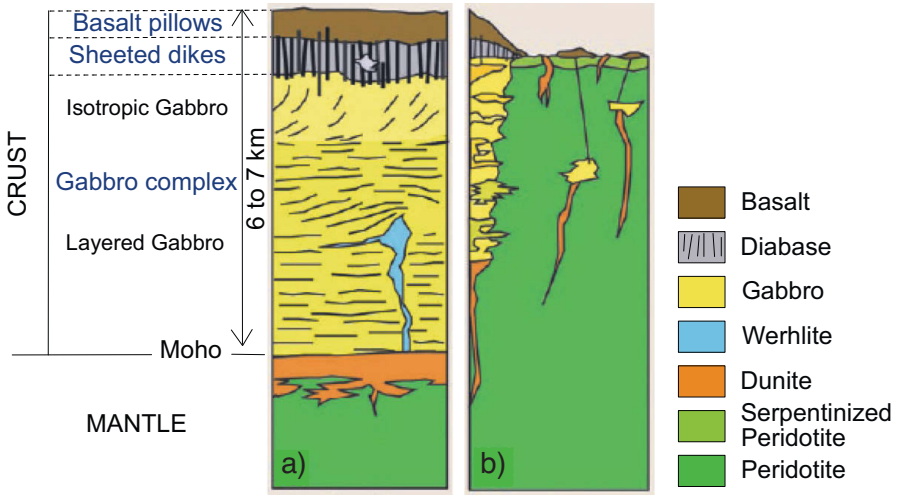

Figure 1.2.1.2. Comparison of the crustal architecture at fast- (a) and ultraslow-spreading (b) ridges, the two end members of the MOR system, after Dick et al., 2006. (a) Schematic of the crust interpreted at the Cocos-Nazca Ridge and the East Pacific Rise following the Penrose model, after Penrose Conference, 1972. (b) Schematic of the crust interpreted at the Southwest Indian Ridge and the Arctic Ridges, after Dick et al., 2003.

1.1.2 Lithospheric structure at ultraslow-spreading and segment ends of slow-spreading ridges

Slow- and ultraslow-spreading ridges display significant variations along-axis in terms of their spreading obliquity, segmentation length, faulting style, magmatism, and volcanism. Large-scale (>200 km) mantle thermal and compositional heterogeneities along-axis result in significant variations in melt supply along the ultraslow-spreading Southwest Indian Ridge (SWIR) (Cannat et al., 2008). Segment centers at MARs show negative residual gravity anomalies suggesting a relatively thick crust topping a hot mantle, in contrast to segment ends where positive residual gravity anomalies point out to a thin

crust and cooler mantle (e.g., Kuo and Forsyth, 1988; Grindlay et al., 1992; Escartín and Lin, 1995).

Similarly, seismic refraction studies at the MAR indicate a crustal thinning toward fracture zones (segment ends) and up to 40 km away from the fracture zone axis (e.g., Detrick & Purdy, 1980; Sinha & Louden, 1983; Whitmarsh & Calvert, 1986). The crustal thinning observed in seismic studies seems controlled by the magma supply and distribution from the center of spreading segments (Whitmarsh & Calvert, 1986), i.e., segment centers.

Seismic and gravity observations indicate that melt distribution is not uniform along segments and that magma is focused toward the segment centers (e.g., Lin et al., 1990). At melt-starved ridge sections, a non-volcanic mode of seafloor spreading was first characterized by Cannat et al. (2006), which results in broad exposures of serpentinized peridotites with little or no axial volcanism. Recent 3D geodynamical modelling results (Liu et al., 2022) suggest that spontaneous self-organization of magma supply controlled by spreading rate, mantle potential temperatures, and thickness of the brittle layer, induces bimodal spreading along melt-poor slow- and ultraslow-spreading ridges: tectonic-magmatic spreading vs. purely tectonic spreading. The former results in hotter, thinner, and elevated magmatic sectios, while the latter results in colder, thicker, and subsidized amagmatic sections (Liu et al., 2022).

Higher REE (rare earth elements) and sodium concentrations of basalts, relative to values normally associated with MOR basalts, are indicative of a lower degree of melting and melt restriction to greater depths at segment ends, near fracture zones and transform faults, and other areas with broad on- and off-axis exposures of serpentinized peridotites (e.g. Dick et al., 1991; Lin et al., 1990; Meyzen et al., 2003; Seyler et al., 2003; White et al., 2001). Furthermore, microseismicity studies at the SWIR have constrained a thick (~20 km) brittle lithosphere based on the depth of observed earthquakes (Schlindwein & Schmid, 2016). Seafloor sampling (dredging, drilling or direct sampling with submersibles) along the MAR and SWIR has evidenced the presence of serpentinized

peridotites within a variety of tectonic settings, sometimes in a complex association with gabbros (e.g., Cannat et al., 1993, Lagabrielle et al., 1998; Sauter et al., 2013; Tucholke and Lin, 1994).

Geological sampling of the seafloor at a melt-starved section of the ultraslow-spreading SWIR at 64°30'E points to the absence of a continuous mafic crust (layers 2 and 3) as ~90% of the samples recovered are serpentinized peridotites (Sauter et al., 2013). Similarly, side-scan sonar images (Cannat et al., 2012; Sauter et al., 2013) have shown ~12-km-wide surfaces interpreted as detachment fault surfaces with intermittent, scattered, and small volcanic patches on top and a scarce, nearly negligible, sediment cover. Similar detachment surfaces have been observed in acoustic back-scatter images at the oceanic core complex (OCC) located at MAR 13°20′N (MacLeod et al., 2009). An OCC is a positive seafloor structure that consists of a footwall, a detachment fault, and a hanging wall. The footwall is characterized by a shallow, broad, striated dome-shaped surface that exposes intrusive (diabase or gabbro) and/or ultramafic (variably serpentinized peridotites) rocks at the seafloor (Blackman et al., 2009). The hanging wall is adjacent and of low-lying topography and is primarily constituted of volcanic rocks (Canales et al., 2004; Blackman et al., 2009). While mantle exhumation dynamics are still not well understood, there is a consensus on the association of exhumed mantle seafloor exposures with long-offset low-angle normal faults or detachments (e.g., Canales et al., 2004; Cannat, 1993; Sauter et al., 2013; Tucholke & Lin, 1994). Figure 1.2.2.1 depicts several schematic cross-sections to explain the flip-flop rolling hinge model suggested to account for the exhumation of the broad mantle domains observed at the SWIR at 64°30'E (Sauter et al., 2013). Footwall flexural bending rotates steep long-offset normal faults, rooted at depths up to 20 km (Bickert et al., 2020; Schlindwein & Schmid, 2016) and with dips around 70° at 7 km depth below the seafloor (dbsf) (deMartin et al., 2007; Parnell-Turner et al., 2017), to low-angle detachment faults with dips ~35° at the seafloor (Cannat et al., 2017; 2019). The detachment faults exhume peridotites in the dome-shaped exposed footwalls (deMartin et al., 2007; Dick et al., 2010; Escartín et al., 2003; Ildefonse et al., 2007; Smith et al., 2006; Tucholke et al., 1998). Successive detachment faults may show an alternating change in the polarity developing a flip-flop fault mode and

exhuming mantle-derived rock on both sides of the spreading axis (Cannat et al., 2019; Reston, 2018; Sauter et al., 2013). Continuous exhumation of mantle-derived rocks has been inferred to last up to ~3 Myr at the MAR (Tucholke et al., 1998) and ~11 Myr at the SWIR at 64°30'E (Sauter et al., 2013). The latter location shows the largest exhumed mantle seafloor domains identified thus far (Cannat et al., 2006), a result of a complex flip-flop detachment faulting that is responsible for the asymmetrical seafloor spreading and accommodates most of the plate divergence in this area (e.g., Sauter et al., 2013; Reston 2018).

While most of the serpentinized peridotites found at the MAR are associated with OCCs and fracture zones, and in complex association with gabbroic rocks, the mantle exhumation dynamics are thought to be very similar to those responsible for the exhumed mantle domains at the seafloor at the SWIR at 64°30'E with a negligible amount of gabbros. At this location, detailed bathymetric and kinematic analyses (Cannat et al., 2019; Reston, 2018) have focused on investigating the seafloor expression of the flip-flop detachment faulting, i.e., the fault emergence on the seafloor and the fault breakaway, where the fault initiated, found at the highest bathymetric depth of the fault surface (Fig. 1.2.2.1). These studies additionally investigated the evolution of the flip-flop detachment faulting system and, consequently, the smooth-seafloor accretion and divergence. Numerical models have also demonstrated that flip-flop detachment faulting can develop in a thick brittle lithosphere by a combination of serpentinization and grain size reduction of dynamically recrystallized olivine in the ductile axial lithosphere (Bickert et al., 2020).

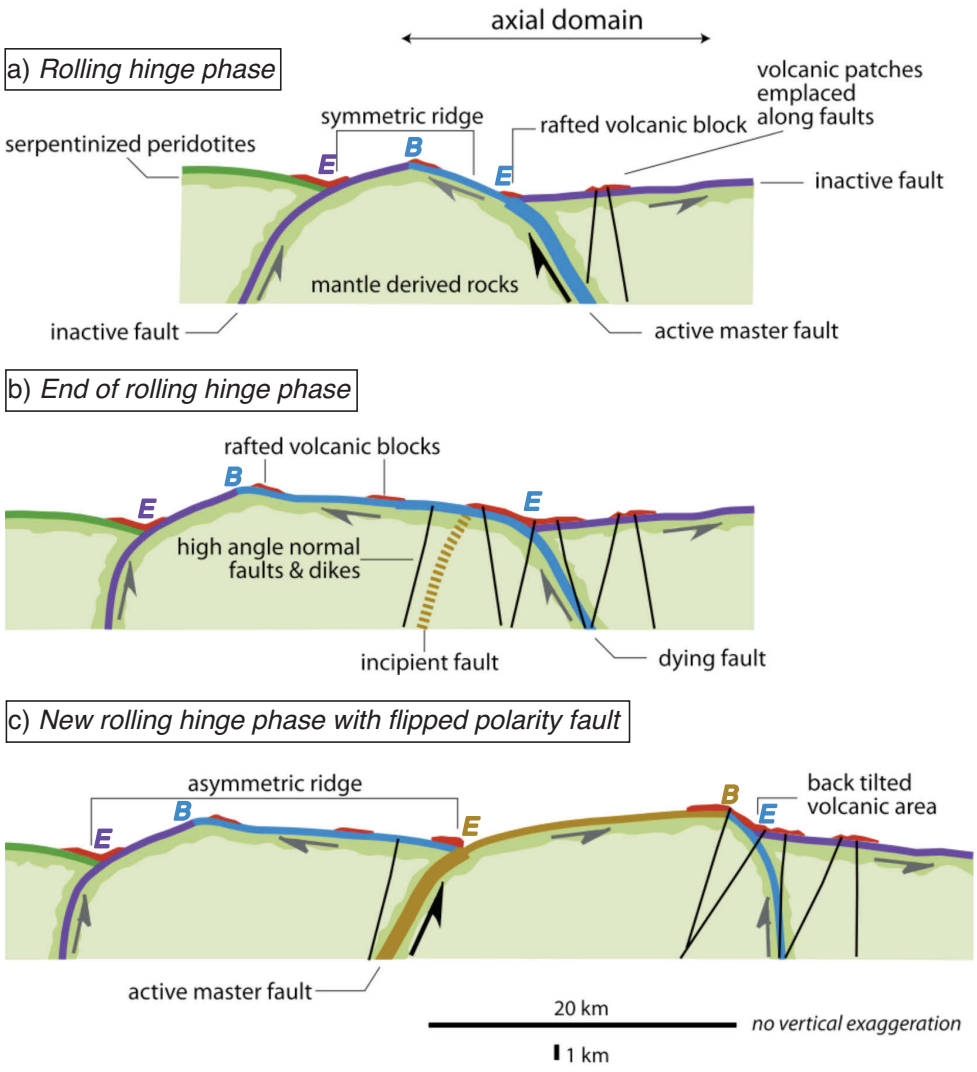

Figure 1.2.2.1. Illustration of the flip-flop rolling hinge model (Sauter et al.2013). This model assumes initial steep-angle normal faults that are rotated and flattened to form low-angle detachment faults during the rolling hinge phase (a) and display exhumed serpentinized peridotites (light green shaded areas) on their footwall and along the fault plane. During the end of the rolling hinge phase (b), the low-angle exhumation fault is abandoned, and a new steep normal fault (thick brown dashed line) cuts up through the weakened serpentinized footwall, initiating a new master detachment fault (c). Successive axial detachments may flip polarity locating mantle-exhumed rocks at both flanks of the ridge and a new rolling hinge phase with flipped polarity begins (c). Part of the footwall of the previous master fault is separated from the exhumed fault surface and becomes the hanging wall of the new master active fault (c). Red bodies on the seafloor in (a, b and c) are volcanic patches and thin solid black lines are high-angle normal faults and dikes. The colors of the faults and the exhumed fault surfaces in (a, b and c) aid to visualize older faults and cross-cutting relationships among them. The faults from older to younger age are represented by green, purple, blue, and brown. The *E*s and *B*s in (a, b and c) indicate the emergence and breakaway, respectively, of each fault. The *E*s and *B*s are colored according to their faults' surfaces.

1.1.3 Serpentinization

The exhumed and exposed peridotites interact with the seawater and become hydrothermally altered, or serpentinized. Serpentinization is a hydrothermal alteration that transforms the magnesium-rich silicate minerals (e.g., olivine) in peridotites into serpentine minerals. It is an exothermic process that releases large amounts of methane and hydrogen to the water column (Alt et al., 2009; Mével, 2003), key to the emergence and thriving of unique microbial communities (e.g., Früh-Green et al., 2018; Kelley et al., 2005; Schrenk et al., 2004). An example of a serpentinite-hosted hydrothermal field supporting microbial life is the recently discovered Old City at the SWIR (Lecoeuvre et al., 2020). Serpentinization also has a pivotal role in the flip-flop detachment faulting by facilitating the development of large-offset low-angle detachment faults (Ildefonse et al., 2007; Lavier et al., 1999; Tucholke et al., 1998). Deformation experiments on peridotites have shown that even small degrees of serpentinization (10–15%) can support the development of detachments by promoting strain localization and weakening of the lithosphere (Escartín et al., 2001). Particularly, lizardite and chrysotile minerals formed during serpentinization, have low fracture strength, low coefficient of internal friction and low coefficient of friction, reducing the strength of an altered or serpentinized peridotite (Escartín et al., 2001).

It used to be thought that serpentinization was a top-down process aided by the thermally induced cracks and fractures, formed as a consequence of the increasing temperature with depth, that act as pathways for seawater to percolate downward and alter the mantle rocks (e.g., Lister, 1974). However, more recent studies suggest that serpentinization is primarily controlled by detachment-related tectonics (e.g., Cannat et al, 2010; 2016; Rouméjon and Cannat, 2014). Detachment faults bring the mantle rocks up to shallower depths and into favorable temperature conditions (<400 °C), thus enhancing the serpentinization of the peridotites. Furthermore, multi-scale (tens of μm to hundreds of m) fractures generate a connected porosity capable of transporting hydrothermal fluids up to 4–5 km dbsf (Rouméjon et al., 2015; Rouméjon and Cannat, 2014).

1.2 Controlled-source marine seismology

Marine seismology has proven to be a very useful tool for comprehensive studies of seafloor structures and has indeed been the primary source of our current knowledge on the nature, formation, and evolution of the oceanic lithosphere.

1.2.1 Development

The birth of controlled- or active-source seismology dates back to 1849 when Robert Mallet designed the first experiment to measure the speed of elastic waves in onshore sand and rocks using dynamite explosions and to 1947 when the first land seismograms recorded compressional (P) and shear (S) waves using a weight drop as the source and a portable seismograph as the receiver (Mintrop, 1947). Soon after World War II, thanks to instrumentation development and the progress in the wave propagation theory, the study of the Earth's crustal structure at deep ocean began (e.g., Ewing et al., 1950; Raitt et al., 1949).

The majority of the early marine seismic refraction studies used first arrival travel times and plotted them in time-distance graphs to fit least-square slope-intercept solutions (e.g., Ewing et al., 1952; Katz et al., 1953; Raitt 1956). Further instrumental developments throughout the 1960s and 1970s, such as of Ocean Bottom Seismometers (OBS) and non-explosive airguns, and progress on the theoretical work, such as the ray method (Červený et al., 1977), together with the digital computer revolution, led to the development of methodologies still used today (e.g., ray tracing and synthetic seismogram methods) to study complex seafloor structures. Modern OBSs are normally equipped with a hydrophone and a 3-component seismometer (one vertical and two horizontal) and are sunk with an anchor to the seafloor where they continuously record seismic signals. The instrument retrieval is performed with an acoustic release command that disconnects the anchor from the OBS and allows the instrument to rise back to the surface. OBS surveys are also known as wide-angle seismic experiments because the large distances between the source and receiver permit the recording of wide-angle refraction and reflection

arrivals. Airguns are usually placed about 10–15 m below the sea level and triggered every tens to hundreds of m, and the OBS receivers, spaced apart several to tens of km, are placed on the seafloor.

Simultaneously, in the 1970s large-scale (100 km or more) near-vertical incidence seismic reflection experiments were enabled thanks to the airgun and streamer development. Airguns release compressed air from a submerged metal cylinder and propagate acoustic signals to distances of tens to hundreds of km and into the Earth's subsurface. A tuned airgun array is normally used to increase the data quality. A multi-channel seismic (MCS) streamer is a 2–15 km long string of hydrophones linearly arranged in a floating cable towed behind the ship to record the near-vertical incidence reflections of signals emitted by the airguns. The relative location of the streamer(s) and the airguns depend on the target and survey design. The streamer head is normally located up to a few hundred metres behind the airgun array, and both airguns and streamer(s) are usually submerged to depths of several to about 25 m. Figure 1.3.1.1 shows a conceptual diagram of a typical MCS and OBS complimentary survey acquisition. Tail buoys at the end of the streamer and airgun array, together with the streamer depth control birds, keep instruments afloat and include a GPS (Global Positioning System) providing accurate position measurements.

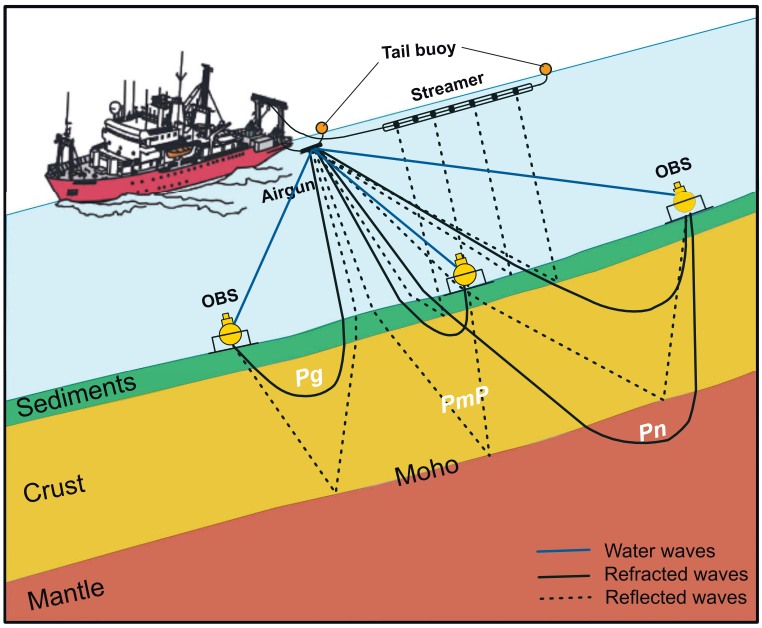

Figure 1.3.1.1. A simplified illustration of wide-angle profiling carried out synchronously with a coincident near-offset multi-channel seismic (MCS) survey. For the wide-angle survey, refracted crustal (Pg) and mantle (Pn) first arrivals are shown in solid black lines and the secondary reflected arrivals from the Moho (PmP) are shown in dashed black lines. Direct arrivals or water waves are shown in solid blue lines. OBS stands for Ocean Bottom Seismometer. For the MCS survey, seafloor and sediment interface layer reflections are shown in dashed black lines.

In the 1980s, the arrival of digital recording and computer data analysis enabled imaging of complex seafloor structures in 2D and 3D and controlled-source seismology experiments moved toward denser data coverage and smaller inter-receiver spacing (Prodehl and Mooney, 2012). The rise in computational resources in the 1990s and early 2000s, and consequently a considerable increase in data storing capabilities, led to further advances in seismic data processing and interpretation, such as travel time and, eventually, full-waveform tomography in laterally heterogeneous media (e.g., Zelt and Smith 1992, Van Avendonk et al., 1998; Korenaga et al., 2000; Pratt, 1999; Virieux and Operto, 2009). During these two decades, large-scale international and interdisciplinary research programs to study seafloor and ocean structures became more frequent, including InterRidge, founded in 1993 to share and promote worldwide MOR research studies.

1.2.2 Application to mid-ocean ridge studies

At fast- and intermediate-spreading rates, controlled-source seismic studies have first identified the so-called axial magma lens (AML), which is located in the mid-crust beneath the sheeted dikes and above the gabbroic layer 3. In reflection images AML stands out as a bright reflection interpreted to correspond to the top of the magma chamber (e.g., Herron et al., 1978; Kent et al., 1990; 2000), and in refraction studies it is characterized by the top of a region of low seismic velocity and high attenuation (e.g., Arnoux et al., 2019; Canales et al., 2014; Dunn et al., 2000) attributed to high temperatures. The AML discovery was followed by additional findings: (1) melt and solid gabbro sills embedded within dunite of the oceanic Moho transition zone (Nedimović et al., 2005); (2) melt lenses embedded within lower crustal gabbros (Canales et al, 2009); (3) off-axis crustal melt lenses (Canales et al, 2012); and (4) sub-axial melt lenses (Marjanović et al., 2014; Carbotte et al., 2020, 2021). Reflection imaging and waveform inversion of MCS data indicate that the mid-crustal AMLs are, in standard MOR settings, usually up to several hundred meters wide and up to 100-150 m thick, while extending for large distances along the ridge axis (e.g., Xu et al, 2014). Thicker and wider AMLs are usually found in anomalous settings, such as the areas exhibiting hotspot-ridge interaction (e.g., Arnulf et al., 2014). Collectively, these discoveries provide critical support for the crustal generation hypothesis from multiple magma bodies and a much more complete understanding of both the magma plumbing system of the largest volcanic system on Earth and oceanic crustal accretion at fast and intermediate spreading rates.

AML-type and other magmatic sills have also been reported at the MAR, for example beneath the Snake Pit hydrothermal area at ~1.2 km dbsf just south of the Kane fracture zone (Calvert, 1995), the Lucky strike axial volcano at ~3.5 km dbsf (Combier et al., 2015), and at the non-transform discontinuity where the Rainbow hydrothermal field is located at ~2–10 km dbsf (Canales et al., 2017). Similarly, magma sills have also been identified at magmatically-robust segments of ultraslow-spreading ridges. For instance, the Dragon Flag Supersegment at the SWIR between the Indomed (~46°00’E) and the Gallieni (~52°00’E) fault zones exhibit an anomalously hot mantle underlying the crust,

estimated to be ~75°C higher than the temperature normally associated with MOR basalts at faster spreading rates (Li et al., 2021). The authors suggest that the anomalously hot mantle may be related to a mantle plume. A 3D controlled-source seismic refraction experiment at the segment center at 50°28'E shows an anomalously thick robust magmatic crust, with an average crustal thickness of 9.5 km on-axis and of 7.1 km off-axis (Jian et al., 2016). A global average thickness for the oceanic crust formed at spreading rates of 20 mm/yr and above is around 6–7 km (Chen, 1992; Christeson et al., 2019; Bown and White, 1994; White et al., 1992). Furthermore, a large region with a low-velocity anomaly at ~4-9 km dbsf indicates the presence of an AML, which suggest that the 9.5-km-thick crust is essentially accreted by magmatism (Jian et al., 2017).

At slow- and ultraslow-spreading rates, a large along-axis crustal thickness variability within and between segments has been determined by controlled-source experiments (e.g., Muller et al., 1999). Magma-rich and magma-starved lithospheric accretion processes can alternate over short periods of time (~400 to ~800 kyr) (e.g., Canales et al., 2000a). The transition from volcanic seafloor to non-volcanic seafloor at a segment can take place over a very short time (~80–160 kyr; e.g., Canales et al., 2000a) and over short distances (~20-50 km; Cannat et al., 2019; Corbalan et al., 2021). This long and short time-scale variability may mask systematic variations in the lithospheric structure related to spreading rates in geophysical and geochemical data (e.g., White et al., 2001). The majority of the studies at ultraslow-spreading ridges attribute the crustal thickness variability to a thin and highly variable lower crust, Layer 3, such as on the Arctic Mohns (Klingelhöfer et al., 2000) and Knipovich ridges (Kandilarov et al., 2008), and the SWIR at 66°E (Minshull et al., 2006). Segment ends at the SWIR at 66°E show a nearly absent Layer 3 (Minshull et al., 2006), and similarly, the SWIR at 57°E shows systematic thinning of crustal Layer 3, sometimes also accompanied by thinning of Layer 2, towards the segment ends (e.g., Muller et al., 2000). Likewise, Jokat & Schmidt-Aursch (2007) interpreted the absence of a basaltic cover or magmatic crust at the non-transform segment end at the Gakkel Ridge, while the structure at the Atlantis Bank at the SWIR at ~57°35'E seems to indicate a nearly absent Layer 2 and a ~2-km-thick Layer 3 topping a 2–3-km-thick layer of serpentinized mantle peridotites (Muller et al., 1997).

Serpentinized peridotites are frequently inferred in the lower crustal layer or topmost mantle and Moho transition zone in many of the controlled-source experiments in ultraslow-spreading ridges (e.g, Kandilarov et al., 2008; 2010; Jokat & Schmidt-Aursch, 2007; Muller et al., 1997).

The association of serpentinized peridotites with long-offset low-angle detachment faults was first made at segment ends and OCCs at slow-spreading ridges (e.g., Cann et al., 1997; Tucholke et al., 1998; Tucholke and Lin 1994). The first conceptual models of the detachment faulting were supported by bathymetric and acoustic backscatter images (e.g., Cann et al., 1997; Tucholke et al., 1998), until the detachment geometry in depth was imaged for the first time in the eastern Central Atlantic (Reston and Ranero, 1999). In this study, a prestack depth migrated MCS section shows a continuous crustal reflection up to ~2 km subbasement depths, with dip decreasing from ~30° at the deepest imaged part to ~20° near the basement. Similar observations of the detachment faults on MCS sections are detected at magma-poor rifted margins, such as the Galician margin (e.g., Nur Schuba et al., 2018) and the Nova Scotian margin (e.g., Jian et al., 2021). Steep-dipping reflections associated with an active axial detachment fault have also been inferred at the ultraslow-spreading SWIR at 64°30'E (Momoh et al., 2017; 2020). Additionally, wide-angle seismic refraction experiments at OCCs have shown large lateral variation in P-wave velocities, with high-velocity anomalies and higher vertical velocity gradients beneath the footwall and low-velocity anomalies and lower gradient beneath the hanging wall (e.g., Blackman et al., 2009; Canales et al., 2008; deMartin et al., 2007).

While the geophysical observations at OCCs and magma-poor rifted margins are likely transferable to the melt-starved ultraslow-spreading segment ridges, there still are many unknowns about their characteristic seismic structure. Given the remarkable variability between and within ultraslow-spreading ridges, further high-resolution seismic imaging and velocity analysis may be crucial for addressing the remaining questions. Moreover, the complex flip-flop detachment faulting proposed for the lithospheric accretion at the magma-poor domains at the SWIR at 64°30'E still lacks subsurface constraints from a well-resolved regional-scale velocity model to extrapolate to depth the geological and

geophysical constraints on the seafloor. Coincident and complimentary MCS data can further benefit a detailed OBS tomographic study by providing the complementary seismic reflection structure for which true fault dips can be estimated via prestack depth migration using the computed tomographic velocity model.

1.3 Significance, aim, scope and structure of this thesis

Ultraslow-spreading oceanic ridges (less than ~20 mm/yr) constitute about 35% of the global ridge system (Dick et al., 2003) and yet their subsurface structure and the associated tectonic processes are poorly understood. At these spreading rates, mantle-derived peridotites can be exposed with little or no presence of volcanic rocks, and thus, classical models of crustal structure do not fit geological and geophysical observations at these ridges. The seismic signature of the exposed peridotites, which are variably serpentinized, is not well characterized, and the processes that lead to peridotite seafloor exposure (mantle exhumation dynamics) are poorly constrained.

Serpentinized peridotites are not only ubiquitous to slow- and ultraslow-spreading ridges but are thought to be present along more than 50% of the world's rifted margins, where they were formed during early stages of amagmatic continental breakup due to mantle exhumation and exposure to seawater (Cannat et al., 2009). Magmatic and amagmatic rifting, and the serpentinization associated with the latter, differently impact post-breakup processes like margin subsidence and sedimentation, which in turn impact petroleum prospectivity of a region (e.g., Play Fairway Analysis Atlas, 2011). Serpentinized peridotites are also widely present in the oceanic lithosphere at subduction zones where they are thought to have a significant impact on the subduction zone processes, such as dehydration and partial melting, and therefore, related natural hazards (e.g., Halpaap et al., 2019).

Therefore, geophysical fingerprinting of serpentinized peridotites is relevant not only for a better understanding of the oceanic lithosphere at ultraslow-spreading ridges but also for deepening our knowledge about magma-poor rifted margins and subduction zones.

However, in these latter settings, the mantle lithosphere is found deeper than at the ridges and is generally covered by a thick post-rift sedimentary package or sedimentary accretionary prism, which hinders the characterization of the mantle serpentinized domains leaving ultra-slow spreading ridges as the optimal site for such studies. Furthermore, geophysical fingerprinting of serpentinized peridotites at ultra-slow spreading ridges appears to have the potential for far-reaching trans-disciplinary implications, such as contributing to a better understanding of the occurrence of serpentinite-hosted hydrothermal fields, producing base knowledge useful to the advancement of the natural carbonation of peridotites and their potential for CO_2 sequestration, or providing insights for risk analysis of future subduction of very hydrated lithosphere formed at ultraslow-spreading ridges.

The French-Canadian marine geophysical project SISMO-SMOOTH (Leroy & Cannat, 2014) collected 2D and 3D MCS and OBS data across and along the SWIR at 64°30′E during the Fall of 2014. Figure 1.4.1 shows the explored seafloor in the eastern SWIR and the SISMO-SMOOTH study area. The seafloor, composed of variably serpentinized peridotites and known as the “smooth-seafloor” (Cannat et al., 2006), exhibits a bathymetry characterized by broad ridges that are 15 to 90 km long and 500 to 2000 m high, with a smooth, rounded topography (Cannat et al., 2006, 2019). This thesis is focused on the analysis and interpretation of regional 2D data collected along two orthogonal ~150-km-long OBS and MCS profiles, the north-south (NS) profile that is perpendicular to the spreading axis and the east-west (EW) profile that is subparallel to it. Figure 1.4.2 shows the data acquisition and the relation of all the OBS and MCS profiles used for this thesis work.

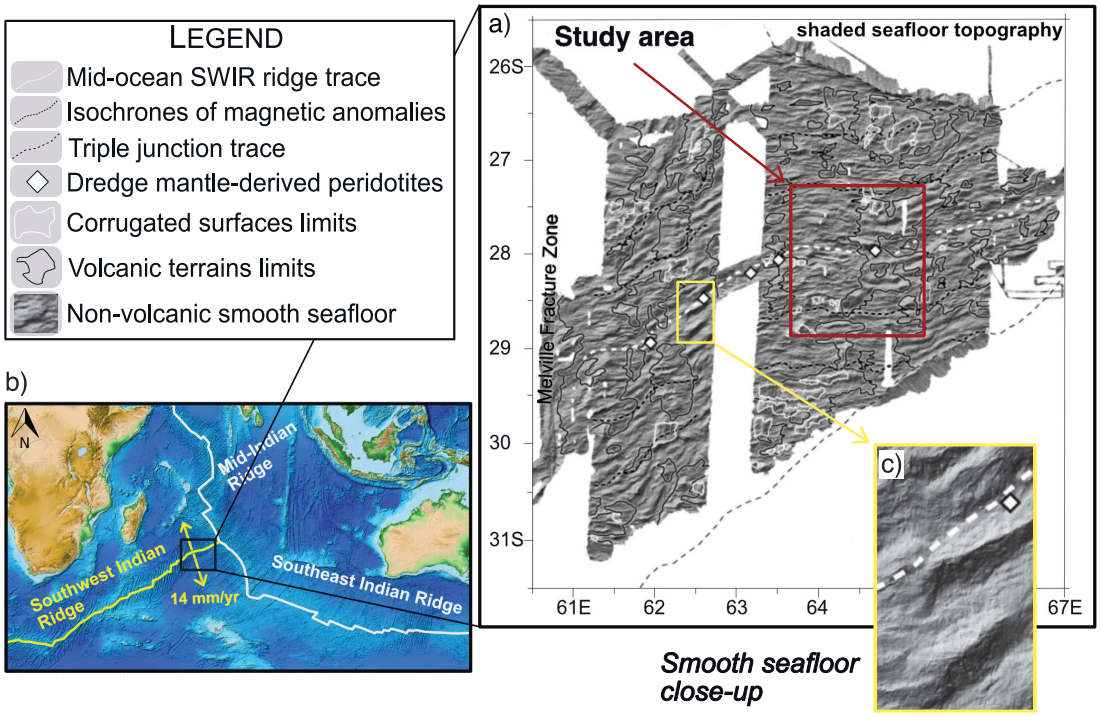

Figure 1.4.1. Thesis study area and the SWIR. (a) Shaded seafloor topography image of the eastern SWIR with an illumination azimuth of 330° (modified from Cannat et al. 2006). The red square delimits the study area of this thesis work, and the yellow square shows a close-up image of the non-volcanic ocean floor characterized by broad ridges with a smooth, rounded topography. (b) ETOPO1 global relief map showing the Southwest Indian Ridge and the location of (a).

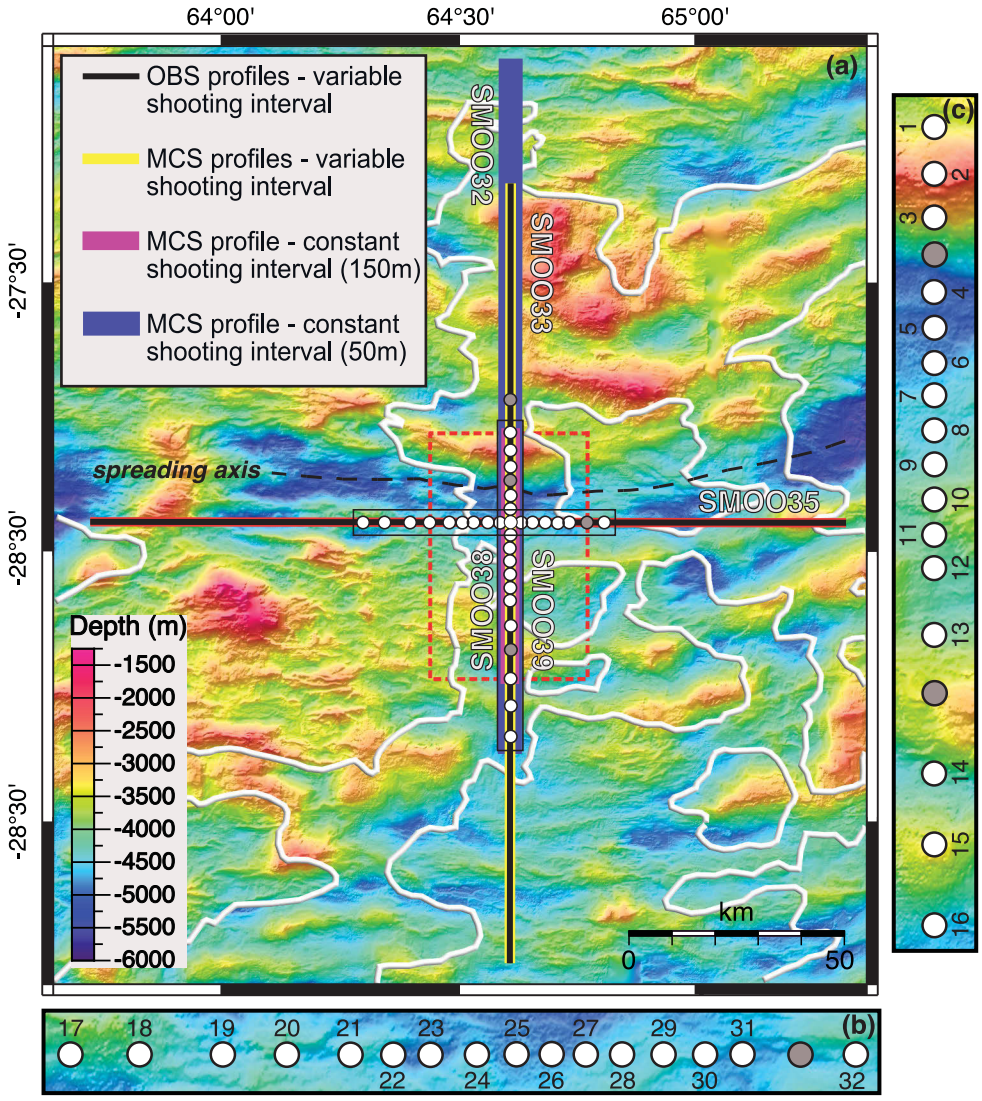

Figure 1.4.2. Thesis study area and data acquisition geometry. (a) Bathymetric map (Cannat et al., 2006; Momoh et al., 2017) of the eastern SWIR with the SISMOSMOOTH Survey (Leroy et al., 2015) acquisition. Shot locations of two regional orthogonal OBS profiles NS (SMOO33) and EW (SMOO35) are shown with solid black lines. White and gray circles with black outlines are the positions of OBS instruments that did and did not provide useful data, respectively. The shooting distance outside the dashed red rectangle is 300 m and inside is 150 m. Coincident MCS profiles (SMOO33 and SMOO35) that share the exact same shot locations and the same variable shooting interval are shown with thick red lines. Coincident shorter MCS profiles with a constant shooting interval of 150 m (SMOO38 and SMOO39) are shown with thicker pink lines. The coincident MCS profile shot every 50 m (SMOO32) is shown with an even thicker dark blue line. Profile SMOO32, SMOO33, and SMOO39 acquisition direction is North to South. Profile SMOO38 acquisition direction is South to North, and SMOO35 is West to East. Dashed black line shows the spreading axis location. Areas bounded by thick white lines delimit the smooth non-volcanic seafloor (Cannat et al., 2019). (b, c) Magnifications of the main map within thin black rectangles show the positions of the OBS instruments along the EW (b) and NS (c) profiles. Only the OBS with useful data are sequentially numbered, first in NS and then EW direction.

The SWIR at 64°30'E displays the widest exhumed mantle domains identified thus far (Cannat et al., 2006) and it is one of the geologically most sampled areas of the ultraslow-spreading seafloor (e.g., Sauter et al., 2013; Rouméjon et al., 2014). Geological sampling in the area nearly exclusively recovered variably serpentinized peridotites with a minor amount (<5%) of basalts and gabbros (Sauter et al., 2013). The dearth of mafic rocks is important because, as experimental studies have shown (e.g., Miller and Christensen, 1997; Christensen, 2004), the range of P-wave velocities in serpentinized peridotites (from ~5 km/s for 100% serpentinization to ~7.95 km/s for 0% serpentinization) overlaps with the range of P-wave velocities of basalts and gabbros –as low as ~2.5 km/s for on-axis lavas (e.g., Berge et al., 1992; Carbotte and Scheirer, 2004) and up to ~7.4 km/s for gabbros on average (e.g., Christensen and Salisbury, 1975). While a high *Vp/Vs* ratio (≥1.9) can be useful to identify serpentinized mantle-derived rocks (Grevemeyer et al., 2018a), P-to-S conversions are not very frequent at young oceanic lithosphere (<10 Ma), making the studies of S-wave velocity (*Vs*) challenging, and in need of very long profiles across the ridge (e.g., ~330-km-long; Funnell et al. 2021). Even in these cases, the S-wave coverage may still be up to four times lower than the P-wave coverage (Funnell et al. 2021). The easier access to the variably serpentinized mantle domains in the study area compared to rifted margins and subduction zones, but also in comparison to other known ridge areas, and the lack of contamination by mafic rocks, makes the SWIR at 64°30'E an ideal natural laboratory and the globally best place for geophysical fingerprinting of serpentinized peridotites.

The aim of this thesis work is to provide geophysical constraints on the seismic characteristic of variably serpentinized peridotites and on the mantle exhumation dynamics responsible for bringing them up to the seafloor. Three key questions that this PhD work addresses are: (i) how deep does serpentinization extend, (ii) is the oceanic Moho at ultraslow oceanic spreading ridges a serpentinization front, (iii) and what is controlling the serpentinization and the serpentinization depth? The proposed work is uniquely well suited for geophysical characterization of the exhumed mantle serpentinized domains because the chosen coincidental and complimentary OBS/MCS profiles: (1) cross the globally widest seafloor mantle domains identified so far, and (2)

the OBS spacing is dense (average ~10 km) for traveltime tomography purposes and the coincident MCS data were collected using a 4.5 km long streamer, thus allowing for accurate definition of detailed regional structure via high-resolution crustal-scale velocity models and reflection images.

This thesis consists of 5 chapters and 5 appendices, which are structured as follows:

Chapter 1: Introduction

In this chapter a concise and comprehensive introduction to key concepts and geological context is given to better understand the following chapters.

Chapter 2: Seismic velocity structure along and across the ultraslow-spreading Southwest Indian Ridge at 64°30′E showcases flipping detachment faults

This chapter is written in article form and was published in the *Journal of Geophysical Research: Solid Earth* as Corbalán, A., Nedimović, M. R., Louden, K. E., Cannat, M., Grevemeyer, I., Watremez, L., & Leroy, S. (2021). Seismic velocity structure along and across the ultraslow-spreading Southwest Indian Ridge at 64°30'E showcases flipping detachment faults (https://doi.org/10.1029/2021JB022177).

In this chapter, I present and interpret two P-wave traveltime tomographic profiles. The two 150-km-long profiles are orthogonal to each other, one across and one along the ridge axis of the ultraslow-spreading SWIR at 64°30′E. The resulting velocity models, constructed by inverting first arrival traveltimes recorded by 32 OBSs (16 along each profile), are the first detailed 2D regional P-wave velocity models developed for an amagmatic ultraslow-spreading ridge segment. Complimentary derivative products used to aid interpretation are velocity anomaly models, vertical velocity gradient models, and uncertainty assessment models. Analysis of all the produced results led to the first subsurface constraints on a system of flipping detachments, depth estimates for the extent of serpentinization, and a hypothesis on what is controlling the serpentinization depth.

The results also suggest that the lithosphere at the ultraslow-spreading SWIR at 64°30′E gradually transitions from highly fractured and fully serpentinized at the top to unaltered peridotites at depth. A major change in the lithospheric structure and composition on the profile subparallel to the ridge is inferred westward, characterized by a change from variably serpentinized peridotite domains in the East to predominately mafic magmatic domains in the West. This change, supported by earlier seafloor mapping and geological sampling, is attributed to a shift in the seafloor accretion mode propelled by an increase in melt supply. The differences in the seismic velocities between the two orthogonal profiles change as a function of depth in amplitude and polarity and are attributed to different sources of seismic anisotropy.

Chapter 3: Evolution of tectonically accreted oceanic topmost lithosphere

This chapter is written in article form as Corbalán, A. & Nedimović, M. R. (2023). Evolution of tectonically accreted oceanic lithosphere.

In this chapter, I present the results from the analysis of the seismic velocity changes along the NS profile as a function of distance and age from the spreading axis. As the lithosphere formed at spreading ridges migrates off-axis driven by mantle convection, it ages and evolves. In this process, the lithosphere undergoes significant physical, chemical, and mechanical changes. Thus, lithospheric evolution carries crucial implications for ocean water chemistry, hydrothermal systems, and microbial ecosystems, to name a few. Such evolution has been observed at magmatically accreted lithosphere as evidenced by its seismic velocity increase. However, information on the evolution of the tectonically accreted topmost lithosphere, which makes up for ¼ of the global oceanic lithosphere, is, still, lacking. Here, I show that the tectonically accreted lithosphere, normally found at ultraslow- and segment-ends of slow-spreading ridges, also evolves but in a faster and fundamentally different way from its magmatically accreted counterpart. Moreover, the inferred greater water content of the tectonically accreted lithosphere throughout the evolution process carries significant implications for past and future subduction zone processes and associated geohazards.

Chapter 4: Seismic reflection structure across the ultraslow-spreading Southwest Indian Ridge at 64°30′E

In this chapter, I present and interpret the results from industry-grade MCS processing of 4 profiles across the SWIR at 64°30'E, which together make a ~180-km-long profile coincident with the NS OBS profile. The already computed (in Chapter 2) tomographic velocity model allows me to run Kirchhoff depth migration and calculate the true dips of the detachment faults. Thus, the resulting prestack depth migrated section provides additional constraints on the faults' geometry responsible for mantle exhumation and continuous lithospheric tectonically accretion. The active detachment fault shows a steeper-angle dip (~45°) compared to the dip angles observed at abandoned detachments (~25°). This is consistent with their different phases in the flip-flop rolling hinge model responsible for lithospheric accretion. The active fault is in a new rolling hinge phase, while the abandoned faults are at the end of the rolling hinge, with their footwalls already rotated and flattened to lower dips. The prestack depth migrated section also provides seismic constraints in serpentinization. Higher serpentinization gradients are found in the footwalls of the active and abandoned detachments, while lower serpentinization gradients are found in the hanging walls. A serpentinization front separating highly fractured and fully serpentinized peridotites above from less fractured and less serpentinized peridotites below is inferred beneath the dome footwall of the active fault. Small-offset faults formed during footwall flexural rotation are identified about 16 and 33 km away from the spreading axis, amongst the inactive faults.

Chapter 5: Conclusions

This final chapter offers a summary of the most important research contributions presented in chapters 2, 3 and 4, and includes recommendations for future work directions.

Appendix A, B, C, D, and E

A: Supporting Information for Chapter 2.

B: Methods for Chapter 3.

C: Supporting Information for Chapter 3.

D: Supporting Information for Chapter 4.

E: Copyright release printable license.

Chapter 2

Seismic velocity structure along and across the ultraslow-spreading Southwest Indian Ridge at 64°30'E showcases flipping detachment faults

Key Points:

- First detailed 2D regional P-wave velocity models across and along an ultraslow-spreading Southwest Indian Ridge amagmatic segment
- A system of flipping detachments is imaged in the subsurface for the first time constrained by the velocity structure
- Lithosphere gradually transitions from highly fractured and fully serpentinized peridotites at the top to unaltered peridotites at depth

2.1 Abstract

We present two ~150-km-long orthogonal 2-D P-wave tomographic velocity models across and along the ridge axis of the ultraslow-spreading Southwest Indian Ridge at 64°30'E. Here, detachment faults largely accommodate seafloor accretion by mantle exhumation. The velocity models are constructed by inverting first arrival traveltimes recorded by 32 ocean bottom seismometers placed on the two profiles. The velocities increase rapidly with depth, from 3–3.5 km/s at the seafloor to 7 km/s at depths ranging from 1.5–6 km below the seafloor. The vertical gradient decreases for velocities >7 km/s. We suggest that changes in velocity with depth are related to changes in the degree of serpentinization and interpret the lithosphere to be composed of highly fractured and fully serpentinized peridotites at the top with a gradual downward decrease in serpentinization and pore space to unaltered peridotites. One active and five abandoned detachment faults are identified on the ridge-perpendicular profile. The active axial detachment fault (D1) shows the sharpest lateral change (horizontal gradient of ~1 s^{-1}) and highest vertical gradient (~2 s^{-1}) in the velocities. In the western section of the ridge-parallel profile, the

lithosphere transitions from non-volcanic to volcanic over a distance of ~10 km. The depth extent of serpentinization on the ridge-perpendicular profile ranges from ~2-5 km, with the deepest penetration at the D1 hanging wall. On the ridge-parallel profile, this depth (~2.5-4 km) varies less as the profile crosses the D1 hanging wall at ~5-9 km south of the ridge axis.

2.2 Plain Language Summary

We investigate the Southwest Indian Ridge lithosphere at 64°30'E, where the Somalian and Antarctic plates move slowly away from each other at less than 14 mm/year. This is one of a limited number of places on Earth where mantle is currently being exhumed to the seafloor. We use seismic sensors, placed across and along the ridge axis, to analyze how seismic waves travel from the energy sources, through the lithosphere, to these sensors. Our results, in the form of two-dimensional velocity models, show that the rock velocities increase rapidly with depth. Lateral and vertical velocity changes delimit a system of detachment faults on the ridge-perpendicular profile, responsible for bringing mantle-derived rocks, peridotites, up to the seafloor. Based on the modeled velocities and velocity changes, and previous extensive seafloor sampling, we suggest that ~75% of the lithosphere in the study area is composed of highly fractured and fully hydrothermally altered peridotites at the top with a gradual downward decrease in alteration and pore space to unaltered peridotites at depth. We also locate the transition to lithosphere with a magmatic component in the western section of the ridge-parallel profile.

2.3 Introduction

The global mid-ocean ridge system consists of spreading centres that greatly differ from each other in their spreading rate, spreading obliquity, melt supply and modes of seafloor accretion. Oceanic ridges are normally classified by their full-spreading rate as fast- (~80–180 mm/yr), intermediate- (~55–70 mm/yr), slow- (20-55mm/yr), and ultraslow-spreading (<~20 mm/yr) (Dick et al., 2003). The scientific community has invested significant effort into studying the oceanic crust formed at fast- (e.g. Aghaei et al., 2014;

Canales et al., 2003; Detrick et al., 1993; Dunn & Toomey, 2001; Grevemeyer et al., 1998; Han et al., 2014; Vera & Diebold, 1994), intermediate- (e.g. Canales et al., 2005; Carbotte et al., 2006, 2008; Nedimović et al., 2005, 2008; Newman et al., 2011; Weekly et al., 2014) and slow-spreading rates (e.g. Arnulf et al., 2012; Barclay et al., 1998; Christeson et al., 2020; Dannowski et al., 2010; Escartín & Canales, 2011; Estep et al., 2019; Kardell et al., 2019; Seher et al., 2010, Xu et al., 2020). Less effort has been directed toward studying the lithosphere formed at ultraslow-spreading ridges, which thus remains relatively less well understood. Yet, the ultraslow-spreading centers constitute about 35% of the global ridge system (Dick et al., 2003). The comparatively smaller effort put toward understanding the lithosphere at ultra-slow ridges is partially a consequence of their remoteness and inaccessibility, as these ridges are located in the Arctic (Gakkel Ridge, Knipovich Ridge, Mohns Ridge, and Kolbeinsey Ridge) and Indian Oceans (Southwest Indian Ridge - SWIR) (Argus et al., 2011; Bird, 2003; Kreemer et al., 2014; Müller et al., 2008).

Early controlled-source seismic surveys (e.g. Ewing & Ewing, 1959; Houtz & Ewing, 1976; Peterson et al., 1974; Raitt, 1963; Talwani et al., 1965, 1971), in situ rock investigations and laboratory velocity measurements on rock samples (e.g. Carlson & Miller, 1997, 2003; Christensen, 1972; Christensen & Salisbury, 1975; Miller & Christensen, 1997), and ophiolite studies (e.g. Christensen, 1978; Christensen & Smewing, 1981) suggest an oceanic crustal structure composed of three seismically identifiable layers that often correspond, from top to bottom, to an extrusive basaltic lava layer (Layer 2A), a sheeted diabase dike layer (Layer 2B), and a Layer 3 comprised of isotropic gabbros at the top and layered gabbros at the bottom topping the uppermost mantle. However, the seismic boundaries do not necessarily correspond to lithological boundaries. For instance, the layer 2A/2B boundary, which is thought to be an alteration front or a major change in porosity, may or may not correspond to a change in lithology (e.g., Berge et al., 1992; Carbotte and Scheirer, 2004; Christeson et al., 2007; Wilcock et al., 1992). Igneous mafic layers 2A, 2B and 3 are often distinguished according to their commonly associated velocity and thickness ranges, as well as their vertical velocity gradients (Christeson et al., 2019; Grevemeyer et al., 2018b; White et al., 1992).

However, identified outcrops of exposed mantle-derived peridotites on the seafloor at slow- and ultraslow-spreading ridges (e.g., Blackman et al., 2002; Cannat et al., 2006; Dick et al., 2008; Ildefonse et al., 2007) have challenged the 3-layer paradigm at slower spreading rates. Moreover, sampling of the seafloor at the SWIR has nearly exclusively (~90%) recovered serpentinized peridotites (Sauter et al., 2013) suggesting the total absence of continuous igneous mafic layers at the sampled locations.

Exhumed mantle seafloor exposures are generally associated with detachment faults (e.g., Canales et al., 2004; Cannat, 1993; Sauter et al., 2013; Tucholke & Lin, 1994) and Oceanic Core Complexes (OCCs) at slow- and ultraslow-spreading ridges (e.g., Dick et al., 2019; Escartín et al., 2003; Sauter et al., 2013; Smith et al., 2006; Zhao et al., 2013; Zhou & Dick, 2013). Widespread detachment faulting indeed plays a central role in oceanic lithosphere accretion and plate divergence accommodation at melt-poor ridge sections of slow- and ultraslow-spreading ridges (Cann et al., 1997; Cannat et al., 2006; Escartín et al., 2008; Sauter et al., 2013; Smith et al., 2006), particularly at segment ends as magma is focused toward the segment centers (Lin et al., 1990) and thus is scarce at the ends. At the slow-spreading Mid-Atlantic Ridge (MAR), the mode of asymmetrical accretion along detachment faults can last for 1–3 Myr (Tucholke et al., 1998) while at the SWIR continuous exhumation of mantle-derived rocks has been occurring during the last ~11 Myr in a flip-flop detachment faulting mode (Sauter et al., 2013). Steep long-offset normal faults rotate and flatten as footwall flexural bending occurs exposing the ultramafic mantle peridotites on the detachment surface (deMartin et al., 2007; Dick et al., 2010; Escartín et al., 2003; Ildefonse et al., 2007; Smith et al., 2006; Tucholke et al., 1998). These long-offset normal faults root on a steeply dipping (~70°) interface (deMartin et al., 2007; Parnell-Turner et al., 2017) at depths up to 20 km (Bickert et al., 2020; Schlindwein & Schmid, 2016).

The exhumed peridotites become hydrothermally altered when in contact with seawater. Peridotite-seawater interactions release large amounts of methane and hydrogen to the water column (Alt et al., 2009; Mével, 2003) making serpentinization relevant to the emergence and thriving of unique microbial communities (e.g., Früh-Green et al., 2018;

Kelley et al., 2005; Schrenk et al., 2004). Serpentinization also plays a crucial role in the detachment faulting and favors the development of large-offset low-angle detachment faults (Ildefonse et al., 2007; Lavier et al., 1999; Tucholke et al., 1998). New steep normal faults may initiate and become the new master detachment faults with the same or reverse polarity (e.g., Reston & McDermott, 2011; Sauter et al., 2013). Successive detachment faults that change polarity develop a flip-flop fault mode (Bickert et al., 2020; Reston, 2018; Sauter et al., 2013) and reveal exhumed mantle domains in this process on both sides of the spreading axis (Cannat et al., 2019; Reston, 2018; Sauter et al., 2013). What causes the abandonment of a fault and the initiation of a new master fault with opposite polarity is still under debate.

Coincident multichannel seismic (MCS) reflection and wide-angle ocean bottom seismometer (OBS) refraction surveys at ultraslow-spreading ridges are critical to understanding the crustal and uppermost mantle structure, the faulting dynamics associated with divergence, and the mechanisms of seafloor accretion. Seismic surveys at ultraslow-spreading ridges beyond the SWIR include work done at the Knipovich (Kandilarov et al., 2008, 2010), Mohns (Klingelhöfer et al., 2000), Gakkel (Jokat & Schmidt-Aursch, 2007), and Mid-Cayman (Van Avendonk et al., 2017; Grevemeyer et al., 2018a) spreading centers. At the SWIR, large efforts have been focused on the Dragon Flag OCC at 49°39’E (e.g. Zhao et al., 2013), the anomalously thick magmatic crust inferred at 50°28’E (e.g. Jian et al., 2016; Li et al., 2015), the Atlantis II Fracture Zone at 57°E (e.g. Muller et al., 1997, 2000), the non-volcanic seafloor exposures at 64°30'E (e.g. Momoh et al., 2017), and the mafic crustal structure at 66°E (e.g. Minshull et al., 2006).

In the Fall of 2014, French and Canadian scientists collaborated on the marine geophysical project SISMO-SMOOTH (Leroy & Cannat, 2014) aboard the R/V Marion-Dufresne to carry out a major 2D and 3D MCS and OBS survey across the SWIR at 64°30'E (Fig. 2.3.1), one of the geologically most sampled areas of the ultra-slow spreading seafloor. This location was also selected because, albeit remote, it does not have ice floes like the ridges in the Arctic Ocean, which allows for low-risk use of long

MCS streamers and large groups of OBSs. The main goal of the SISMO-SMOOTH project was to determine the seismic reflection and velocity structure of an ultraslow-spreading ridge to investigate the geophysical fingerprints of variably serpentinized mantle peridotites, map the lithospheric fabric, and better understand the mantle exhumation dynamics, all in an area where the mode of oceanic lithosphere accretion has been interpreted to form broad exposures of exhumed mantle (Cannat et al., 2006). The first results from the analysis of the collected data were focused on the 2D and 3D MCS reflection imaging (Momoh et al., 2017, 2020). Here, we present the results from a tomographic analysis of two orthogonal ~150-km-long OBS profiles, the north-south (NS) profile that is perpendicular to the spreading axis (SMOO33; Figs. 2.3.1a and 2.3.1c) and the east-west (EW) that is subparallel to it (SMOO35; Figs. 2.3.1a and 2.3.1b). The seismic velocity structure imaged along these two profiles provides new information on the subsurface expression of the detachment fault system, including the distribution of the detachment faults, the degree of exhumed mantle serpentinization and its anisotropy, and the east-west transition from predominantly exhumed mantle to more magma-rich lithosphere.

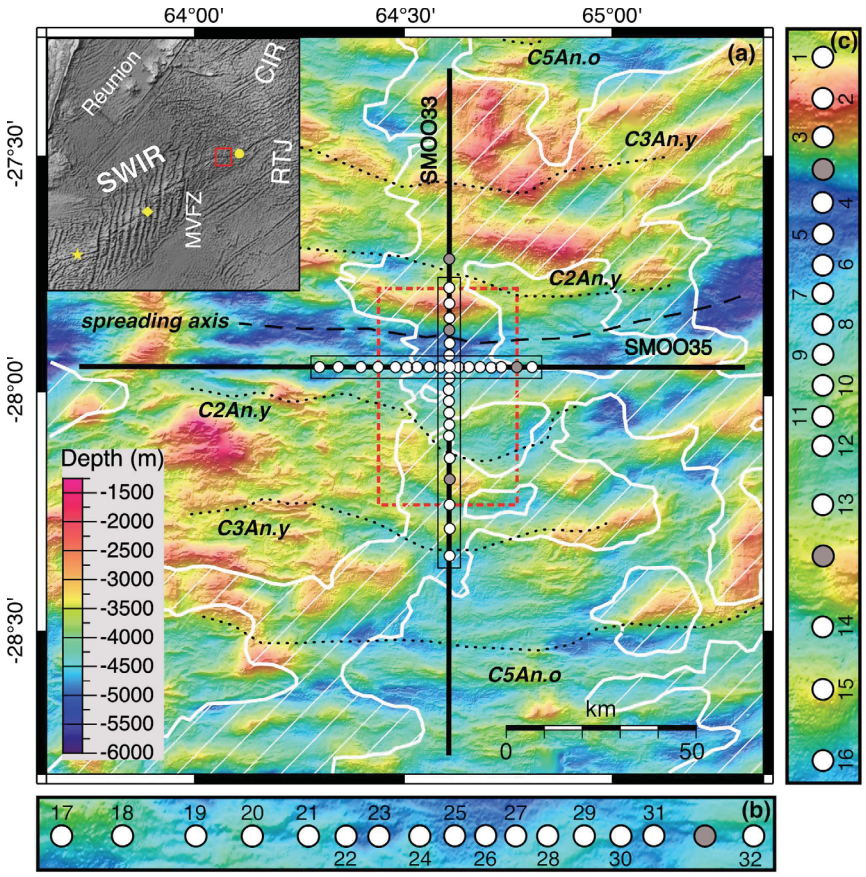

Figure 2.3.1. (a) Two regional orthogonal OBS profiles NS (SMOO33) and EW (SMOO35) from the SISMOSMOOTH Survey (Leroy et al., 2015) overlay a bathymetry map (color background; Cannat et al., 2006; Momoh et al., 2017). Thick black lines outline shot locations, and white and gray circles with black outlines are the positions of OBS instruments that did and did not provide useful data, respectively. The shooting distance inside the dashed red rectangle is 150 m and outside 300 m. Dashed black line shows the spreading axis location. Dotted black lines indicate the magnetic anomalies isochrons C2An.y (2.581 Ma), C3An.y (5.894 Ma), and C5An.o (10.949 Ma) (Cande & Kent, 1995; Cannat et al., 2006; Sauter et al., 2008; Reston, 2018). Areas filled with inclined thin white lines and bounded by thick white lines delimit the smooth non-volcanic seafloor (Cannat et al., 2019). Inset in the top left shows the location of the Southwest Indian Ridge (SWIR) relative to the Réunion Island, the Central Indian Ridge (CIR), the Melville Fracture Zone (MVFZ), and the Rodriguez Triple Junction (RTJ). Red rectangle shows the limits of the study area presented in the main figure. The yellow star, diamond and circle indicate the locations of earlier SWIR investigations at 50°E, 57°E and 66°E, respectively. (b, c) Magnifications of the main map within thin black rectangles show positions of the OBS instruments along the EW (b) and NS (c) profiles. Only the OBS with useful data are sequentially numbered, first in NS and then EW direction.

2.4 Study area

The SWIR is an ultraslow-spreading center (Dick et al., 2003; Sauter & Cannat, 2010) with a full spreading rate of <14 mm/year (Kreemer et al., 2014). Variations in melt-supply, mantle thermal and compositional heterogeneities, and changes in spreading obliquity along this ridge result in significant large-scale variations of the accreted lithosphere (Cannat et al., 2008). For instance, the easternmost SWIR, east of the Melville Fracture Zone (61°E) and west of the Rodriguez Triple Junction (70°E), is considered to be an endmember in the global ridge system where the interplay between plate- and mantle-driven processes results in a thin or absent mafic igneous crust with a complex relationship between intermittent volcanic edifices, corrugated volcanic seafloor and extensive exhumed mantle domains (Cannat et al., 2003, 2006). At 66°E the mafic igneous crust is estimated to be 2.2-5.4 km thick (Minshull et al., 2006), less than the global average of ~6 km (Chen, 1992; Christeson et al., 2019), while the SWIR at 50°28'E shows an anomalously thick (~9.5 km) crust (Jian et al., 2016). At 64°30'E, which is at the center of our study area (Fig. 2.3.1), the SWIR exhibits the widest non-volcanic seafloor documented thus far (Cannat et al., 2006) with on-axis volcanic centres inferred to the east and west (Cannat et al., 2003; Schlindwein & Schmid, 2016).

In the last two decades, several surveys have focused on studying the SWIR at 64°30'E and have used gravity (Cannat et al., 2006), magnetics (Sauter et al., 2008) and side-scan sonar (Sauter et al., 2013) to identify and map the extension of these non-volcanic seafloor domains (Fig. 2.3.1a) known as “smooth-seafloor” (Cannat et al., 2006). Variably serpentinized mantle-derived rocks, peridotites, are the dominant lithology at the “smooth-seafloor” (Sauter et al., 2013) and coincide with high residual mantle Bouguer gravity anomaly (RMBA; 30–50 mGal) (Cannat et al., 2006). The seafloor topography is characterized by rounded broad ridges with a height ranging from 500 to 2000 m and a length ranging from 15 to 90 km (Cannat et al., 2006, 2019). Sixteen dredges collected across-axis in the amagmatic corridor of the SWIR at 64°30'E nearly exclusively recovered variably serpentinized peridotites with a minor amount (<5%) of basalts and gabbros (Sauter et al., 2013). Oxygen isotope analyses on these samples suggest relatively

high serpentinization temperatures (271–366°C) and in-situ and bulk-rock analyses of the samples support seawater as the serpentinizing fluid, ruling out leaching of basalts or gabbros (Rouméjon et al., 2014). Moreover, the scarcity of melt products is expected as a result of the very low melt supply inferred in the area based on large axial depth and high mean basalt sodium content (Cannat et al., 2008; Meyzen et al., 2003; Seyler et al., 2003).

Momoh et al. (2017) studied the 3D seismic reflection structure at the SWIR at 64°30'E and suggested that the uppermost lithosphere consists of a 4–5 km thick layer mostly composed of serpentinized peridotites with a small proportion of igneous rocks derived from occasional and incipient magmatism. Two main packages of seismic reflections are imaged across the ridge axis: (1) a group of subparallel reflections dipping south at 50–60° in the footwall and (2) a group of north dipping reflections in the hanging wall of the active detachment fault (Momoh et al., 2017). The former are interpreted to be related to the damage zone of the active axial fault, and the latter are suggested to represent either the damage zone of a previously active fault's footwall or to be related to recent tectonic extension occurring on the hanging wall. Similarly, Momoh et al. (2020) proposed that the crustal-type seismic velocities are related to extensive tectonic damage and hydrothermal alteration of both peridotites and occasional intruding gabbros. Serpentinization and incipient magmatism are thought to occur in two successive phases: first when mantle-rocks are exhumed on the active detachment fault footwall and later when these rocks constitute the hanging wall of the next detachment fault (Cannat et al., 2019; Momoh et al., 2020).

Microseismicity studies have constrained a thick (20–25 km) brittle lithosphere in the vicinity of our study area (Schlindwein & Schmid, 2016). As a consequence of the virtually-zero melt supply, the seafloor is largely created by successive, flipping polarity, detachment faults that form broad unroofed mantle domains both north and south of the spreading axis (Cannat et al., 2006, 2019; Sauter et al., 2013; Reston, 2018). Active and abandoned detachment fault surfaces have been imaged with side-scan sonar at the SWIR at 64°30'E (Sauter et al., 2013) and seismic reflections associated with the currently active axial detachment fault have been observed in 3D MCS data (Momoh et al., 2017).

Numerical models have demonstrated that a combination of serpentinization and grain size reduction in thick brittle lithosphere can generate flip-flop detachment faulting (Bickert et al., 2020). Detailed bathymetric and kinematic analysis have been carried out to investigate the emergence and breakaway of the interpreted faults and explain the mantle exhumation dynamics at detachment-dominated spreading ridges (Cannat et al., 2019; Reston, 2018). Still lacking, however, is a well-resolved regional-scale velocity model capturing these detachment faults, active and abandoned, to back up or rebut the proposed lithospheric accretion models.

2.5 Data acquisition and analysis

2.5.1 Seismic experiment

The MD 199 - SISMO-SMOOTH Cruise 2014 (Leroy & Cannat, 2014; Leroy et al., 2015) in the easternmost SWIR collected a variety of datasets including pseudo-3D MCS (Momoh et al., 2017), 2D MCS (Momoh et al., 2020), 3D wide-angle OBS, and 2D wide-angle OBS. The 3D MCS and 3D OBS data are focused in narrow (1.8x24 km and 20x30 km, respectively) rectangles at the ridge axis, while the 2D profiles extend ~150 km across and along the spreading axis. In this paper, we show and interpret the results from analysis of the regional 2D OBS wide-angle data set (Fig. 2.3.1). Shots for the 3D MCS survey recorded by OBSs 4-13 on the NS profile (Fig. 2.3.1) were used by Momoh et al. (2017) to form a simple velocity model for migration of the reflection signal. However, none of the regional 2D OBS shots recorded by the 32 OBSs on the NS and the EW profile (Fig. 2.3.1), which provide a far greater source-receiver offset range and crossing ray area that are needed for extracting high-quality detailed velocity information, have been analyzed prior to this study.

The seismic source consisted of two linear arrays of 7 air guns towed at an average depth of 14 m with a total nominal volume of 6790 in3. Three different types of short-period OBS were used to record the wide-angle data: 16 Canadian OBSs from Dalhousie University, 7 French OBSs from the Institut National des Sciences de l'Univers du

CNRS, and 9 micro OBSs from the National Central University of Taiwan. All the OBSs recorded continuously at a sampling rate of 250 Hz (4 ms) with one hydrophone and a 3 orthogonal component geophone. The OBS spacing ranges from 3 to 10 km. For presentation purposes, OBS names used during the survey were converted to sequential numbers (Fig. 2.3.1; Table A.1). OBSs north of OBS 1, and between OBSs 3 and 4, OBSs 13 and 14, and OBSs 31 and 32 were lost during the survey or recorded unusable data. The white circles in Figure 2.3.1 are the 32 OBS instruments used for the modeling. These OBSs form the two ~150 km long wide-angle seismic profiles. The EW profile (SMOO35) lies in the spreading axis direction, and the NS profile (SMOO33) is orthogonal to and crosses the spreading axis (Fig. 2.3.1a). The NS profile cuts through the inferred detachment faults and practically all of its OBSs lie within the previously mapped smooth seafloor. The EW profile is presumed to transition from volcanic seafloor in the west to exhumed mantle at the seafloor in the east.

2.5.2 Data processing

The OBSs were relocated to their true positions on the seafloor (more information in Supporting Information) and the data were bandpass filtered using a minimum phase trapezoidal band-pass filter with corner frequencies 1-5-18-25 Hz. PASTEUP software (Fujie et al., 2008) was used to manually pick the first break of arrivals on the OBS records. Two examples of OBS gathers for the NS and the EW profiles, with and without picks, are shown in Figure 2.5.2.1. More examples are shown in Supporting Information (Figs. A.1-A.4). The picking was carried out on unfiltered data as much as possible, with the filtered data used only to extend the picks to further offsets. Where first arrivals are not clear at long offsets, arrivals of the first water multiple were picked where possible and then time-shifted until picks from the multiple for near and/or mid offsets coincided with equivalent picks for the first arrivals. The 2D bathymetry from a previous multibeam survey (Cannat et al., 2006) was plotted in a separate window above the OBS data window as a function of model distance and source-receiver offset to help guide the picking process and identify seafloor diffractions. First arrivals were picked to offsets of up to ~90 km along the NS profile, and ~60 km along the EW profile. Assigned pick

uncertainty is offset dependent as follows: 30 ms for high-quality waveforms at offsets <6.5 km; 60 ms for offsets between 6.5 km and 12 km; 100 ms for offsets between 12 km and 20 km; 120 ms for offsets >20 km; and 150 ms for time-shifted multiple arrival picks. A total of 6,523 and 4,193 first arrival picks were made for the NS and the EW profile, respectively. Secondary arrivals, such as Moho reflections, were not found in the OBS records, and sediment arrivals were negligible.

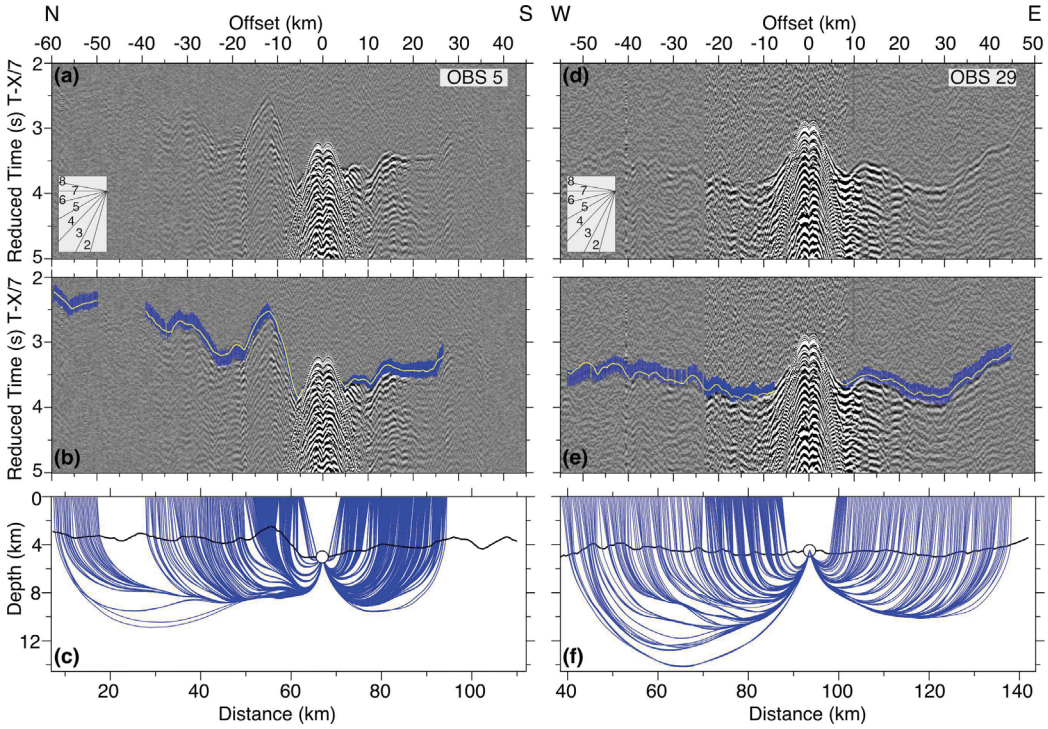

Figure 2.5.2.1. Example OBS gathers for the NS and EW profiles (a and d) are shown together with related first arrival traveltime picks (b and e) and calculated ray paths (c and f). (a) Hydrophone data for OBS 5 on the NS profile and (d) vertical geophone data for OBS 29 on EW profile after application of a reduction velocity of 7 km/s and band-pass filtering (1-5-18-25 Hz). Insets show the linear moveout of different phase velocities in km/s. (b and e) Same as a and b but with picked (centers of blue error bars) and modeled (yellow curves) first arrival traveltimes superimposed. Synthetic traveltimes and raypaths were computed by ray tracing through the final velocity model. (c and f) Raypath diagram for the modeled first arrival traveltimes in b and e. Black thick line is the seafloor and white circles with thin black outlines show the OBS locations.

2.5.3 Traveltime tomography

We performed P-wave traveltime tomography using TOMO2D (Korenaga at al., 2000). Traveltimes of P-wave first refracted arrivals and later Moho reflection arrivals (PmP) are

commonly used for joint inversion of the regional 2D velocity structure in a sheared mesh model hung from the seafloor (e.g., Watremez et al., 2015). We, however, do not model the Moho reflection because of the lack of PmP arrivals in the data. In the TOMO2D method, forward modeling is first applied to find the shortest raypath from the shot to the receiver for each arrival, followed by a least-squares regularized inversion, in which the starting velocity model is perturbed and updated until the targeted chi-squared (χ^2) or the set number of maximum iterations is reached (Korenaga et al., 2000). Application of smoothing and optional damping constraints is used to regularize the iterative inversion process (Korenaga et al., 2000). Thus, damping and smoothing weighting factors control the data fitting and the smoothness of the model, and similarly, the correlation lengths for the velocity nodes control the inversion stability. The final TOMO2D product is a minimum-structure smooth velocity model, meaning that minimum a priori information is used to resolve the minimum or simplest structure needed to explain the data. This approach reduces subjective input from the interpreter in the development of the final tomographic model.

Cells in our models, which are 160 km long and 30 km deep, are 1 km wide and 500 m high. The starting 1D velocity model is based on the 1D average velocity of Momoh et al. (2017) and the average velocity structure reported at other ultraslow-spreading centers bearing serpentinized mantle domains (e.g., Grevemeyer et al., 2018a; Van Avendonk et al., 2017). We opted for simplicity and, after taking into consideration the expected geology, settled on a 1D starting velocity model with 3 velocity-depth points: 4 km/s velocity at the seafloor, 6.5 km/s at 2 km depth below the seafloor (dbsf), and 8.0 km/s at 5 km dbsf. For consistency, the same 1D starting velocity model extended in 2D by hanging it off the seafloor was used for both orthogonal profiles. Figures 2.6.1.1a and 2.6.1.1d show the starting velocity model extended in 2D for both the NS and EW profile, respectively. For the NS profile, the starting velocity model produced a χ^2 of 11.97 and an RMS traveltime residual of 208 ms. For the EW profile, it produced a χ^2 of 15.37 and an RMS traveltime residual of 261 ms. We set our inversion to run 5 iterations and use the same parametrization values for both profiles to prevent modeling inconsistencies (more information in Supporting Information).

2.6 Results

2.6.1 Velocity models

Figure 2.6.1.1b shows the final velocity model for the NS profile. The model is shown over the areas with ray coverage and the calculated raypaths are shown in Figure 2.6.1.1c overlaying the final velocity model. The model converges to an RMS traveltime residual of 53 ms and a χ^2 of 1.10. Similarly, the final velocity model of the EW profile is shown in Figure 2.6.1.1e and the calculated raypaths are shown in Figure 2.6.1.1f. The EW model converges to an RMS traveltime residual of 55 ms and a χ^2 of 0.86. Figure A.5 shows the evolution of χ^2 as a function of iteration number for both models. Most of the lateral and vertical velocity variations are found in the central parts of the models, below the areas covered by the OBSs, and therefore in the areas where there are crossing raypaths (Figs. 2.6.1.1c and 2.6.1.1f). Toward the profile ends, which are sections covered by shots but no OBSs, or sections with no crossing raypaths, the velocity structure in the final models mostly follows the seafloor topography and the starting velocity models.

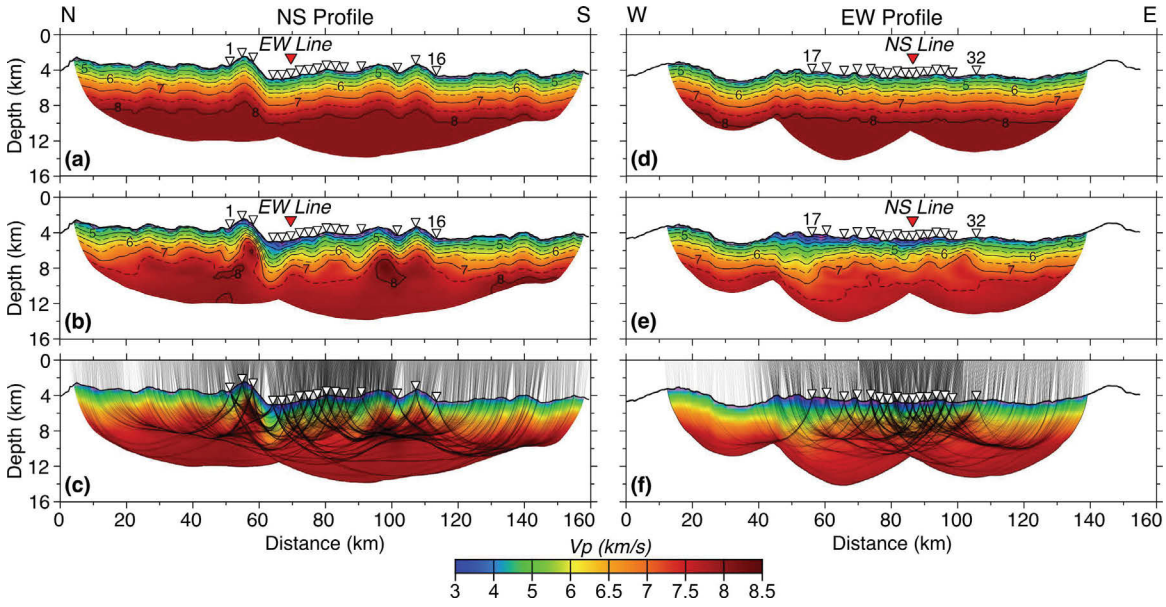

Figure 2.6.1.1. Results from first arrival traveltime tomographic inversion of the NS and EW profiles: (a, d) Starting velocity models; (b, e) final tomographic models; (c, f) raypaths (black lines) of the first arrivals traced through the final velocity models (b, e), for the NS and EW

profiles, respectively. Iso-velocity contours are shown every 0.5 km/s in (a, b, d and e); solid black at every km/s and dashed in between. White inverted triangles show the positions of the OBSs on the seafloor. Red triangles show the location at which the profiles cross each other.

Traveltimes are well fitted at all model distances (Figs. A.6a and A.6b) with the majority of traveltime residuals, calculated as the difference between the observed and calculated traveltimes, reduced by the inversion to ±60 ms (Figs. A.6c and A.6d).

The final velocity models (Figs. 2.6.1.1b and 2.6.1.1e) show that seismic velocities increase rapidly with depth with velocities ranging from ~3.5 km/s at the seafloor to 7 km/s at 1.5–5.5 km dbsf at the NS profile, and from ~3 km/s at the seafloor to 7 km/s at 2-6 km dbsf at the EW profile. The NS profile reaches velocities in the range of 7.8–8.4 km/s, while the EW profile only reaches velocities in the range of 7.6–7.8 km/s. The NS profile shows greater lateral changes in the velocities than the EW profile, including a sharp lateral change (horizontal gradient of ~1 s^{-1} at ~62 km model distance) at the highest topographic feature. Within the area of OBS coverage, the EW profile also shows a smooth trend of increasing velocities toward the East, which is accentuated between OBSs 30 and 32. Similarly, a distinct increase in the velocities is observed between OBSs 17 and 18. Both profiles show high vertical velocity gradient (velocity contours closely spaced) in upper sections of the models (velocities <7 km/s) and a considerably lower vertical gradient (sparse velocity contours) in deeper sections (velocities >7 km/s).

2.6.2 Uncertainty assessment

2.6.2.1 Checkerboard Tests

We assess the resolution of our models with checkerboard tests as follows. Checkerboard patterns for a set of different horizontal and vertical cycle lengths with a ±5% periodic velocity perturbation are added to our two final velocity models. The chosen cell widths and heights are: 25x10 km (Figs. 2.6.2.1.1a and 2.6.2.1.1d), 12.5x5 km (Figs. 2.6.2.1.1b and 2.6.2.1.1e), and 5x2.5 km (Figs. 2.6.2.1.1c and 2.6.2.1.1f). The perturbed velocity models are used as the starting velocity models for the inversions. The recovered

perturbations are obtained by subtracting the input velocity models from the corresponding final inverted velocity models for different cell sizes. The extent of perturbation recovery at any particular section of our models is a measure of resolvability of corresponding velocity anomalies for that model area. The input and inverted perturbation models are compared for the two profiles in Figure 2.6.2.1.1. Full-size checkerboard test figure is included in Appendix A (Fig. A.7). Large structures are resolved across the profiles where there is any ray coverage (Figs. 2.6.2.1.1a and 2.6.2.1.1d). Structures 12.5 km wide and 5 km high are resolved in the areas below the seafloor encompassing the first and last OBS location to depths of ~5 km. In these central areas, structures as small as 5x2.5 km are also resolved but the depth or resolvability below the seafloor is reduced to ~2–3 km. In all the checkerboard tests, the resolved cells are smeared toward profile ends and with increasing depth, with the resolution progressively declining.

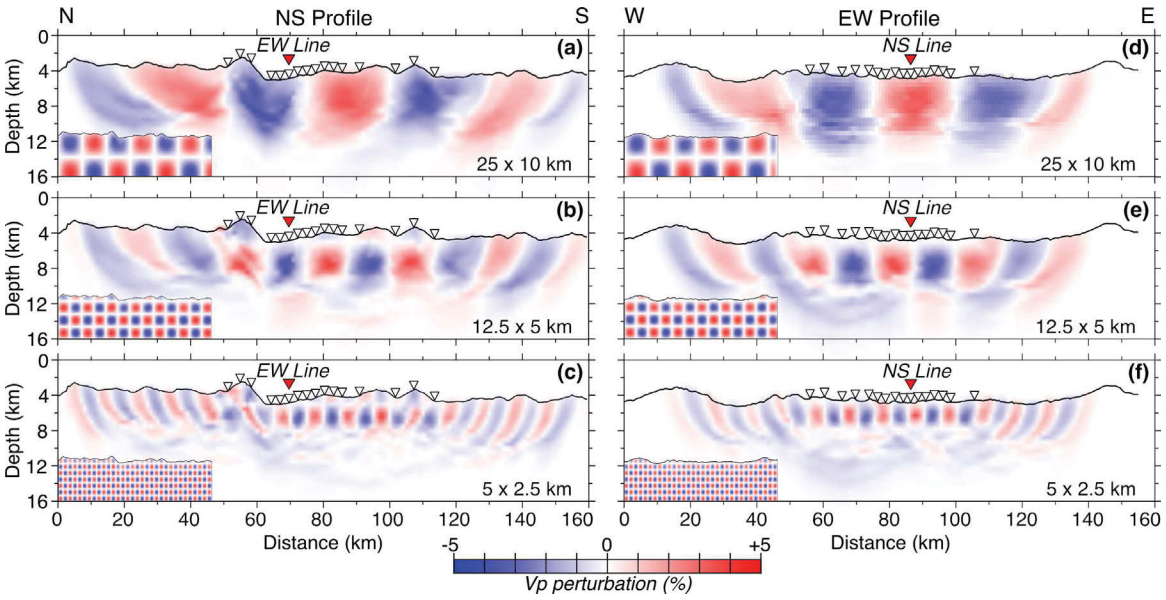

Figure 2.6.2.1.1. Checkerboard resolution tests for the NS (left column) and EW (right column) profiles for perturbation cells: 25 km wide x 10 km high (a and d), 12.5 km wide x 5 km high (b and e), 5 km wide x 2.5 km high (c and f). The input perturbed model is shown in the bottom left inset and the recovered perturbed model is the full-size figure. White and red inverted triangles as in Figure 2.6.1.1 caption.

2.6.2.2 Monte Carlo Analysis

We run a nonlinear Monte Carlo analysis (e.g., Tarantola, 1987) to estimate velocity uncertainty across our models following the strategy of Korenaga et al. (2000). For this analysis, the input velocity model (or starting velocity model) is randomized to create a set of 100 different input models (Fig. A.8). This is done by randomizing the velocities of the three nodes of the starting velocity model within a ±6% range and by randomizing the depths to the two sub-seafloor layer interfaces or inflection points within a ±1.1 km range. The 100 randomized 1D starting velocity models are used to form 100 randomized 2D starting velocity models and run 100 inversions (for both NS and EW profiles) using the same inversion parameters applied to calculate the final velocity models (Figs. 2.6.1.1b and 2.6.1.1e). The resulting tomographic models are averaged to produce average velocity models for the NS and EW profiles (Figs. 2.6.2.2.1a and 2.6.2.2.1d) and compute standard deviations of the P-wave velocities across these models (Figs. 2.6.2.2.1b and 2.6.2.2.1e). The results show that the inversion process is stable as the average velocity models (Figs. 2.6.2.2.1a and 2.6.2.2.1d) are very similar to the final velocity models (Figs. 2.6.1.1a and 2.6.1.1d) for both profiles. The standard deviation of seismic velocities for most of the lithosphere at central parts of the models is <~0.1 km/s (Figs. 2.6.2.2.1b and 2.6.2.2.1e). Larger standard deviations are observed in the areas that are less well resolved as indicated by the checkerboard patterns (Fig. 2.6.2.1.1), in areas with lower ray density (Figs. 2.6.2.2.1c and 2.6.2.2.1f) and especially where there are no crossing rays (Figs. 2.6.1.1c and 2.6.1.1f), and below the seafloor where no instruments were deployed. The ray density is presented by the derivative weight sum (DWS; Toomey & Foulger, 1989), a nondimensional relative indicator of ray coverage.

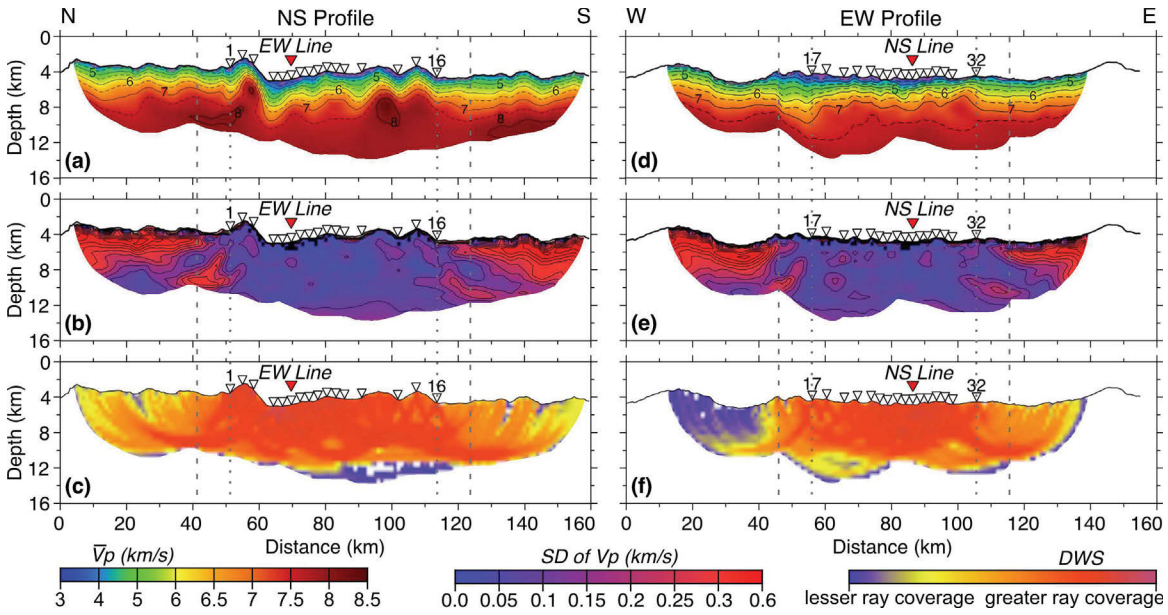

Figure 2.6.2.2.1. Results from the Monte Carlo analysis. Averaged final velocity models for the NS (a) and EW (d) profiles. Iso-velocity contours are shown every 0.5 km/s in (a and d); solid black at every km/s and dashed in between. Standard deviation of the P-wave velocity calculated via the Monte Carlo analysis for the NS (b) and EW (e) profiles. Solid black contours are shown every 0.05 km/s in (b and e). Derivative weight sums (DWS) indicating the ray coverage for the NS (c) and EW (f) profiles. In all panels, the dotted light grey vertical lines mark the end of the best resolved areas, and the dashed light grey vertical lines mark the ends of the well resolved areas. White and red inverted triangles as in Figure 2.6.1.1 caption.

2.6.3 Derivatives of the velocity models

To aid the discussion, we plot 1D velocity-depth functions (Fig. A.9) extracted at every 1 km distance within the best resolved areas of the two average velocity models (Figs. 2.6.2.2.1a and 2.6.2.2.1d). We use these functions to determine the average 1D velocity-depth functions and the extent of the velocity-depth envelopes for both profiles (Fig. A.9). We further augment our interpretation by computing and plotting velocity anomalies (Figs. 2.6.3.1a and 2.6.3.1c) and vertical velocity gradients (Figs. 2.6.3.1b and 2.6.3.1d) for both the NS and EW profile. The 2D velocity anomalies are calculated as the difference between the average velocity models (Fig. 2.6.2.2.1a and 2.6.2.2.1b) and the respective average 1D velocity-depth functions (Fig. A.9). The vertical velocity gradients are calculated by computing the central first derivative of the average velocity models (Fig. 2.6.2.2.1a and 2.6.2.2.1b).

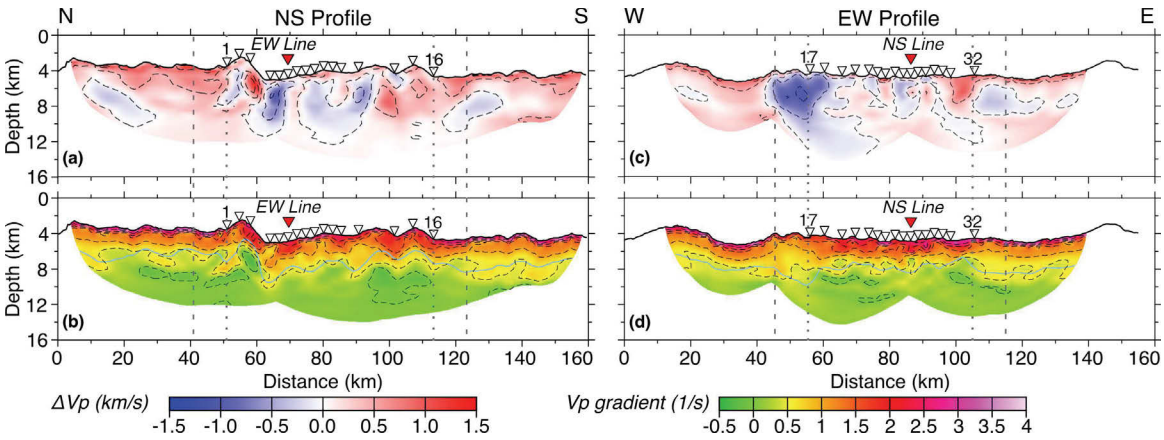

Figure 2.6.3.1. Velocity anomaly (top panels) and velocity gradient (bottom panels) results for the NS and EW profiles, respectively. Dashed black contours are shown every 0.5 km/s in (a and c) and every 0.5 s^{-1} in (b and d). The depth to the 7 km/s velocity contour is shown in (b) and (d) in a solid light blue line. White and red inverted triangles as in Figure 2.6.1.1 caption. Vertical dotted and dashed light grey lines as in Figure 2.6.2.2.1 caption.

2.7 Discussion

The final and average P-wave tomographic velocity models for the NS and EW profiles give insight into the subsurface structure of the SWIR at 64°30'E. In the following subsections, we discuss (1) the ridge structure and the distribution of the active fault and the older and now inert detachment faults; (2) the inferred lithospheric composition and its anisotropy; and (3) the velocity structure in our study area in the context of the known velocity structure elsewhere at the SWIR. We limit our discussion only to the geological structures that can be resolved as indicated by the checkerboard tests, and the areas of the velocity models that show standard deviations of <~0.1 km/s (Figs. 2.6.2.2.1b and 2.6.2.2.1e) and/or high ray coverage (Figs. 2.6.2.2.1c and 2.6.2.2.1f). This effectively limits our detailed interpretation to the best resolved areas (within the dotted light grey vertical lines in Fig. 2.6.2.2.1) with crossing rays and OBSs on the seafloor (51 to 114 km model distance for the NS profile and 55 to 106 km for the EW profile), with the regional interpretation extended to include the well resolved areas (within the dashed light grey vertical lines in Fig. 2.6.2.2.1) found up to ~10 km away from the first/last OBS on both profiles, as indicated by the Monte Carlo analysis results (Fig. 2.6.2.2.1)

2.7.1 Ridge structure

2.7.1.1 Delineation of detachment faults on the NS profile

The information extracted from the NS profile (Figs. 2.6.2.2.1a, 2.6.3.1a and 2.6.3.1b), which cuts across the SWIR at 64°30'E, is particularly useful for subsurface identification of the active and abandoned detachment faults. We first interpret a sharp lateral change in the velocities (a horizontal gradient of ~1 s^{-1} at ~62 km model distance; Figs. 2.6.2.2.1a and 2.6.3.1a) and a high vertical velocity gradient (1.5–2.5 s^{-1}; Fig. 2.6.3.1b) coincident with the shallow section (top 2 km, i.e., depth 0-2 km below seafloor) of the highest topographic feature (~51-62 km model distance) as the seismic expression of an active axial detachment fault (hereafter D1; Fig. 2.7.1.1.1). This bathymetric high is characterized by higher velocity than the surrounding regions (Fig. 2.6.2.2.1a) and its top surface has previously been interpreted as an active axial detachment fault based on side-scan sonar (Sauter et al., 2013), bathymetric and kinematic analysis (Cannat et al., 2019; Reston, 2018), and seismic reflection data (Momoh et al., 2017, 2020). Therefore, our velocity model supports these earlier interpretations as it shows the footwall exhuming (or bringing up to shallow depth) rocks of high velocities, those corresponding to lithologies typically found at greater depths, which become superimposed by the lower velocity rocks of the hanging wall at the topographic low immediately south. This north-south transition at ~62 km model distance from the detachment footwall to the detachment hanging wall is characterized by an abrupt decrease in the vertical gradient, from a high of 1.5–2.5 s^{-1} to a low of 0.5–1.0 s^{-1}, as well as by a switch in polarity of the largest velocity anomaly, from 1.5 km/s to -1.5 km/s.

Elsewhere, the NS profile exhibits smoothly varying low to moderate vertical velocity gradient values (<1.5 s^{-1}), except for several locations that show similar lateral changes in the vertical velocity gradient to D1, with higher vertical gradients (1.5–2.0 s^{-1}) juxtaposed with lower gradients (0–1.0 s^{-1}) at alike depths (~top 2 km). These are found at model distances of about 50 km, 74 km, 87 km, 101 km, and 113 km (Fig. 2.6.3.1b). The velocity anomalies (Fig. 2.6.3.1a) at these model distances also show a similar change to

D1, with a switch in the polarity from positive to negative anomaly, except at 50 km where the switch in polarity is reversed. Additionally, the velocities (Fig. 2.6.2.2.1a) across the profile show a repeat drop pattern that coincides with the changes observed in the vertical velocity gradient and velocity anomalies. While the identified vertical velocity gradient, velocity, and velocity anomaly changes are not as pronounced as for the interpreted active detachment fault D1, they are clearly recognizable and we interpret them to indicate the subsurface location of the abandoned detachment faults (D2 at ~50 km, D3' at ~74 km, D3 at ~87 km, D5 at ~101 km, and D7 at ~113 km; Fig. 2.7.1.1.1b).

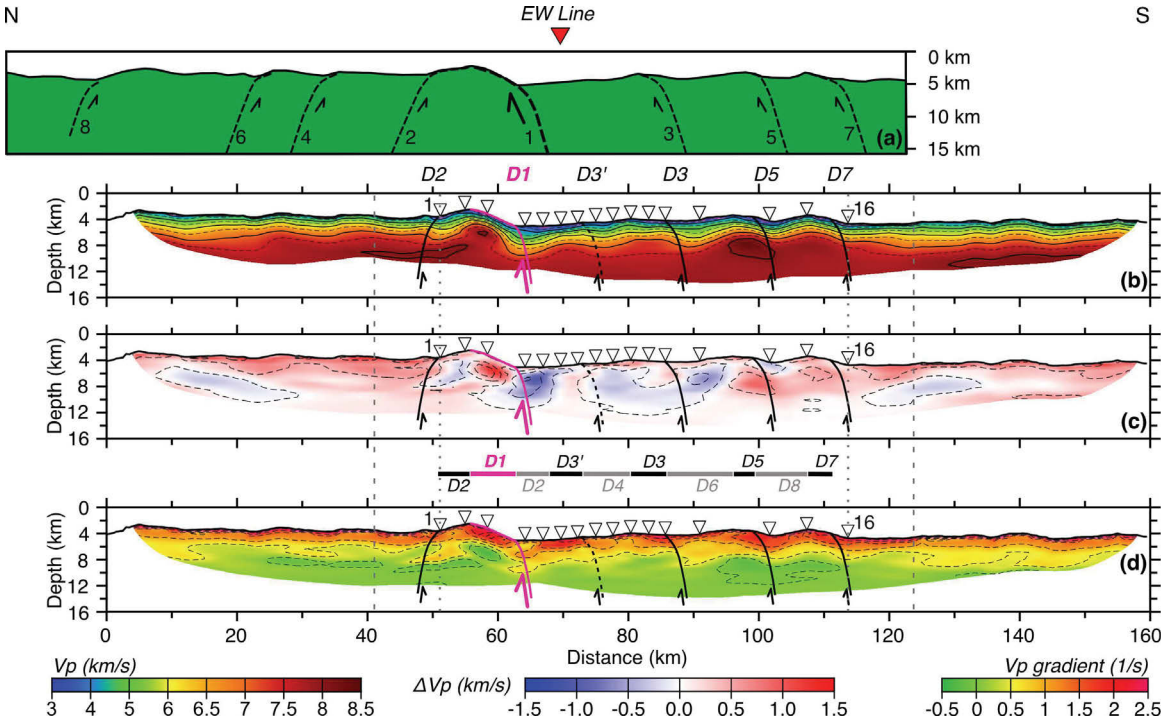

Figure 2.7.1.1.1. Comparison of a (a) conceptual model based on previous interpretations (Cannat et al., 2019; Reston, 2018; Sauter et al., 2013) depicting the sequence of flipping rolling-hinge faults (black dashed lines) along the NS profile and (b) the average velocity model from Figure 2.6.2.2.1a, (c) velocity anomalies from Figure 2.6.3.1a, and (d) vertical gradient from Figure 2.6.3.1b, with interpreted locations of corresponding faults (solid lines) for the best resolved area (51-114 km). In (a), previously interpreted faults are numbered 1–8 from youngest to oldest. In (b, c, and d) the identified faults are named *D2*, *D1*, *D3′*, *D3*, *D5*, *D7*, and are equivalent to faults *2*, 1, 3, 5, and 7 in (a) omitting *D3′* that is not inferred in (a). *D* stands for detachment. *D1* is the active detachment fault (solid pink line), and the fault numbers increase sequentially to describe older abandoned faults (solid black lines). Inset between (c) and (d) shows the interpreted extension of each detachment footwall surface located on the seafloor. The thin rectangle in pink limits the extension of *D1* footwall surface, the black rectangles limit the extension of *D2*, *D3′*, *D3*, *D5* and *D7* footwall surfaces, and the grey rectangles limit the extension of *D2*, *D4*, *D6*, and *D8* hanging wall surfaces. Iso-velocity contours are shown every 0.5 km/s in (b); solid black at

every km/s and dashed in between. Dashed black contours are shown every 0.5 km/s in (c) and every 0.5 s^{-1} in (d). White and red inverted triangles as in Figure 2.6.1.1 caption. Vertical dotted and dashed light grey lines as in Figure 2.6.2.2.1 caption.

2.7.1.2 Comparisons with earlier interpretations

In Figure 2.7.1.1.1, we compare our interpretation on the location of the detachment faults with that of previous interpretations (Cannat et al., 2019; Reston, 2018; Sauter et al., 2013), which are primarily based on observed bathymetric features, i.e., the location of the breakaway and emergence points on the fault surfaces. For simplicity, we list the detachment faults previously inferred from 1 to 8, with 1 being the youngest and 8 being the oldest fault (Fig 2.7.1.1.1a). Our velocity model (Fig. 2.7.1.1.1b), the velocity anomalies (Fig. 2.7.1.1.1c), and the vertical velocity gradient (Fig. 2.7.1.1.1d), provide supporting evidence for the existence of faults 1–3, 5 and 7. The reverse polarity in the pattern observed in the velocity anomalies at ~50 km model distance (Fig 2.7.1.1.1c), at the interpreted location of *D2*, coincides with the previously interpreted location of fault 2 (Cannat et al., 2019; Reston, 2018; Sauter et al., 2013), only offset by ~1 km south. Fault *D2* was active prior to *D1* and thus it shows opposite polarity. Similarly, the interpreted location for fault *D1* is comparable to the location of the previously interpretated fault 1, only offset by ~1 km north (Fig. 2.7.1.1.1). Previously interpreted locations of faults 5 and 7 are identical to the interpreted locations of *D5* and *D7* in this work, respectively, while fault 3 is offset by ~4 km north from *D3* (Fig. 2.7.1.1.1). The locations of faults *D1* and *D3* are also consistent with previously identified south dipping reflections in MCS data (Momoh et al., 2017, 2020) interpreted to be related to fault damage in the footwall. The results presented here also demarcate an abandoned detachment *D3′* that has not been inferred previously. Detachment *D3′* may have been missed in other models (Cannat et al., 2019; Reston, 2018; Sauter et al., 2013) because its seafloor expression shows a smoother emergence topography in comparison to the other interpreted faults based on bathymetry. One possible cause for this is a relatively short lifespan of the *D3′* fault, which precluded full development of the characteristic seafloor geometry of a detachment fault. Alternatively, the velocity signature observed at ~74 km model distance may possibly be related to recent extensional damage occurring in the hanging wall of *D1* as

proposed by Momoh et al. (2020), since no south dipping reflections related to this fault are imaged in MCS data (Momoh et al., 2017). However, given the resolution of our model, the presence of fault *D3′* provides an explanation that is more consistent with the velocity, velocity anomaly, and vertical gradient patterns observed at the locations of other interpreted faults (Figs. 2.7.1.1.1b, 2.7.1.1.1c, and 2.7.1.1.1d).

For our study area, Cannat et al. (2019) estimated the duration of the active deformation period for each detachment fault. The active life for these detachments ranges from 0.6 Myr to 2.8 Myr, with an average life of 1.35 Myr. Our interpretation of an additional detachment fault (*D3′*; Fig. 2.7.1.1.1) combined with the adjustment in the location of *D3* calls for a reevaluation of these age numbers. However, we can only estimate total fault longevity for detachments *D1* and *D2*, and partial longevity for faults south of *D1* since our NS velocity model does not resolve the location of the faults north of *D2* (Table 2.7.1.2.1). Like Cannat et al. (2019), we estimate the partial and total fault lifespans based on the horizontal distance between faults' emergence and breakaway points (Table 2.7.1.2.1). The inset shown in between Figures 2.7.1.1.1c and 2.7.1.1.1d illustrates the interpreted extension of each detachment footwall surface on the seafloor used for our calculations. Portions of each abandoned fault footwall are located both north and south of the spreading axis, except for the active detachment (*D1*) that has not yet been cut off by a new master fault and carried away from the axis. Portions of *D4*, *D6* and *D8*, the faults inferred further north of *D2* but not resolved by our velocity model, are also considered based on earlier interpretations of seafloor data (Cannat et al., 2019; Reston 2018; Sauter et al., 2013) to estimate the ages in Table 2.7.1.2.1. Our calculations point to a duration of ~0.7 Myr for *D2*, half the previously suggested age, and ~0.5 Myr for *D1*, larger than the previously suggested age (0.3 Myr).

Detachment # ***(Youngest to oldest)***	**Dip**	**Horizontal distance from fault emergence to adjacent fault breakaway** ***(km)***	**Horizontal distance from fault breakaway to adjacent fault emergence** ***(km)***	**Estimated partial fault duration based on distance** ***(Myr)***	**Estimated total fault duration** ***(Myr)***
D1 *(active)*	South	7.1	0	0.51	0.51
D2 *(North of D1)*	North	5.0	-	0.36	0.72
D2 *(South of D1)*	North	-	5.1	0.36	
D3'	South	5.1	*Unknown*	0.36	*Unknown*
D4	North	*Unknown*	7.3	0.52	*Unknown*
D3	South	5.5	*Unknown*	0.39	*Unknown*
D6	North	*Unknown*	10.2	0.73	*Unknown*
D5	South	3.4	*Unknown*	0.24	*Unknown*
D8	North	*Unknown*	8.0	0.57	*Unknown*
D7	South	3.9	*Unknown*	0.28	*Unknown*

Table 2.7.1.2.1. Estimated detachment fault longevity based on the horizontal distance between faults' emergence and breakaway locations of the inferred faults across the profile SMOO33 (NS profile).

2.7.2 Lithospheric composition

2.7.2.1 Exhumed mantle area

In order to relate the modeled velocities to the subsurface lithology, we assume that the investigated area is composed of exhumed mantle rocks ranging from variably serpentinized and fractured peridotites at shallower depths, to unaltered peridotites at greater depths. This is followed by conversion of the seismic velocities along the NS and EW profiles (Figs. 2.6.2.2.1a and 2.6.2.2.1d) to degree of serpentinization (Figs. 2.7.2.1.1a and 2.7.2.1.1b) using a linear relationship for partially-serpentinized peridotites (Fig. 2.7.2.1.1c) from Carlson & Miller (2003). These authors used empirical data (Christensen, 1978, 1996; Miller & Christensen, 1997) to evaluate how the relationship between P-wave velocities and the degree of serpentinization changes with different confining pressure and temperature. We choose the relationship for a temperature of 300°C, in agreement with the high serpentinization temperatures suggested for the rock

samples analyzed along the NS profile (Rouméjon et al., 2014). Albeit converting seismic velocities to degree of serpentinization is a simplification of the causes for the velocity heterogeneities, especially at the top of the model, it allows us to discuss how deep serpentinization may extend and what may control such depth.

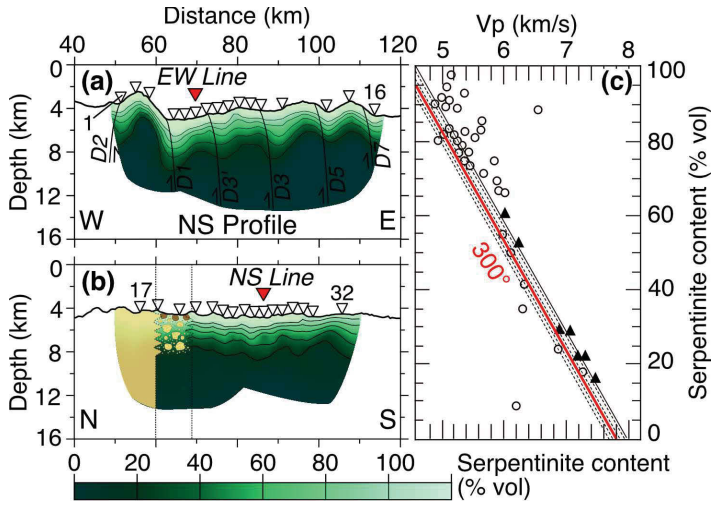

Figure 2.7.2.1.1. Estimated degree of serpentinization for the NS (a) and EW (b) profiles based on their tomographic velocities (Figs. 2.6.2.2.1a and 2.6.2.2.1d) and the linear relationship (c) of serpentinite content with P-wave velocity from Carlson and Miller (2003) for a temperature of 300°C, in agreement with oxygen isotopes studies in the area (Rouméjon et al., 2015). Black triangles in (c) are laboratory measurements of P-wave velocities in serpentinized peridotites at 25°C and at 200 MPa and open circles are velocity measurement at other confining pressure (up to a 1000 MPa). Carlson & Miller (2003) collected data points from several studies (Christensen, 1978, 1996; Miller & Christensen, 1997). Dashed lines show the approximate relationships at temperatures of 100, 200, 300, 400, and 500°C corrected from the best fitting relationship measured at 200 MPa (solid black line). In (a) the solid black lines show the detachment faults' locations interpreted in Fig. 2.7.1.1.1. In (b) the dotted lines show the location at which there is a change in the lithosphere (volcanic before 59 km, non-volcanic after 69 km, and transitional in between) as discussed in the text. Solid black contours in (a and b) show serpentinite content at every 20% vol. White and red inverted triangles in (a) and (b) as in Figure 2.6.1.1 caption.

While our assumption of the exhumed mantle domains throughout the study area is a simplification of the true geology, it is supported by several lines of evidence and justified by our intent of carrying out a first-order interpretation of the subsurface geology. First, earlier rock sampling of the seafloor in our study area (Rouméjon et al., 2014; Sauter et al., 2013) has predominately retrieved peridotites and the extent of the mapped smooth seafloor (Cannat et al., 2006) (Fig. 2.3.1), interpreted to represent exhumed mantle domains, covers majority (~¾) of the area along the NS and EW profiles

contained by the OBS instruments. Second, no reflection Moho has been identified in the pseudo-3D MCS dataset by Momoh et al. (2017), which indicates the lack of a distinct and seismically-well characterized Moho in our study area. Reflection Moho is often well imaged in upper oceanic lithosphere formed at faster spreading mid-ocean ridges where a 3-layer mafic oceanic crust tops the ultramafic uppermost mantle (e.g., Aghaei et al., 2014; Bouhalanis et al., 2020). Third, no wide-angle Moho reflected arrivals (PmP) are identified in the OBS data examined in this work, and these arrivals are routinely observed and picked in data collected worldwide in oceanic lithosphere formed at faster spreading rates (e.g., Canales et al., 2000b; Horning et al., 2016). Furthermore, the lack of PmP arrivals in our study area is consistent with observations from other ultraslow spreading ridges dominated by magma starved spreading conditions (Grevemeyer et al., 2018a).

We interpret the uppermost lithosphere to be composed of highly fractured and fully serpentinized peridotites at the top with a gradual decrease in pore space volume and serpentinization degree to unaltered peridotites at depth (Figs. 2.7.2.1.1a and 2.7.2.1.1b). The velocities lower than 4.5 km/s at the top of the model may be representative of peridotites that are fully serpentinized and heavily fractured. Geologically, these low velocities could also be representative of basalts. However, this possibility is highly unlikely because, whereas scattered low-volumetric basalts may be found across the study area (Sauter et al., 2013), the results of the extensive seafloor studies and the lack of Moho reflections in both wide-angle OBS and MCS data (e.g., Cannat et al., 2006; Sauter et al., 2013; Momoh et al., 2015) clearly indicate that a continuous basaltic top layer is not present.

While our first order interpretation is comparable to that of Momoh et al. (2017), the higher resolution and lateral variability of the new results presented in this work make it possible to carry out a detailed interpretation. Serpentinization seems more extensive and penetrates deeper along the NS profile than the EW profile. For example, 20% serpentinization extends to up to ~5 km dbsf on the NS profile and up to ~3–4 km dbsf on the EW profile, with the anomaly being the location of the active detachment fault (D1)

footwall where the 20% serpentinization contour is found at the shallowest depths of ~1.5–2 km dbsf (Figs. 2.7.2.1.1a and 2.7.2.1.1b).

The change from relatively large and quickly decreasing vertical velocity gradients (1.5-2.5 s^{-1}) at velocities <7 km/s, to relatively low and gradually decreasing vertical velocity gradients (<0.5 s^{-1}) at velocities >7 km/s (Figs. 2.6.3.1b and 2.6.3.1d) likely illustrates a change in the porosity and permeability regime that impacts the serpentinization process for the upper and lower sections of the profiles. These low and gradually decreasing vertical velocity gradients within deeper sections of the models also indicate that the Moho transition is not an abrupt serpentinization or alteration front, as has been suggested for the study area and elsewhere along the SWIR (e.g., Dick et al., 2019; Mével, 2003; Minshull et al., 1998, 2006), but rather a gradual transition from hydrated peridotites to unaltered peridotites. The smoother gradient of seismic velocities above 7 km/s in the EW profile suggests a more uniform upper mantle in comparison to the NS profile.

From Figure 2.7.2.1.1a, we further decipher the following: (i) Despite the similar penetration depth of serpentinization on both sides of individual detachment faults, for similar depths on both sides of the detachment, serpentinization is more pervasive in the hanging walls than in the footwalls. This is possibly due to the continuous exhumation of the footwalls that leaves hanging walls longer exposed to water at temperatures that are more optimal for the serpentinization to take place (e.g., D1, Fig. 2.7.2.1.1a); (ii) The depth and degree of serpentinization depends on the length of time the detachments were active. For example, amongst the abandoned detachments south of D1, the 20% serpentinization contour reaches deeper levels around faults D3’ and D3 than around D5 and D7, which agrees with the estimated longer active life for faults D3’ and D3 (Table 2.7.1.2.1). Therefore, we suggest that the bulk of the serpentinization occurs while detachment faults are active, with much diminished alteration after the lithosphere migrates off-axis. The longer a particular detachment is active, the deeper serpentinization reaches due to both more extensive deformation of the fault walls resulting in greater porosity and permeability and longer exposure to seawater. The overall increase in velocity and, therefore, decrease in estimated degree of

serpentinization from the active to abandoned detachment faults is possibly caused by a reduction in porosity by closure of cracks and fractures once fault activity stops and the fault moves away from the ridge axis.

2.7.2.2 EW transition from exhumed mantle to volcanic seafloor

Earlier work on seafloor mapping in the study area (Cannat et al., 2006) indicated that the EW profile crosses a transition within the uppermost lithosphere from exhumed and serpentinized ultramafic mantle domains in the east to volcanic and magmatic mafic domains in the west (Fig. 2.3.1). This transition was initially interpreted to occur at the OBS 25 location (model distance ~84 km; Fig. 2.3.1) (Cannat et al., 2006). Cannat et al. (2019) later proposed a wider transitional domain from the detachment-dominated asymmetric topography, characteristic of non-volcanic seafloor, to the magmatic symmetric topography, characteristic of volcanic seafloor. The authors examined four ridge-perpendicular bathymetric profiles spread over a distance of ~50 km and observed a change in the seafloor topography across the profiles from ridge-asymmetric topography, indicative of non-volcanic seafloor, to ridge-symmetric topography, indicative of volcanic seafloor. The distance between the profile showing asymmetric topography and the closest profile showing ridge-symmetric topography is 32.6 km. A profile showing transitional bathymetry is found in between these two profiles, which led the authors to interpret that the transitional region occurs over a 20-30 km distance.

Our velocity, velocity anomaly, and vertical velocity gradient models (Fig. 2.7.2.2.1) also suggest a major change in the lithospheric structure and composition along the profile. This change occurs over a distance of ~10 km between OBSs 18 and 20 (model distance ~59-69 km; Fig. 2.7.2.2.1). In Figure 2.7.2.2.1 we plot the limits of the interpreted volcanic and non-volcanic seafloor as proposed by Cannat et al. (2006, 2019) and in this study. The recent interpretation by Cannat et al. (2019) put the transitional area at model distance of ~54-86 km, which is wider but in broad agreement with the results from this work.

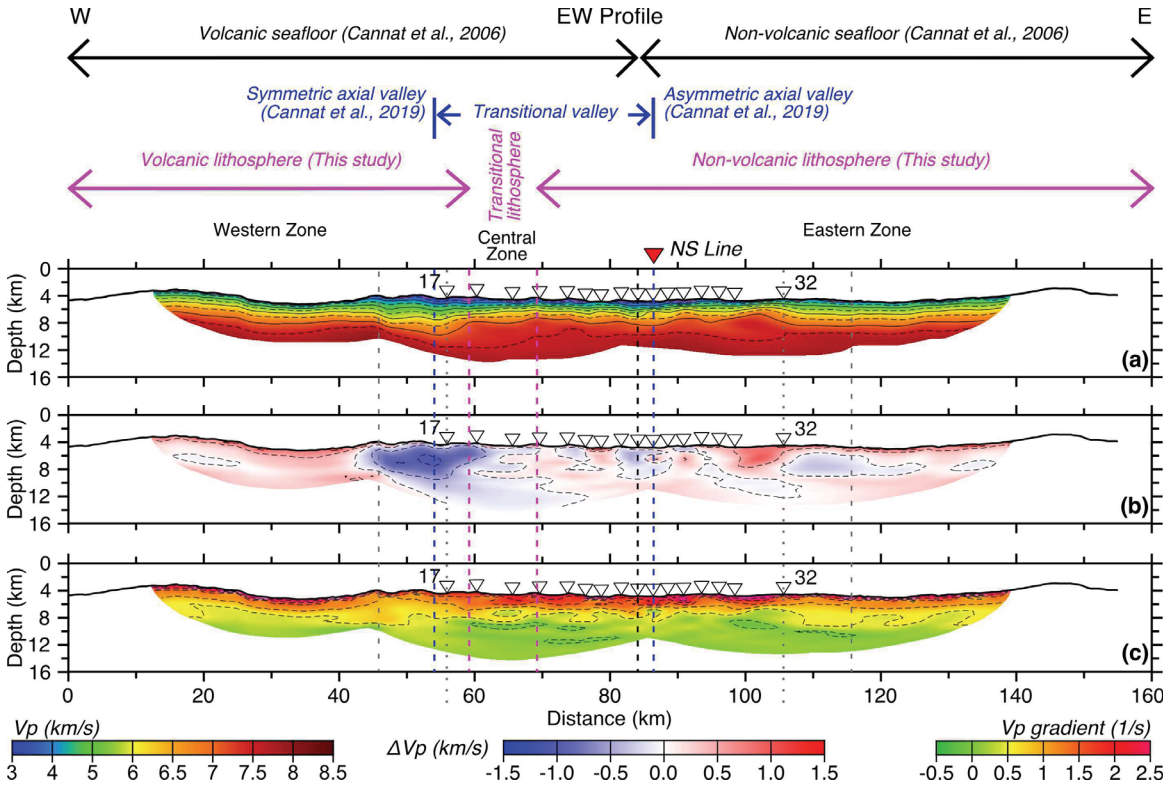

Figure 2.7.2.2.1. Comparison of the (a) average velocity model from Figure 2.6.2.2.1d, (b) velocity anomalies from Figure 2.6.3.1c, and (c) vertical gradient from Figure 2.6.3.1d, along the EW profile. Arrows in the top of the figure show the different interpretations of the proposed transition from volcanic to non-volcanic lithosphere: Cannat et al. (2006) in black, Cannat et al. (2019) in blue, and this study in pink. The blue short straight lines indicate the location of Cannat et al. (2019) bathymetric profiles that show contrasting symmetric and asymmetric axial valleys and constrain the transitional zone. The black, blue, and pink dashed lines extend the limits of the different interpretations across (a, b, and c). The pink arrows also delimit the three zones in the EW model: western, central, and eastern. White and red inverted triangles as in Figure 2.6.1.1 caption. Vertical dotted and dashed light grey lines as in Figure 2.6.2.2.1 caption.

The observed changes in velocity, velocity anomaly, and vertical velocity gradient divide the EW profile into three distinctive zones: eastern (model distance >69 km), central (model distance from 59 to 69 km), and western (model distance <59 km). The eastern zone shows high and laterally variable seismic velocities at shallow depths, reaching 4–4.5 km/s within 0.5 km dbsf and 7 km/s at depths 2–3.5 km dbsf (Fig. 2.7.2.2.1a), an overall positive velocity anomaly including a larger positive anomaly (0.5-1 km/s) at model distances 99–106 km (Fig. 2.7.2.2.1b), and a high vertical velocity gradient of 1–2 s^{-1} (Fig. 2.7.2.2.1c). These characteristics are consistent with exhumed and variably serpentinized mantle peridotites, where serpentinization extent diminishes as a function of

depth. A low in the velocities that corresponds with a low velocity anomaly (Fig. 2.7.2.2.1b) and a more moderate vertical gradient than for the neighboring areas (Fig. 2.7.2.2.1c) is observed within model distances 81–86 km (below OBSs 24-26; Fig. 2.7.2.2.1a). We speculate that this is indicative of a ~5km-wide volcanic dike injection, a feature resolvable in our model (Fig. 2.6.2.1.1f), that could be responsible for the lower RMBA values (10–0 mGal) that led to the interpretation of this area and the area further west as volcanic seafloor (Cannat et al., 2006). Other smaller low velocity anomalies, e.g., below OBSs 21 and 22 (model distances 73–76 km; Fig. 2.7.2.2.1b) and below OBS 28 (model distances 90–92 km; Fig. 2.7.2.2.1b) may suggest the presence of additional smaller dikes that are not fully resolvable by our data. Detailed seafloor mapping in our study area with side-scan sonar shows small sparse lava patches on top of the exhumation surfaces (Sauter et al., 2013). Our results bolster the argument that the lava patches are erupted directly onto the exhumed surface by small offset high-angle normal faults (Cannat et al., 2019; Sauter et al., 2013), as opposed to being allochthonous rafted volcanic blocks transported to the surface off-axis by successive detachments (Reston, 2018). Furthermore, the presented evidence of volcanic dike injections within the "smooth-seafloor" favors the interpretation by Sauter et al. (2013) that the abandonment of the active axial detachment fault and consequent activation of the successive detachment fault may be a consequence of increased diking.

The western zone shows sharply lower seismic velocities that reach 3.5 km/s at 0.5 km dbsf and 7 km/s at 4–5.3 km dbsf (Fig. 2.7.2.2.1a), a large negative velocity anomaly of -1.5–-1 km/s (Fig. 2.7.2.2.1b), and a moderate to low vertical velocity gradient of 0.5–1 s^{-1} (Fig. 2.7.2.2.1c). These characteristics are consistent with top of the lithosphere being partially constructed by mafic magmatic rocks. This interpretation is further supported by analysis of the ray coverage or the DWS (Fig. 2.6.2.2.1e). Although the ray density at all ends of the seismic profiles is gradually reduced with increasing shot distance from the last OBS (Figs. 2.6.2.2.1c and 2.6.2.2.1e), the reduction at the west end of the EW profile (Fig. 2.6.2.2.1f) is considerably greater than at the three other profile ends, which is indicative of a major change in the nature of the lithosphere. This more rapid drop in ray density also coincides in an apparent westward velocity increase at the western limit of

the well resolved area (Fig. 2.7.2.2.1a), but this is an artifact. The inverted velocity model follows the starting velocity model in areas of low ray coverage (i.e., outside the well resolved area), and in the well resolved section of the western zone seismic velocities are considerably slower than the starting velocity model. This forces a gradual lateral change from the well resolved area. On the contrary, in the east the starting and the average velocity models have similar velocities and no lateral change is observed across the limit of the well resolved area.

In between the eastern and western zones is the central zone, which displays gradual westward changes in the velocities (decreasing; Fig. 2.7.2.2.1a), velocity anomaly (from low positive to low negative Fig. 2.7.2.2.1b), and vertical velocity gradient (vertically less variable, Fig. 2.7.2.2.1c). We interpret this as indicative of a transition from the amagmatic upper lithosphere of the eastern zone to the mafic magmatic rocks toping the lithosphere of the western zone and also likely an indicator of a transitional lithosphere that is heterogeneous in its composition with layers of mafic extrusive and intrusive rocks laterally intertwined with layers of fully and partially serpentinized ultramafic rocks (Fig. 2.7.2.1.1b).

2.7.2.3 Anisotropy

We extract 1D velocity-depth functions at the crossing point between the NS and EW velocity profiles (Fig. 2.7.2.3.1a) to evaluate if there is directional dependence in seismic velocities or seismic anisotropy (Fig. 2.7.2.3.1). The difference between these two 1D velocity-depth functions is shown in Figure 2.7.2.3.1b (dashed blue line), and the corresponding anisotropy is shown in Figure 2.7.2.3.1c. Both velocity functions are nearly coincident for the first 0.5 km dbsf. At greater depth, from ~0.5 to ~2.2 km dbsf, velocities on the EW profile are faster (up to ~5% difference) than on the NS profile. The velocity relationship reverses from ~2.2 to ~6 km dbsf, with the NS profile being faster (up to ~5% difference). At depths greater than 6 km dbsf, the two velocity-depth functions are again nearly coincident.

Figure 2.7.2.3.1b also compares the difference in the two velocity-depth functions to the standard deviation (SD) estimated for the NS and EW velocity models at their crossing point. The SD-depth functions are similar for both profiles at the crossing point, with most SD values being <±0.1 km/s. The P-wave velocity difference near the function peaks reaches or approaches ±0.4 km/s, which is at least several times greater than the SD of both velocity models indicating that the difference in velocities we observe falls well within the estimated uncertainty. While some of the differences in velocities at the two crossing profiles may be due to the limitations of modeling wave propagation in 2D, most of the observed differences can be attributed to seismic anisotropy thus rendering our results a useful first-order approximation.

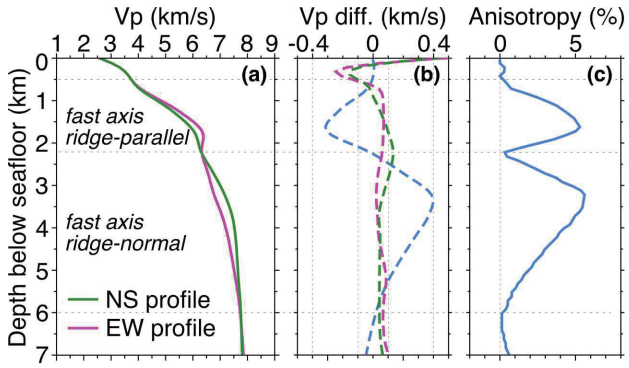

Figure 2.7.2.3.1. (a) Comparison of the 1D velocity-depth functions extracted from the NS (green) and EW (pink) profiles at their crossing point. (b) Dashed blue line shows the difference between NS and EW velocities presented in (a), and green and pink dashed lines show the standard deviation of the velocities presented in (a) (from Figs. 2.6.2.2.1b and 2.6.2.2.1e). (c) Functional fit of % of anisotropy with depth in light blue. The horizontal dashed grey lines in (a, b and c) indicate the depths for the anisotropy consistent with a fast axis aligned in a ridge-parallel direction (~0.5 to ~2.2 km dbsf) and for the anisotropy consistent with a fast axis aligned in a ridge-normal direction (~2.2 to 6 km dbsf).

The velocity differences in the shallower zone (~0.5 to ~2.2 km dbsf) are consistent with the anisotropy reported at other ridges near the spreading axis of 1%–12% at shallow to intermediate depths (0–3 km) and with the fast axis aligned in a ridge-parallel direction (e.g., Seher et al., 2010; Weekly et al., 2014). This anisotropy is associated with the alignment of vertical cracks within the crust in the ridge axis direction (Dunn & Toomey, 2001). Christeson et al. (2019) synthesized the oceanic crustal structure formed at spreading ridges with half-spreading velocities greater than 5 mm/yr from 2D seismic

profiles and documented that anisotropy may be restricted to the upper crust in areas near the ridge axis. Cracks induced by stresses related to the footwall exhumation and bending at shallow to intermediate levels both in the footwall and the hanging wall, as well as extensive extensional damage on the hanging wall, have been suggested in our study area (Cannat et al., 2019; Momoh et al., 2017, 2020). Therefore, we suggest the uppermost anisotropy is due to the preferential distribution of cracks parallel or subparallel to the axis at depths from ~0.5 to ~2.2 km dbsf. We expect that the top 0.5 km dbsf are also characterized by axis parallel or subparallel cracks and the resulting anisotropy but, due to the discussed limitations of our data and velocity models, this anisotropy was not possible to resolve.

With greater depth, the increasing lithospheric pressure gradually closes the cracks thus removing the source of the ridge-parallel anisotropy. Serpentinization also diminishes with increasing depth leading to increased ratio of olivine minerals versus serpentine or other alteration minerals, thus generating anisotropy with the ridge-normal fast direction that starts to prevail at ~2.2 km dbsf. Our data can resolve the ridge-normal fast anisotropy to 6 km dbsf, after which the model resolution is insufficient for this purpose. Velocities from 6–~7 km dbsf have diminished resolution and are already influenced by the starting velocity model through smoothing. This uppermost mantle, ridge-normal anisotropy is related to the lattice-preference orientation of olivine minerals in the direction of lithospheric strain (Hess 1964), which is consistent with the near-orthogonal spreading direction attributed to our study area (Cannat et al., 2008), and has been reported for older oceanic crust (e.g., Ismaïl & Mainprice, 1998; VanderBeek et al., 2016).

2.7.3 Comparison of velocity-depth fields

We compare the average 1D velocities and velocity field envelopes of the NS and EW profiles (Fig. A.9) with corresponding results from previously published ridge-normal and ridge-parallel seismic profiles, respectively, at other locations along the SWIR.

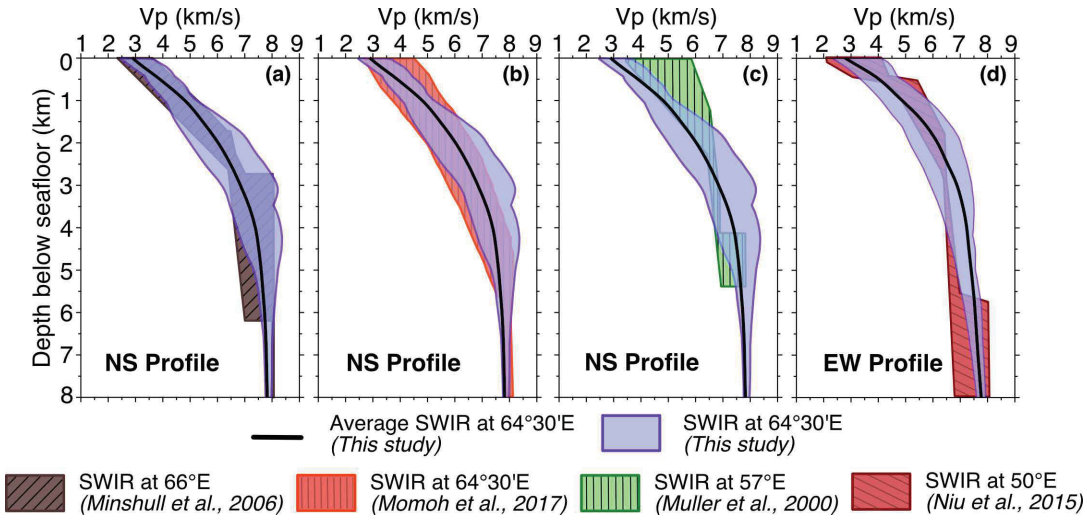

Figure 2.7.3.1. Comparison of the average 1D velocity-depth profiles (thick black line) and 1D velocity-depth fields (light purple areas bounded by dark purple lines) from this study with the velocity fields from earlier studies of the SWIR at the following locations: (a) 66°E (Minshull et al., 2006); (b) 64°30'E (Momoh et al., 2017); (c) 57°E (Muller et al., 2000); and (d) 50°E (Niu et al., 2015). Note that the locations of the earlier work done at 66°, 57° and 50°E are shown in the Figure 2.3.1 inset with yellow circle, diamond and star, respectively, while the work done at 64°30'E coincides with our study area.

Figure 2.7.3.1 displays a comparison of our results at 64°30'E with velocity fields from earlier work at the SWIR. From East to West, shown are velocity fields at 66°E (Minshull et al., 2006) (Fig. 2.7.3.1a), 64°30'E (Momoh et al., 2017) (Fig. 2.7.3.1b), 57°E (Muller et al., 2000) (Fig. 2.7.3.1c), and 50°E (Niu et al., 2015) (Fig. 2.7.3.1d).

Our NS profile velocity envelope and that of Momoh et al. (2017) (Fig. 2.7.3.1b), both from 64°30'E, are mostly in general agreement. Momoh et al. (2017) shows little structure with velocities smoothly increasing with depth, from ~2.7 km/s to 4.5 km/s at the seafloor to ~7–8 km/s at 5 km dbsf. The NS velocity model constrains the velocities at the seafloor to a narrower and slower range (~2.5–3.7 km/s), increasing to a similar range by about 1.4 km dbsf, and becoming overall higher for depths up to ~5 km dbsf. Momoh et al.'s (2017) velocities show smooth vertical velocity gradient changes with depth, while the NS velocities indicate a more complex structure for how the velocity gradient changes with depth and show a higher vertical velocity gradient at the top that it is reduced to a lower velocity gradient for depths greater than ~2 km dbsf. While our interpretation is broadly similar to that of Momoh et al. (2017), the NS velocity model has recovered

deeper and more detailed velocity information thus providing more constraints on the lithospheric structure. This is likely because the NS profile is longer (150 km vs. 43 km) and has more OBSs (16 vs. 8) than the profiles used by Momoh et al. (2017), resulting in denser and deeper ray coverage with a larger range of source-receiver offsets.

Minshull et al. (2006) at 66°E (Fig. 2.7.3.1a) show velocities at the seafloor ranging from ~2.3–3.5 km/s and increasing at a high vertical velocity gradient up to ~6.4–7 km/s at ~2.7 km dbsf. At depths greater than ~2.7 km dbsf, the velocities increase at a low-velocity gradient and range from ~6.5–7 to 8 km/s. The average velocities for the NS profile fit well with the velocity field of Minshull et al. (2006). The NS velocity field also presents a similar range and vertical gradient for depths up to 1 km dbsf but it has a lower low and a higher high velocity for depths of 1–3.5 km dbsf. At greater depths, the NS profile velocities are overall higher than the velocities at 66°E. Despite the significant similarities in velocities between the two models, large differences exist on the lithospheric structure interpretation in these two study areas that are only ~150–200 km apart. Minshull et al. (2006) suggested a crustal structure composed of mafic oceanic layers 2 and 3, with a mean crustal thickness of 4.2 km, and constrained the Moho with PmP arrivals and complementary gravity data. They interpreted that serpentinized peridotites do not form the dominant lithology in the seismic lower crust and instead they suggested a Layer 3 with a variable thickness (0.5–3 km) governed by melt focusing toward segment centers.

The presence of Segment-8 volcano at ~65°40'E (Cannat et al., 2006; Schlindwein & Schmid, 2016) could explain some of the differences between the two results and interpretations. Velocity structure of Minshull et al. (2006) shows a higher gradient for the top and lower gradient for the bottom of the model than the NS profile, which is consistent with a high-gradient Layer 2 on top of a low-gradient Layer 3, while the SWIR at 64°30'E has a gradual decrease in the vertical velocity gradient consistent with a gradual decrease in serpentinization and pore pressure with depth. However, Minshull et al. (2006) used a layered modeling and inversion procedure constrained by model parametrization of two crustal layers. The wide-angle data were collected on 8 OBSs

(~10–30 km spacing) with no coincident MCS data to guide the layered inversion. Therefore, we speculate that a fair amount of variably serpentinized peridotites may be present in the subsurface at the SWIR at 66°E based on the overlap of the NS profile velocity envelope with Minshull et al. (2006) velocities, and that a denser seismic survey followed by first arrival traveltime tomography for a single model layer would provide a better and more detailed comparison.

The SWIR at 57°E (Fig. 2.7.3.1c), across the Atlantic Bank, shows velocities ranging from 3.5 km/s to ~5.8 km/s at the seafloor (Muller et al., 2000). This velocity range gradually narrows to 6.4–6.9 km/s for depths ~2.2–4.1 km dbsf as the vertical velocity gradient decreases. For depths greater than 4.1 km dbsf the velocities range from ~6.8–7.8 km/s. The authors interpreted magmatic oceanic crust composed of layers 2 and 3 on top of the uppermost mantle rocks. The NS profile velocities are overall in disagreement showing slower velocities for depths up to ~2.6 km dbsf and higher velocities for greater depths. We interpret the topmost ~2.6 km dbsf on the NS profile, characterized by lower velocities than those from Muller et al. (2000), to represent fully serpentinized and highly fractured peridotites at the top that gradually transition to ~40% serpentinized peridotites with minor fractures at the bottom. The NS profile velocities continue to increase with increasing depth, though at a reduced gradient, due to continued fracture closure and further diminishing serpentinization. The Moho at the SWIR at 57°E is constrained by PmP reflections and gravity modeling, in contrast to our study area where the amagmatic seismic crust lacks any shreds of evidence of a Moho. However, the results from Muller et al. (2000) likely have greater uncertainties than our results since they use only 8 OBSs (~5–15 km spacing) and do not have coincident reflection data, which are used to guide layered modeling and inversion.

The velocity field at the segment center at 50°E (Fig. 2.7.3.1d, Niu et al., 2015) can be divided in 4 sections: (1) top one (0-~0.6 km dbsf), with a mostly moderate gradient and velocities ranging from ~2 km/s to ~4 km/s; (2) a high gradient section underneath (0.6–2.8 km dbsf) with velocities of ~4.4–6.5 km/s; (3) a low gradient section (2.8–5.5 km dbsf) further down with a narrow range of velocities (6.5–7 km/s); and (4) a low gradient

section (depth > 5.5 km dbsf) at the bottom with velocities ranging from 6.6 km/s to 8.1 km/s. The NS profile velocities are mostly in agreement within the top section, lower than velocities of Niu et al. (2015) in the top part and in agreement with the bottom part of the second section, are significantly higher in the third section, and somewhat higher in the fourth section. Niu et al. (2015) interpreted layers 2A, 2B, and 3 overlying the uppermost mantle. The investigated segment center at 50°E has an anomalously thick crust, ranging from ~5.5 km to 10.2 km, and a robust and well-imaged axial magma chamber (Niu et al., 2015; Jian et al., 2016, 2017). This interpretation is consistent with a magma-rich spreading center and, as such, it differs from magma-starved spreading interpreted at 64°30'E.

2.8 Conclusions

We constrain tomographic velocity structure across- and along-axis the ultraslow-spreading SWIR at 64°30'E by inverting first arrivals from two ~150-km-long orthogonal wide-angle OBS profiles. Our major findings and conclusions are the following:

1. About 75% of the investigated uppermost lithosphere appears to be composed of highly fractured and fully serpentinized peridotites at the top, with a gradual decrease in pore space volume and serpentinization degree to unaltered peridotites at depth. Key evidence for this are seismic velocities that increase rapidly with depth, changing from 3–4 km/s at the seafloor to 7 km/s at depths ranging from 1.5–6 km dbsf, much lower vertical velocity gradient for velocities >7 km/s that gradually reduces with increasing depth, and no distinct and seismically well-characterized Moho observable in the data.

2. A system of detachment faults is imaged in the subsurface for the first time in our study area by the profile that crosses the ridge axis. We interpret a sharp lateral change (horizontal gradient ~1 s^{-1}) in velocities, switch in polarity of the largest velocity anomaly, from 1.5 km/s to -1.5 km/s, and high vertical gradient (~2 s^{-1}) in the velocities coincident with the shallow section (top 2 km) of the highest

topographic feature as the seismic expression of an active axial detachment fault. Five abandoned detachment faults are also identified based on anomalously high velocities and vertical gradients that characterize the footwalls on all identified detachment faults, with the opposite characterizing the hanging walls. Serpentinization across-axis is controlled by the longevity of detachments and fault block movement, with longer-lived faults showing deeper serpentinization extent and footwalls showing less pervasive serpentinization due to continuous exhumation.

3. Comparison of the 1D velocity-depth functions at their crossing point between the two orthogonal profiles suggests an up to 5% ridge-parallel fast-axis anisotropy from ~0.5 to ~2.2 km dbsf attributed to the preferential distribution of cracks parallel to the ridge, and a similar magnitude but reversed polarity ridge-normal fast-axis anisotropy at >~2.2 km dbsf that we attribute to the lattice-preference orientation of olivine minerals in the less serpentinized peridotites.

4. Upper lithospheric composition along the western half of the axis-parallel profile seems to transition over a distance of ~10 km from the variably serpentinized peridotites domains in the East to predominately mafic magmatic domains in the West. The exhumed mantle domains show high and laterally variable seismic velocities at shallow depths, reaching 4–4.5 km/s within the first 0.5 km dbsf and 7 km/s at depths 2–3.5 km dbsf, a high vertical velocity gradient of 1–2 s^{-1}, and an overall positive velocity anomaly (up to 0.5–1 km/s). The mafic domains show sharply lower seismic velocities that reach 3.5 km/s at 0.5 km dbsf and 7 km/s only at 4–5.3 km dbsf, a moderate to low and smoother vertical velocity gradient of 0.5–1 s^{-1}, and a large negative velocity anomaly of -1.5–-1 km/s. We suggest that the change in the seafloor accretion mode is propelled by a westward increase in melt supply.

5. Comparison of velocity structure from our results at the ultraslow-spreading SWIR at 64°30'E with the velocity structure elsewhere at the SWIR has shown an

overall agreement of our results with studies at amagmatic segments, a disagreement with identified anomalously magma-rich segments, and mixed results for magma-starved segments, such as the SWIR at 66° and 57° E. This work has also demonstrated the challenges in carrying out meaningful velocity structure comparisons when the data resolution and techniques used to determine the velocities are not the same (e.g., layered modeling vs. tomography).

Chapter 3

Evolution of tectonically accreted oceanic topmost lithosphere

3.1 Abstract

Oceanic lithosphere formed at the global mid-ocean ridge system makes up >60% of the Earth's solid surface (Ito & Dunn, 2009). Its topmost ~6 km are accreted magmatically, where mafic melt is available, or tectonically, where this melt is absent. The magmatically accreted lithosphere is known to evolve with age as demonstrated by its velocity increase (Carlson, 1998; Christeson et al., 2019; Grevemeyer et al., 1999; Grevemeyer & Weigel, 1996; Nedimović et al., 2008; Newman et al., 2011). Information on if and how the tectonically accreted lithosphere changes with time, which represents a quarter of the global accretion is still lacking. Here we show that the tectonically accreted lithosphere, composed of exhumed ultramafic rocks, also evolves. The increase in velocities from 0–6 Ma is ~53% greater than for the magmatically accreted topmost lithosphere. Most of this velocity increase takes place at depths of 1.5–4.5 km, deeper than for the magmatically accreted lithosphere. The overall alteration of the tectonically accreted lithosphere relative to the magmatically accreted one is, however, greater than what the velocity increase alone indicates. This is because progressive serpentinization with aging of the topmost 1.5–2.5 km of lithosphere reduces velocities, thus counterbalancing the velocity increase due to crack closure and pore infilling. Our work implies that the tectonically accreted oceanic lithosphere evolves differently from and much faster than its magmatic counterpart.

3.2 Introduction

At nearly 65,000 km in length, the global mid-ocean ridge system is heterogenous and shows remarkable differences in the spreading velocity (DeMets et al., 2010), axial morphology (Carbotte et al., 2016) , and modes of seafloor accretion (Cannat et al., 2006).

The topmost ~6 km of lithosphere formed at fast (~80–180 mm/yr) and intermediate (~55–70 mm/yr) spreading rates, as well as at the magmatically robust segment centers of slow (~20–55 mm/yr) spreading ridges, is characterized by a magmatically accreted 6–7 km-thick "layer-cake" or Penrose model structure called oceanic crust. From top to bottom, oceanic crust consists of: Layer 2A, a basaltic extrusive layer; Layer 2B, formed by injection of sheeted vertical diabase dikes; and Layer 3, composed of isotropic and layered gabbros topping the uppermost mantle (Houtz & Ewing, 1976; Ewing & Houtz, 1979: White et al., 1992). The topmost lithosphere formed at ultraslow-spreading (<~20 mm/yr) ridges, and segment ends of slow-spreading ridges, is more heterogeneous and the "layer-cake" model often does not apply. The melt tends to be focused on the segment centers (Lin et al., 1990), and the crust thins in the direction of the melt-starved segment ends where layers 2 and 3 may be discontinuous or absent (Dunn et al., 2005; Minshull et al., 2006; Muller et al., 1999; Muller et al., 2000; Blackman et al., 2002). At slow- and ultraslow-spreading ridge sections where the melt budget is reduced to near nil, uppermost lithospheric accretion shifts to being tectonically controlled and wide-spread mantle exhumation occurs along long-offset, low-angle detachment faults (Sauter et al., 2013; Smith et al., 2006; Tucholke et al., 1998).

The topmost lithosphere formed at spreading ridges migrates off-axis driven by mantle convection, and it is chemically, physically and mechanically differentiated in the process (Ito & Dunn, 2009). These changes have important implications for hydrothermal systems, ocean water chemistry, microbial ecosystems, subduction zone processes, and heat and mass exchange between the Earth's solid interior and the oceans (Ito & Dunn, 2009; Bach & Früh-Green, 2010). Therefore, evolution of oceanic lithosphere has direct societal impacts (Halpaap et al., 2019). A geophysical observation that demonstrates upper crustal evolution is the increase in seismic velocities as a function of the distance from the ridge axis, and thus age. This velocity change has been observed in the magmatically accreted topmost lithosphere, where Layer 2A velocities nearly double in 10–15 Ma (Christeson et al., 2019; Grevemeyer et al., 1999; Nedimović et al., 2008). Layer 2B has also been shown to evolve, but differently and independently from Layer 2A, with its evolution being mostly confined to 0–0.5 Ma old crust (Newman et al.,

2011). The increase in layers 2A and 2B velocities with age has been attributed to porosity reduction by infilling of pore space with secondary alteration minerals (Houtz & Ewing, 1976; Carlson, 2010) and/or by a change in the crack morphology (Carlson, 2014; Wilkens et al., 1991). Velocity–lithospheric age dependency has occasionally been observed for Layer 3 and/or the uppermost mantle, but the overall velocity increase for these layers is minor (<~5%) (Christeson et al., 2019; Grevemeyer et al., 1998).

3.3 Velocity change in tectonically accreted topmost lithosphere

Here we examine a ridge-perpendicular P-wave velocity model crossing the Southwest Indian Ridge (SWIR), an endmember ultraslow-spreading ridge with a full-spreading rate of <14 mm/year (Kreemer et al., 2014), in an area (64°30' E; Fig. 3.3.1) where lithosphere accretes tectonically (Cannat et al., 2006; Sauter et al., 2013; Corbalán et al., 2021; Momoh et al., 2017). The velocity model (Fig. 3.3.2a) was formed by inverting first arrival traveltimes from a 150-km-long ocean bottom seismometer (OBS) profile (Corbalán et al., 2021), SMOO33 (Fig. 3.3.1 and Appendix C.1). Earlier geophysical and rock sampling studies in our study area (Cannat et al., 2006; Sauter et al., 2013; Sauter et al., 2008) have mapped the globally widest exhumed mantle seafloor domains identified thus far (Cannat et al., 2006) (Fig. 3.3.1). These domains are characterized by variably serpentinized mantle-derived rocks, peridotites, forming broad rounded 15–90 km long ridges with a height ranging from 500 to 2000 m (Cannat et al., 2006; Cannat et al., 2019). The 16 dredges collected along the SMOO33 profile recovered almost exclusively serpentinized peridotites with a minor amount (<5%) of mafic rocks (Sauter et al., 2013). The side-scan sonar imagery revealed active and abandoned detachment fault surfaces at the seafloor that, together with detailed bathymetric and kinetic analysis, manifest the flip-flop detachment faulting as the mechanism for tectonic accretion of oceanic lithosphere by mantle exhumation (Sauter et al., 2013; Cannat et al., 2019; Reston, 2018). The tomographic velocity model (Fig. 3.3.2a) shows the system of detachment faults in the subsurface (Corbalán et al., 2021). The location of the fault emergences (*E*) inferred from the velocity model (Fig. 3.3.2a), together with the previously inferred locations of breakaways (*B*) and faults (*E)* resolved using seafloor imaging (Sauter et al., 2013;

Cannat et al., 2019; Reston, 2018) (Fig. 3.3.2a,b), allow us to estimate the lithospheric age along the SMOO33 profile (see Appendix B.1) and evaluate the relationship between velocity and lithospheric age. Calculated ages from *B3* (breakaway of fault numbered 3) to *E9* (emergence of fault numbered 9) are shown in Figure 3.3.2b.

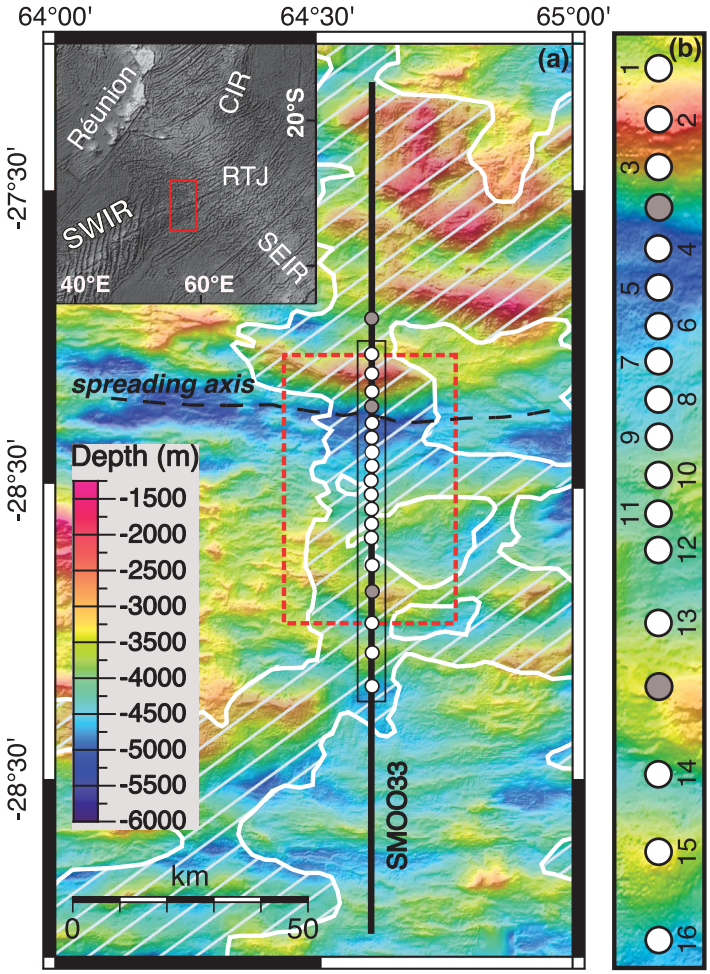

Figure 3.3.1. Location of the study area and OBS survey. (a) Regional OBS profile SMOO33 from the SISMOSMOOTH Survey (Leroy et al., 2015) overlying a color bathymetry map (Cannat et al., 2006; Momoh et al., 2017). Thick black line depicts shot locations, and white and gray circles with black outlines are the positions of OBS instruments that did and did not provide useful data, respectively. The shooting distance inside the dashed red rectangle is 150 m and outside 300 m. Two tuned linear arrays with 7 air guns each towed at an average depth of 14 m and with a total nominal volume of 6,790 in^3 were used as seismic source. Dashed black line shows the spreading axis location. Highlighted area bounded and filled by white lines delimits the smooth non-volcanic seafloor (Cannat et al., 2006; 2019). Inset in the top left shows the location of the Southwest Indian Ridge (SWIR) relative to Réunion Island, the Central Indian Ridge (CIR), the Southeast Indian Ridge (SEIR), and the Rodriguez Triple Junction (RTJ). Red rectangle shows the limits of the study area presented in the main figure. (b) Magnification of the main map within the thin black rectangle details the positions of the OBS instruments. Only the OBS with

useful data are sequentially numbered in NS direction. The OBS spacing ranges from 3 to 10 km. The color scale for the bathymetry is the same as in the main map.

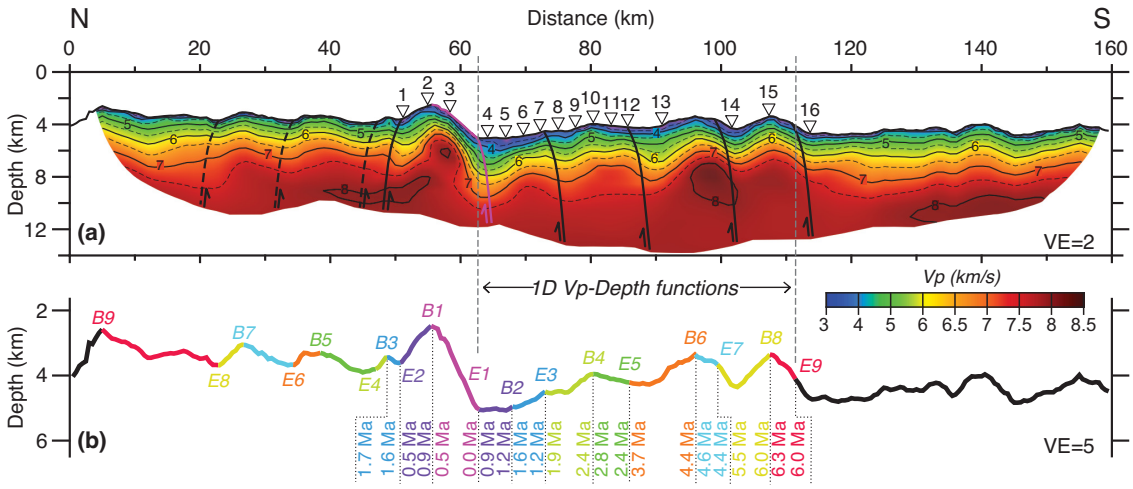

Figure 3.3.2. Tomographic velocity model with interpretation of the detachment fault locations and lithospheric ages. (a) Results from the first arrival traveltime tomographic inversion of the SMOO33 profile (Corbalán et al., 2021). Thick black solid and black dashed lines show interpreted locations of abandoned detachment faults based on the velocity model and seafloor studies (Cannat et al., 2019; Corbalán et al., 2021; Sauter et al., 2013), and based only on the seafloor studies (Cannat et al., 2019; Corbalán et al., 2021; Sauter et al., 2013), respectively. Thick pink solid line illustrates the active detachment fault. White inverted triangles show the positions of the OBSs on the seafloor. Colour scale at the bottom right defines P-wave velocity. (b) Vertically exaggerated (VE=5) seafloor topographic profile along SMOO33 with each successive flip-flop fault surface colour coded. The location of the emergence and breakaway for each fault is indicated by E_N and B_N, respectively, where N indicates the fault number. Faults are sequentially numbered from youngest to oldest from 1 to 9. Ages for each fault surface, where possible to constrain, are presented at the bottom of the figure. A pattern of ages increasing in an alternating opposite direction is observed and it is consistent with the proposed mechanism of seafloor accretion in the study area.

To avoid spatially overlapping samples and to comply with the lateral resolution limits of our velocity model, we extract 1D velocity-depth functions 2.5 km to the right of the identified *E* and *B* locations (Fig. 3.3.2b) from *E1* to *B8*. This effectively comprises the region south of the spreading axis within the best-resolved area in our velocity model (see Appendix C, Fig. C.1). The 1D functions sample the velocity every 0.1 km for depths below the seafloor (dbsf) from 0.5 km to 5.5 km. We disregard depths 0–0.5 km dbsf because they show SD >~0.1 km/s due to data and velocity model limitations and choose to sample only up to depths where there are still crossing rays (5.5 km dbsf; Appendix C, Fig. C.1). Next, the sampled velocities are grouped into 1 km depth ranges (0.5–1.5 km,

1.5–2.5 km, 2.5–3.5 km, 3.5–4.5 km, and 4.5–5.5 km) and plotted in two scatter plots: one versus distance (Fig. 3.3.3b) and other versus age (Figs. 3.3.3c). In Figure 3.3.3 a general increase in the velocities with distance and age can be observed. We fit a linear regression function and a fifth order polynomial curve to evaluate the velocity-distance and velocity-age dependence. We refer to the linear regression to describe the general increase in velocities with distance and age and use the fifth order polynomial fits to support our conclusions (see Appendix C.1).

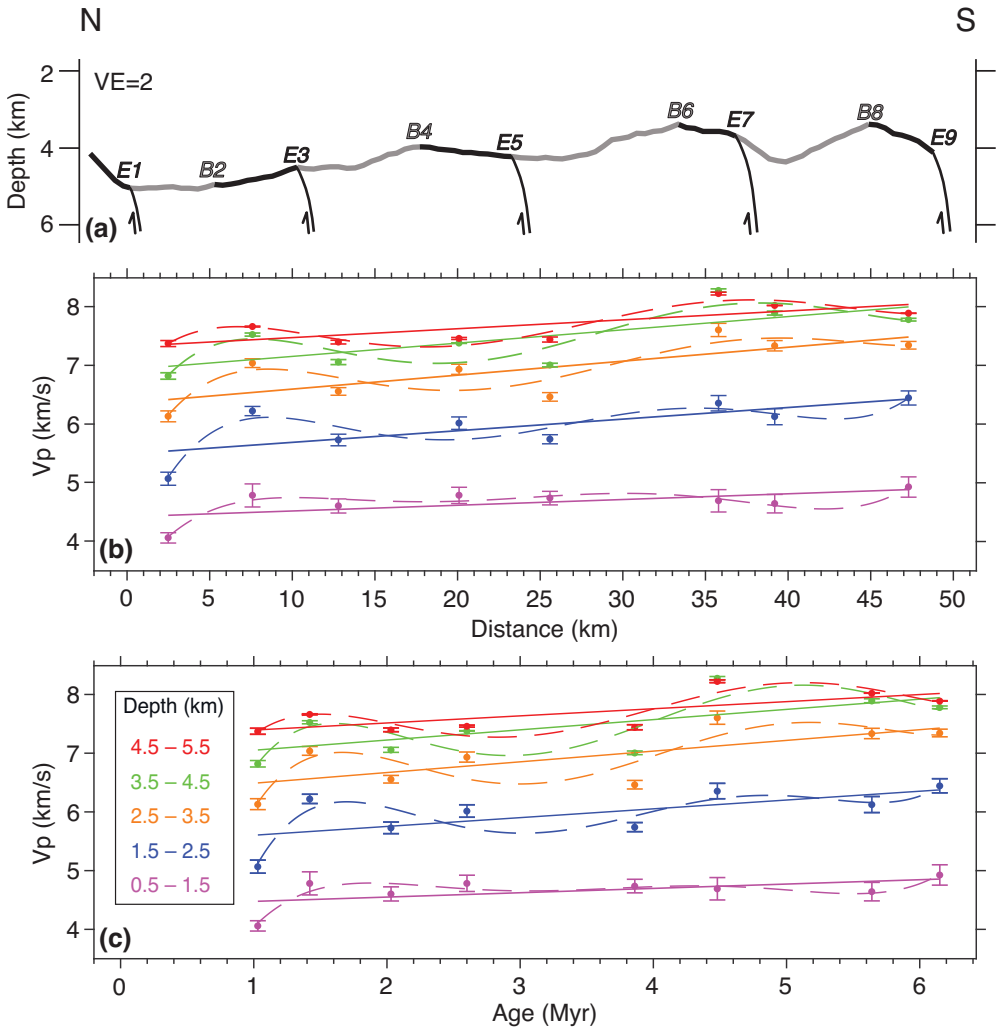

Figure 3.3.3. Upper lithospheric velocity change at the SWIR as a function of both increasing distance from the ridge axis and increasing age. (a) Vertically exaggerated (VE=2) seafloor topographic profile along SMOO33 from E_1 to E_9, with notation for the location of emergences (*E)* and breakaways (*B)* as in Figure 2 caption. Alternating fault surfaces are shown in black and grey. P-wave velocity as a function of (b) distance from the ridge axis and (c) lithospheric age. In both (b) and (c), coloured circles represent the average velocity for each of the five depth groups

(0.5–1.5 km dbsf in pink; 1.5–2.5 km dbsf in blue; 2.5–3.5 km dbsf in orange; 3.5–4.5 km dbsf in green; and 4.5–5.5 km dbsf in red) at each extraction location positioned 2.5 km to the right of each *E* and *B*, starting at *E1* and finishing at *B8*. 1D velocity-depth functions are extracted with a depth sampling of 0.1 km and then averaged for each depth group. The standard error of the mean pertinent to each average value of each group is shown with thin-coloured vertical lines and horizontal bars using the same colour code as for the circles. Linear regression fits and five-degree polynomial fits for each group are shown as solid lines and dashed lines, respectively, in the corresponding colours (see legend in Fig. 3.3.3c).

The slopes of the linear models (Fig. 3.3.3b,c) indicate that the velocity increase with distance and age is greater at depths 1.5–4.5 km dbsf (with an average gradient of 0.022 s^{-1} and 0.169 km s^{-1}/Ma, respectively) than at depths 0.5–1.5 km dbsf (gradient of 0.010 s^{-1} and 0.074 km s^{-1}/Ma, respectively) and 4.5–5.5 km dbsf (gradient of 0.015 s^{-1} and 0.121 km s^{-1}/Ma, respectively). See Appendix C, Table C1 for the full regression values and fit statistics. The velocity increase at 1.5–4.5 km dbsf is ~16% in 6 Ma. A velocity increase of ~10% in 6 Ma is determined for the shallowest and the deepest depth groups. Numerous alternative approaches to sampling of the velocity model yield similar fits and uncertainties (Figs. C.2a-d; Tables C.2a-d), pointing to the robustness of the presented velocity-age dependency.

A correlation in across-axis thermal changes with seismic velocity changes is dismissed. 1D geothermal evolution modelling (see Appendix B.2) shows <1% velocity variation with modelled thermal changes for lithosphere 0–6 Ma old at 0–6 km dbsf (Fig. C.3), indicating that the thermal evolution has a negligible effect on the velocity. This is in agreement with experimental studies on serpentinized peridotites (Carlson & Miller, 2003) and seafloor geological observations that evidence a slow and diffuse hydrothermal fluid discharge at the only serpentinite-hosted hydrothermal field known at the SWIR (Lecoeuvre et al., 2020). The same insignificant effect is observed up to 100 Myr (Appendix C, Fig. C.4) in our geothermal modelling, which seems to indicate that temperature has a negligible effect on velocities even at ages at which the plate is likely to be approaching or entering a subduction zone.

3.4 Comparison with magmatically accreted topmost lithosphere

A schematic comparison of evolution from 0–6 Ma is shown for (1) lithosphere formed at magmatically-robust ridges, where the topmost section is magmatically accreted to form a Penrose type layer-cake igneous crust (Fig. 3.4.1a,b), and for (2) lithosphere formed at amagmatic sections of the global mid-ocean ridge system, where the corresponding topmost section is comprised on tectonically accreted partially serpentinized mantle peridotites (Fig. 3.4.1c,d). Much of the velocity increase within the Penrose type layer-cake igneous crust is confined to Layer 2, and the bulk of that is within the several hundred meters thick, high-porosity Layer 2A (Carlson, 1998; Grevemeyer et al., 1999; Nedimović et al., 2008). Modern seismic velocity compilations for crust formed at spreading rates greater than ~14 mm/yr show a global velocity increase of Layer 2A of ~31% for crustal ages 0–6 Ma (Christeson et al., 2019). This drops by nearly half to 18% for the top 200 m of Layer 2B (Newman et al., 2011). For the same crustal age range, top of Layer 3 shows <6% velocity increase, and base of Layer 3 <1% velocity increase (Christeson et al., 2019). Assuming a 6.15-km-thick igneous crust with layers 2A, 2B, and 3 thicknesses of 0.50 (Berge et al., 1992; Carbotte & Scheirer, 2004), 1.34 and 4.31 km^3, respectively, and a 9% increase at the base of Layer 2B, the overall velocity increase for the magmatically accreted oceanic crust aged 0–6 Ma is ~8.5%.

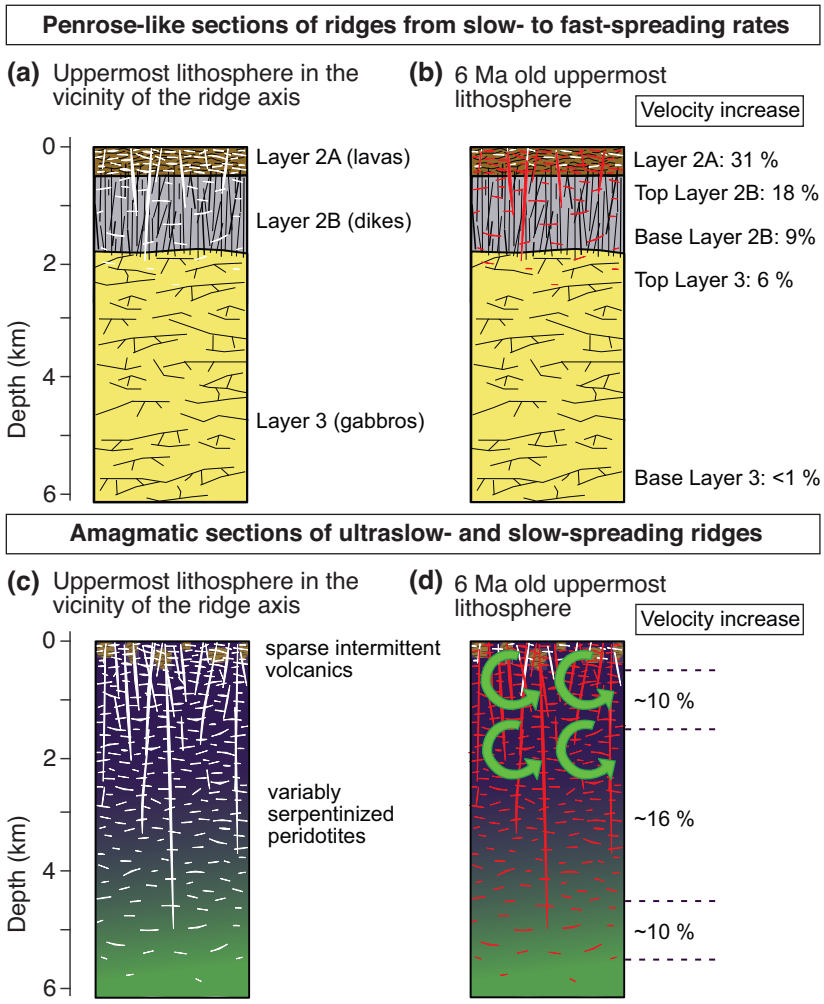

Figure 3.4.1. Schematic comparison of evolution of uppermost oceanic lithosphere formed by magmatic (a and b) and tectonic (c and d) accretion from 0 (a and c) to 6 Ma (b and d). The magmatically accreted lithosphere is represented by layers 2A, 2B, and 3 (a and b), with thicknesses of 0.5, 1.34, and 4.31 km, respectively, based on a recent global compilation[3]. The topmost ~6 km of the tectonically accreted lithosphere is represented by a single layer of peridotites that are progressively less serpentinized with increasing depth (c and d). Open and filled cracks, fractures, and faults in (a–d) are displayed with white and red sub-horizontal and sub-vertical areas, respectively. Increases in layer velocities from 0–6 Ma, reported on the right-hand side in (b), come from literature[3,7], and in (d) from the work presented here. Because the velocity increase over 6 Ma in (d) varies with depth, it is reported for 3 sublayers (0.5–1.5, 1.5–4.5, and 4.5–5.5 km dbsf) that best summarize this velocity change. Green circular arrows in (d) depict the area where the velocity increase with lithospheric age due to the crack closure and pore infilling by mineral precipitation in the top 1.5–2.5 km is counteracted by the increasing volume of serpentinites and the decreasing volume of peridotites.

If the velocity increase for the tectonically accreted lithosphere at 0–0.5 and 5.5–6 km dbsf is the same as for the measured adjoining 0.5–1.5 and 4.5–5.5 m dbsf intervals, respectively, our work suggests that the overall velocity increase for tectonically accreted

top ~6 km of oceanic lithosphere aged 0–6 Ma is ~13%. This is ~53% higher than for the magmatically accreted crust, at least in our study area.

Sealing of cracks caused by the reduction of tensile stresses (Fleitout & Froidevaux, 1982; Neves et al., 2004) and pore space reduction due to the precipitation of hydrothermal alteration minerals (Houtz & Ewing, 1976; Carlson, 2010; Wilkens et al., 1991) are the processes identified to drive the progressive porosity decrease and, therefore, the velocity increase with age in the magmatically accreted crust. Typical values of porosity in newly accreted igneous crust are 15–30% for Layer 2A (Wilkens et al., 199; Funnell et al., 2021; Johnson et al., 2000; Pezard, 1990), <10% for Layer 2B and <5% for Layer 3 (Carbotte & Scheirer, 2004). Therefore, there is progressively less room for crack sealing and pore closure with increasing depth, which in turns means less velocity change as a function of lithospheric age, as observed for oceanic layers 2A, 2B and 3 (Figs. 3.4.1a,b).

Serpentinized peridotites exhibit a wide range of bulk porosity values: <5% in ophiolite complexes (Bonnemains et al., 2016), <13% at the mid-Atlantic Ridge near the Kane fracture zone (Bonnemains et al., 2016), and 0.3–26% porosity in laboratory measurements (Hatakeyama & Katayama, 2020), with the overall representative value of <=10% (Hatakeyama & Katayama, 2020) that is on par with the porosity of layer 2B. However, the tectonically accreted uppermost lithosphere composed of serpentinized peridotites endures highly significant vertical faulting (Wilkens et al., 1991) and is in general subjected to greater brittle deformation than its magmatically accreted counterpart. For example, at the SWIR at 64°30' E part of the highly fractured and weakened exhumed footwall on a detachment fault becomes part of the hanging wall of the next detachment in the flip-flop faulting mode (Sauter et al., 2008; Cannat et al., 2019) (Fig. C.5). As a result, the already fractured hanging wall is once again subjected to deformation with additional faults, fissures, and cracks with larger aspect ratios developing (Katayama et al., 2021). Thus, it is likely that the topmost sections of the tectonically accreted oceanic lithosphere have initial porosity that is >10%, perhaps even

comparable to the porosity of Layer 2A, with the porosity gradually reducing with depth due to reduction in deformation and increasing pressure.

If the crack sealing and pore infilling are the main drivers for the evolution of the tectonically accreted uppermost lithosphere, as is the case for the magmatically accreted crust (Houtz & Ewing, 1976; Carlson, 2010; Carlson, 2014; Wilkens et al., 1991), then the general pattern of the velocity increase from 0–6 Ma (Fig. 3.4.1) should be similar for both with the main feature being velocity change that diminishes with depth. The main difference would be that the tectonically accreted uppermost lithosphere would exhibit a more gradual velocity decrease with depth, unlike the magmatically accreted crust that shows a more layered pattern (White et al., 1992).

3.5 Serpentinization: a counteracting process

Measured velocities from 0–6 Ma for the tectonically accreted top ~6 km of lithosphere in our study area, however, do not follow the expected pattern. The velocity increase for the 1.5–4.5 km dbsf interval of ~16% in 6 Ma is on par with the velocity increase in Layer 2B, which is expected considering similar porosities of vertical diabase dikes and serpentinized peridotites. But this interval is nearly as thick as Layer 3, and it is surprising that the change in velocity over the span of 6 Myr varies little within this thick interval as a function of depth. Only at a greater depth, within the 4.5–5.5 km dbsf interval, does the velocity change over the 0–6 Ma interval start to drop significantly to ~10%, and presumably even more so further down. What appears most puzzling is the lower velocity change over 0–6 Ma for 0.5–1.5 km dbsf interval of ~10%, as the greatest initial porosity and the most voluminous hydrothermal fluid flow are expected for the shallow-most portion of the lithosphere.

We propose that the progressive serpentinization with aging of the top 1.5–2.5 km of the tectonically accreted lithosphere is probably as impactful for its evolution as are the crack closure due to tensile stress reduction or pore infilling by mineral precipitation. Serpentinization of exhumed peridotites has been well documented for tectonically

accreted lithosphere (Rouméjon & Cannat, 2014; Rouméjon et al., 2015) but how this serpentinization changes with depth and age has not. We suggest that the velocity increase with lithospheric age due to the crack closure and pore infilling in the top 1.5–2.5 km is counteracted by the increasing volume of serpentinites and the decreasing volume of peridotites. Volume expansion during serpentinization may also cause higher aspect ratio and a largely varied scale fractures that further reduce the velocities (Hatakeyama & Katayama, 2020). Laboratory experiments on variably serpentinized peridotites indicate a linear inverse relationship between P-wave seismic velocities and serpentinization (Christensen, 1972; Christensen, 2004; Hyndman & Peacock, 2003), from ~8 km/s at 0% serpentinization to ~5 km/s at 100% serpentinization. Rock sampling studies in our study area show high degrees of serpentinization in rocks tens of kilometers off-axis (Rouméjon & Cannat, 2014; Rouméjon et al., 2015). The velocities across the SWIR at 64°30' E translate into very high degree of serpentinization for the top 0.5–2.5 km accompanied by high fracturing and indicate that the largest depth extent of serpentinization is ~5 km (Corbalán et al., 2021).

Because serpentinization acts as a counterbalance to crack closure and pore infilling when it comes to velocity increase with aging of the topmost 1.5–2.5 km of the tectonically accreted lithosphere, the change in the top ~6 km of this lithosphere from 0–6 Ma relative to the magmatically accreted crust is likely significantly greater than the 53% we computed based on the velocity increase alone. This not only implies that the tectonically accreted oceanic lithosphere evolves faster and in a fundamentally different way from its magmatically accreted counterpart, but that its water content must also be significantly greater as serpentinization is a key mechanism to chemically embed water.

None of the existing tectonically accreted lithosphere is presently subducting. However, this must have been a common occurrence in the Earth's past, and it will be in the future when the Arctic, Atlantic, and Indian ocean basins start to close. Considering that the water released from the subducting oceanic lithosphere is thought to have a first order impact on the intraslab and subduction thrust earthquakes (Halpaap et al., 2019), as well as on arc magmatism (Grove et al., 2012), it is likely that the geohazards associated with

subduction of tectonically accreted oceanic lithosphere are different than what we observe in the present-day subduction zones. For example, it is likely that the subduction of water-rich, tectonically accreted lithosphere results in greater arc magmatism and intraslab earthquake activity. This can, perhaps, be verified through studies of past global plate motions and velocities to identify continental areas composed of past forearcs that have experienced subduction of water-rich, tectonically accreted oceanic lithosphere.

Chapter 4

Seismic reflection structure across the ultraslow-spreading Southwest Indian Ridge at 64°30′E

4.1 Abstract

I present results from a ~180-km-long multichannel seismic reflection profile across the spreading axis of the ultraslow-spreading Southwest Indian ridge (64°30'E). Here, the lithosphere is tectonically accreted by long-offset, low-angle detachment faults, and subsequent mantle exhumation. Available tomographic velocity information allows me to run Kirchhoff depth migration and compute the true dips of the detachment faults. The active detachment fault shows a steeper-angle dip (~45°) compared to the dip angles observed at abandoned detachments (~25°). This is consistent with their different phases in the flip-flop rolling hinge model responsible for lithospheric accretion. The active fault is in a new rolling hinge phase, while the abandoned faults are at the end of the rolling hinge, with their footwalls already rotated and flattened to lower dips. Higher serpentinization gradients are found in the footwalls of the active and abandoned detachments, while the hanging walls are characterized by lower serpentinization gradients. A set of reflections identified as D reflections beneath the dome footwalls of the active fault and the southernmost inactive fault are interpreted as serpentinization fronts separating highly fractured and fully serpentinized peridotites above from less fractured and less serpentinized peridotites below. Beneath two breakaways south of the spreading axis, reflections with contrasting dip and dip direction to adjacent reflections are interpreted as small-offset faults formed during flexural rotation of the footwall when each block was the footwall block of an active detachment fault.

4.2 Introduction

Ultraslow-spreading oceanic ridges (full spreading rate <~20 mm/yr) make up for ~35% of the global ridge system (Dick et al., 2003) and yet little is known of their lithospheric structure and associated tectonic processes. Fault style and axial morphology at slow- and ultraslow-spreading ridges show remarkable differences from the observed at fast- and intermediate-spreading rates. For instance, at fast rates, the seafloor exhibits a relatively gentle topography, with a roughly dome-shaped rise flanked by normal faults and an axial high of a few hundred meters at the crest (e.g., Buck et al., 2005; Carbotte et al., 2016; Heezen, 1960). While at slow-spreading ridges, the topography is more rugged and presents a 1–3-km-deep, 20–30-km-wide axial valley (e.g., Buck et al., 2005; Carbotte et al., 2016). Inward-facing faults (dip towards the axis) are predominant at slow-spreading ridges, while at fast-spreading ridges inward- and outward-facing faults (dip away from the axis) are present in a similar distribution (Carbotte & Macdonald, 1990).

Long-offset, low-angle normal faults or detachments are observed at segment-ends of slow-spreading ridges and ultraslow-spreading ridges (e.g., Tucholke et al., 1998; Sauter et al., 2013). These detachment faults have initially steep angles (~70° at 7 km dbsf; deMartin et al., 2007; Parnell-Turner et al., 2017) and are rotated and flattened during their footwall exhumation, in response to isostatic rebound of the footwall block, to form low-angle (from <20° to ~35° at the seafloor; Cannat et al., 2019; Smith et al., 2006) detachment surfaces (e.g., Wernicke and Axen, 1988; Buck 1988). Exhumed mantle rocks, peridotites, exposed on the seafloor along the footwalls of these detachments are observed at oceanic core complexes (OCC) at slow-spreading ridges, such as the 13°20′N OCC on the Mid-Atlantic Ridge (MAR) (MacLeod et al., 2009), and at ultraslow-spreading ridges, such as the Atlantis Bank on the Southwest Indian Ridge (SWIR) at 57°10′E (Dick et al., 2019). An OCC is a shallow, broad, domal footwall, with a corrugated and striated top surface, juxtaposed to a low-lying topography hanging wall primarily constituted of volcanic rocks (e.g., Blackman et al., 2009; Canales et al., 2004; Whitney et al., 2013). They are predominantly formed at segment-ends and during episodes of rifting when tectonic stresses overplay magmatic processes (Blackman et al.,

2009; Buck et al., 2005). Tectonic stresses are dominant over magmatic processes at segment ends because of their limited melt-budget available, as magma is focused on the segment centers (Lin et al., 1990).

Seafloor sampling confirms melt-starved conditions in areas where long-offset, low-angle normal detachment faults are inferred. Along the slow-spreading MAR and ultraslow-spreading SWIR, serpentinized peridotites are commonly observed within a variety of tectonic settings, sometimes in a complex association with gabbros at OCCs (e.g., Cannat et al., 1993, Lagabrielle et al., 1998; Sauter et al., 2013; Tucholke and Lin, 1994), others in large amounts and with minor contribution of basalt and gabbros (e.g., Sauter et al., 2013). At the SWIR at 64°30' E, smooth and low-backscatter surfaces imaged with side-scan sonar, together with the composition of rocks samples dredged across the ridge axis, evidence broad exposures of variably serpentinized peridotites on the seafloor continuously covering tens of kilometers away from the ridge axis (Sauter et al., 2013). Detachment-related tectonics seem to control serpentinization by bringing peridotites up to shallow depths and favorable temperature conditions (<400°C) aided by a multi-scale fracture network that can transport hydrothermal fluids up to 4–5 km dbsf (Cannat et al, 2010; 2016; Rouméjon et al., 2015; Rouméjon and Cannat, 2014). Serpentinization also promotes strain localization and weakening of the lithosphere which supports the development of detachment faults (Escartín et al., 2001).

Geological and geophysical observations at slow- and ultraslow-spreading ridges mark a shift in the seafloor accretion paradigm. Oceanic crust is not only accreted by volcanism and magmatic processes. Detachment faults may take over for a period of time and be the loci of plate spreading and responsible for asymmetrical oceanic lithospheric accretion. Continuous exhumation of mantle-derived rocks occurred indeed for ~11 Myr at the SWIR (Sauter et al., 2013) and tectonic accretion at the MAR has been inferred to last up to ~3 Myr (Tucholke et al., 1998).

Controlled-source multichannel seismic (MCS) reflection has proven to be a very useful tool for studying seafloor structures and the ocean subsurface structure. One of the

earliest seismic sections with geometrical constraints on detachment faults at OCCs is from the Eastern-Central Atlantic (Ranero & Reston, 1999). A crustal reflection is traced continuously for 2 km below the basement with dips ranging from ~20° at its shallowest depths (near the basement) to ~30° at its deepest parts (2 km subbasement). Outward-facing dipping reflections beneath the fault emergence and/or the hanging wall indicate smaller dips (~6-14°) for the detachment fault at the Atlantis Massif OCC (MAR, 30° 10'N; Canales et al., 2004), and higher dips (~45-60°) for the active detachment fault at the SWIR at 64°30' E (Momoh et al., 2017). The dips in the later study might not represent true dips as the velocity model used for the depth conversion shows extremely smooth lateral and vertical velocity changes. Further constraints on detachment faults' dips are needed to better constrain the general fault geometry of oceanic detachment faults and to compare the changes between different geological settings (e.g., broad seafloor mantle domains versus OCCs) and across slow- and ultraslow-spreading ridges.

Another significant reflection identified at a few OCCs is the D reflection (Canales et al., 2004). It is a sharp, coherent reflection at ~0.2-0.25 s two-way travel time (TWT) below the seafloor across the central dome of the Atlantis Massif OCC. At this location, Canales et al. (2004) suggested that the D reflection and the presently exposed detachment surface are two separate detachments faults, and that the Atlantis Massif OCC formed by sequential slip on these two faults that merge at depth. The lithosphere between these two faults is interpreted to be composed of highly serpentinized peridotite, whereas the lithosphere below the D reflection is interpreted to be less altered mantle, which results in a strong impedance contrast of the D reflection. This reflection has also been inferred at one OCC, CT2, in the Parece Vela Basin (eastern Philippine Sea), but most of the imaged OCCs in this basin do not show organized internal reflectivity (Ohara et al., 2007).

While recent studies have provided more constraints on the seismic reflection structure of the detachment faults at ultraslow-spreading ridges (Momoh et al., 2017; 2020), there still are missing true fault dips computed with a well-resolved regional-scale velocity model (Corbalan et al., 2021), and may shed light in the still debatable fault geometry and

changes in dip with depth applicable not only to ultraslow-spreading ridges but also to OCCs elsewhere.

4.3 Study area

The ultraslow-spreading SWIR at 64° 30'E displays the globally widest exhumed seafloor domains identified thus far (Cannat et al., 2006; 2019). The extension of these domains has been mapped using extensive geological sampling (Sauter et al., 2013), petrological analyses (e.g., Cannat et al., 2008; Meyzen et al., 2003; Rouméjon et al., 2014; Seyler et al., 2003), gravity (Cannat et al., 2006) and magnetic (Sauter et al., 2008) data, and side-scan sonar studies (Sauter et al., 2013). Variably serpentinized mantle-derived rocks, peridotites, are the dominant lithology with a negligible contribution of basalt and gabbros (<5% in 16 dredges collected across-axis; Sauter et al., 2013). A very low melt supply in the study area is further supported by high normalized REE (rare earth elements) and sodium concentrations of recovered basalts (Meyzen et al., 2003). These observations indicate a large axial depth, a lower degree of melting and melt restriction to greater depths (Cannat et al., 2008; Meyzen et al., 2003; Seyler et al., 2003). Consistently, microseismicity studies have inferred the base of the brittle lithosphere at depths of around 20–35 km (Schlindwein & Schmid, 2016), considerably deeper than at melt-rich mid-ocean ridge segments (e.g., ~6 km at the center and 10–15 km at the end of the Lucky Strike segment center at MAR; Dusunur et al., 2009).

Detailed bathymetric, kinematic and side-scan sonar studies have suggested that a complex system of cross-cutting detachment faults with alternating polarity, are responsible for the exhumation of perdiotites and the asymmetrical oceanic lithospheric accretion in the study area (Cannat et al.; 2019; Sauter et al., 2013; Reston 2018). The mechanism of mantle exhumation and mode of seafloor accretion can be explained with the flip-flop rolling hinge model (Buck, 1988; Buck et al., 2005; Sauter et al., 2013). This model illustrates initial steep-angle normal faults that are rotated and flattened during the rolling hinge phase to form low-angle detachment faults displaying variably serpentinized peridotites in their exposed footwall block. When one fault is abandoned and cut by a new

steep normal fault with opposite polarity, part of the footwall becomes the hanging wall of the new active detachment fault. Successive and alternating polarity detachments locate peridotites on both sides of the spreading axis and result in an asymmetrical seafloor topography (e.g., Cannat et al., 2019; Sauter et al., 2013).

A regional-scale travel time tomographic velocity model has imaged a velocity structure consistent with the flip-flop rolling hinge model (Corbalán et al., 2021). A sharp lateral change (horizontal gradient ~1 s^{-1}) in velocities from the high-topography central dome (interpreted to be the footwall with higher seismic velocities) to the juxtaposed low-lying bathymetry (interpreted to be the hanging wall with lower seismic velocities) is accompanied by a switch in polarity of the largest velocity anomaly, from 1.5 to −1.5 km/s, and a high vertical gradient (~2 s^{-1}) in the top 2 km. Corbalán et al. (2021) interpret these observation as the seismic expression of the active axial detachment fault. Similar patterns of high velocities and vertical gradients juxtaposed to low velocities and vertical gradients serve to identified five abandoned detachment faults elsewhere in the model. 3D MCS studies in the study area have shown evidence of detachment faults (Momoh et al., 2017; 2020) with outward-facing dipping reflections in the location of some previously interpreted faults, but with some packages of reflections whose dip is not consistent with the flip-flop faulting model. A group of sub-horizontal reflections are also identified in the interpreted hanging wall and attributed to the seismic expression of a damage zone due to recent extensional stresses NS oriented in the hanging wall or that occurred in the previously active fault's footwall (Momoh et al. 2017).

4.4 Seismic reflection data acquisition and processing

4.4.1 Seismic data acquisition

The SISMOSMOOTH 2014 seismic experiment (Leroy & Cannat, 2014) was a joint Canadian and French effort to carry out a major 2D and 3D MCS and ocean bottom seismometer (OBS) survey across the SWIR at 64°30′E (Figure 4.4.1.1). The main objective was to characterize the seismic reflection and velocity structure of the oceanic

lithosphere formed at the ultraslow-spreading SWIR to understand better the mantle exhumation dynamics that brings large areas of mantle-derived peridotites to the surface and to examine the geophysical fingerprints of the variably serpentinized peridotites in the uppermost lithosphere. The first results from the analysis of the 3D MCS and selected 2D MCS collected data are shown in (Momoh et al., 2017, 2020). Results from the analysis of two orthogonal ~150-km-long OBS profiles (Figure 4.4.1.1) along and across the spreading ridge axis are shown in Chapter 2 and Corbalan et al. (2021). Here, I present the results from the coincident MCS across-axis profiles (Figure 4.4.1.1) with the OBS north-south (NS) profile, which includes MCS profiles SMOO32, SMOO33, SMOO38, and SMOO39.

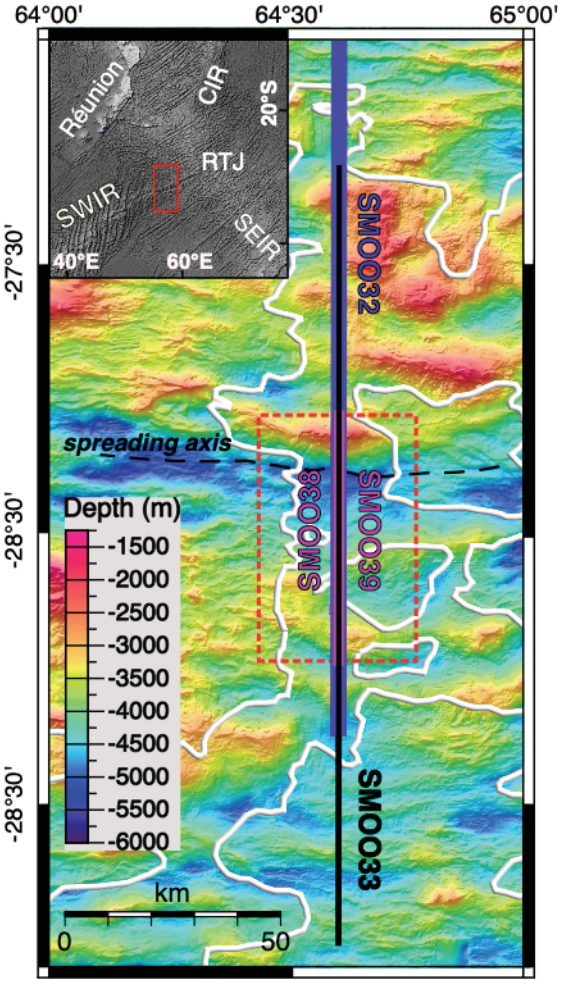

Figure 4.4.1.1. Location of the study area and MCS survey. Inset in the top left shows the location of the Southwest Indian Ridge (SWIR) relative to the Réunion Island, the Central Indian Ridge (CIR), the Southeast Indian Ridge (SEIR) and the Rodriguez Triple Junction (RTJ). Red rectangle shows the limits of the study area presented in the main figure. Main map shows the 4 MCS profiles (SISMOSMOOTH Survey; Leroy et al., 2015) processed in this thesis overlying a color bathymetry map (Cannat et al., 2006; Momoh et al., 2017). Solid blue, black, and purple lines depicts shot locations with different shooting distance interval. MCS profiles with a constant shooting interval of 150 m (SMOO38 and SMOO39) are shown with thick purple lines. MCS profile SMOO33 with a variable shooting distance (150 m inside the dashed red rectangle and 300 m outside) is shown in black. MCS profile shot every 50 m (SMOO32) is shown with a thick dark blue line. Areas bounded by thick white lines delimit the smooth non-volcanic seafloor (Cannat et al., 2019).

To collect the SISMO-SMOOTH MCS data, a 360-channel digital streamer with a 4.5-km-long active section was towed at a depth of 18 m for the SMOO32 profile and 22.5 m for the rest of the profiles. The inter-receiver spacing was 12.5 m. Recording time was 18 s, except for SMOO32 where it is reduced to 12 s. Sample rate was 2 ms for all the profiles. The seismic source for SMOO32 consisted of two linear arrays of 11 airguns with a total volume of 2625 in^3 towed at a mean depth of 12 m, and 14 airguns with a total volume of 6790 in^3 towed at a mean depth of 14 m for the rest of profiles. The two arrays of sources were fired every 20 s (~50 m at a velocity of 5 kts) for SMOO32, and every 150 m in the central part (area inside the dashed red rectangle in Figure 4.4.1.1) and 300 m in the distal parts (area outside the dashed red rectangle in Figure 4.4.1.1) for the rest of profiles. The differences in survey geometry for SMOO32 and the rest of profiles is due to the fact that SMOO32 was collected along other 2D MCS profiles, while the rest of the profiles were collected during the collection of wide-angle long-offset seismic OBS data. Nevertheless, considering these differences, all the data can be used together to perform MCS data processing and later interpretation of the NS profile reflection images. The four profiles can be used jointly or independently at all or selected processing steps.

The MCS streamer had 17 compasses placed at 300 m intervals to record the inclinations and azimuth of the streamer at those locations at each shot and with the floating birds they served as control depth monitors for monitoring during acquisition. Similarly, the exact position of the research vessel and the end of the streamer were recorded by two differential global positioning satellite (GPSs) receivers on board and another GPS receiver placed on a tail buoy at the end of the streamer. The resulting nominal geometry is that the minimum distance between a shot and first receiver, offset, is 177 m and the maximum offset is 4,665 m. The total length of the NS profile spans 180.2 km across the axial valley (Fig. 4.4.1.1).

4.4.2 Multichannel Seismic Reflection data processing

4.4.2.1 Navigation and geometry QC

To confidently interpret seismic reflection images is essential to know the exact position of sources and receivers at each shot. Long MCS streamers rarely follow the projected straight line during the acquisition because the ocean currents tend to feather (deviate) the cable from its nominal or intended position. For example, an average value of 10° feathering in a 4.5-km-long streamer results in a maximum deviation of ~780 m. During the data acquisition survey, stored SEG-D data were converted to SEG-Y on board and the correct source and receiver locations were calculated with the navigation files and the compasses along the streamer and added to the SEG-Y headers. Thus, the SEG-Y data used in this work have the true geometry already embedded. GMT (Wessel & Smith, 1998) plotting was used to QC (Quality Control) the source and receiver positions. I use industry grade Omega Geophysical Data Processing SLB software for the MCS processing. The full processing workflow is shown in a schematic form in Figure 4.4.2.1.1. The effects of each processing step are demonstrated with data examples from the SIMOSMOOTH MCS profiles.

The first step in the processing flow is to load the SEG-Y data to Omega and the QC step. During this step I realized that while the source and receiver positions were correct, the data were missing the mid-point locations. I calculated the mid-points based on the source-receiver pairs and added them to the data headers. Figure 4.4.2.1.2 shows the survey geometry and the source, receiver and mid-point locations. Data from SMOO33 north of the dashed red rectangle in Figure 4.4.1.1 was discarded because neither the SEG-Y nor the raw navigations files have the source-receiver locations. The rest of SMOO33 is split into two during the processing steps, SMOO332 and SMOO333, because of their difference in the shooting interval. The former is the central part of the profile with a shooting interval of 150 m, and the latter is the southernmost part with a shooting interval of 300 m.

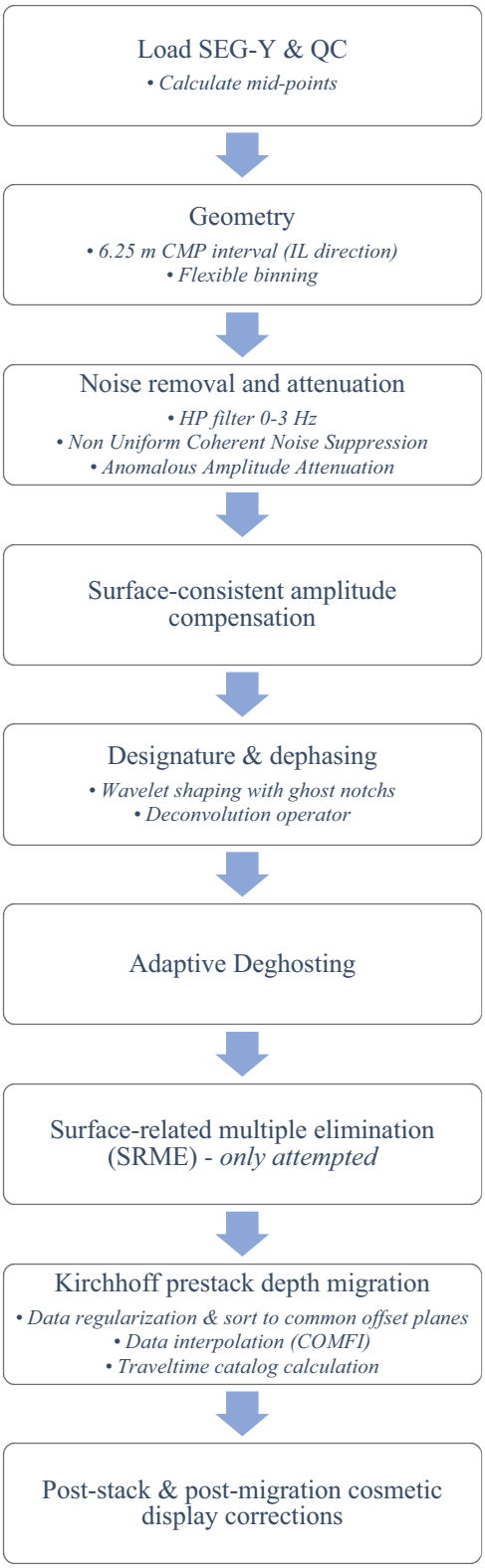

Figure 4.4.2.1.1. Flowchart with the processing sequence. IL stands for Inline; CMP stands for common-mid point and COMFI stands for Compact Fourier Interpolation.

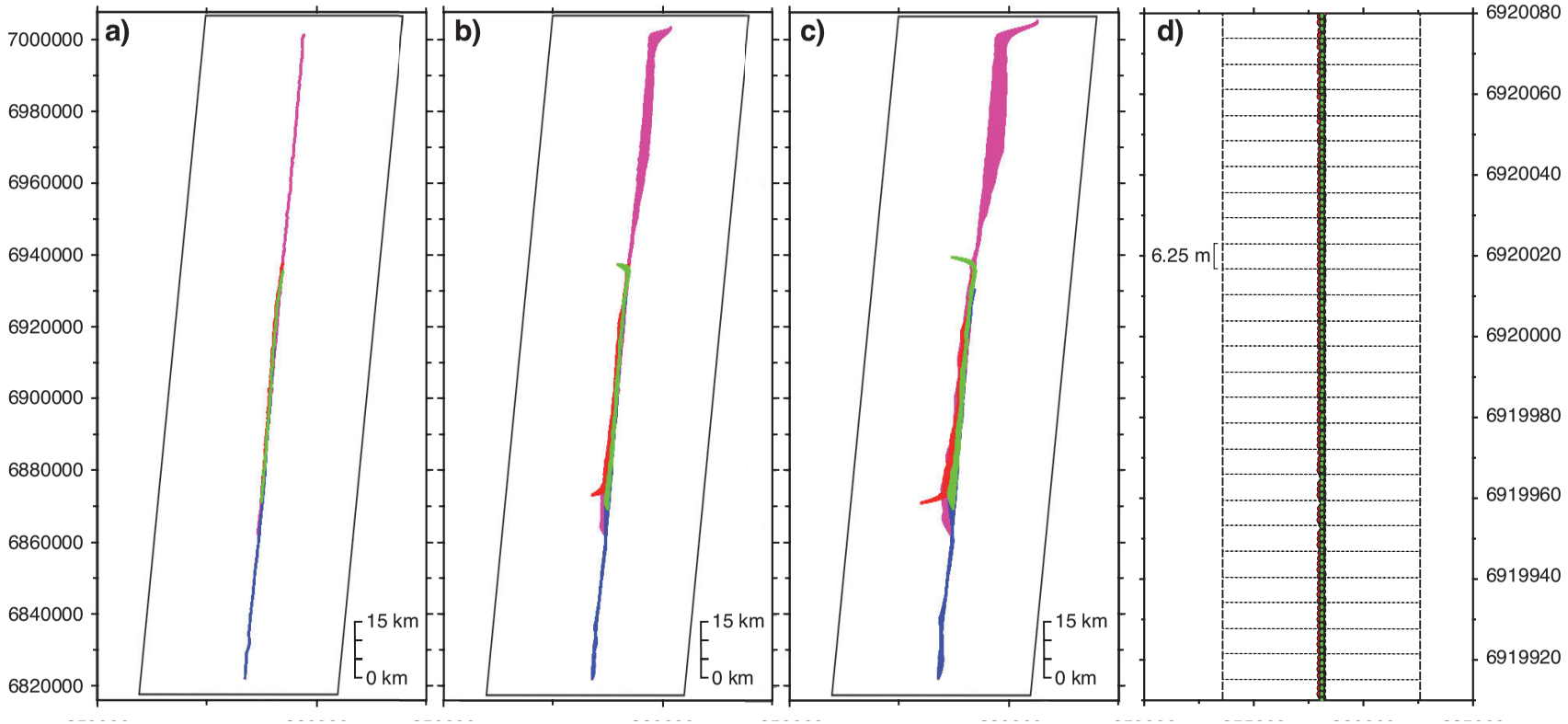

Figure 4.4.2.1.2. UTM maps showing the acquisition geometry. Full-survey maps showing the (a) source positions, (b) mid-points positions, and (c) receiver positions for SMOO32 in pink, SMOO33 in blue, SMOO38 in red, and SMOO39 in green. In (a–c) black inclined square shows the boundary of the 3D grid with an azimuth of 180.9°. (d) Magnification of the central part of the survey showing the mid-point locations and the bin sizes with flexible binning applied (bin extension in the crossline direction).

To gather and sort all source-receiver pairs sharing the same common mid-point gather (CMP), I assigned a 3D rectangular grid. Since SMOO profiles are not exactly coincident in all their shots, I fit a linear regression line to all the midpoints in Matlab to produce a master (horizontal) grid that it has the same azimuth (180.9°) of the fitted line and contains all the mid-points. The 3D grid has 37,420 inlines (IL; lines in the NS direction, the shooting direction) and 364 crosslines (XL; lines in the EW direction, perpendicular to the shooting direction). Each cell in the grid, limited by 2 ILs and 2 XLs, is a bin. The bin size is chosen by the processer, but it is normally chosen in relation to the survey geometry. A standard value is to choose half the inter-receiver spacing for the IL bin size and double the inter-receiver spacing for the XL bin direction. I choose a binning size of 6.25 m by 25 m in the IL and XL direction. However, a flexible binning approach (i.e., bin extension to cover all data wide-wise in one bin in the XL direction) is commonly used throughout the processing steps to produce stacks of all lines combined along the NS profile, along the best-fitting line for all the mid-points including data that would otherwise lie outside of the static bin.

The survey geometry yields a nominal full-fold or common bin coverage for the SMOO32 profile of 45 traces per CMP bin and 15 traces per CMP bin for profiles SMOO38, SMOO39 and central parts of SMOO33. The nominal full fold for the outer parts of SMOO33 profile is 7.5 traces per CMP bin. Fold coverage maps (Fig. D.1a–e in Appendix C) indicate a similar coverage with a fold coverage of 44.4 for about 46.3% of SMOO32 data and 15.3 for 65–70% of the data pertaining profiles with a shooting interval of 150m (SMOO332, SMOO38, SMOO39). Profile SMOO333, shot every 300 m, shows a fold coverage of 7–8 for about 88% of the data.

A stack of all lines merged along the NS profile is shown in Figure 4.4.2.1.3, using a constant water velocity (1500 m/s) for the normal moveout (NMO) correction. Only the area of interest for chapters 2 and 3 are shown in the stacks displayed in this chapter. This area is the one covered with OBS on the seafloor, crossing rays in the subsurface in travel time tomography and with a standard deviation in velocity of <~0.1 km/s in the tomographic model (Corbalán et al., 2021).

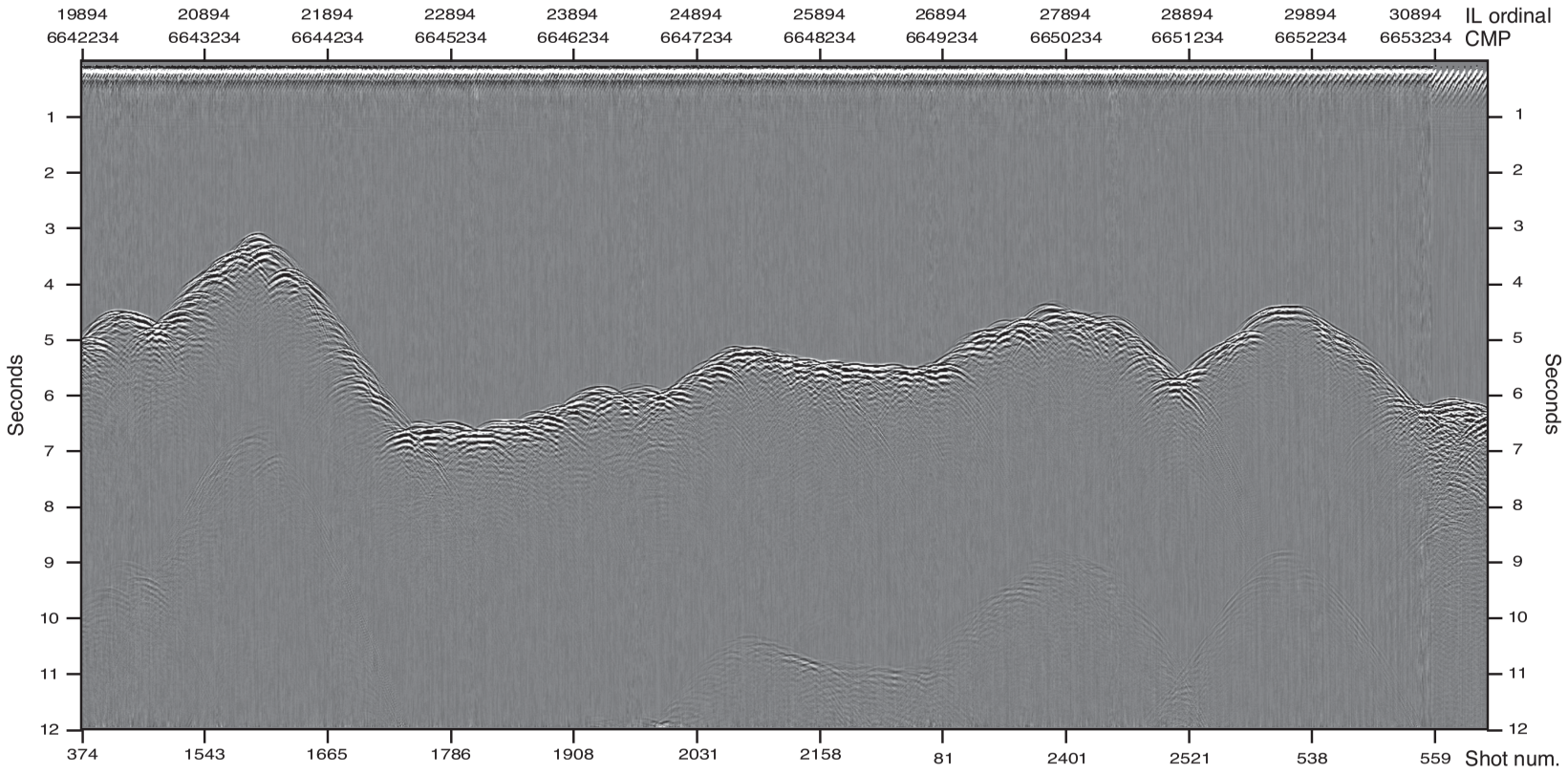

Figure 4.4.2.1.3. Raw seismic stack section of MCS NS profile in time domain.

4.4.2.2 Resampling and spherical divergence correction

Given that our data size is not very large and that we observe useful information for frequencies above 125 Hz (Appendix C, Fig. C2), we choose not to resample to 4 ms, which would reduce the maximum signal frequency from 250 Hz to 125 Hz and possibly introduce minor vertical resolution degradation. This step is commonly used to reduce data size by half when processing large amounts of data and when there is no useful signal above 125 Hz. Similarly, many academic studies next apply a spherical divergence correction, although in industry this is no longer standard. It is now preferable not to change the amplitudes permanently so early in the processing workflow and to use amplitude corrections if needed to visualize the data. Similarly, time function gains are used before some processing steps and immediately removed afterwards if this improves the algorithm performance (e.g., during Anomalous Amplitude Attenuation, AAA).

4.4.2.3 Noise removal

Noise removal is the next step, in order to increase the signal-to-noise (S/N) ratio and remove or attenuate unwanted noise that may be masking reflections from geological structures. First, the signals were high pass (HP) filtered at 3 Hz. Figure 4.4.2.3.1 shows an example of a common shot gather before the HP, after, and their difference to show that only unwanted noise has been removed.

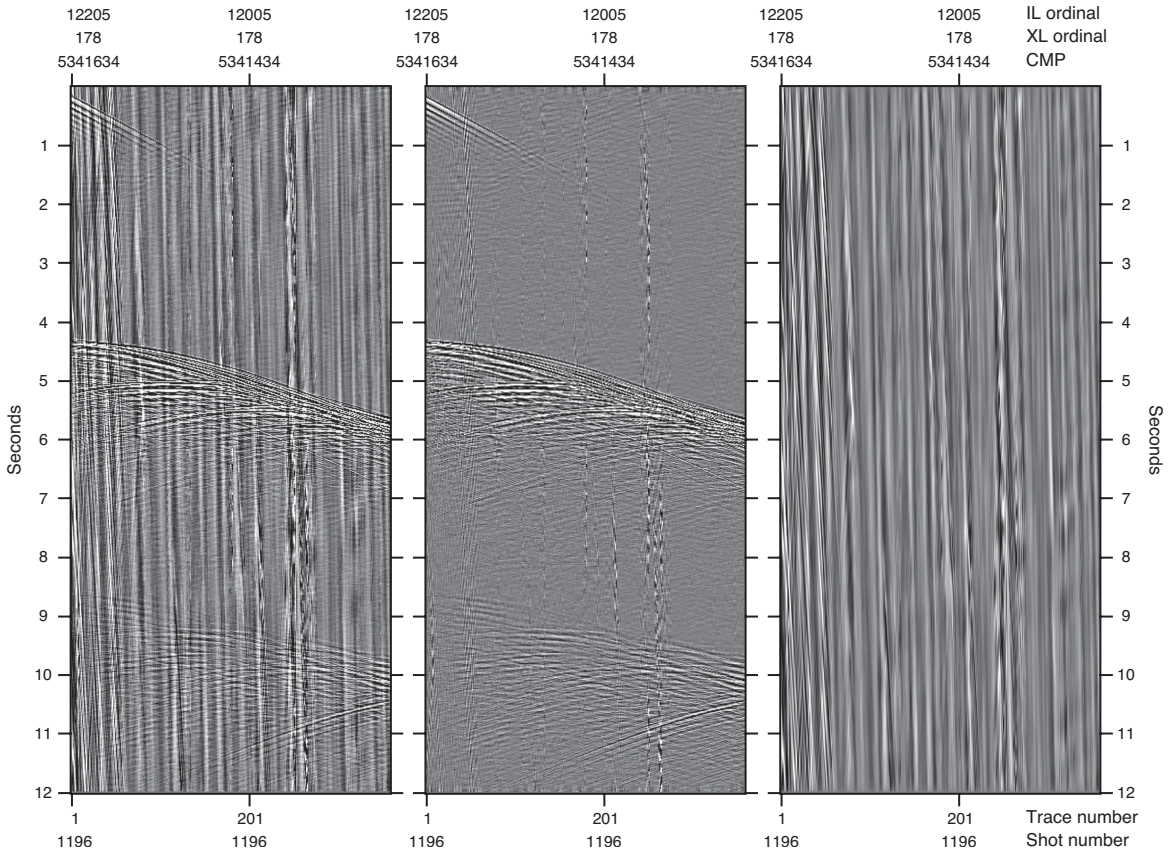

Figure 4.4.2.3.1. HP filtered shot gather before (left), after (middle) and their difference (right). Shot gather 1196, Line SMOO32.

I next use a Non-Uniform Coherent Noise Suppression (NUCNS) dip filter to remove coherent noise. The coherent noise suppression approach estimates noise in the frequency-space (f-x) domain in common shot gathers that can be removed from the signal. It removes coherent noise (e.g., shot-generated) with an apparent velocity in the frequency-wavenumber (f-k) domain different to the velocity of reflected signals. Compared to traditional f-k filters, the main advantage is that NUCNS is significantly less prone to introduce artifacts. Fan filters are defined with corner-frequencies 0-2-4-6 Hz, a 7-traces filter length and a stop-, pass-low velocity of 5, 10 m/s, respectively, and a stop-, pass-high velocity of 1200, 200 m/s, respectively. Additional benefits to this approach are its anti-alias protection, to avoid wrap-around of noise fan filters toward the signal in the f-k domain, and its additional signal protection, to minimize the possibility of the noise model containing any signal. To protect the signal, a fan filter in the f-k domain is applied with a pass-, stop-velocity of 1000, 8000 m/s, respectively, and a cosine taper in between.

Figure 4.4.2.3.2 shows a common shot gather before and after the NUCNS and their difference.

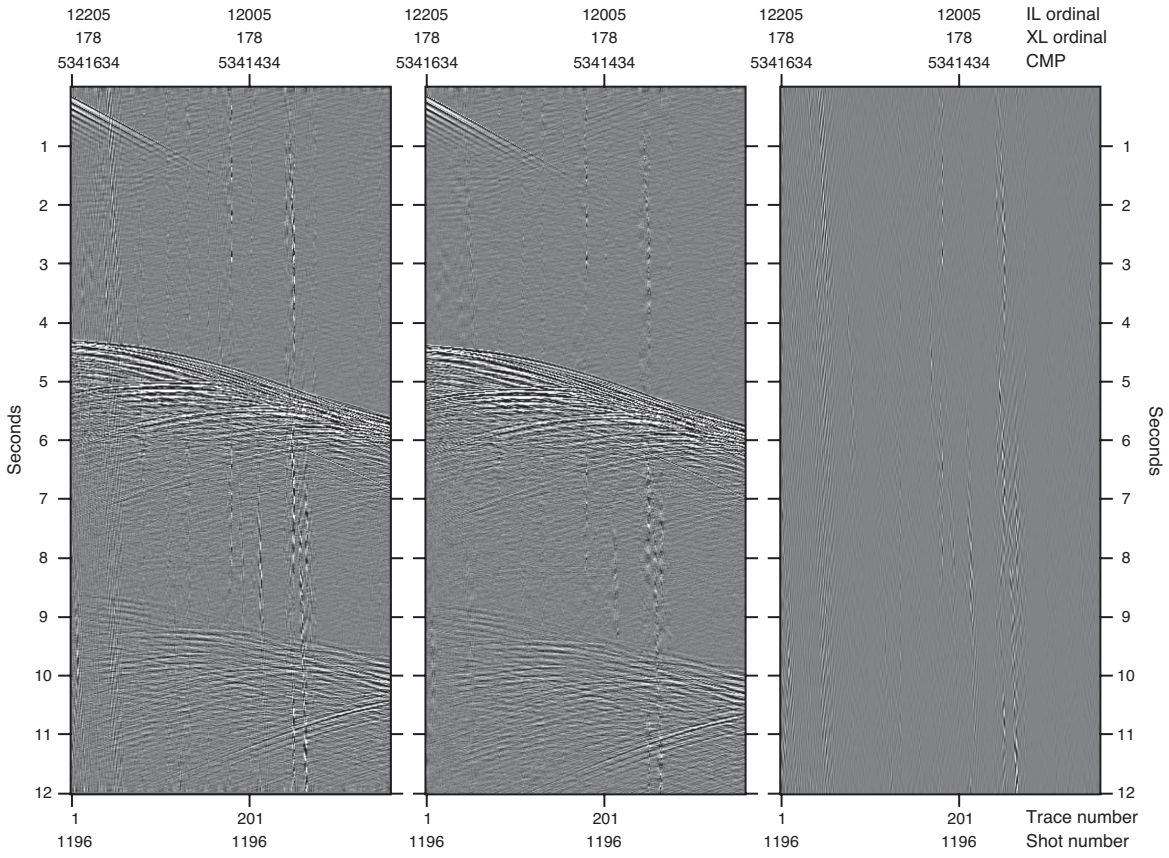

Figure 4.4.2.3.2. NUCNS filtered shot gather before (left), after (middle) and their difference (right). Shot gather 1196, Line SMOO32.

Next, a sequence of multiple AAA is applied to further attenuate unwanted noise. AAA is commonly used in industry. The AAA algorithm discriminates anomalous amplitudes (noise) within specified frequency bands, based on a computed threshold. If a trace or multiple traces in a frequency band are considered anomalous because their amplitudes exceed the threshold, the amplitudes are reduced. The algorithm calculates the median amplitude for the selected number of traces and time window length and the median deviation. The threshold is computed by multiplying the median deviation by a specified factor. For instance, the first AAA applied to the SISMO-SMOOTH MCS data focuses on removing spikes. The entire time-window length and bandwidth (0 to Nyquist), and a

very high threshold factor (100) are employed. All the AAAs are applied only from the seafloor downwards, as this approach introduced less artifacts and showed a better performance. The parameters for all the AAAs are summarized in Appendix D (Table D.1). Figure 4.4.2.3.3 shows an example of a shot gather before and after AAA processing. Figure 4.4.2.3.4 shows an example before and after the complete sequence of noise removal processing (HP, NUCNS, and AAAs).

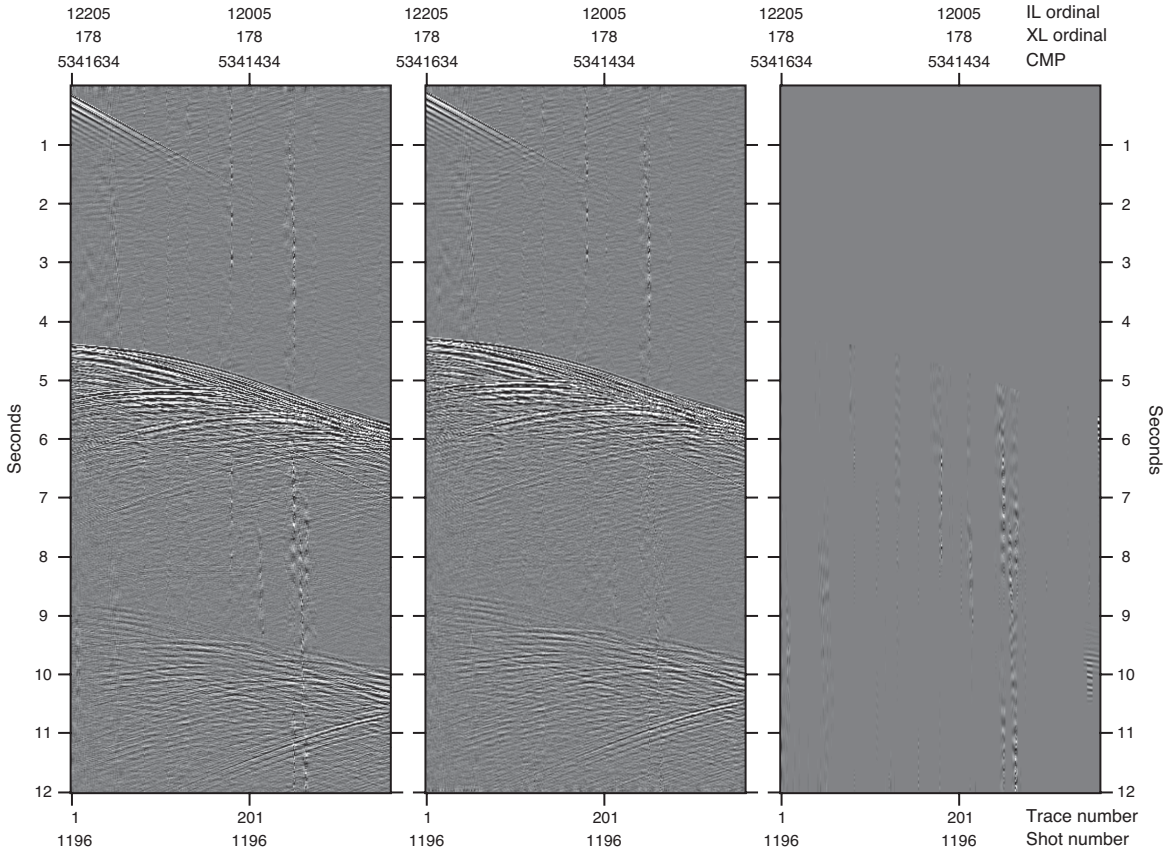

Figure 4.4.2.3.3. A shot gather before (left) the applied sequence of AAA, after (middle) and their difference (right). Shot gather 1196, Line SMOO32.

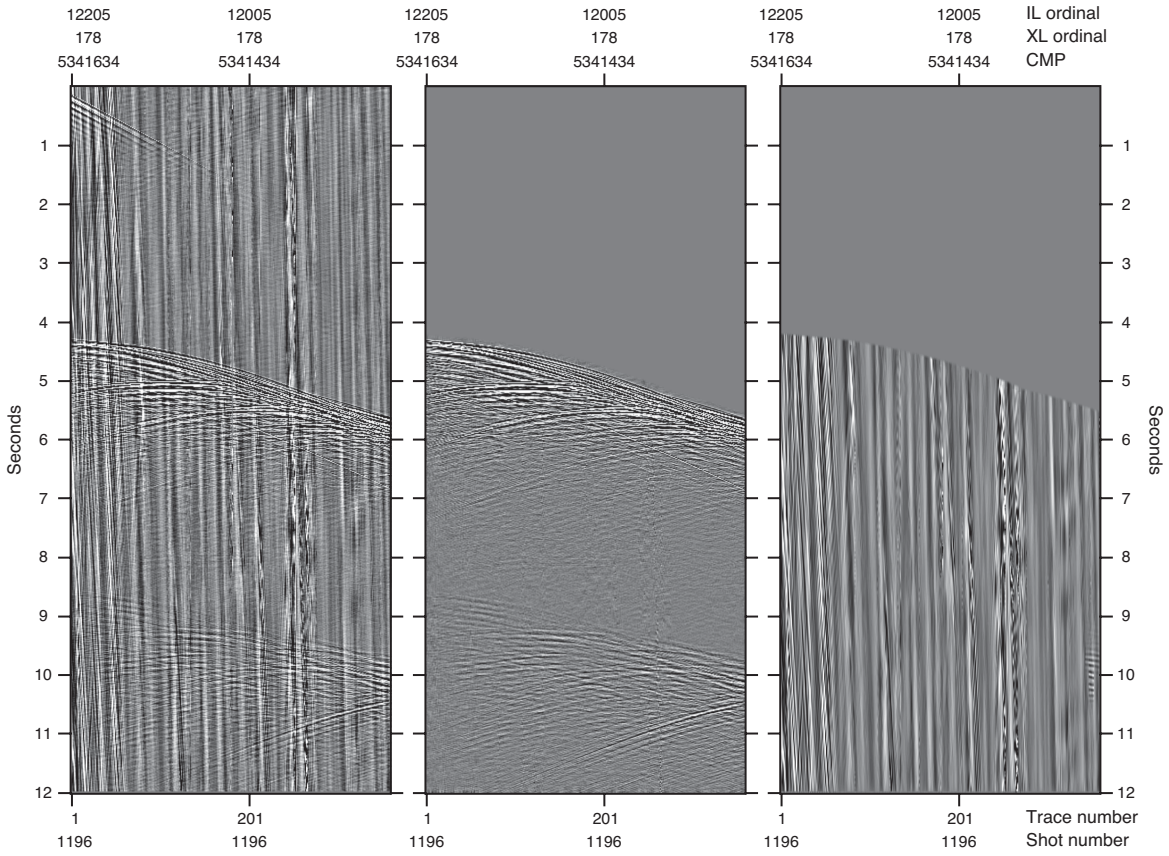

Figure 4.4.2.3.4. A shot gather before any noise removal is applied (left), after the complete sequence of noise removal is applied (middle) and their difference (right). Panels in the middle and right are muted at 100 ms above the seafloor. Shot gather 1196, Line SMOO32.

A water velocity stack of the NS profile after the noise attenuation step is shown in Figure 4.4.2.3.5. Common shot gathers from each profile are processed independently in this step and merged for stacking and presentation purposes.

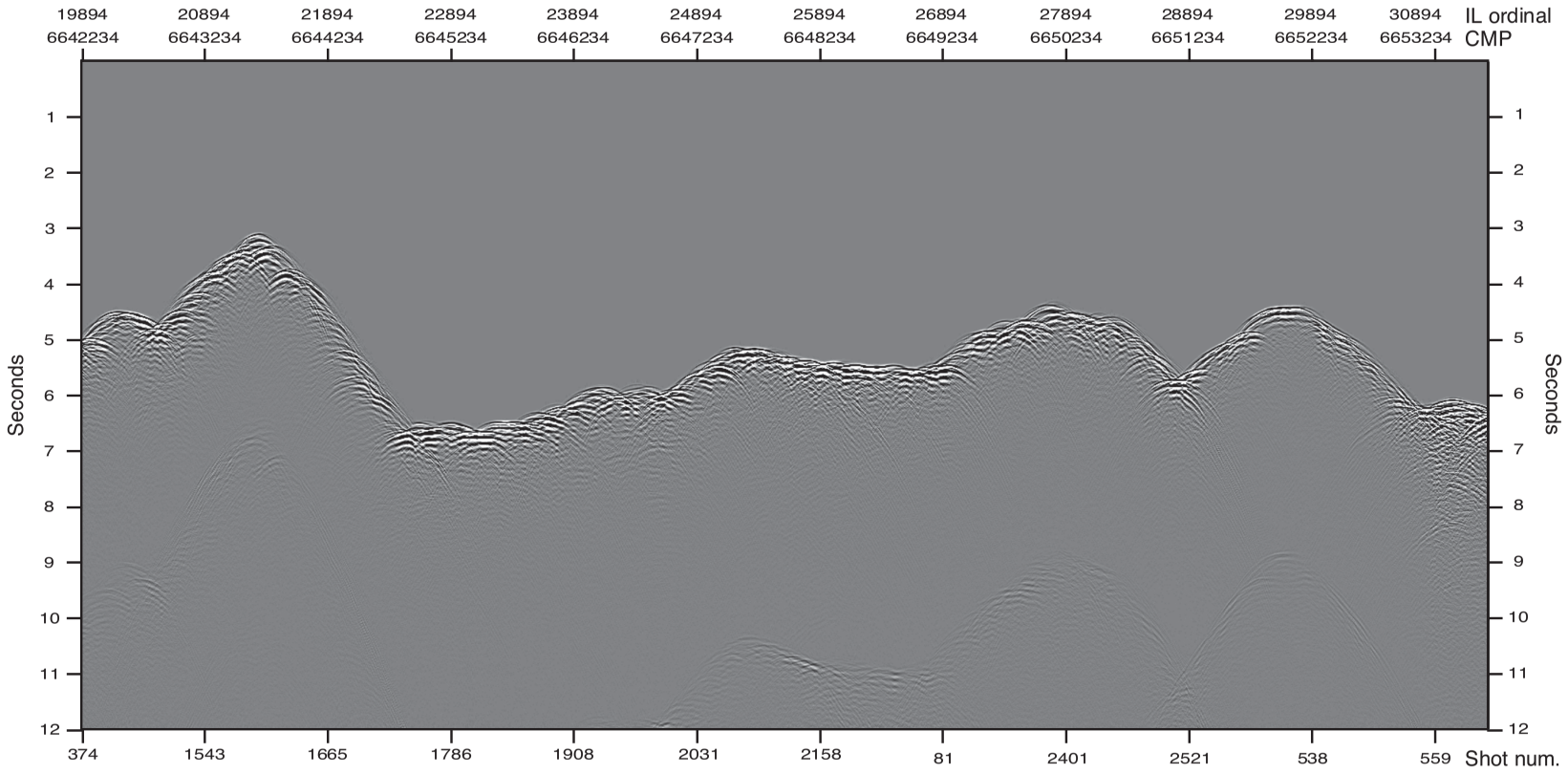

Figure 4.4.2.3.5. Seismic stack section of MCS NS profile in time domain after noise removal.

4.4.2.4 Surface consistent amplitude compensation

Following noise removal, I applied a surface-consistent amplitude compensation (SCAC) to balance the amplitudes and correct variations related to near surface recording conditions, such as the shot strength and the receiver coupling. The first step in SCAC analysis is to estimate the contribution of the source, receiver, offset and the Earth's reflectivity (usually referred to as the CMP component) to the observed seismic trace amplitudes and calculate scaling factors to equalize the amplitudes trace-to-trace. This is achieved by calculating the log Root-Means Square (RMS) values for each trace and each component and using a least-squares minimization to solve a surface-consistent model for shot, receiver, offset and CMP. An example of the RMS amplitudes of data traces from Line SMOO39 before and after SCAC and their difference is shown in Figure 4.4.2.4.1. Common shot gathers from each profile are processed independently in this step and amplitudes are scaled to RMS amplitudes. There is no clear visual difference before and after applying SCAC, so no shot gather example is shown. A water velocity stack of the NS profile after the noise attenuation step is shown in Figure 4.4.2.4.2.

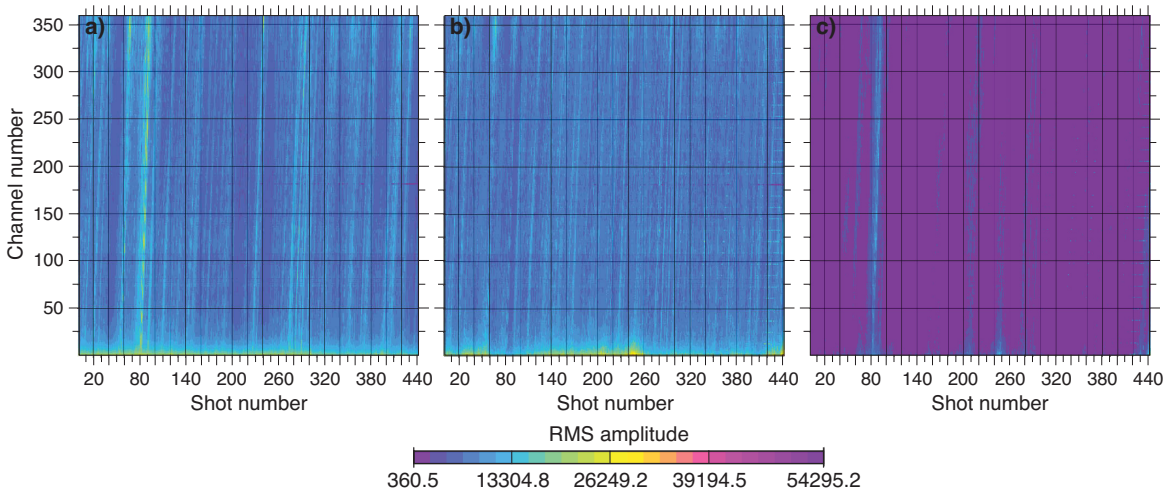

Figure 4.4.2.4.1. RMS amplitude of Line SMOO039 before (left), and after applying SCAC (middle). The difference between the two is shown in the right.

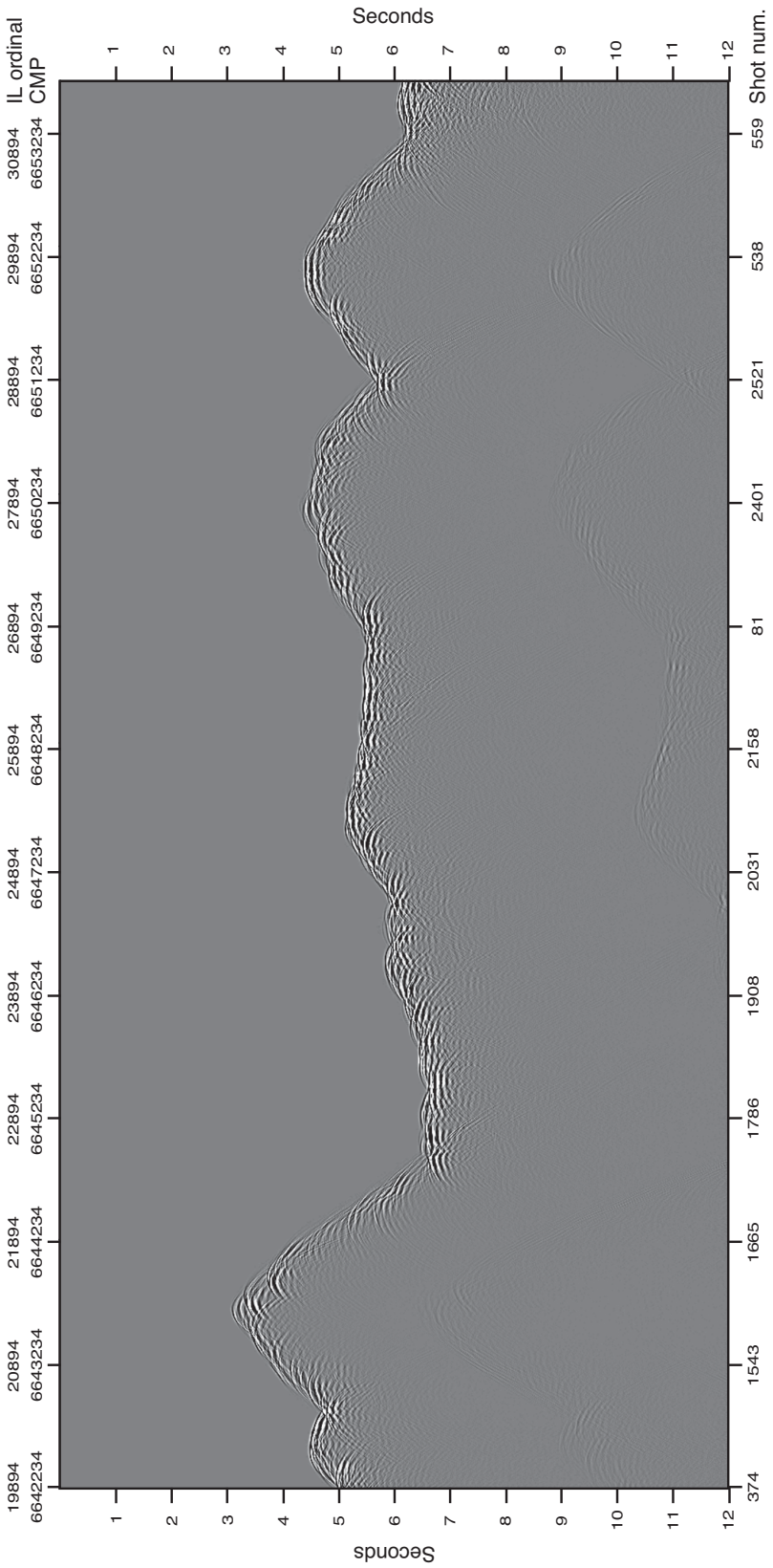

Figure 4.4.2.4.2. Seismic stack section of MCS NS profile in time domain after applying SCAC.

4.4.2.5 Designature, debubble and dephase

This processing step compresses or shapes the wavelet to a sharper zero-phase wavelet, increases the temporal (vertical) resolution, and removes reverberations (repeating signals) due to the source bubble pulse. If the source signature wavelet is accurately known, for example when the airguns have hydrophones placed right above, then a deterministic convolution can be followed. However, the SISMO-SMOOTH survey did not acquire this information, so I followed a statistical approach to first derive the source wavelet (air gun signature deconvolution) and then carry out the debubble and dephase. The estimated source wavelet (Appendix D, Fig. D.2) is extracted by stacking the matching traces via autocorrelation of their spectral estimates computed from the seafloor to 4 s below the seafloor (i.e., designature window length 4 s) and a constant autocorrelation half-length of 2 s. All the common shot gathers from all lines were used together in the autocorrelation. Next, a filter operator was designed (Appendix D, Fig. D.3) based on the extracted source wavelet and a sequence of actions performed on the wavelet: first to remove the bubble effect, I designed a deconvolution operator with a 10% white noise percentage, 73 ms prediction distance, and 2048 ms operator length; second the zero-phase equivalent wavelet is computed; and third, I inserted the source and receiver ghost notches in the wavelet to aid the next step of deghosting. These steps aim to derive a wavelet closer to the true source wavelet. While common shot gathers from each profile are processed independently in this step, the filter operator used in all profiles stays the same (Appendix D, Fig. D.3) for consistency.

The effect of this processing step is shown in figures 4.4.2.5.1, 4.4.2.5.2, 4.4.2.5.3, 4.4.2.5.4. Figure 4.4.2.5.1 shows an example of a common shot gather before and after designature and Figure 4.4.2.5.2 shows a common far-offset gather before and after applying designature. Figure 4.4.2.5.3 shows how the frequency spectra of the data has changed from the raw data following noise attenuation and SCAC and after applying designature. Figure 4.4.2.5.4 shows a water velocity stack of the NS profile after this processing step is applied.

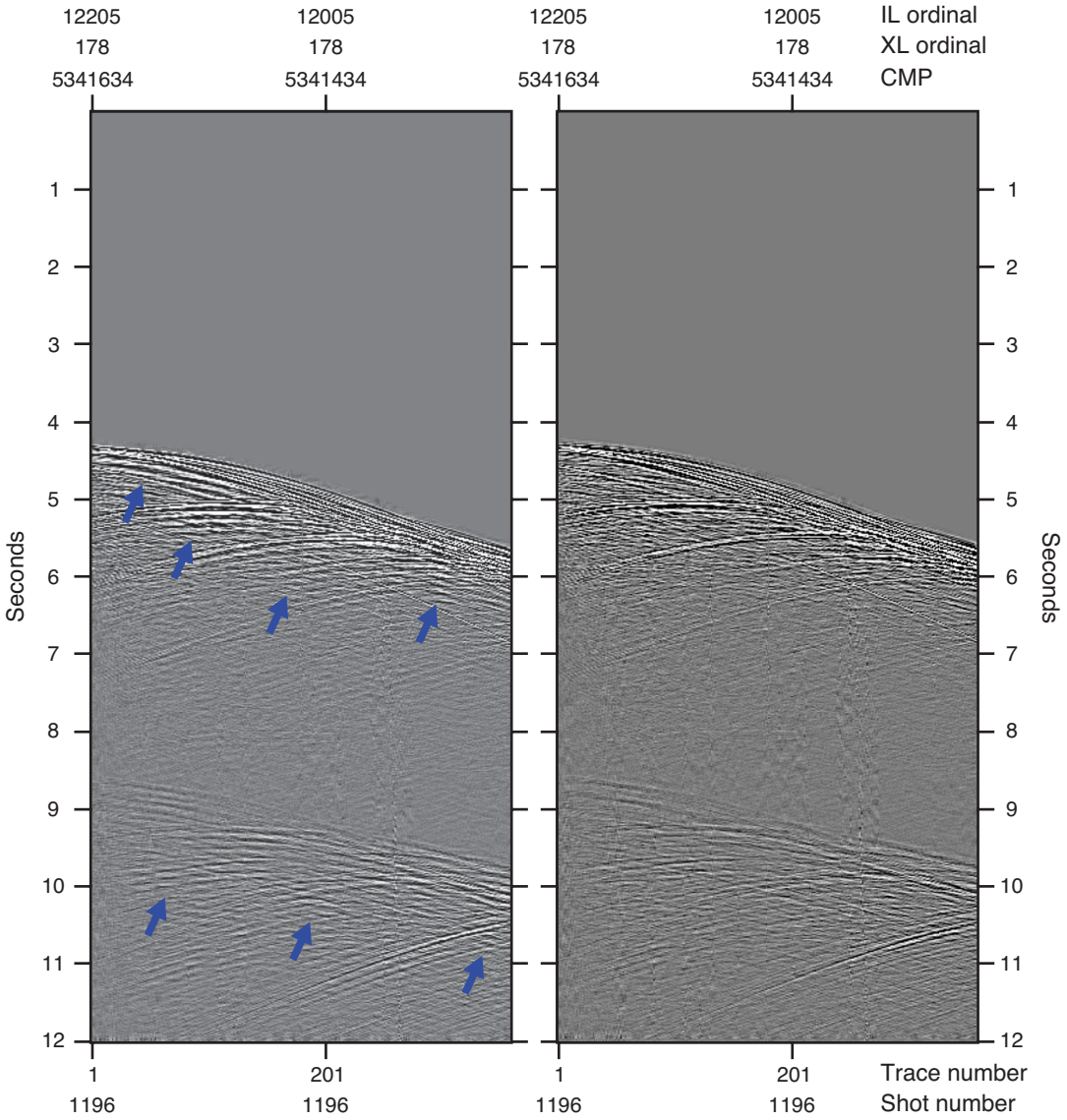

Figure 4.4.2.5.1. A shot gather before designature is applied (left) and after (right). Blue arrows indicate the repeated signals typical of the air gun bubble effect existing in the (left) and removed in the (right). Panels are muted at 100 ms above the seafloor. Shot gather 1196, Line SMOO32.

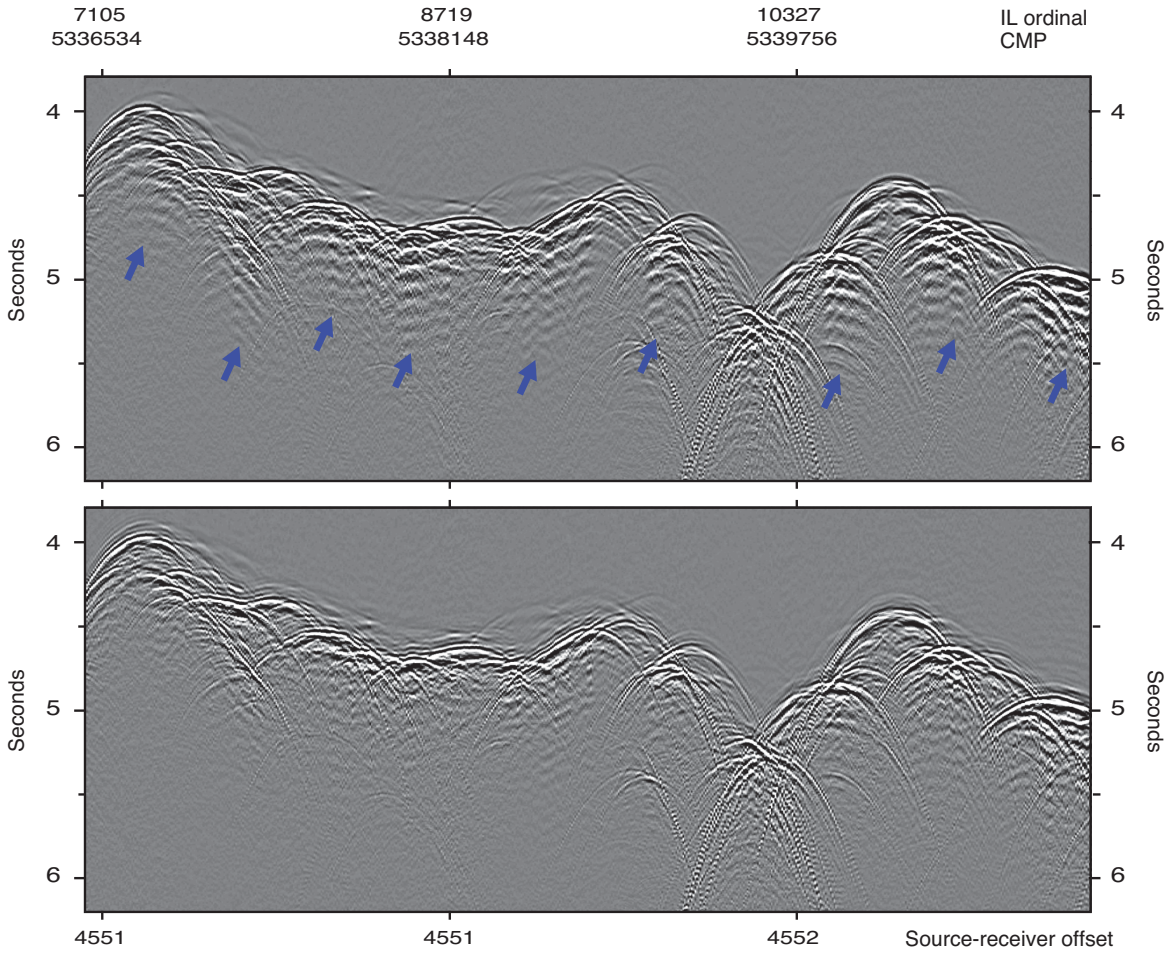

Figure 4.4.2.5.2. A common offset gather before designature is applied (top) and after (bottom). Blue arrows indicate the repeated signals typical of the air gun bubble effect existing in the (top) and removed in the (bottom). Shot gather 1196, Line SMOO32.

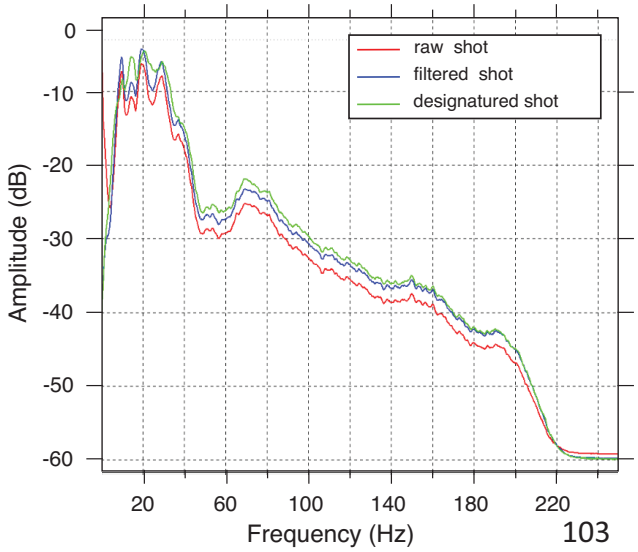

Figure 4.4.2.5.3. Amplitude spectra of an unprocessed shot gather (red), same gather after noise attenuation (blue), and after designature (green). Amplitude spectra is smooth by a frequency smoothing bandwidth of 1 Hz. Shot gather 1196, Line SMOO32.

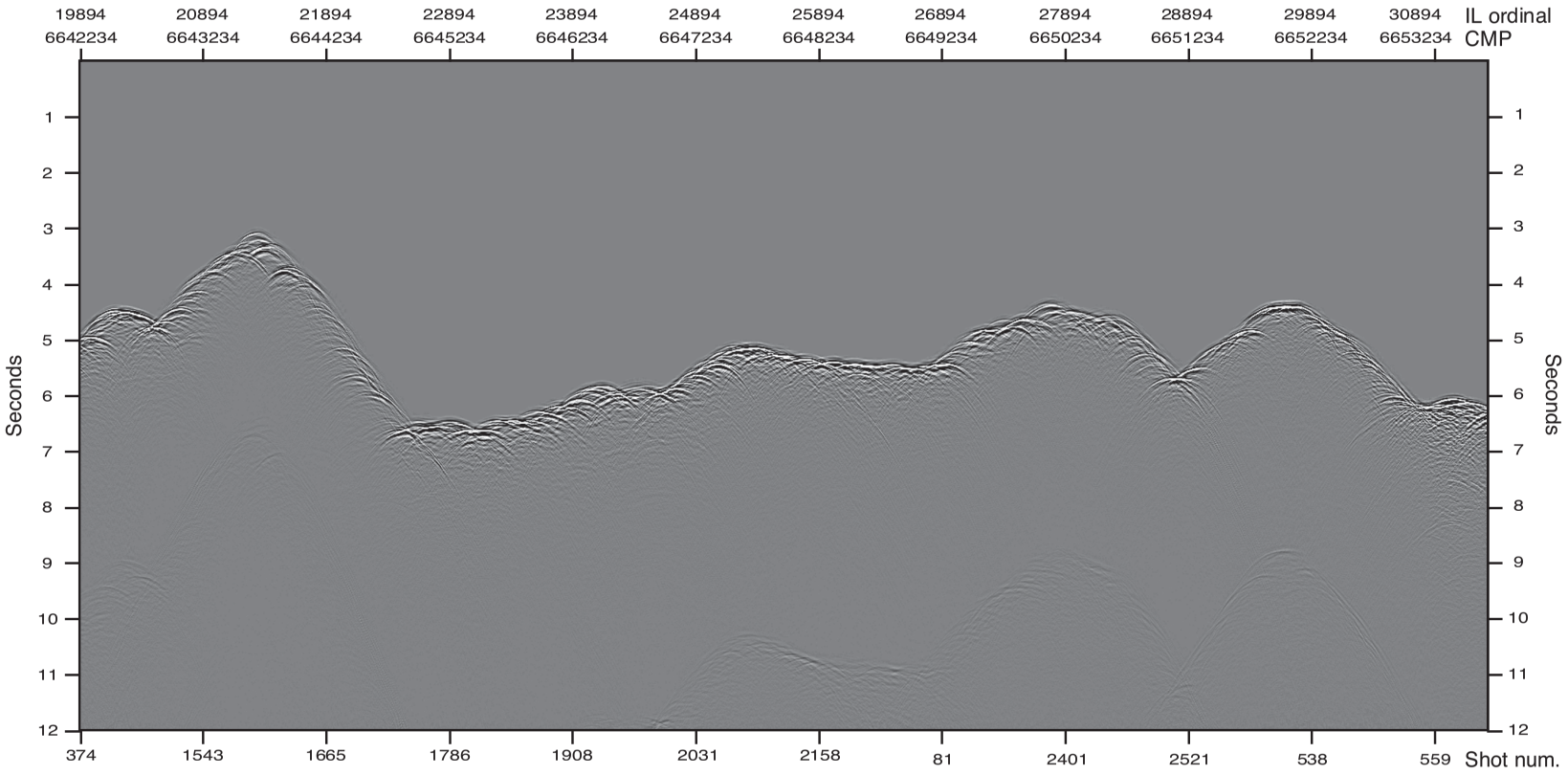

Figure 4.4.2.5.4. Seismic stack section of MCS NS profile in time domain after designature.

4.4.2.6 Adaptive deghosting

Adaptive deghosting (AD) is used to attenuate ghost reflections, originating at the source and/or the receiver locations, which may cause loss of frequency content by destructive interreference with the primary signal. Ghost reflections are due to energy travelling upward to the sea surface and down to the seafloor or the receiver. A rule of thumb to calculate the ghost frequency notches is to divide the water velocity (normally assumed to be 1500 m/s) by 2 times the distance from the sea surface to the source location for estimating the source ghost frequency notch, and by 2 times the distance from the sea surface to the streamer location for estimating the receiver frequency notch. These estimations are normally taken into consideration when designing an MCS survey, and source and receiver depths are usually chosen so that these frequency notches are beyond the range of frequencies of interest for the survey. In the SISMO-SMOOTH MCS data, a source ghost notch can be expected around 62 Hz for SMOO32 and 54 Hz for the rest of lines, and a receiver ghost notch can be expected around 42 Hz for SMOO32 and 33 Hz for the rest of lines.

The AD algorithm used decomposes the wavefield in upgoing wavefield and down going wavefield in the τ-p domain to remove the upgoing wavefield related to the ghost notches. The detailed methodology and mathematical theory are described in Rickett et at. (2014). Furthermore, it can remove the effect of the source and receiver ghost notches simultaneously in a single pass and adapts to errors in the water velocity or the source/receiver depth. Common shot gathers from each profile are processed independently in this step and merge together for stacking and presentation purposes. An interpolation within each shot gather is required to fill in missing traces. As a result of the AD process, the amplitude/frequency spectrum is broadened and flattened, and the output data are redatummed to the sea surface. Figure 4.4.2.6.1 shows a common shot gather from line SMOO32 before and after AD. Figure 4.4.2.6.2 shows the spectrum before and after AD for another common shot gather. Figure 4.4.2.6.3 shows a water velocity stack of the NS profile after the AD processing step is applied.

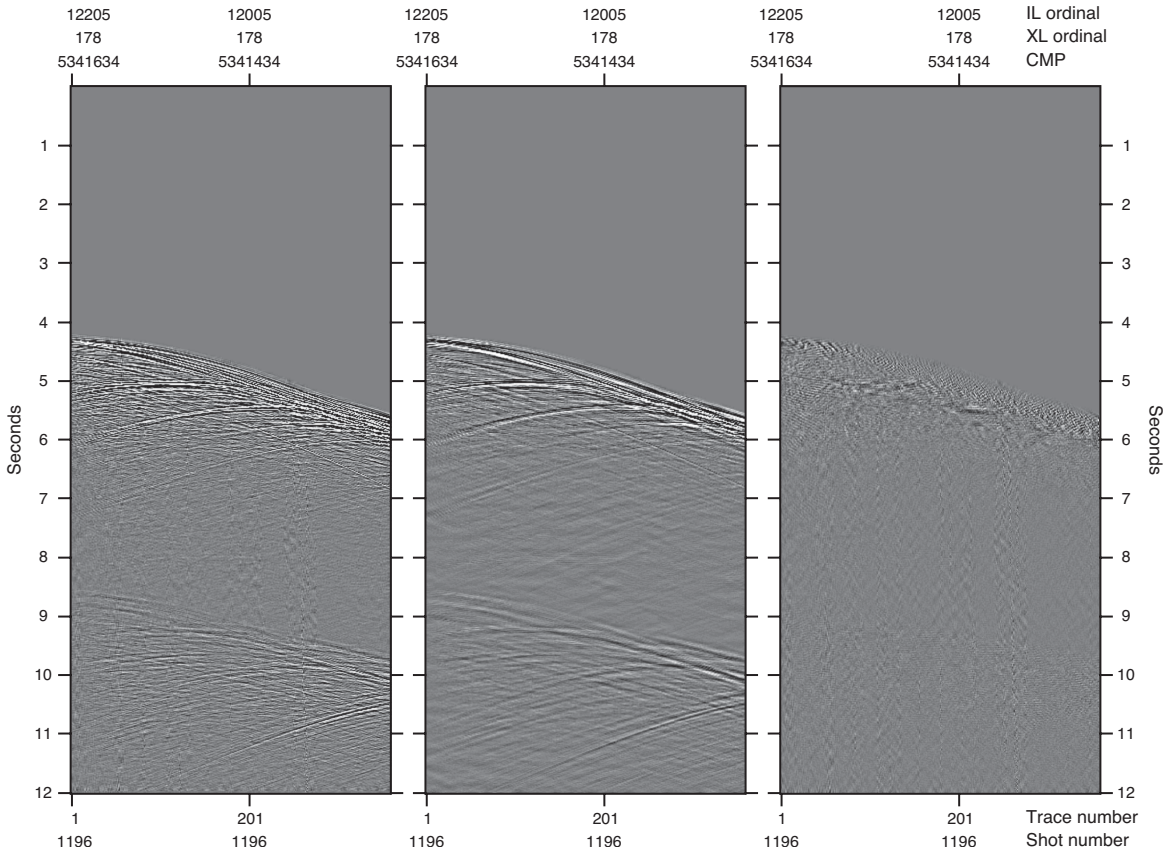

Figure 4.4.2.6.1. A shot gather before (left) the applied AD, after (middle) and the residuals (right). Shot gather 1196, Line SMOO32.

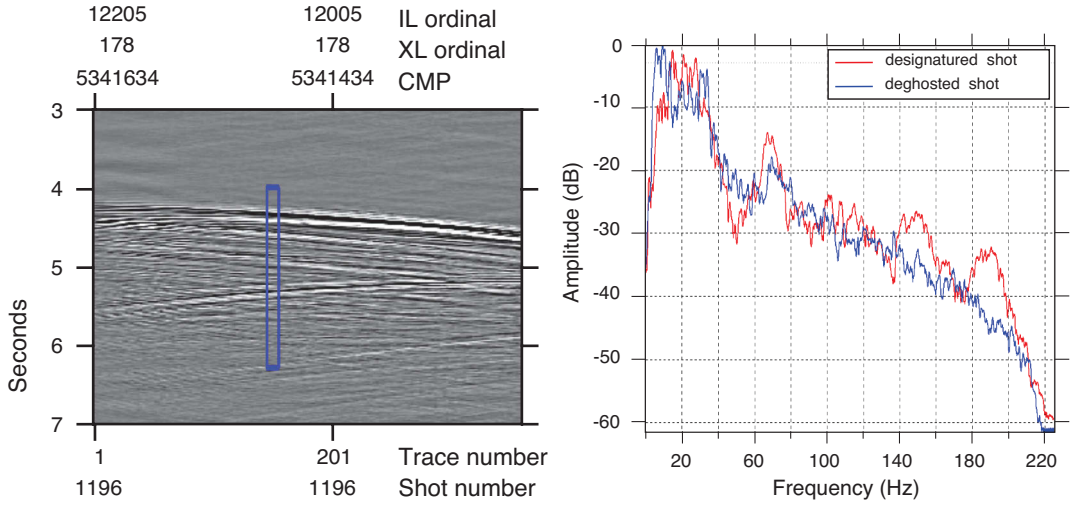

Figure 4.4.2.6.2. Amplitude spectra of a shot gather before (red) and after AD (blue). The blue rectangle in the left show the window selected for the spectral analysis. Amplitude spectra is smooth by a frequency smoothing bandwidth of 1 Hz. Shot gather 1206, Line SMOO32.

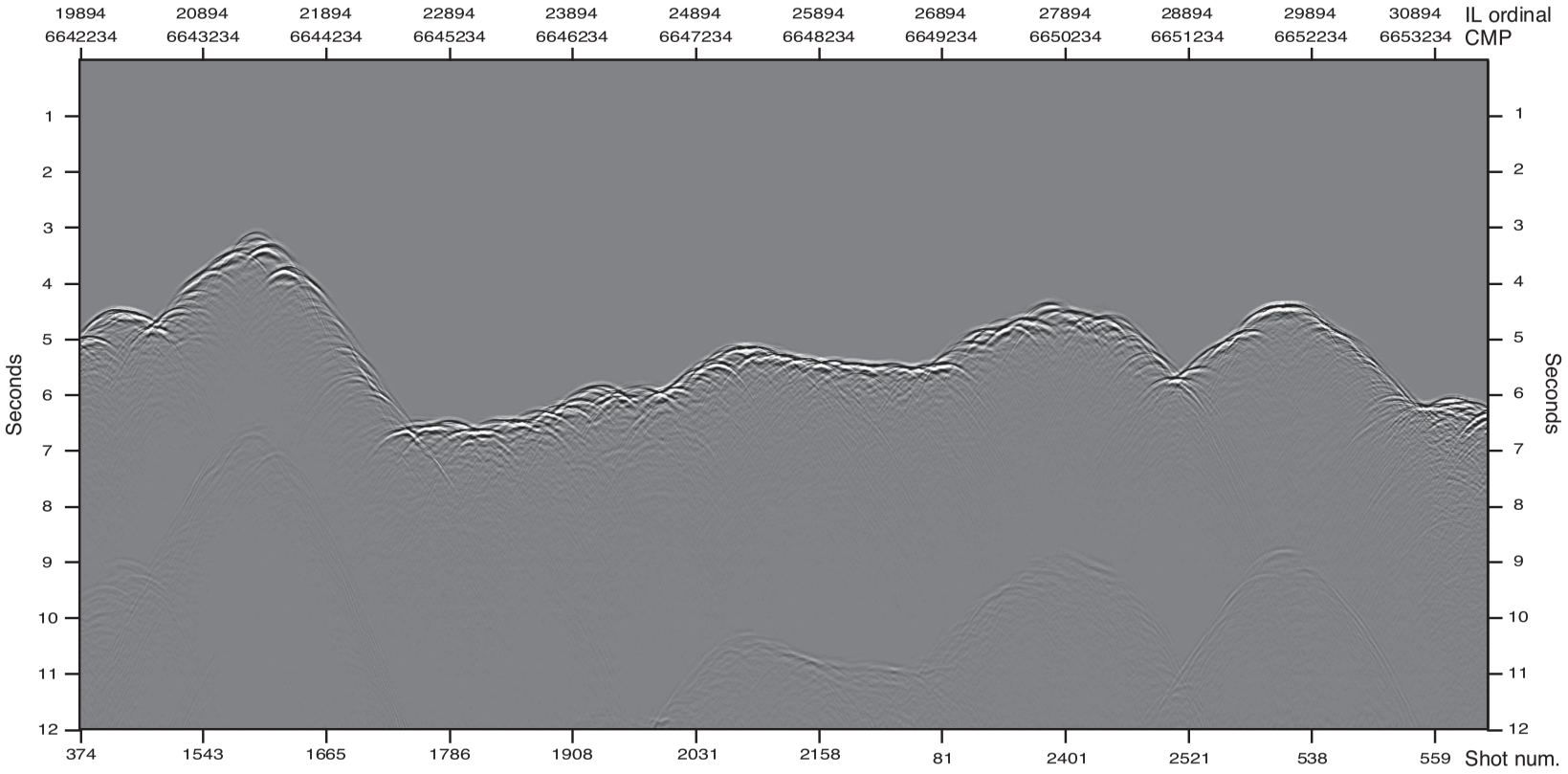

Figure 4.4.2.6.3. Seismic stack section of MCS NS profile in time domain after AD.

4.4.2.7 2D pre-stack Kirchhoff depth migration

Seismic migration is an essential step in the processing workflow as it attempts to correct the distortions of the geological structure inherent in the data by repositioning reflections into their true geological position in the subsurface, and thus, in both space and time. Reflections' amplitudes are summed up and move up-dip along a hyperbolic diffraction curve until the summed amplitude is located in the curve apex. Migration improves the seismic data lateral (spatial) resolution, as it collapses the Fresnel zone, and collapses diffractions to their point of origin. Dipping reflective events made of many diffraction hyperbolas superposed (Huygen's principle), are steepened and shortened because of the migration process. The quality of the diffraction summations, the shape of the hyperbola, and the performance of the migration process itself, is greatly controlled by the velocity field. The advantage of using depth migration versus time migration is that it can better handle lateral velocity variations. Normally, if no velocity information is known, one needs to perform seismic velocity analysis in the MCS data to determine CDP stacking velocities. Then, the most recommended approach is to employ a time migration algorithm, such as the pre-stack Kirchhoff time migration (KTM), to obtain more accurate velocity information, and use it to further constrain the velocity field with tomography on the MCS data, and finally run a Kirchhoff depth migration (KDM). This approach is frequently used both in industry and academia when there is no velocity information from a complimentary dataset, such as a coincident OBS survey, and for sedimentary basins.

In this thesis, to take advantage of the complimentary OBS/MCS datasets available and because there are only few reflections to pick in constant-velocity stacks (CVS) to determine CDP stacking velocities, pre-stack KDM is employed with the velocity information computed in Chapter 2 (Corbalan et al., 2021). Pre-stack depth migration (PSDM) is often recommended for imaging complex structures and areas with strong velocity contrasts (Reston et al., 2004). To carry out the migration, I first rearrange the data from common shot gathers to common offset planes and grouped all data in 30 groups. The first group contains all data for offsets between 0–300 m, the last group contains data with offsets between 4500–4750 m, and the 28 groups in from 300 to 4500

m are split up every 150 m. Different arrangements were tested, but the first offset plane with the smallest source-receiver offsets and the last offset plane always entailed a larger offset range to counterbalance the low fold coverage at the ends of the MCS lines. The goal was to have a similar amount of traces in each of the common offset plane. Omega KDM algorithm manual strongly recommends this type of data sorting as input data for optimum performance. Data is then regularized with a Compact Fourier Interpolation (COMFI), a weighted multi-dimensional least-squares interpolation, to positioned weighted-summed output trace in the center of each cell or bin within the offset planes. A time-variant low-pass (LP) high-cut filter is then applied to the data to attenuate high frequency noise in the deeper part of the section. The filter was designed with high-cut down 3 dB at 55 Hz with a 45 dB/octave slope for 2.5–4 s below the seafloor, 15 Hz and 25 dB/octave slope for 4–7 s below the seafloor, and 10 Hz and 20 dB/octave slope from 7 s below the seafloor.

The KDM algorithm runs in a 2-step process. First, it calculates traveltimes from each shot location to each point in the output 3D traveltime cube and creates a traveltime catalog of all the possible raypaths based on the shot locations and 3D grid points. The raypaths are directly controlled by the velocity cube provided. I used industry grade Petrel E&P software to create the cube based on the velocities shown in Chapter 2, Chapter 3 and Corbalán et al. (2021). The second step is the main migration step, and it uses the traveltime catalog created in the first step, and the regularized, interpolated and filtered seismic data. Different values of migration aperture were tested, e.g., constant aperture vs time-variant aperture, and the best results were found with a 5500 m varying aperture with a 30° dip at 3.8 s, 50° at 5.5s, 60° at 7.5 s, and 89° at 9 s and below.

Figure 4.4.2.7.1 shows an example of the output migrated gathers for input data not interpolated with COMFI, whereas Figure 4.4.2.7.2 shows an example of the output migrated gathers for input data interpolated with COMFI. As with the migrated gathers, the stack sections of migration performed with or without interpolation do not show strong differences, but there seems to be a slight improvement with the interpolated data.

Figures 4.4.2.7.3 shows an example of the mute used before stacking, and Figure 4.4.2.7.4 shows a seismic stack section of the migrated gathers with interpolated data.

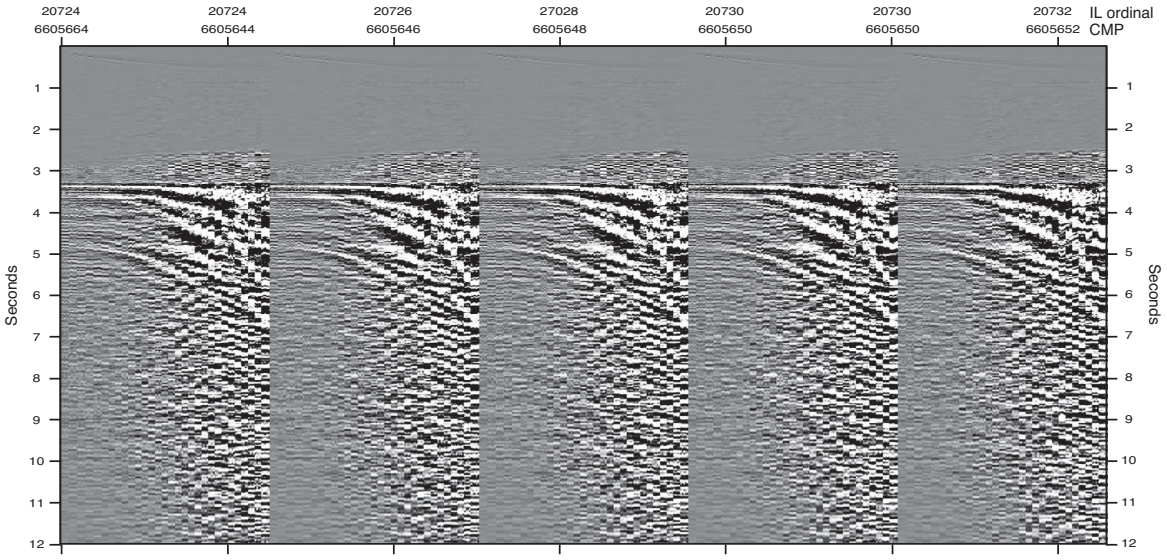

Figure 4.4.2.7.1. A common reflection point or migrated gather, output of the migration run with no interpolated data. Line SMOO32.

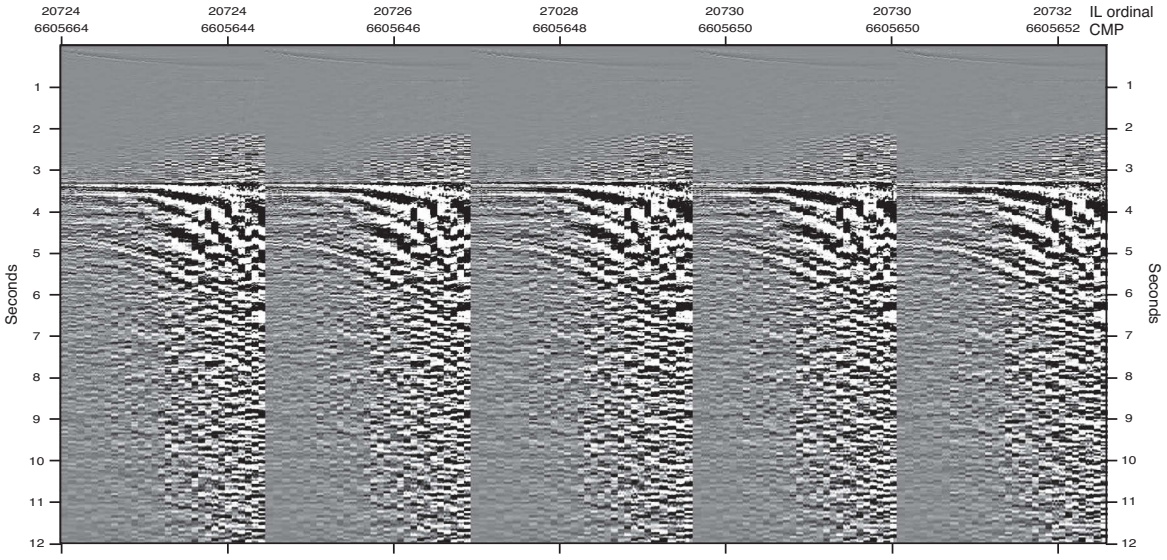

Figure 4.4.2.7.2. Same common reflection point or migrated gather than in Figure 4.4.2.7.1, but output of the migration run with interpolated data. Line SMOO32.

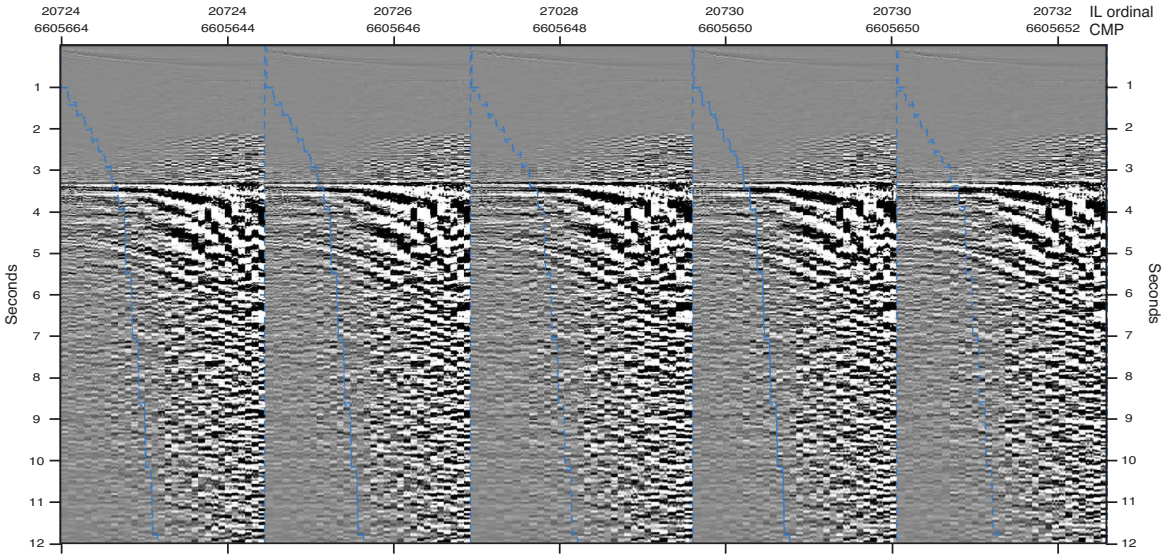

Figure 4.4.2.7.3. Same common reflection point or migrated gather than in Figures 4.4.2.7.1 and 4.4.2.7.2 showing in blue the mute selection. Data to the right of the blue line will be muted before stacking the migrated gathers. Line SMOO32.

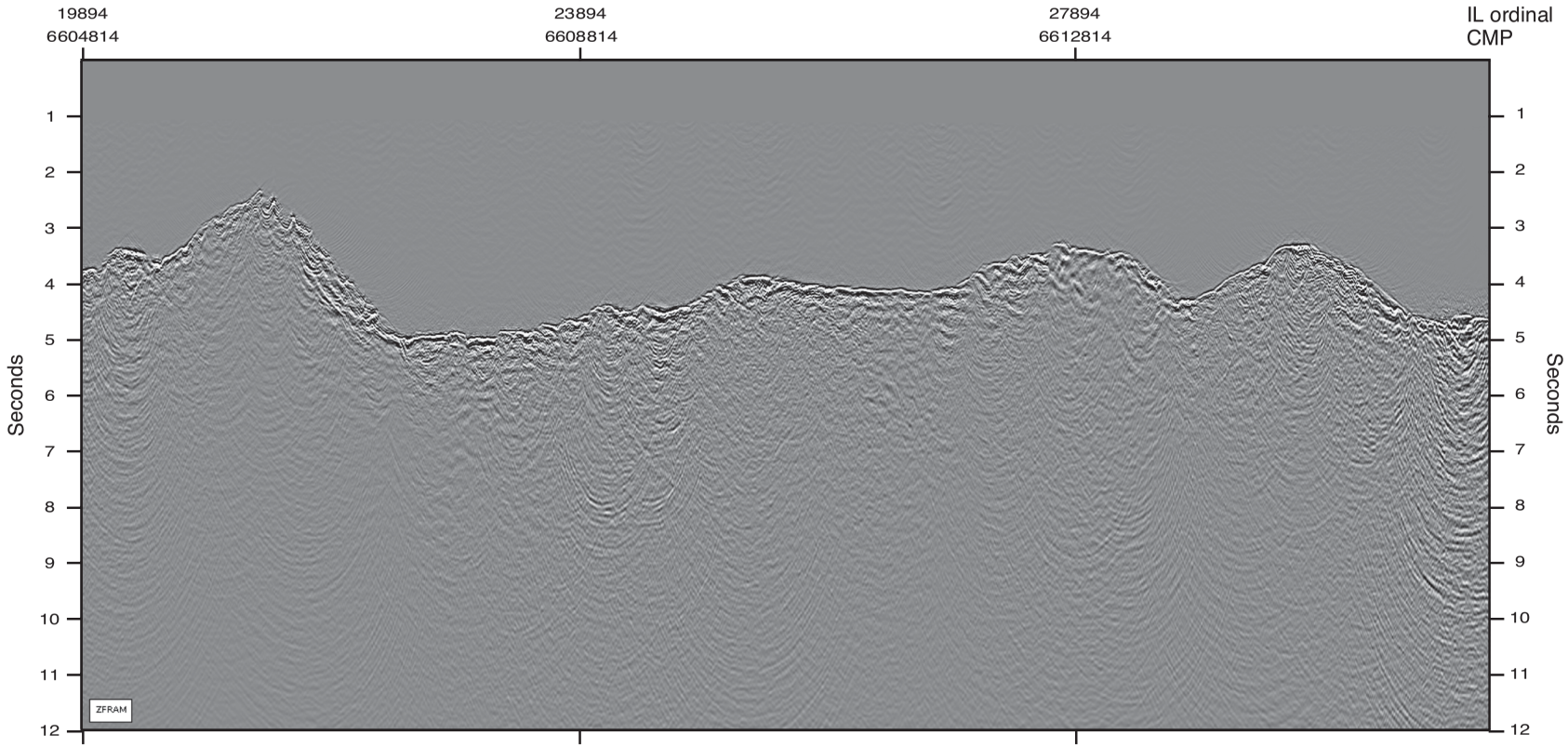

Figure 4.4.2.7.4. Prestack depth migrated section of MCS NS profile in time domain after KDM. A zero-phase bandpass (BP) filter is applied with corner frequencies 2-5-18-25 Hz.

The velocity model, computed from OBS data with an inherently coarser resolution than MCS data, might not be entirely accurate and velocities might be too high as reflections in the migrated gathers (Fig. 4.4.2.7.1 and 4.4.2.7.2), although only a few, do not appear flat. A quick test on migrating with a velocity model derived from the MCS velocity spectrum or semblance, seemed to flatten more the reflections in the migrated gathers, but there was no improvement on the final stack section. Future work in Chapter 5 discusses other approaches to constrain the velocity field better to be used in the MCS processing.

4.5 Results

The depth migrated stack section (Fig. 4.4.2.7.4) does not show much organized internal reflectivity or many continuous coherent reflections. However, this is not entirely surprising as previous MCS results in equivalent or same geological areas (e.g., Canales et al., 2004; Momoh et al., 2017; 2019; Ohara et al., 2007) also do not show many coherent reflections. The lack of organized internal reflectivity is likely due to the complex seafloor and steeply dipping slopes of seafloor structures together with a large acoustic impedance between seawater and peridotites exposed on the seafloor. Furthermore, the SISMO-SMOOTH data available for this thesis come with limitations, as the shooting interval is considerably greater than standard MCS acquisition (300/150 m versus 37.5 m) for most lines, except for line SMOO32 which it is still larger (50 m versus 37.5 m). This study area would greatly benefit from higher quality MCS data, such as for example the one shown in Canales et al. (2004) with a 6-km-long streamer (versus 4.5 km) and 37.5 m shooting interval.

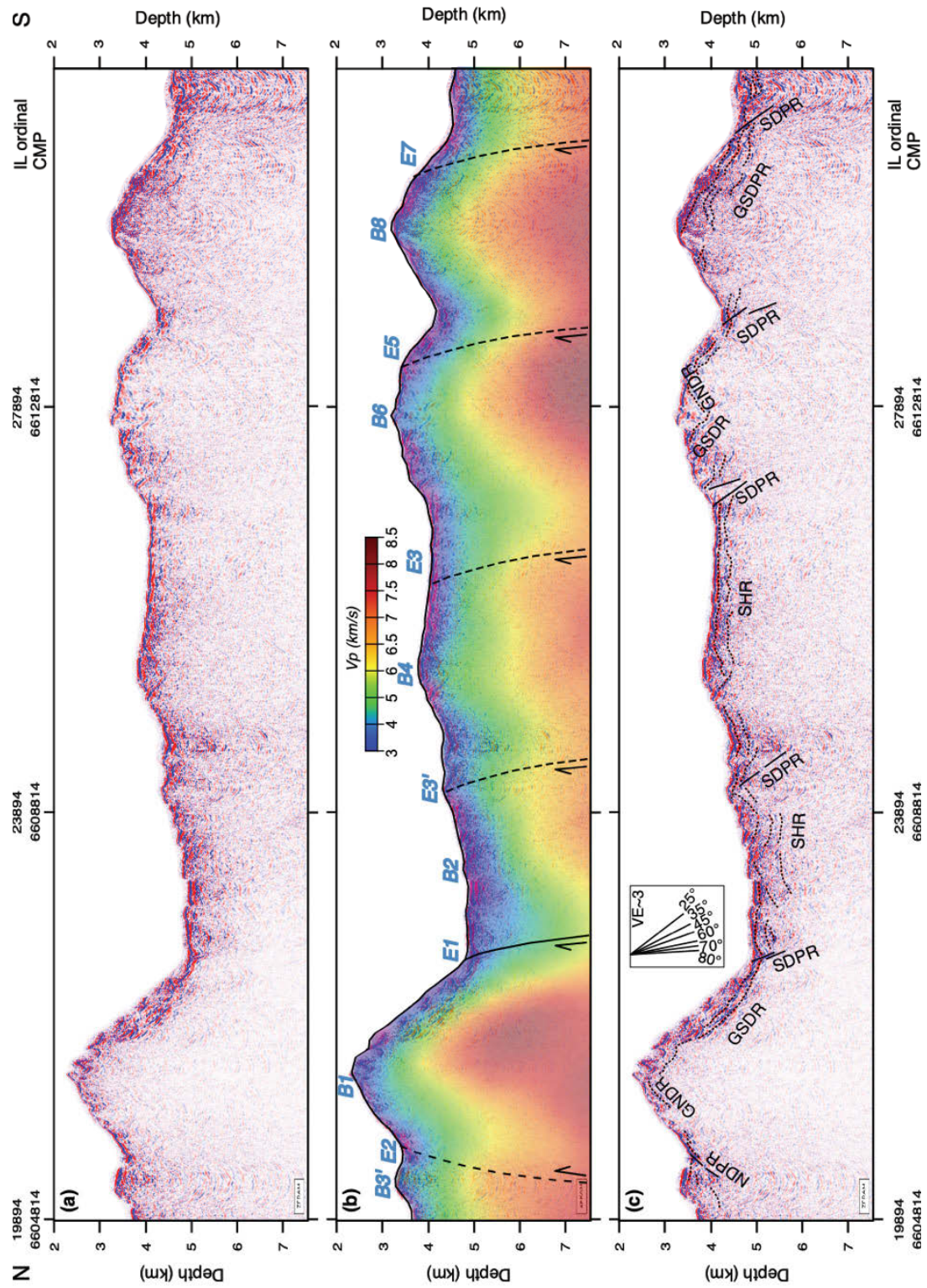

Figure 4.5.1. Seismic reflection section across the SWIR at 64°30'E. Prestack depth migration section with BP (2-5-18-25 Hz) and amplitudes in red-blue colour scale (a). In (b) the tomographic velocity model used for the migration (Corbalán et al., 2021) is overlay with 50% transparency on (a). Detachment faults' locations and geometry inferred with OBS traveltime

tomography (Corbalán et al., 2021) are drawn. Solid black line marks the currently active fault, and the dashed black lines mark the abandoned detachment faults. The location of the emergence and breakaway for each fault is indicated by E_N and B_N, respectively, where N indicates the fault number. Faults are numbered 1-8 from youngest to oldest. The location of fault 3', younger than fault 3, is based only on P-wave travel time tomography (Corbalán et al., 2021). Other fault locations are based on the tomographic model and previous studies (see Chapter 2 or Corbalán et al., 2021). In (c) subfigure (a) is shown with my interpretation drawn on top. Identified reflections are grouped as follows: south dipping sub-vertical planar reflections (SDPRs); north dipping sub-vertical planar reflections (NDPRs); sub-horizontal reflections (SHRs); gently south dipping reflections (GSDRs); and gently north dipping reflections (GNDRs). Reflections that are likely related to faults are drawn as solid lines, while reflections that are interpreted to mark changes in the degree of serpentinization and serpentinization gradients are delineated by dotted lines. Dip angles corrected for the vertical scale of the section (VE~3) for 25°, 35°, 45°, 60°, 70° and 80° are given as a reference.

Nonetheless, the results from the processing of the SISMO-SMOOTH MCS data has yielded useful additional constraints in the detachment fault's geometry and serpentinization gradients. In Figure 4.5.1a, a close-up plot from 2 to 7.5 km in the vertical depth scale is shown with amplitudes in red-blue color scale with no overlain interpretations. In Figure 4.5.1b, the same image is overlayed by the velocity model used for migration (Corbalán et al., 2021, and Chapter 2). Location of estimated faults from previous OBS tomographic results (Corbalán et al., 2021; Chapter 2) are also drawn on top and faults names are the same as in Chapter 2 (Corbalán et al., 2021). In Figure 4.5.1c, the same prestack depth migrated section is shown with my interpretation on top.

Five main packages of reflections are identified in the topmost ~1 km of the prestack migrated data: south dipping sub-vertical planar reflections (SDPRs); north dipping sub-vertical planar reflections (NDPRs); sub-horizontal reflections (SHRs); gently south dipping reflections (GSDRs); and gently north dipping reflections (GNDRs) (Fig. 4.5.1c). Several of the identified reflections are also observed in Momoh et al. (2020), such as the SDPRs and NDPR associated with the largest changes in topography (near *E2*, *E1*, and *E5* in Figure 4.5.1) and the SHR between *E1* and *E3'*. Comparison with previous results (Momoh et al., 2017; 2020) is difficult because the published sections that are coincident with our NS MCS section and show clearer reflectivity are time-migrated sections. The depth-migrated section shown by Momoh et al (2020) displays a similar reflection structure, but thicker packages of reflections. The differences mainly stem from the

differences in the processing approach. Momoh et al. (2020) did not have a well-resolved velocity model to be used in depth migration, so they applied poststack time migration. The migration methodology also differs as they used an explicit finite difference time migration, and I use a Kirchhoff depth migration. The velocities they use are a combination of an extremely smooth velocity model with very small lateral or vertical changes (Momoh et al., 2017) and semblance-based velocity picked on sparse seismic reflections. They converted their time section to depth using the smooth velocity model in Momoh et al. (2017). Dip angles are however comparable: 25° for the SDPR and NDPR for the reflections identified in the vicinity of inactive detachment faults, and ~45° for the reflections in the vicinity of the active detachment fault (*E1*). Internal reflectivity below the active detachment exposed surface (in the footwall block) is better resolved in the work shown in this thesis, which indicates that Kirchhoff migration handles steep dip and large lateral variations better than finite difference migration.

4.6 Discussion

The three northernmost interpreted fault locations (*E2*, *E1* and *E3'*) on the MCS data correspond well with most faults' location in the tomographic velocity model (Fig. 4.5.1b). The three southernmost fault locations, *E3*, *E5* and *E7* are offset by ~4.6, ~2.5, and ~2.6 km, respectively. The seismic signature of *E3* in the depth migrated section is perhaps the less evident, and therefore, less reliable of all reflections interpreted in relation to the detachment faults. All reflections associated to inactive detachment faults show a dip of ~25°, and the reflections associated with the active fault which shows a steeper dip of ~45°. I interpret this difference to be due to the different phases on which the abandoned versus active faults are situated within the rolling-hinge flip-flop model. The active fault is in a new rolling-hinge phase, with its footwall being continuously exhumed and rotating, while the abandoned faults are now at the end phase of the rolling hinge, with their footwalls rotated and flattened before their abandonment. These dips agree with the dips suggested by Momoh et al. (2020).

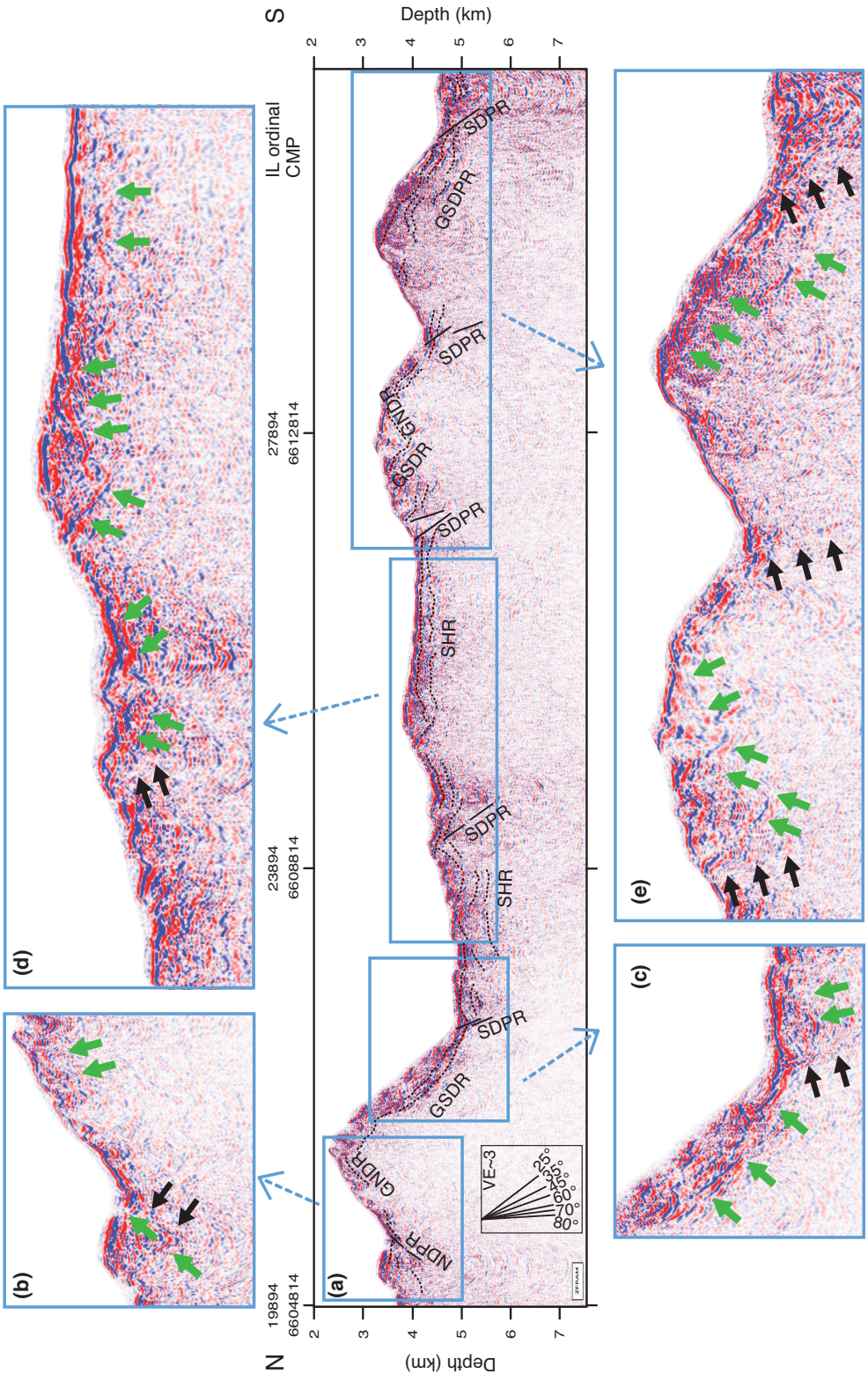

Figure 4.6.1. Depth-migrated section across the SWIR at 64°30'E. (a) Full-figure of the section with the identifies seismic reflection drawn on top. Dip angles corrected for the vertical scale of the section (VE~3) for 25°, 35°, 45°, 60°, 70° and 80° are given as a reference. Reflections

grouped as in Figure 4.5.1 (SDPRs, NDPRs, SHRs, GSDRs and GNDRs). (b-e) are magnification of the main figure (a). Reflections that are interpreted to depict faults are drawn as solid lines in (a) and are indicated in (b-e) with black arrows. Reflections that are interpreted to mark changes in the degree of serpentinization and serpentinization gradients are delineated by dotted lines in (a) and are indicated in (b-e) with green arrows.

Figure 4.6.1 shows close-up images of Figure 4.5.1c and indicates the reflections that are likely related to the active and inactive detachment faults (black arrows) and the ones likely related to serpentinization gradients and small faults and fluid pathways (green arrows). GSDRs beneath the *E1* and *E7* footwall surfaces resemble the D reflection identified in time-migrated sections across the Atlantis OCC (MAR at 30°10'N) and at similar positions within the fault surface (profiles 4 and 6 in Canales et al., 2004), across the widest are along-extension. Singh et al. (2004) showed a complex reflectivity associated with the D reflection that can extend 0.7 s below the seafloor (Blackman et al., 2009). There are two proposed alternatives for the origin of the D reflection with great implications for the detachment fault system at the Atlantis OCC (Canales et al., 2004). One is that the D reflection is a serpentinized front that separates highly serpentinized peridotites from much less altered peridotites below. The other is that the OCC is formed by slip on two detachment faults, and the D reflection is the seismic signature of the first detachment and detachment two is the currently active fault. Canales et al. (2004) suggests the latter is more likely for the Atlantis OCC because of two reasons: (1) the D reflection is smooth and continuous and observations of the reflection in different profiles across- and along-axis that are difficult to reconcile with the 3D fault geometry.

Furthermore, the D reflection, although less coherent, is observed in a section that is consider mainly formed by gabbroic rocks. However, in the study area of this thesis, and the areas where the interpreted D reflections are observed (GSDRs beneath the *E1* and *E7* footwall surfaces; Fig. 4.6.1) the amount of gabbroic rocks is negligible, and I suggest the D reflections are more likely to represent serpentinization fronts between highly fractured, fully serpentinized peridotites and less fractured, less serpentinized peridotites. This is also in agreement with Figure 2.7.2.1.1 (Chapter 2 and Fig. 8 in Corbalán et al., 2021). However, this serpentinization front is different from traditional interpretations of a Moho that is a serpentinized front with serpentinized peridotites above and unaltered

peridotites beneath (e.g., Minshull et al., 1998, 2006), as the transition from hydrated peridotites to unaltered peridotites is gradual (Corbalán et al., 2021). I instead suggest that the D reflections are part of a package of reflections that indicate serpentinization fronts within a serpentinization gradient, but that only prominent changes in acoustic impedance are imaged and that others are difficult to resolved due to the scattered returns below the rough seafloor.

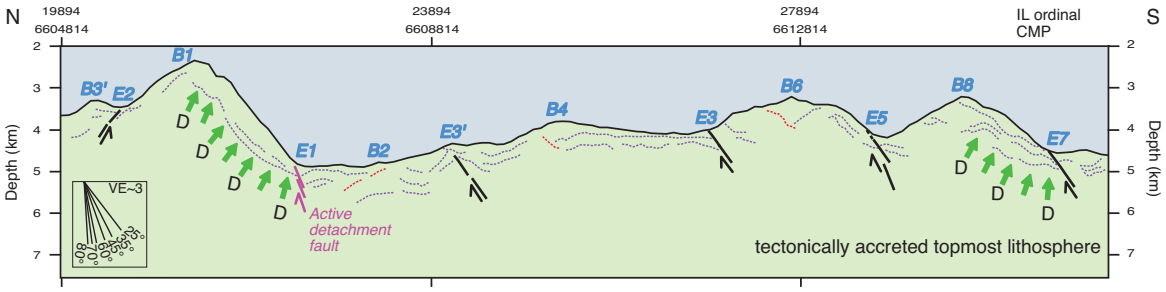

Figure 4.6.2. Interpretation of the reflections identified in the NS (across-axis) MCS profile at the SWIR at 64°30'E. Solid pink and black lines depict the active and inactive detachment faults, respectively. The location of the emergence and breakaway for each fault is indicated by EN and BN, respectively, where N indicates the fault number. Faults are numbered 1-8 as in Figure 4.5.1. Dip angles corrected for the vertical scale of the section (VE~3) for 25°, 35°, 45°, 60°, 70° and 80° are given as a reference. Reflections that are interpreted to depict active and inactive faults are drawn as pink and black solid lines, respectively. Reflections that are interpreted to mark changes in the degree of serpentinization and serpentinization gradients are delineated by dotted lines. Reflections identified as D reflections amongst them are indicated with green arrows. Reflections with contrasting dip and dip directions between neighboring reflections are colored red.

An interpretation of the reflectivity structure at the SWIR at 64°30' E is shown in Figure 4.6.2. The D reflections and the locations of the active and inactive detachment faults as discussed above are included. SHRs that nearly follow the topography, GNDR and GSDR are interpreted as corresponding to changes in the degree of serpentinization and therefore indicators of serpentinization gradients (Figs. 4.6.1 and 4.6.2). Higher vertical serpentinization gradients are observed on the footwall, and lower on the hanging wall, consistent with the vertical velocity gradients (Fig. 4.5.1b). Below the footwall surface, the area on where serpentinization gradients are identified is narrower and it gradually widens toward the breakaway, and this area is even wider in the interpreted hanging walls.

A few striking reflections (marked in red in Fig. 4.6.2) are observed below the *B2, B6* and *B4*, in a contrasted different direction to adjacent reflections and forming obtuse angles with the adjacent reflections. Furthermore, the dip of the reflections is similar and in the same direction to the dip of the corresponding inactive detachment, i.e., dip of reflection below *B2* is similar to dip and dip direction below *E2*, and dips of reflections below *B4* and *B6* are similar to dips and dips direction below *E3–E7*. The explanation for the reflections below *E2* seems hard to discern as they are located in the hanging wall of the currently active detachment fault that is subjected to extensive deformation. It is hard to speculate whether they correspond to a structure formed when this block was part of the footwall of *E2* or if it is a structure formed while the block was in the hanging wall of *E1*. In contrast, I suggest the reflections below *B4* and *B6*, located within what once was the footwall of detachment faults further north *E2*, are small-offset faults that formed during flexural rotation of the footwall.

4.7 Conclusions

Seismic reflection structure crossing the axis of the ultraslow-spreading SWIR at 64°30'E is constrained with the SISMO-SMOOTH MCS data acquired with a 4.5-km-long active-section streamer. Industry-grade software Omega is used for the MCS processing and the workflow is explained with details throughout the text. The results of each processing step are demonstrated with the SISMO-SMOOTH MCS data. A prestack depth migration section across the spreading axis and performed with tomographic velocities computed from a coincident OBS profile, yields the following major findings and conclusions:

1. Prestack depth migration section shows the flip-flop detachment faults' geometry. Abandoned detachment faults have a dip of ~25°, while the active fault displays a steeper dip (~45°). The steeper active fault is in a new rolling-hinge phase, while the gentler abandoned faults are at the end of the rolling hinge, with their footwalls rotated and flattened to lower dips.

2. Higher serpentinization gradients are found in the footwalls of the active and abandoned detachments, and lower serpentinization gradients are found in the hanging walls. Reflections identified as D within the serpentinized gradients are interpreted to mark a serpentinization front separating highly fractured and fully serpentinized peridotites above from less fractured and less serpentinized peridotites below.

3. A few contrasting reflections in dip and dip orientation below *B6* and *B4* are interpreted as the seismic signature of small-offset faults formed during flexural rotation of the footwall when each block was the footwall block of an active detachment fault.

Chapter 5

Conclusions and future work

5.1 Conclusions

The ultraslow spreading (full spreading rate of <14 mm/year; Kreemer et al., 2014) Southwest Indian Ridge (SWIR) is one of the most variable mid-ocean ridges in its lithospheric structure and modes of seafloor accretion (e.g., Cannat et al., 2006; Dick et al., 2003). The SWIR segment at 64°30'E is of particular interest as it shows the globally widest exhumed mantle domains on the seafloor (Cannat et al., 2006), with very little contribution from mafic igneous rocks (<5% gabbros and basalts; Sauter et al., 2013). A complex detachment fault system of consecutive faults that alternate polarity is presumed to be responsible for the continuous mantle exhumation at the SWIR at 64°30'E (Cannat et al., 2019; Reston 2018; Sauter et al., 2013). Most previous studies have focused on seafloor observations (e.g., Cannat et al., 2006; Reston 2018; Sauter et al., 2008; 2013), but little is known about the structure in depth. To study the lithospheric structure at the SWIR at 64°30'E at depth and to provide a well-resolved regional-scale velocity model to back up or refute the proposed lithospheric accretion model, a coincident wide-angle seismic refraction Ocean Bottom Seismometer (OBS) and a near-incident multichannel seismic (MCS) reflection survey was carried out along a ~150-km-long profile across the spreading axis (i.e., ridge-perpendicular). A complimentary ridge-parallel OBS/MCS ~150-km-long profile was acquired to study the seismic anisotropy at its crossing point with the ridge-perpendicular profile. The on-axis profile is also used to study the variability of the lithospheric structure, which transitions from an exhumed mantle domain to a volcanic seafloor, based on previous geological mapping (Cannat et al., 2006; 2019).

Traveltime tomography performed on the two orthogonal profiles (Chapter 2) is consistent with a topmost lithosphere composed of highly fractured and fully

serpentinized peridotites at the top, with a gradual decrease in pore space volume and degree of serpentinization to unaltered peridotites at depth. This interpretation is applicable to about ¾ of the investigated topmost lithosphere. The other ¼ is located at the western section of the ridge-parallel profile and appears to represent transitional lithosphere toward magmatically-robust lithosphere. A general velocity increase with distance southward was observed along the ridge-normal profile. To investigate the evolution along exhumed mantle domains, I focused on the ridge-perpendicular profile from Chapter 3 onwards. Four MCS profiles, acquired along the ridge-perpendicular profile during the MD 199-SISMO-SMOOTH Cruise 2014 (Leroy & Cannat, 2014; Leroy et al., 2015), were processed. Industry-grade software and MCS processing workflow were employed on the MCS data. The results from this work, shown in Chapter 4, provide additional constraints on the faults' geometry responsible for mantle exhumation and continuous lithospheric tectonic accretion. The already computed and coincident tomographic velocity model allowed a Kirchhoff depth migration to determine the true dips of the detachment faults. The active detachment fault shows a steeper-angle dip (~45°) compared to the dip angles observed at abandoned detachments (~25°). This is consistent with their different phases in the flip-flop rolling hinge model: the active fault is in a new rolling hinge phase, while the abandoned faults are at the end of the rolling hinge phase. Three groups of reflections show contrasting dip and dip orientation to adjacent reflections, which I interpret to be related to small-offset faults formed during flexural rotation of the footwall.

The main results of our studies at the SWIR at 64°30'E are summarized in the following sections.

5.1.1 Ridge-normal detachment faulting system

The ridge-perpendicular velocity model and its derivatives, the vertical velocity gradient and the velocity anomaly models, delineate a system of detachment faults cutting across the SWIR at 64°30'E. Detachment faults are represented by high velocities, a positive velocity anomaly, and a high vertical velocity gradient in the footwall, and low velocities,

negative velocity anomaly, and a low vertical velocity gradient in the hanging wall. The most pronounced changes in the vertical velocity gradient (from ~2 s^{-1} to ~0.5 s^{-1}), lateral velocities (horizontal gradient ~1 s^{-1}), and velocity anomaly (from 1.5 to −1.5 km/s) are observed at the interpreted location of the active detachment fault. Our results support the proposed seafloor accretion model, the flip-flop rolling hinge model (e.g., Buck, 1988; Sauter et al., 2013), and provide the first constraints at depth of the system of flipping detachments. One active and five abandoned detachment faults are identified. All the active and abandoned detachments are located south of the spreading axis and are south dipping, except for one abandoned detachment identified north of the spreading axis and with an inverted polarity (north dipping). The intersection between the footwall and hanging wall of the active detachment fault marks the location of the spreading axis. A new abandoned detachment is constrained by the velocity structure for the first time. It may have been missed in previous studies based on seafloor observations (Cannat et al., 2019; Reston 2018; Sauter et al., 2013) because of its smoothly emergent seafloor topography.

The locations of all the active and abandoned detachments are compared to the locations previously suggested, based on seafloor observations in Chapter 2. Calculated seafloor ages, based on the horizontal distance between the detachment faults' emergence and breakaway, using a constant spreading rate of 14 mm/yr, allows us to determine the relationship between serpentinization and longevity of the faults. Serpentinization appears to be controlled by the longevity of the detachments and fault block movement: longer-lived faults show deeper serpentinization extent on the hanging wall, while their footwalls show less pervasive serpentinization due to the continuous exhumation process. A prestack depth migrated section across-axis corroborates the first-order control of detachment faults with serpentinization. Seismic reflections indicate that higher serpentinization gradients are found within the footwalls of the active and abandoned detachments, while the hanging walls are characterized by lower serpentinization gradients. A set of reflections identified as D reflections beneath the dome footwalls of the active fault seem to indicate a serpentinization front separating highly fractured and fully serpentinized peridotites above from less fractured and less serpentinized peridotites

below. Small-offset faults formed during footwall flexural rotation are identified beneath two breakaways about 16 and 33 km away from the spreading axis.

5.1.2 Along-axis seafloor transition

The observed changes in the velocity model and its derivatives, the vertical velocity gradient and velocity anomaly models, divide the ridge-parallel profile into three distinctive zones: an eastern zone (model distance from 69 to 140 km) interpreted to be composed of exhumed and variably serpentinized peridotites with serpentinization gradually decreasing as a function of depth; a central zone (model distance from 59 to 69 km) characteristic of a transitional lithosphere; and a western zone (model distance from ~10 to 59 km) showing a sharp lateral change to lower seismic velocities and more moderate vertical velocity gradient than eastern adjacent zones indicative of a lithosphere partially constructed by magmatism. The transitional topmost lithosphere is considered to be heterogeneous in its composition with intertwined layers of fully and partially serpentinized peridotites and layers of mafic extrusive and intrusive rocks. Our results indicate that this transition occurs over a distance of ~10 km and suggest that the change in the seafloor accretion mode indicates a westward increase in melt supply.

Comparison of extracted 1D velocity-depth functions at the crossing point between the ridge-parallel and ridge-normal profiles indicates up to ~5% ridge-parallel fast-axis seismic anisotropy from ~0.5 to ~2.2 km dbsf, i.e., ridge-parallel velocities are faster than ridge-normal velocities. A similar magnitude ridge-normal (reversed polarity) fast-axis anisotropy exists from ~2.2 km to ~6 km dbsf. I suggest that the uppermost anisotropy is due to the preferential distribution of cracks parallel or subparallel to the axis, and the lowermost anisotropy is attributed to the lattice-preference orientation of olivine minerals in the less serpentinized peridotites in the near-orthogonal spreading direction (i.e., the lithospheric strain direction).

5.1.3 Lithospheric evolution

A detailed analysis of the seismic velocity changes as a function of distance and age from the spreading axis along the ridge-perpendicular velocity model provides the first evidence for evolution of oceanic topmost lithosphere accreted by tectonic processes. While detailed knowledge on the evolution of the magmatically accreted topmost oceanic lithosphere, the crust, has been gathered since the 1970s through observations of seismic velocity increase with age, how and if the tectonically accreted topmost oceanic lithosphere evolves is still not known. Yet, the latter is representative of the lithosphere found at a quarter of the global mid-ocean ridge system. The results from this analysis reveal that the tectonically accreted lithosphere is not only fundamentally different in its origin from the magmatically accreted lithosphere, but also evolves differently and much faster that the magmatically accreted lithosphere.

The increase in velocities in 6 Ma for the topmost ~6 km lithosphere is ~53% greater than for the magmatically accreted topmost ~6 km lithosphere in 6 Ma. The bulk of the increase takes place at depths of 1.5–4.5 km, deeper than for the magmatically accreted lithosphere (0.5–1 km). However, at the topmost 1.5–2.5 km, progressive serpentinization with aging reduces the velocities and counterbalances the velocity increase due to crack closure and pore infilling. Thus, the change in the top ~6 km of this lithosphere from 0–6 Ma relative to the magmatically accreted crust is likely significantly greater than the 53% computed based on the velocity increase alone.

The results from Chapter 3 imply a significantly greater water content in the tectonically accreted topmost lithosphere as it migrates off the ridge axis given that serpentinization is a crucial mechanism to embed water chemically. Past and future subduction of water-rich tectonically accreted topmost lithosphere likely has and likely will result in greater arc magmatism and intraslab earthquake activity than currently observed, which has important implications for continental crust genesis and geohazard analysis.

The three initially proposed questions are answered through this work and summarize as follows:

(i) *How deep does serpentinization extend?*
Serpentinization extends up to ~5 km and ~3–4 km below the seafloor across and along the spreading axis, respectively.

(ii) *Is the oceanic Moho at ultraslow oceanic spreading ridges a serpentinization front?*
No distinct and seismically well-characterized Moho is observed. Most of the investigated lithosphere gradually transitions from highly fractured and fully serpentinized peridotites at the top to unaltered peridotites at depth.

(iii) *What is controlling the serpentinization and the serpentinization depth?*
Detachments seem to control serpentinization and serpentinization across-axis. Footwalls show less pervasive serpentinization than hanging walls, and longer-lived faults show deeper serpentinization extent.

5.2 Future work

5.2.1 Extend OBS ridge-normal profile further north

The best resolved area (standard deviation of seismic P-wave velocities <~0.1 km/s) in the ridge-normal velocity model extends ~50 km south and ~12 km north of the spreading axis. This is the area in which I analyze the velocity increase dependency on distance and age south of the spreading axis. Due to data coverage limitations, this analysis cannot be extended further north. Seafloor mapping suggests that exhumed and variably serpentinized mantle domains extend for more than 60 km north of the spreading axis (Cannat et al., 2006; 2019). It would be interesting to extend the ridge-normal profile further north for two main reasons. The first reason is to determine if the age/distance dependency observed in the seismic velocities and the lithospheric evolution in the north

is comparable to the one observed in the south. Second, if greater distances from the ridge axis, and longer source-receiver offsets, are achieved during data acquisition there may be more opportunities to encounter P-to-S conversions and to produce a Vp/Vs model to further constrain the differences between lithosphere predominantly accreted by tectonism and by magmatism. For example, Grevemeyer et al. (2018a) give an example of how profiles extending ~100-120 km away from the ridge axis allow for detailed Vp/Vs modeling. While the ~50 km transect analyzed south of the spreading axis corresponds to ~6 Ma, continuous exhumed mantle domains last up ~11 Ma north of the spreading axis (Sauter et al., 2103). If the ridge-normal profile were to be extended up to that age or even further north, the velocity-age dependency analysis could also be extended to ages considered to correspond to mature crust at faster-spreading ridges (e.g., >7.5 Ma in Christeson et al., 2019) and to ages at which Layer 2A doubles its velocity at faster-spreading ridges (.e.g., Grevemeyer et al., 1999; Nedimović et al., 2008).

I searched for S-waves in the OBS data acquired along the ridge-parallel and ridge-perpendicular profiles. Only one clear S-wave was found in OBS C38, located three OBSs before the southernmost OBS in the ridge-normal profile, which is confined to offsets of 25-45 km (Fig. 5.2.1.1).

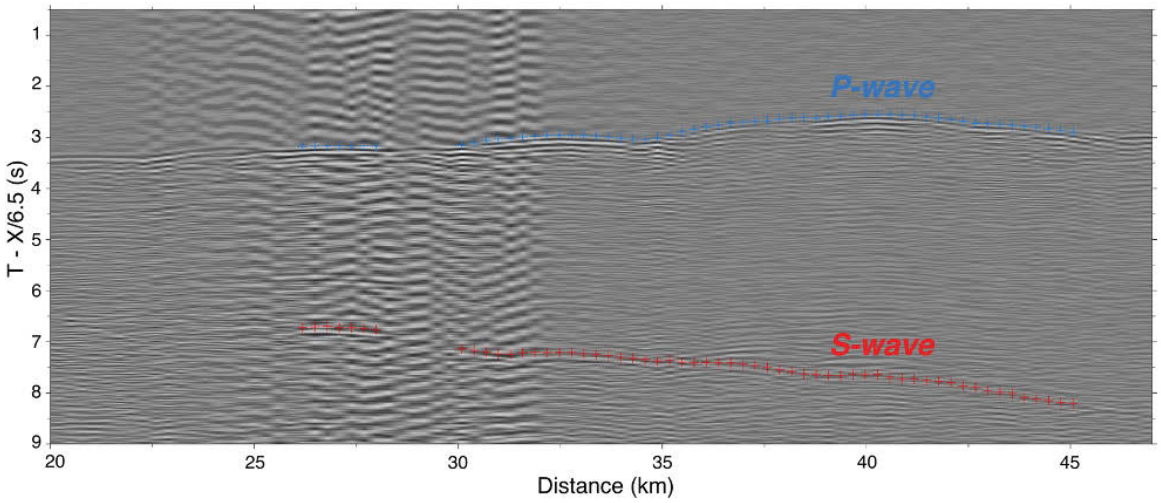

Figure 5.2.1.1. OBS C38 vertical channel record containing the P-wave and the S-wave and the time hand-picked in blue and red, respectively. The time vertical axis is shown with a reducing velocity of 6.5 km/s.

These offsets relate the S-wave to the seafloor mapped as transitional from the nonvolcanic, exhumed, mantle-derived "smooth-seafloor" (Cannat et al., 2006) to volcanic seafloor. Therefore, I would recommend extending the profile further north than the smooth–volcanic seafloor transition to increase the probability of observing P-to-S conversions. Similar to Prada et al. (2016), I plot the P-wave travel times (Tp) and S-wave travel time (Ts) in a scatter plot and estimate the Vp/Vs ratio by fitting a linear regression function (Fig. 5.2.1.2). The Vp/Vs ratio is 1.78±0.19, within the range of gabbroic rocks but very close to the limit of the serpentinite range (Vp/Vs > 1.8; Carlson & Miller, 1997). This limit, i.e., the boundary between gabbroic rocks and variably serpentinized peridotites might not be as abrupt as presented in Figure 5.2.1.2 as Vp/Vs of peridotites with a low degree of serpentinization might not be conclusive enough to distinguish them from gabbros (e.g., Calvert & Potts, 1985) and dunites with ~20% degree of serpentinization can display Vp/Vs between 1.7–1.8 (Christesen, 2004). However, this simplification is enough to show the type of work that one would be able to do if more S-wave arrivals were identified in the data. If the extension profile extends further north, one might find S-waves from both the exhumed mantle and the volcanic domains, and it would be very interesting to compare and contrast the differences.

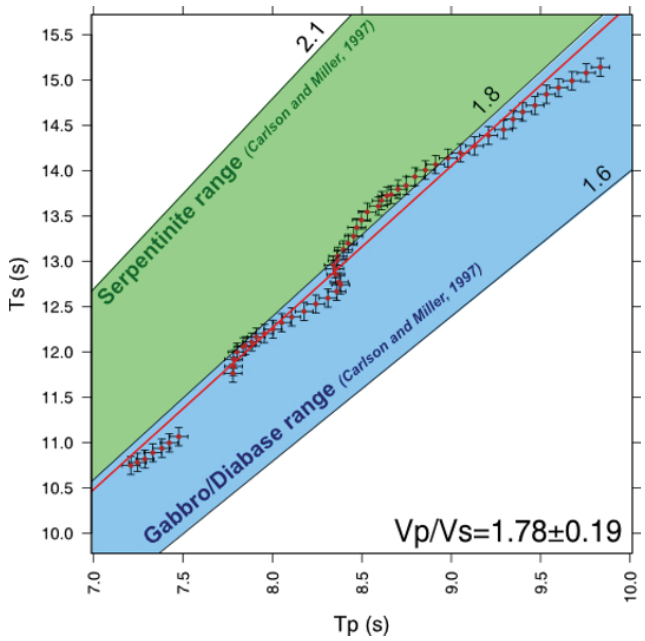

Figure. 5.2.1.2. Tp-Ts diagram showing the distribution of travel times of P- and S-waves (red dots). The error bars represent picking error uncertainties. The green area limits the Vp/Vs range characteristic of Serpentinite and the blue does for Gabbro/Diabase range, both based on empirical analysis (Carlson and Miller, 1997). The red line depicts the linear regression function, from which a Vp/Vs of 1.78±0.19 is derived.

5.2.2 Relationship between fault geometry and lateral velocity variations along the OBS ridge-parallel profile

A regional eastward trend of increasing seismic velocities was observed on the ridge-parallel profile. The velocity trend was investigated examining the lateral variations in 1D velocity-depth functions extracted from the best resolved area (standard deviation of seismic P-wave velocities <~0.1 km/s) of the ridge-parallel profile. The westernmost 1D profiles (Figure 5.2.2.1a) are found at the greatest distance from the spreading axis and overall show the lowest velocities, with velocities increasing with proximity to the widest area along-extension of the active detachment surface, hereafter called the apex. The 1D velocities continue to increase eastward after crossing the apex, as the distance between the 1D profiles and the spreading axis is reduced (Figure 5.2.2.1a). The primary geometrical cause for the velocity increase from west to east may be related to the decrease in the shortest distance between the ridge-parallel profile and the active detachment fault. When this distance is small, the first arriving seismic energy, following

the path of shortest time, may have traveled off the profile and through the footwall, which is rich in high-velocity peridotites. The shortest distance from the ridge-parallel profile to the active detachment may be a function of both (a) the separation between the profile and the seafloor trace of the ridge axis, and (b) the subsurface geometry of the active detachment fault, in particular its overall dip. In Figure 5.2.2.1, the relationship between the fault's subsurface geometry, the distance between the ridge axis and the profile, and the lateral velocity changes is examined. I first assign a simplify fault geometry of 35° dip at 0 km, 70° at 5 km, and 80° dip at 15 km below seafloor based on seafloor and geophysical observations and numerical models in oceanic detachment faults (Bickert et al., 2020; Cannat et al., 2019; deMartin et al., 2007; Parnell-Turner et al., 2017). Next, I can evaluate the change in the shortest distance between the ridge-parallel profile and the active detachment, as a function of the assigned uncertainty in the fault geometry of ±10° and the separation between the ridge-parallel profile and the seafloor trace of the ridge axis (Fig. 5.2.2.1b). This simple exercise suggests that about half (3/5) of the increasing velocity in the eastward direction along the ridge-parallel profile can be attributed to the changing separation between the ridge-parallel profile and the interpreted seafloor location of the spreading axis. In contrast, the other half (2/5) of the same effect is attributable to the changing active detachment fault dip. Thus, it is plausible that the active axial detachment fault dip gradually changes from gentler angles in the east to steeper dip angles in the west, including potential termination of the fault (Fig. 5.2.2.1c).

This hypothesis of a lateral and gradual change of fault dip along the spreading axis would benefit from including high-quality MCS data along the profile. The MCS data acquired during the MD 199-SISMO-SMOOTH Cruise 2014 (Leroy & Cannat, 2014; Leroy et al., 2015) along the ridge-parallel profile has a large shooting interval (150–300m), which, considering the highly scattering seafloor, makes it very unlikely to image enough reflections in the subsurface and provide further constraints on the fault dip hypothesis. Chapter 4 and the processing of the MSC lines available during this thesis is another indication of this limitation. Furthermore, in the ridge-perpendicular profile, there is at least one MSC line with a 50 m shooting interval, closer to a typical high-quality MCS shooting interval of 37.5 m. Therefore, I would recommend acquiring true high-

resolution MCS data along the ridge-perpendicular profile, to test the dip hypothesis and further define the fault geometry and its lateral changes. Perhaps, this also would be a good opportunity to test recently improved pneumatic sources (e.g., Tune Pulsed Source from Sercel), that are capable of producing low-frequency signals. Such a source would be ideal for challenging targets such as sub-basalt, below a salt-diapir, and within exhumed mantle domains. In addition, it would help attenuate the high-frequency noise that is highly absorbed and scattered at the top of complex geological structures (Ronen, 2022), such as the ones found on the seafloor at the SWIR at 64°30'E.

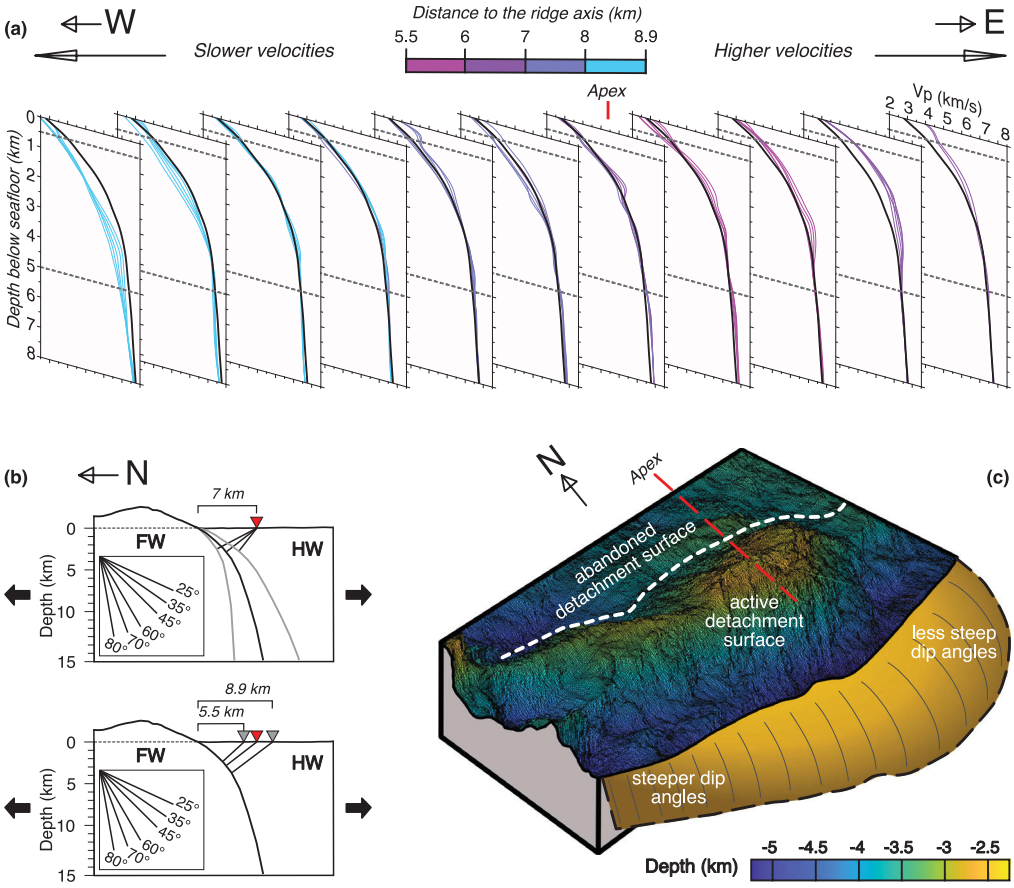

Figure 5.2.2.1. Relationship between the variations in the ridge-parallel model velocities and the shortest distance between this profile and the active axial detachment fault. (a) Velocity-depth 1D profiles from the best-resolved area of the ridge-parallel profile grouped in 5 km intervals and colored by their normal distance to the spreading axis. The average 1D velocity-depth profile for the ridge-parallel model is shown with a thick black line for each 5 km interval. We focus on the depth below the seafloor from 0.5 km to 5 km because (a) the top 0.5 km are not as well resolved by tomography due to the near vertical ray paths at the top of the model, and (b) the lower

resolution below 5 km. In (a,c) the apex refers to the widest area along-extension of the active detachment surface. (b) Schematic illustration of a detachment fault showing how the shortest distance between the ridge-parallel profile and the active detachment fault varies when the fault geometry changes (top) and when the distance from the ridge-parallel profile to the ridge axis changes (bottom). The red triangles indicate the location at where this distance is ~7 km. The grey triangles (bottom) show the minimum and maximum horizontal distances. The grey lines (top) show the change in the fault geometry of ± 10° dip from the interpreted geometry in black. (c) Conceptual model of the detachment fault plane (in a gradient yellow) hanging-off the spreading axis and with the 3D bathymetry plotted in the top of the box diagram. The relative variations in the fault dip from steeper angles at the west to gentler angles to the east are illustrated with thin black lines.

5.2.3 Downward continuation and streamer tomography

Downward continuation of the multichannel seismic (MCS) data has proven very useful to constrain the uppermost ~1 km P-wave velocity structure in areas of large water depth and rough seafloor, such as the Oceanic Core complex (OCC) on the Mid-Atlantic ridge 30° N (Harding et al., 2007). Downward continuation simulates an on-bottom refraction experiment, but with a significant increase in data coverage and resolution, typical of MCS data and comparable to seafloor geology (Arnulf et al., 2011; 2014). In this method, shots' and receivers' locations of the MCS streamer are redatummed closer to the seafloor by collapsing the direct water wave, and crustal refractions previously found only at far offsets and normally masked by the strong seafloor reflection at near offsets, are shifted in front of the seafloor reflection and emerge as near-offset crustal refractions (e.g., Arnulf et al., 2014; Henig et al., 2012).

There are two main alternative techniques to the best of my knowledge: (1) use a downward continuation method such as the Synthetic Ocean Bottom Experiment (SOBE), to compute the uppermost velocity structure, in combination with a travel time tomography method, to construct the deeper velocity structure (e.g., Arnulf et al., 2011); and (2) use a combination of SOBE and a full waveform inversion (FWI) method to obtain a high resolution model for the topmost velocity structure (e.g., Arnulf et al., 2012). Given the characteristics of our MCS data acquisition, I would be more inclined to recommend the first alternative, and perhaps use the most sophisticated velocity model to explore other depth migration algorithms, such as Reverse Time Migration, which is

typically considered more useful in complex geological settings and rough seafloor (such as the SWIR at 64°30'E). However, this approach is very computationally expensive and benefits from having an accurate high-resolution velocity model. Alternatively, I would recommend using SOBE combined with FWI only for ridge normal MCS profile SMOO32, which has a geometry acquisition more similar to standard high-resolution MCS data (e.g., 50 m shooting interval compared to the standard 37.5 m).

5.2.4 Full-waveform inversion of the OBS data

Travel time tomography is useful for providing long wavelength, smoothed, gridded velocity models. As our resolution tests in Chapter 2 have shown, the uppermost lithospheric structure can be studied up to spatial scales of 5 km horizontally and 2.5 km vertically. Full waveform inversion (FWI) is more suited for detailed studies of the topmost lithosphere, as it provides higher-resolution velocity models. The main advantage of FWI over travel time tomography is that the inversion minimizes the difference between the calculated and the observed data taking into account not only travel times but also amplitudes, which are more sensitive to short-wavelength structures (e.g., Shipp and Singh, 2002; Wang et al., 2014). Travel time tomography is still a key and necessary first step, as the computed final velocity models are excellent starting velocity models for FWI. The latter has proven particularly useful when imaging low-velocity features, such as an Axial Magma Chamber (AMC) (e.g., Jian et al., 2017), where seismic attenuation of energy travelling through the centre of the low-velocity anomaly diminishes the resolution in imaging these types of features (Jian, 2017).

Travel time tomography at the SWIR at 64°30' E (Chapter 2 and Corbalán et al., 2021) indicates quite smoothly varying velocities, with an overall gradual increase in velocities with depth, in accordance with seafloor observations. Perhaps the most interesting areas to study with FWI would be the transitional and non-volcanic topmost lithosphere found at the ridge-parallel profile (Fig. 2.7.2.2.1 in Chapter 2) and the hanging wall block in the ridge-perpendicular profile, to look for indications of small-scale (<5km horizontally) occasional dike injections. FWI typically benefits from very dense OBS coverage (i.e.,

receiver spacing of 1-2 km), so another approach would be to focus on the central area of the ridge-parallel (OBSs 4–12 as in Chapter 2) and the ridge-perpendicular (OBSs 21–31 as in Chapter 2), with the smallest receiver spacing (~2.5–3 km). If small-scale dike injections exist in these central areas, it would then be possible to study their relationship with the scattered volcanic patches observed in the seafloor with side-scan sonar (Sauter et al., 2013). Nonetheless, studies such as Jian et al. (2017) have produced reliable and interesting results employing FWI with sparse OBS data (OBS spacing between 5 and 10 km and >10 km for some OBSs) so even the first approach or a full FWI model is plausible.

A higher resolution P-wave velocity for the ridge-perpendicular profile, even if only for the hanging wall block, would provide additional information on the detachment fault system. Furthermore, a combination of using downward continuation to constrain the topmost structure and FWI to construct the deeper structure may provide higher-resolution results.

5.2.5 Application to the Nova Scotia rifted margin

The Nova Scotia margin displays a remarkable along-strike change in rifting architecture, as it transitions from an extremely amagmatic rift segment in the north (Funck et al., 2004; Lau et al., 2018; 2019), to a magma-poor segment in central Nova Scotia (Wu et al., 2006), and a presumed magma-rich rift segment in the south (Keen and Potter, 1995). At present, the magma-rich rifting style is attributed to the southern segment based on the high-amplitude (~300 nT) East Coast Magnetic Anomaly (ECMA) at the continent-ocean transition (COT) and its coincidence with seaward-dipping reflections (SDRs) identified in standard crustal multichannel seismic (MCS) data (Keen and Potter, 1995). These geophysical observations are interpreted to be associated with the emplacement of a large syn-rift volcanic extrusive body (Keen and Potter, 1995). While seismic velocity constraints exist for the north and central margin (Funck et al., 2004; Lau et al., 2018; 2019; Wu et al., 2006), the southernmost wide-angle seismic reflection and refraction line acquired along the margin in the early 2000s, Ocean Bottom Seismometer (OBS)

SMART Line 3, has not been processed. No seismic velocity constraints exist for the SW Nova Scotia margin.

Serpentinized mantle-derived rocks are thought to be present along more than 50% of the world's rifted margins, and they have indeed been inferred in the northeast (Funck et al., 2004; Lau et al., 2018; 2019) and central Nova Scotia (Wu et al., 2006) at the COT zones. Magma-poor ultraslow- and slow-spreading ridges are considered modern analogous of early rifting stages (corresponding to the COT zones at modern rifted margins) at magma-poor rifted margins (Cannat et al., 2008). However, in these geological settings, a thick post-rift sedimentary layer covers the crust and hinders the imaging of underlying exhumed mantle rocks. The geophysical fingerprints established at the SWIR, and in this thesis, may allow for a re-evaluation of existing seismic velocity models and a better understanding of the exhumed serpentinized mantle domains at these rifted margins. Furthermore, a regional interpretation of the crustal structure and rifting style along the Nova Scotia margin would benefit from the integration of the already acquired and available multiple OBS (SMART Line 1 [Funck et al., 2004], OETR-2009 profile [Lau et al., 2018], OCTOPUS profile [Lau et al., 2019], SMART Line 2 [Wu et al., 2006]) and MCS (Shell 3D volume, NovaSPAN, and UNCLOS) datasets with a proposed tomographic velocity model of SMART Line 3 (Fig. 5.2.5.1).

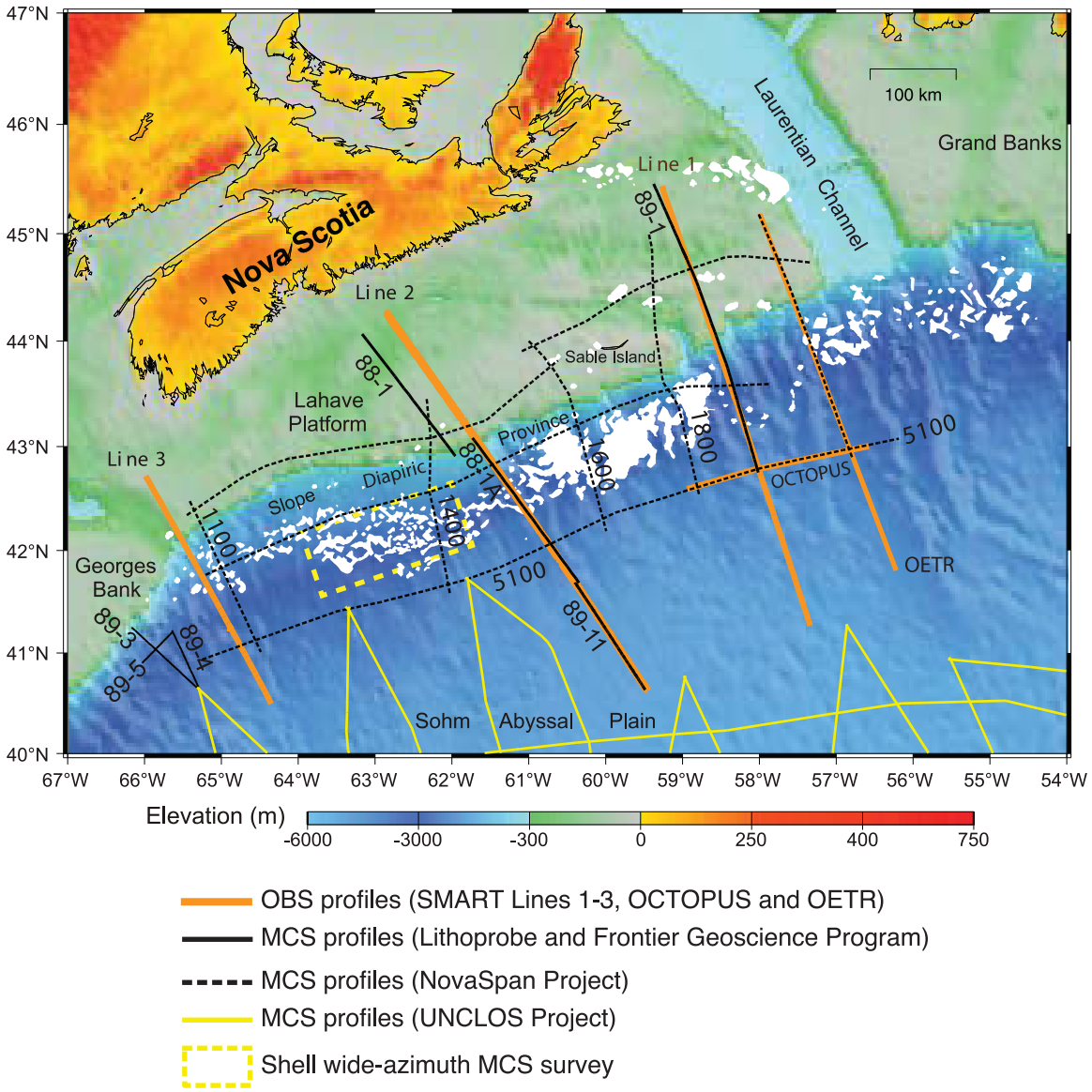

Fig. 5.2.5.1. Nova Scotia rifted margin with location of all the datasets available to the Dalhousie Imaging Group (M.R. Nedimović, private communication, Apr. 2020).

Bibliography

Aghaei, O., et al. (2014). Crustal thickness and Moho character of the fast-spreading East Pacific Rise from 9° 42′ N to 9° 57′ N from poststack-migrated 3-D MCS data. *Geochemistry, Geophysics, Geosystems*, 15(3), 634-657. https://doi.org/10.1002/2013GC005069

Alt, J., et al. (2009). Drilling in Serpentine Sea. In White Paper "Serpentine Sea" Presented at the INVEST Conference (pp. 23–25).

Anderson, O. L., Schreiber, E., Liebermann, R. C. & Soga, N. Some elastic constant data on minerals relevant to geophysics. *Rev. Geophys.* 6(4), 491– 524 (1968).

Argus, D.F., Gordon, R.G., & DeMets, C. (2011). Geologically current motion of 56 plates relative to the no-net-rotation reference frame. *Geochemistry, Geophysics, Geosystems*, 12(11).

Arnoux, G. M., Toomey, D. R., Hooft, E. E. E., & Wilcock, W. S. D. (2019). Seismic imaging and physical properties of the Endeavor segment: Evidence that skew between mantle and crustal magmatic systems governs spreading center processes. *Geochemistry, Geophysics, Geosystems*, 20, 1319–1339. https://doi.org/10.1029/2018gc007978

Arnulf, A.F., Harding, A.J., Singh, S.C., Kent, G.M. & Crawford, W. (2012). Fine-scale velocity structure of upper oceanic crust from full waveform inversion of downward continued seismic reflection data at the Lucky Strike Volcano, Mid-Atlantic Ridge. *Geophysical Research Letters*, 39(8).

Arnulf, A. F., Singh S. C., Harding A. J., Kent G. M., & Crawford W. (2011), Strong seismic heterogeneity in Layer 2A near hydrothermal vents at the Mid-Atlantic Ridge, *Geophys. Res. Lett.*, 38, L13320, doi:10.1029/2011GL047753.

Arnulf, A. F., Harding A. J., Kent G. M., Singh S. C., & W. C. Crawford (2014), Constraints on the shallow velocity structure of the Lucky Strike Volcano, Mid-Atlantic Ridge, from downward continued multichannel streamer data, *J. Geophys. Res. Solid Earth*, 119, 1119–1144, doi:10.1002/2013JB010500.

Arnulf, A. F., Singh, S. C., & Pye, J. W. (2014), Seismic evidence of a complex multi-lens melt reservoir beneath the 9° N Overlapping Spreading Center at the East Pacific Rise, *Geophys. Res. Lett.*, 41, 6109– 6115, doi:10.1002/2014GL060859

Bach, W. & Früh-Green G. L. Alteration of the Oceanic Lithosphere and Implications for Seafloor Processes. *Elements* 6(3): 173–178 (2010).

Barclay, A.H., Toomey, D.R., & Solomon, S.C. (1998). Seismic structure and crustal magmatism at the Mid-Atlantic Ridge, 35° N. *Journal of Geophysical Research: Solid Earth*, 103(B8), 17827-17844.

Barruol, G., et al. (2019). Large-scale flow of Indian Ocean asthenosphere driven by Réunion plume. *Nat. Geosci.* 12, 1043–1049.

Berann, H.C., Heezen, B.C. & Tharp, M. (1977). Manuscript painting of Heezen-Tharp "World Ocean Floor" map. https://www.loc.gov/item/2010586277/

Berge, P. A., G. J. Fryer, & R. H. Wilkens (1992). Velocity- porosity relationships in the upper oceanic crust: Theoretical considerations, *J. Geophys. Res.*, 97, 15,239–15,254, doi:10.1029/92JB01464

Bird, P. (2003). An updated digital model of plate boundaries. *Geochemistry, Geophysics, Geosystems*, 4(3).

Bickert, M., Lavier, L., & Cannat, M. (2020). How do detachment faults form at ultraslow mid-ocean ridges in a thick axial lithosphere? *Earth and Planetary Science Letters*, 533. https://doi.org/10.1016/j.epsl.2019.116048

Blackman, D. K., et al. (2002). Geology of the Atlantis Massif (Mid-Atlantic Ridge, 30 N): Implications for the evolution of an ultramafic oceanic core complex. *Mar. Geophys. Res.* 23(5), 443– 469.

Blackman, D.K., Canales, J.P. and Harding, A. (2009). Geophysical signatures of oceanic core complexes. *Geophysical Journal International*, 178: 593-613. https://doi.org/10.1111/j.1365-246X.2009.04184.x

Blackman, D.K., Karson, J.A., Kelley, D.S. *et al.* (2022). Geology of the Atlantis Massif (Mid-Atlantic Ridge, 30° N): Implications for the evolution of an ultramafic oceanic core complex. *Marine Geophysical Research,* 23, 443–469. https://doi.org/10.1023/B:MARI.0000018232.14085.75

Bonnemains, D. et al. Magnetic signatures of serpentinization at ophiolite complexes. *Geochem. Geophys. Geosyst*. 17, 2969– 2986 (2016).

Boulahanis, B., Carbotte, S.M., Huybers, P.J., Nedimović, M.R., Aghaei, O., Canales, J.P., & Langmuir, C.H. (2020). Do sea level variations influence mid-ocean ridge magma supply? A test using crustal thickness and bathymetry data from the East Pacific Rise. *Earth and Planetary Science Letters*, 535. https://doi.org/10.1016/j.epsl.2020.116121

Bown, J. W., & White, R. S. (1994). Variation with spreading rate of oceanic crustal thickness and geochemistry. *Earth and Planetary Science Letters*, 121(3-4), 435-449.

Bratt, S. R., & Purdy, G. M. (1984). Structure and variability of oceanic crust on the flanks of the East Pacific Rise between 11° and 13°N. *Journal of Geophysical Research: Solid Earth*, 89, 6111–6125.

Bronner, A. et al. Magnetic signature of large exhumed mantle domains of the Southwest Indian Ridge – results from a deep-tow geophysical survey over 0 to 11 Ma old seafloor. *Journal of Geophysical Research: Solid Earth* 5, 339–354 (2014).

Buck, R.W., 1988, Flexural rotation of normal faults: *Tectonics*, v. 7, p. 959–973.

Buck, W., Lavier, L. & Poliakov, A. Modes of faulting at mid-ocean ridges. *Nature* 434, 719–723 (2005). https://doi.org/10.1038/nature03358

Calvert, A.J., (1995). Seismic evidence for a magma chamber beneath the slow-spreading Mid-Atlantic Ridge, *Nature*, 377, 410-414.

Calvert, A. J., & Potts, C. G. (1985). Seismic evidence for hydrothermally altered mantle beneath old crust in the Tydeman fracture zone. *Earth and planetary science letters*, 75(4), 439-449.

Canales, J.P., Detrick, R. S., Toomey, D. R., & Wilcock, W. S. D. (2003). Segment-scale variations in the crustal structure of 150-300 kyr old fast spreading oceanic crust (East Pacific rise, 8°15'N-10°5'N) from wide-angle seismic refraction profiles. *Geophysical Journal International*, 152(3), 766–794. https://doi.org/10.1046/j.1365-246X.2003.01885.x

Canales, J. P., J. A. Collins, J. Escartín, and R. S. Detrick (2000a), Seismic structure across the rift valley of the Mid-Atlantic Ridge at 23°20′ (MARK area): Implications for crustal accretion processes at slow spreading ridges, *J. Geophys. Res.*, 105(B12), 28,411– 28,425, doi:10.1029/2000JB900301

Canales, J.P., Detrick, R.S., Lin, J., Collins, J. A., & Toomey, D.R. (2000b). Crustal and upper mantle seismic structure beneath the rift. *Journal of Geophysical Research*, 105(B2), 2699–2719.

Canales, J.P., Detrick, R.S., Carbotte, S.M., Kent, G.M., Diebold, J.B., Harding, A., et al. (2005). Upper crustal structure and axial topography at intermediate spreading ridges: Seismic constraints from the southern Juan de Fuca Ridge. *Journal of Geophysical Research: Solid Earth*, 110(B12).

Canales, J. P., Dunn, R. A., Arai, R., & Sohn, R. A. (2017). Seismic imaging of magma sills beneath an ultramafic-hosted hydrothermal system. *Geology*, 45(5):451–454.

Canales, J. P., Dunn, R. A., Ito, G., Detrick, R. S., & Sallarès, V. (2014). Effect of variations in magma supply on the crustal structure of mid-ocean ridges. The Galapagos: A Natural Laboratory for the Earth Sciences, 204, 363. https://doi.org/10.1002/9781118852538.ch17

Canales, J. P., Tucholke, B. E., & Collins, J. A. (2004). Seismic reflection imaging of an oceanic detachment fault: Atlantis megamullion (Mid-Atlantic Ridge, 30 10′N). *Earth and Planetary Science Letters*, 222(2), 543–560. https://doi.org/10.1016/j.epsl.2004.02.023

Canales, J.P., Tucholke, B.E., Xu, M., Collins, J.A. & Dubois, D.L., 2008. Seismic evidence for large-scale compositional heterogeneity of oceanic core complexes, *Geochem. Geophys. Geosyst*., 9, Q08002, doi:10.1029/2008GC002009.

Cann, J.R., Blackman, D.K., Smith, D.K., McAllister, E., Janssen, B., Mello. S., et al. (1997). Corrugated slip surfaces formed at ridge–transform intersections on the Mid-Atlantic Ridge. *Nature* 385, 329–332. https://doi.org/10.1038/385329a0

Cannat, M. (1993). Emplacement of mantle rocks in the seafloor at mid-ocean ridges. *Journal of Geophysical Research*, 98(B3), 4163–4172. https://doi.org/10.1029/92jb02221

Cannat, M., Agrinier, P., Bickert, M., Brunelli, D., Hamelin, C., Lecoeuvre, A., Lie Onstad, S., Maia, M., Prampolini, M., Rouméjon, S., Vitale Brovarone, A., Besançon, S., Assaoui, M. (2017). Mid ocean ridge processes at very low melt supply: submersible exploration of smooth ultramafic seafloor at the Southwest Indian Ridge, 64°E (Abstract). AGU, New Orleans.

Cannat, M., Céline, R.J., & Fujimoto, H. (2003). Melt supply variations to a magma-poor ultra-slow spreading ridge (Southwest Indian Ridge 61° to 69°E). *Geochemistry, Geophysics, Geosystems*, 4(8), 1–21. https://doi.org/10.1029/2002GC000480

Cannat, M., Fontaine, F., & Escartin, J. (2010). Serpentinization and associated hydrogen and methane fluxes at slow spreading ridges. Diversity of hydrothermal systems on slow spreading ocean ridges, pages 241–264.

Cannat, M., Manatschal, G., Sauter, D., & Peron-Pinvidic, G. (2009). Assessing the conditions of continental breakup at magma-poor rifted margins: What can we learn from slow spreading mid-ocean ridges? *Comptes Rendus Geoscience*, 341(5), 406-427.

Cannat, M., et al. (2008), Spreading rate, spreading obliquity, and melt supply at the ultraslow spreading Southwest Indian Ridge, *Geochem. Geophys. Geosyst.*, 9, Q04002, doi:10.1029/2007GC001676.

Cannat, M., et al. (2019). On spreading modes and magma supply at slow and ultraslow mid-ocean ridges. Earth and Planetary Science Letters, 519, 223–233. https://doi.org/10.1016/j.epsl.2019.05.012

Cannat, M., et al. (2006). Modes of seafloor generation at a melt-poor ultraslow-spreading ridge. Geology, 34(7), 605–608. https://doi.org/10.1130/G22486.1

Cannat, M., Sauter, D., & Rouméjon, S. (2012). Formation of an ultramafic seafloor at the Southwest Indian Ridge 62-65E: Internal structure of detachment faults and sparse volcanism documented by side-scan sonar and dredges. In: AGU Fall Meeting Abstracts.

Carbotte, S. M., & D. S. Scheirer (2004), Variability of ocean crustal structure created along the global mid-ocean ridge, in Hydrogeology of the Oceanic Lithosphere, edited by E.E. Davis and H. Elderfield, pp. 59–107, Cambridge Univ. Press.

Carbotte, S.M., et al. (2006). Rift topography linked to magmatism at the intermediate spreading Juan de Fuca Ridge. *Geology*, 34(3), 209-212.

Carbotte, S. M., Smith, D. K., Cannat, M., & Klein, E. M. (2016). Tectonic and magmatic segmentation of the Global Ocean Ridge System: A synthesis of observations. *Geological Society Special Publication*, 420(1), 249–295. https://doi.org/10.1144/SP420.5

Carbotte, S. M. & Macdonald, K. C. (1990). Causes of variation in fault-facing direction on the ocean floor. *Geology* 18, 749–752.

Carbotte, S.M., et al. (2008). Variable crustal structure along the Juan de Fuca Ridge: Influence of on-axis hot spots and absolute plate motions. *Geochemistry, Geophysics, Geosystems*, 9(8).

Carlson, R. L. Seismic velocities in the uppermost oceanic crust: Age dependence and the fate of layer 2A. *J. Geophys. Res*. 103(B4), 7069– 7077, (1998).

Carlson, R. L. How crack porosity and shape control seismic velocities in the upper oceanic crust: Modeling downhole logs from Holes 504B and 1256D. *Geochem. Geophys.*, 11, Q04007 (2010).

Carlson, R. L. The influence of porosity and crack morphology on seismic velocity and permeability in the upper oceanic crust. *Geochem. Geophys.* 15, 10–27 (2014).

Carlson, R. L., & Miller, D. J. (1997). A new assessment of the abundance of serpentinite in the oceanic crust. *Geophysical Research Letters*, 24(4), 457–460. https://doi.org/10.1029/97gl00144.

Carlson, R. L. & Miller, D. J. (2003). Mantle wedge water contents estimated from seismic velocities in partially serpentinized peridotites. *Geophys. Res. Lett.* 30, 1250.

Carter, D.J.T. (1980). Echosounding correction tables (formerly Matthews tables), Hydrographic Department, Ministry of Defence, Taunton, UK.

Červený, V., Molotkov, I. A., & Pšencik, I. (1977). Ray method in seismology: Univerzita Karlova. *Prague, Czeckoslovakia*.

Chen, Y. J. (1992). Oceanic crustal thickness versus spreading rate. *Geophysical Research Letters*, 19(8), 753–756. https://doi.org/10.1029/92gl00161

Chen, J., Cannat, M. & Crawford, W. C. (2020). Microseismicity constraints on brittle lithosphere thickness at a nearly amagmatic spreading corridor of the ultraslow Southwest Indian Ridge. AGU Fall Meeting abstract T026-0013.

Christensen, N.I. (1972). The abundance of serpentinites in the oceanic crust. *The Journal of Geology*, 80(6), 709-719.

Christensen, N.I. (1978). Ophiolites, seismic velocities and oceanic crustal structure. *Tectonophysics*, 47(1-2), 131-157.

Christensen, N.I. (1996). Poisson's ratio and crustal seismology. *Journal of Geophysical Research: Solid Earth*, 101(B2), 3139-3156.

Christensen, N. I. (2004). Serpentinites, peridotites, and seismology. *International Geology Review*, 46(9):795–816.

Christensen, N.I. & Salisbury, M.H. (1975). Structure and constitution of the lower oceanic crust. *Reviews of Geophysics*, 13(1), 57-86. https://doi.org/10.1029/RG013i001p00057

Christensen, N.I. and Shaw, G.H. (1970). Elasticity of mafic rocks from the mid-Atlantic ridge: *Geophys. J. Roy. Astron. Soc*., v.20, p. 271-284.

Christensen, N.I. & Smewing, J.D. (1981). Geology and seismic structure of the northern section of the Oman ophiolite. *Journal of Geophysical Research: Solid Earth*, 86(B4), 2545-2555.

Christeson, G. L., Goff, J. A., & Reece, R. S. (2019). Synthesis of oceanic crustal structure from two-dimensional seismic profiles. *Reviews of Geophysics*, 57, 504–529. https://doi.org/10.1029/2019RG000641

Christeson, G. L., Karson, J. A., & McIntosh, K. D. (2010), Mapping of seismic layer 2A/2B boundary above the sheeted dike unit at intermediate spreading crust exposed near the Blanco Transform, *Geochem. Geophys. Geosyst.*, 11, Q03015, doi:10.1029/2009GC002864.

Christeson, G. L., Purdy, G. M., & Fryer, G. J. (1992), Structure of young upper crust at the East Pacific Rise near 9°30'N, Geophys. Res. Lett., 19(10), 1045–1048, doi:10.1029/91GL00971

Christeson, G.L., et al. (2020). South Atlantic Transect: Variations in Oceanic Crustal Structure at 31° S. Geochemistry, Geophysics, Geosystems, 21(7). https://doi.org/10.1038/nature05517

Christeson, G. L., McIntosh, K. D., & Karson, J. A. (2007). Inconsistent correlation of seismic layer 2a and lava layer thickness in oceanic crust, *Nature*, 445(7126), 418–421, doi:10.1038/nature05517

Combier, V., et al. (2015). Three-dimensional geometry of axial magma chamber roof and faults at Lucky Strike volcano on the Mid-Atlantic Ridge. *Journal of Geophysical Research: Solid Earth*, 120(8):5379–5400.

Corbalán, A., et al. (2021). Seismic velocity structure along and across the ultraslow-spreading Southwest Indian Ridge at 64°30'E showcases flipping detachment faults. *Journal of Geophysical Research: Solid Earth*, 126, e2021JB022177. https://doi.org/10.1029/2021JB022177

Cochran, J. R., Kurras, G. J., Edwards, M. H., & Coakley, B. J. (2003). The Gakkel Ridge: Bathymetry, gravity anomalies, and crustal accretion at extremely slow spreading rates, *J. Geophys. Res.*, 108, 2116, doi: 10.1029/2002JB001830

Dannowski, A., et al. (2010). Seismic structure of an oceanic core complex at the Mid-Atlantic Ridge, 22 19′ N. *Journal of Geophysical Research: Solid Earth*, 115(B7).

deMartin, B. J., Sohn, R. A., Canales, J. P., & Humphris, S. E. (2007). Kinematics and geometry of active detachment faulting beneath the Trans-Atlantic Geotraverse (TAG) hydrothermal field on the Mid-Atlantic Ridge. *Geology*, 35, 711–714. https://doi.org/10.1130/g23718a.1

DeMets, C., Gordon, R. G., & Argus, D. F. (2010). Geologically current plate motions. *Geophysical journal international*, *181*(1), 1-80.

Detrick, R.S., et al. (1993). Seismic structure of the southern East Pacific Rise. *Science*, 259(5094), 499-503.

Detrick Jr, R. S., & Purdy, G. M. (1980). The crustal structure of the Kane fracture zone from seismic refraction studies. *Journal of Geophysical Research: Solid Earth*, 85(B7), 3759-3777.

Dick, H. J. B., Lin, J., & Schouten, H. (2003). An ultraslow-spreading class of ocean ridge. *Nature*, 426(6965), 405–412. https://doi.org/10.1038/nature02128

Dick, H. J. B., Tivey, M. A., & Tucholke, B. E. (2008). Plutonic foundation of a slow-spreading ridge segment: Oceanic core complex at Kane Megamullion, 23 30′N, 45 20′W. *Geochemistry, Geophysics, Geosystems*, 9(5). https://doi.org/10.1029/2007gc001645

Dick, H. J. B., Lissenberg, C. J., & Warren, J. M. (2010). Mantle melting, melt transport, and delivery beneath a slow-spreading ridge: The Paleo-MAR from 23°15′N to 23°45′N. *Journal of Petrology*, 51(1–2), 425–467. https://doi.org/10.1093/petrology/egp088

Dick, H.J.B., et al. (2019). Dynamic accretion beneath a slow-spreading ridge segment: IODP Hole 1473A and the Atlantis Bank Oceanic Core Complex. *Journal of Geophysical Research: Solid Earth*, 124(12), 12631-12659.

Dick, H. J., Natland, J. H., & Ildefonse, B. (2006). Past and future impact of deep drilling in the oceanic crust and mantle. *Oceanography*, *19*(4), 72-80.

Dick, H.J. B., et al. (1991): Petrography and geochemical composition of the Atlantis II Fracture Zone. *PANGAEA*, https://doi.org/10.1594/PANGAEA.757822

Dietz, R. (1961). Continent and Ocean Basin Evolution by Spreading of the Sea Floor. *Nature* 190, 854–857. https://doi.org/10.1038/190854a0

Dunn, R.A., & Toomey, D.R. (2001). Crack-induced seismic anisotropy in the oceanic crust across the East Pacific Rise (9°30'N). *Earth and Planetary Science Letters*, 189(1–2), 9–17. https://doi.org/10.1016/S0012-821X(01)00353-3

Dunn, R. A., Toomey, D. R., & Solomon, S. C. (2000). Three-dimensional seismic structure and physical properties of the crust and shallow mantle beneath the East Pacific Rise at 9°30'N. *Journal of Geophysical Research*, 105, 23537–23555. https://doi.org/10.1029/2000jb900210

Dunn, R. A., Lekić, V., Detrick, R. S. & Toomey, D. R. Three-dimensional seismic structure of the Mid-Atlantic Ridge (35°N): Evidence for focused melt supply and lower crustal dike injection. *J. Geophys. Res.* 110, B09101 (2005).

Dusunur, D. et al. (2009). Seismological constraints on the thermal structure along the Lucky Strike segment (Mid-Atlantic Ridge) and interaction of tectonic and magmatic processes around the magma chamber. *Marine Geophysical Research*, 30, 105-120.

Escartín, J., Hirth, G., & Evans, B. (2001). Strength of slightly serpentinized peridotites: Implications for the tectonics of oceanic lithosphere. *Geology*, 29 (11): 1023–1026. doi: https://doi.org/10.1130/0091-7613(2001)029<1023:SOSSPI>2.0.CO;2

Escartín, J., & Lin, J. (1995), Ridge offsets, normal faulting, and gravity anomalies of slow spreading ridges, *J. Geophys. Res.*, 100(B4), 6163– 6177, doi:10.1029/94JB03267.

Escartín, J., Mével, C., MacLeod, C. J., & McCaig, A. M. (2003). Constraints on deformation conditions and the origin of oceanic detachments: The Mid-Atlantic Ridge core complex at 15 45′N. *Geochemistry, Geophysics, Geosystems*, 4(8). https://doi.org/10.1029/2002gc000472

Escartín, J., et al. (2008). Central role of detachment faults in accretion of slow-spreading oceanic lithosphere. Nature, 455(7214), 790-794.

Escartín, J. & Canales, J. P., (2011). Detachments in Oceanic Lithosphere: Deformation, Magmatism, Fluid Flow, and Ecosystems. Eos Trans. AGU, 92(4), 31.

Estep, J., Reece, R., Kardell, D.A., Christeson, G.L. & Carlson, R.L. (2019). Seismic layer 2A: Evolution and thickness from 0-to 70-Ma crust in the slow-intermediate spreading South Atlantic. Journal of Geophysical Research: Solid Earth, 124(8), 7633-7651.

Evans, B. & Goetze, C. The temperature variation of hardness of olivine and its implication for polycrystalline yield stress. J. Geophys. Res. 84(B10), 5505– 5524 (1979).

Ewing, J. & Ewing, M. (1959). Seismic-refraction measurements in the Atlantic Ocean basins, in the Mediterranean Sea, on the Mid-Atlantic Ridge, and in the Norwegian Sea. Geological Society of America Bulletin, 70(3), 291-318.

Ewing, J. & Houtz, R. (1979). Acoustic Stratigraphy and Structure of the Oceanic Crust. *In Deep Drilling Results in the Atlantic Ocean: Ocean Crust* (eds M. Talwani, C.G. Harrison and D.E. Hayes). https://doi.org/10.1029/ME002p0001

Ewing, M., Sutton, G.H., & Officer, C.B. (1952). Seismic refraction measurements in the Atlantic Ocean basin, Part IV: *Bulletin of the Seismological Society of America*, v. 42, p. 1353–242.

Ewing, M., Worzel, J.L., Hersey, J.B., Press, F., & Hamilton, G.R. (1950). Seismic refraction measurements in the Atlantic Ocean basin, Part 1: *Bulletin of the Seismological Society of America*, v. 40, p. 233–242.

Fleitout, L. & Froidevaux, C. Tectonics and topography for a lithosphere containing density heterogeneities. Tectonics 1(1), 21– 56 (1982).

Früh-Green, G. L., et al. (2018). Magmatism, serpentinization and life: Insights through drilling the Atlantis Massif (IODP Expedition 357). *Lithos*, 323, 137–155. https://doi.org/10.1016/j.lithos.2018.09.012

Fujie, G., Kasahara, J., Murase, K., Mochizuki, K. & Kaneda, Y. (2008). Interactive analysis tools for the wide-angle seismic data for crustal structure study (Technical Report). Exploration Geophysics, 39(1), 26-33.

Funck, T., Jackson, H. R., Louden, K. E., Dehler, S. A., & Wu, Y. (2004). Crustal structure of the northern Nova Scotia rifted continental margin (eastern Canada). *Journal of Geophysical Research*, 109, B09102. https://doi.org/10.1029/2004JB003008.

Funnell, M.J., Robinson, A.H., Hobbs, R.W., & Peirce, C. (2021). Evolution and properties of young oceanic crust: constraints from Poisson's ratio, *Geophysical Journal International*, Volume 225, Issue 3, Pages 1874–1896, https://doi.org/10.1093/gji/ggab062

Fox, P.J. & Gallo, D.G. (1984). A tectonic model for ridge-transform-ridge plate boundaries: Implications for the structure of oceanic lithosphere. *Tectonophysics*, 104(3-4), 205-242.

Gholamrezaie, E., Scheck-Wenderoth, M., Sippel, J. & Strecker, M.R. (2018).Variability of the geothermal gradient across two differently aged magma-rich continental rifted margins of the Atlantic Ocean: the Southwest African and the Norwegian margins. *Journal of Geophysical Research: Solid Earth*. 9(1), 139-158.

Grevemeyer, I., et al. (1998). Seismic structure and crustal ageing at 14°S on the East Pacific Rise. *Geophys. J. Int.* 135, 573–584.

Grevemeyer, I., et al. (2019). Constraining the maximum depth of brittle deformation at slow- and ultraslow-spreading ridges using microseismicity. Geology 47, 1069–1073

Grevemeyer, I., et al. (2018a). Episodic magmatism and serpentinized mantle exhumation at an ultraslow-spreading centre. *Nature Geosci.* 11, 444–448 https://doi.org/10.1038/s41561-018-0124-6

Grevemeyer, I., Kaul, N., Villinger, H. & Weigel, W. (1999). Hydrothermal activity and the evolution of the seismic properties of upper oceanic crust. J. *Geophys. Res.* 104(B3), 5069–5079. https://doi.org/10.1029/1998JB900096.

Grevemeyer, I., Ranero, C. R., & Ivandic, M. (2018b). Structure of oceanic crust and serpentinization at subduction trenches. Geosphere, 14(2), 395–418. https://doi.org/10.1130/GES01537.1

Grevemeyer, I., & Weigel, W. (1996). Seismic velocities of the uppermost igneous crust versus age. *Geophys. J. Int.* 124(2), 631–635.

Grevemeyer, I., Weigel, W., & Jennrich, C. (1998). Structure and ageing of oceanic crust at 14 ° S on the East Pacific Rise. *Geophysical Journal International*, 135, 573–584.

Grindlay, N.R., Fox, P.J. & Vogt, P.R., (1992). Morphology and tectonics of the Mid-Atlantic Ridge (25◦-27◦30'S) from sea beam and magnetic data, *J. geophys. Res*., 97, 6983–7010.

Grove, T. L., Till, C. B. & Krawczynski, M. J. (2012).The role of H2O in subduction zone magmatism. Annu. Rev. Earth Planet Sci. 40, 413-439.

Han, S., et al. (2014). Architecture of on-and off-axis magma bodies at EPR 9 37–40′ N and implications for oceanic crustal accretion. *Earth and Planetary Science Letters*, 390, 31-44.

Halpaap, F., et al. (2019). Earthquakes track subduction fluids from slab source to mantle wedge sink. *Sci Adv*., 5(4). doi:10.1126/sciadv.aav7369

Hekinian, R. (2014). Fracture Zones and Transform Faults. *Sea Floor Exploration: Scientific Adventures Diving into the Abyss*, 255-300.

Henig, A. S., D. K. Blackman, A. J. Harding, J.-P. Canales, & G. M. Kent (2012), Downward continued multichannel seismic refraction analysis of Atlantis Massif oceanic core complex, 30°N, Mid-Atlantic Ridge, *Geochem. Geophys. Geosyst.*, 13, Q0AG07, doi:10.1029/2012GC004059.

Katayama, I. et al. (2021). Crack geometry of serpentinized peridotites inferred from onboard ultrasonic data from the Oman Drilling Project. *Tectonophysics* 814, 228978.

Hatakeyama, K. & Katayama, I. (2020). Pore fluid effects on elastic wave velocities of serpentinite and implications for estimates of serpentinization in oceanic lithosphere. *Tectonophysics* 775, 228309.

Heezen, B.C., Tharp, M., and Ewing, M. (1959). The Floors of the Oceans, 1. The North Atlantic. *Geol. Soc. Am*, p 122.

Heezen, B.C. (1960). The Rift in the Ocean Floor. *Scientific American*, 203, 98-110. http://dx.doi.org/10.1038/scientificamerican1060-98

Heirtzler, J.R., Dickson, G.O., Herron, E.M., Pitman, W.C., & Le Pichon, X. (1968). Marine magnetic anomalies, geomagnetic field reversals and motions of the ocean floor and continents. *J. Geophys. Res.*, 73, 2119-2136.

Herron, T. J., W. J. Ludwig, P. L. Stoffa, T. K. Kan, & P. Buhl (1978), Structure of the East Pacific Rise crest from multichannel seismic reflection data, *J. Geophys. Res.*, 83, 798–804.

Hess, H.H. (1962). History of Ocean Basins. *Petrologic Studies: A Volume to Honor A. F. Buddington*, *Geological Society of America*, 599-620.

Hess, H.H. (1964). Seismic anisotropy of the uppermost mantle under oceans. *Nature*, 203(4945),629-631.

Hill, M.N. (1957). Recent geophysical exploration of the ocean floor: *Phys. Chern. Earth*, v.2, p. 129-163.

Horning, G., et al. (2016). A 2-D tomographic model of the Juan de Fuca plate from accretion at axial seamount to subduction at the Cascadia margin from an active source ocean bottom seismometer survey. *Journal of Geophysical Research: Solid* Earth, 121(8), 5859-5879. https://doi.org/10.1002/2016JB013228

Houtz, R., & Ewing, J. (1976). Upper crustal structure as a function of plate age. *Journal of Geophysical Research*, 81(14), 2490–2498. https://doi.org/10.1029/jb081i014p02490

Hughes, D. S. & Maurette C. (1956). Dynamic Elastic Moduli of Iron, Aluminum, and Fused Quartz. *J. Appl. Phys.* 27, 1184-1186.

Hyndman, R.D. & Peacock, S.M. (2003). Serpentinization of the forearc mantle. *Earth Planet. Sci. Lett.* 212(3-4), 417-432.

Ildefonse, B., et al. (2007). Oceanic core complexes and crustal accretion at slow-spreading ridges. *Geology*, 35(7), 623–626. https://doi.org/10.1130/g23531a.1

Ismaïl, W.B., & Mainprice, D. (1998). An olivine fabric database: an overview of upper mantle fabrics and seismic anisotropy. *Tectonophysics*, 296(1–2), 145–157. https://doi.org/10.1016/S0040-1951(98)00141-3

Ito, G. & Dunn R. (2009). Mid-ocean ridges: Mantle convection and formation of thEe lithosphere. *Encyclopedia of Ocean Sciences*, 4030-4044, doi:10.1016/B978-012374473-9.00654-8

Jian, H. (2017). Seismic crustal structure of the ultraslow spreading Southwest Indian Ridge segment at 50◦28'E. Thèse de doctorat de l'Institut de Physique du Globe de Paris

Jian, H., et al. (2016). Seismic structure and magmatic construction of crust at the ultraslow-spreading Southwest Indian Ridge at 50°28'E. *Journal of Geophysical Research*, 121, 18–42. https://doi.org/10.1002/2016JB013377

Jian, H., Nedimović, M. R., Canales, J. P., & Lau, K. W. H. (2021). New insights into the rift to drift transition across the northeastern Nova Scotian margin from wide-angle seismic waveform inversion and reflection imaging. *Journal of Geophysical Research: Solid Earth*, 126, e2021JB022201. https://doi.org/10.1029/2021JB022201

Jian, H., Singh, S. C., Chen, Y. J., & Li, J. (2017b). Evidence of an axial magma chamber beneath the ultraslow-spreading Southwest Indian Ridge. *Geology*, 45(2), 143–146. https://doi.org/10.1130/G38356.1

Johnson, H. P., Pruis, M. J., Van Patten, D. & Tivey, M. A. Density and porosity of the upper oceanic crust from seafloor gravity measurements. *Geophys. Res. Lett.* 27(7), 1053-1056 (2000).

Jokat, W., & Schmidt-Aursch, M. C. (2007). Geophysical characteristics of the ultraslow spreading Gakkel Ridge, Arctic Ocean. *Geophysical Journal International*, 168(3), 983–998. https://doi.org/10.1111/j.1365-246X.2006.03278.x

Kandilarov, A., et al. (2010). Crustal structure of the ultra-slow spreading Knipovich Ridge, North Atlantic, along a presumed ridge segment center. *Marine Geophysical Research*, 31(3), 173–195. https://doi.org/10.1007/s11001-010-9095-8

Kandilarov, A., Mjelde, R., Okino, K., & Murai, Y. (2008). Crustal structure of the ultra-slow spreading Knipovich Ridge, North Atlantic, along a presumed amagmatic portion of oceanic crustal formation. *Marine Geophysical Research*, 29(2), 109–134. https://doi.org/10.1007/s11001-008-9050-0

Kardell, D.A., Christeson, G.L., Estep, J.D., Reece, R.S. & Carlson, R.L. (2019). Long-lasting evolution of layer 2A in the Western South Atlantic: Evidence for low-temperature hydrothermal circulation in old oceanic crust. *Journal of Geophysical Research: Solid Earth*, 124(3), 2252-2273.

Katz, S., Edwards, R.S., & Press, F. (1953). Seismic-refraction profile across the Gulf of Maine: *Bulletin of the Seismological Society of America*, v. 64, p. 249–251.

Keen, C. E., & Potter, D. P. (1995). The transition from a volcanic to a nonvolcanic rifted margin off eastern Canada. *Tectonics*, 14, 359–371. https://doi.org/10.1029/94TC03090.

Kelley, D. S., et al. (2005). A serpentinite-hosted ecosystem: The Lost City Hydrothermal Field. *Science*, 307(5714), 1428–1434. https://doi.org/10.1126/science.1102556

Kelly, S., Butler, J.P. & Beaumont, C. (2016). Continental collision with a sandwiched accreted terrane: Insights into Himalayan–Tibetan lithospheric mantle tectonics. *Earth Planet. Sci. Lett.* 455, 176-195.

Kent, G., Harding, A., & Orcutt, J. (1990). Evidence for a smaller magma chamber beneath the east pacific rise at 9°30'N. *Nature*, 344(6267):650.

Kent, G., et al. (2000). Evidence from three-dimensional seismic reflectivity images for enhanced melt supply beneath mid-ocean-ridge discontinuities. *Nature*, 406(6796):614.

Klingelhöfer, F., Géli, L., Matias, L., Steinsland, N., & Mohr, J. (2000). Crustal structure of a super-slow spreading centre: A seismic refraction study of Mohns Ridge, 72°N. *Geophysical Journal International*, 141(2), 509–526. https://doi.org/10.1046/j.1365-246X.2000.00098.x

Korenaga, J. et al. (2000). Crustal structure of the southeast Greenland margin from joint refraction and reflection seismic tomography. *J. Geophys. Res.* 105, 21591–21614.

Korenaga, J., Holbrook, W. S., Kent, G. M., Kelemen, P. B., Detrick, R. S., Larsen, H. C., et al. (2000). Crustal structure of the southeast Greenland margin from joint refraction and reflection seismic tomography. *Journal of Geophysical Research*, 105, 21591–21614. https://doi.org/10.1029/2000JB900188

Kreemer, C., Blewitt, G., & Klein, C. E. (2014). A geodetic plate motion and Global Strain Rate Model. *Geochemistry, Geophysics, Geosystems*, 15, 3849–3889. https://doi.org/10.1002/2014GC005407

Kuo, B.Y. & Forsyth, D.W. (1988). Gravity anomalies of the ridge-transform system in the South Atlantic between 31 and 34.5◦S: upwelling centers and variations in crustal thickness, *Mar. geophys. Res.*, 10, 205–232.

Lagabrielle, Y., Bideau, D., Cannat, M., Karson, J.A., & Mével, C. (1998). Ultramafic-mafic plutonic rock suites exposed along the Mid-Atlantic Ridge (10°N–30°N). Symmetrical-asymmetrical distribution and implications for seafloor spreading processes. *Faulting and magmatism at Mid-Ocean Ridges. Geophysical Monograph 106.* American Geophysical Union.

Lau, K.W.H., Nedimović, M.R., & Louden, K.E. (2018). Continent-ocean transition across the northeastern Nova Scotian margin from a dense wide-angle seismic profile. *Journal of Geophysical Research: Solid Earth*, 123, 4331–4359. https://doi.org/10.1029/2017JB015282.

Lau, K. W. H., Nedimović, M. R., & Louden, K. E. (2019). Along-strike variations in structure of the continent-ocean transition at the northeastern Nova Scotia margin from wide-angle seismic observations. *Journal of Geophysical Research: Solid Earth*, 124, 3172–3196. https://doi.org/10.1029/2018JB016894.

Lavier, L. L., Buck, W. R., & Poliakov, N. B. (1999). Self-consistent rolling-hinge model for the evolution of large-offset low-angle normal faults. *Geology*, 27, 1127–1130.

Lecoeuvre, A., et al. (2021). Microbial ecology of the newly discovered serpentinite-hosted Old City hydrothermal field (southwest Indian ridge). *ISME J* 15, 818–832.

Le Pichon, X. (1968). Sea-floor spreading and continental drift. *J. Geophys. Res.*, 73(12), 3661– 3697, doi:10.1029/JB073i012p03661.

Leroy, S., & Cannat, M. (2014). MD 199/SISMO-SMOOTH cruise, Marion Dufresne R/V. https://doi.org/10.17600/14003300

Leroy, S., et al. (2015). Anatomy of ultra-slow spreading Southwest Indian Ridge: The 2014 SISMOSMOOTH cruise. Abstract V21A-3027 Paper presented at the 2015 AGU, San Francisco, CA, 14–18 Dec.

Lesher, C.E. & Spera, F.J. Thermodynamic and transport properties of silicate melts and magma. in The encyclopedia of volcanoes (ed. Haraldur Sigurdsson) 113-141 (2015).

Li, J., et al. (2015). Seismic observation of an extremely magmatic accretion at the ultraslow spreading Southwest Indian Ridge. *Geophysical Research Letters*, 42(8), 2656–2663. https://doi.org/10.1002/2014GL062521

Li, J., et al. (2021). Anomalously hot mantle source beneath the Dragon Flag Supersegment of the Southwest Indian Ridge: New evidence from crystallisation temperatures of mid-ocean ridge basalts. *Lithos*, Volumes 396–397, 10622. https://doi.org/10.1016/j.lithos.2021.106221

Lin, J., Purdy, G. M., Schouten., Sempere, H. J. C., & Zervas, C. (1990). Evidence from gravity data for focused magmatic accretion along the Mid-Atlantic Ridge. *Nature*, 344, 627–632. https://doi.org/10.1038/344627a0

Lister, C. (1974). On the penetration of water into hot rock. *Geophysical Journal International*, 39(3):465–509.

Liu, M., Gerya, T., & Rozel, A. B. (2022). Self-organization of magma supply controls crustal thickness variation and tectonic pattern along melt-poor mid-ocean ridges. *Earth and Planetary Science Letters*, 584, 117482.

Macdonald, K. C., Scheirer, D. S., & Carbotte, S. M. (1991). Mid-ocean ridges: Discontinuities, segments and giant cracks. *Science*, 986-994.

MacLeod, C., et al. (2009). Life cycle of oceanic core complexes. *Earth and Planetary Science Letters*, 287(3):333–344.

Mével, C. (2003). Serpentinization of abyssal peridotites at mid-ocean. *Comptes Rendus Geoscience*, 335(10–11), 825–852.

Meyzen, C., Toplis, M. J., Humler, E., Ludden, J., & Mével, C. (2003). A discontinuity in mantle composition beneath the southwest Indian ridge. *Nature*, 421, 731–733.

Miller, D. J. & Christensen, N. I. (1997). Seismic velocities of lower crustal and upper mantle rocks from the slow-spreading Mid-Atlantic Ridge, south of the Kane Transform Zone (MARK). In: *Proceedings-Ocean drilling Program Scientific Results*, pages 437–456. National Science Foundation.

Minshull, T.A., Muller, M.R., Robinson, C.J., White, R.S., & Bickle, M.J. (1998). Is the oceanic Moho a serpentinization front? Geological Society, London, Special Publications, 148(1), 71–80. https://doi.org/10.1144/GSL.SP.1998.148.01.05

Minshull, T. A., Muller, M. R., & White, R. S. (2006). Crustal structure of the Southwest Indian Ridge at 66°E: Seismic constraints. Geophysical Journal International, 166(1), 135–147.

Mintrop, L. (1947). 100 Jahre physikalische Erdbebenforschung und Sprengseismik, Die Naturwissenschaften, v.34, p. 257–262, 289–295.

Morgan, W.J. (1968) Rises, trenches, great faults, and crustal blocks. *J. Geophys. Res.*, 73(6).

Momoh, E., Cannat, M., & Leroy, S. (2020). Internal structure of the oceanic lithosphere at a melt-starved ultraslow-spreading mid-ocean ridge: Insights from 2-D seismic data. Geochemistry, Geophysics, Geosystems, 21, e2019GC008540. https://doi.org/ 10.1029/2019GC008540.

Momoh, E., Cannat, M., Watremez, L., Leroy, S., & Singh, S. C. (2017). Quasi-3-D seismic reflection imaging and wide-angle velocity structure of nearly amagmatic oceanic lithosphere at the ultraslow-spreading Southwest Indian Ridge. Journal of Geophysical Research: Solid Earth, 122, 9511–9533. https://doi.org/10.1002/2017JB014754.

Moser T.J. (1991). Shortest path calculation of seismic rays. Geophysics, 56, 9–159. https://doi.org/10.1190/1.1442958

Moser T.J., Van Eck T., & Nolet G. (1992). Hypocenter determination in strongly heterogeneous earth models using the shortest path method. Journal of Geophysical Research: Solid Earth, 97, 6563–6572. https://doi.org/10.1190/1.1442958.

Muller, M.R., Robinson, C.J., Minshull, T.A., White, R.S., & Bickle, M.J. (1997). Thin crust beneath Ocean Drilling Program Borehole 735B at the Southwest Indian Ridge? *Earth and Planetary Science Letters*, 148(1–2), 93–107. http://dx.doi.org/10.1016/S0012-821X(97)00030-7

Muller, M.R., Minshull, T.A. & White, R.S. (1999). Segmentation and melt supply at the Southwest Indian Ridge. *Geology*, 27(10), 867-870.

Muller, M. R., Minshull, T. A., & White, R. S. (2000). Crustal structure of the Southwest Indian Ridge at the Atlantis II Fracture Zone. *Journal of Geophysical Research*, 105(B11), 25809 – 25828.

Muller, R.D., Sdrolias, M., Gaina, C., & Roest, W.R. (2008). Age, spreading rates, and spreading asymmetry of the world's ocean crust. *Geochemistry, Geophysics, Geosystems*, 9(4), 1–19. https://doi.org/10.1029/2007GC001743

Nedimović, M., Carbotte, S., Harding, A. et al. Frozen magma lenses below the oceanic crust. *Nature* 436, 1149–1152 (2005). https://doi.org/10.1038/nature03944

Nedimović, M.R., Carbotte, S.M., Diebold, J.B., Harding, A.J., Canales, J.P., & Kent, G.M. (2008). Upper crustal evolution across the Juan de Fuca ridge flanks. *Geochemistry, Geophysics, Geosystems*, 9(9). https://doi.org/10.1029/2008GC002085

Needham, H. D., & J. Francheteau (1974). Some characteristics of the rift valley in the Atlantic Ocean near 36°48'N, *Earth Planet. Sci. Lett.*, 22, 29-43.

Neves, M. C., Bott, M. H. P., & Searle, R. C. (2004). Patterns of stress at midocean ridges and their offsets due to seafloor subsidence. *Tectonophysics* 386(3-4), 223-242.

Newman, K.R., Nedimović, M.R., Canales, J.P. & Carbotte, S.M. (2011). Evolution of seismic layer 2B across the Juan de Fuca Ridge from hydrophone streamer 2-D traveltime tomography. *Geochemistry, Geophysics, Geosystems*, 12(5).

Niu, X., et al. (2015), Along-axis variation in crustal thickness at the ultraslow spreading Southwest Indian Ridge (50°E) from a wide-angle seismic experiment, *Geochemistry, Geophysics, Geosystems*, 16, 468– 485, doi:10.1002/2014GC005645

Nur Schuba, et al. (2018). A low-angle detachment fault revealed: Three dimensional images of the S-reflection fault zone along the Galicia passive margin, *Earth and Planetary Science Letters*, 492, https://doi.org/10.1016/j.epsl.2018.04.012

OETR, 2011. Play Fairway Analysis Atlas. NSDOE Records Storage File No. 88-11-0004-01, 347p.

Ohara, Y., Okino, K. & Kasahara, J. (2007). Seismic study on oceanic core complexes in the Parece Vela back-arc basin, *Island Arc*, 16, 348–360, doi:10.1111/j.1440–1738.2007.00591.x.

Papazachos C., & Nolet G. (1997). P and S deep velocity structure of the Hellenic area obtained by robust nonlinear inversion of travel times. *Journal of Geophysical Research: Solid Earth*, 102(B4), 8349–8367. doi: https://doi.org/10.1029/96JB03730.

Parnell-Turner, R., et al. (2017). Oceanic detachment faults generate compression in extension. *Geology*, 45, 923–926. https://doi.org/10.1130/G39232.1

Peterson, J.J., Fox, P.J., & Schreiber, E. (1974). Newfoundland ophiolites and the geology of the oceanic layer. *Nature*, 247(5438), 194-196.

Pezard, P. (1990). Electrical properties of mid-ocean ridge basalt and implications for the structure of the upper oceanic crust in Hole 504B. *J. Geophys. Res.* 95, 9237–9264.

Pitman, W.C., Kerron, E.M. & Heirtzler, J.R. (1968). Magnetic anomalies in the South Pacific Ocean and sea-floor spreading, *J. Geophys. Res.*, 73(6).

Pitman, W.C., & Heirtzler, J. R. (1966). Magnetic Anomalies over the Pacific-Antarctic Ridge. *Science*, 154 (3753). 1164-1171. doi:10.1126/science.154.3753.1164

Prada, M., Ranero, C.R., Sallarès, V., Zitellini, N., & Grevemeyer, I. (2016). Mantle exhumation and sequence of magmatic events in the Magnaghi–Vavilov Basin (Central Tyrrhenian, Italy): New constraints from geological and geophysical observations. *Tectonophysics*. http://dx.doi.org/10.1016/j.tecto.2016.01.041.

Pratt, R. G. (1999), Seismic waveform inversion in the frequency domain, part I: Theory and verification in a physical scale model, *Geophysics*, 64,888–901, doi:10.1190/1.1444597.

Prodehl, C., & W. D. Mooney (2012), Exploring the earth's crust: history and results of controlled-source seismology, 208.

Raitt, R. W. (1949). Studies of cocean-bottom structure off southern California with explosive waves: *Bulletin of the Geological Society of America*, v.60 (12.2): 1915.

Raitt, R. W. (1956) Seismic-refraction studies of the Pacific Ocean basin: Part 1: crustal thickness of the central equatorial pacific. *GSA Bulletin*, v. 67 (12): 1623–1640. https://doi.org/10.1130/0016-7606(1956)67[1623:SSOTPO]2.0.CO;2

Raitt, R. W. (1963). In M. N. Hill (Ed.), The crustal rocks. *The sea* (Vol. 3, pp. 85–102) New York: Wiley Interscience.

Ranero, C.R. & Reston, T.J., 1999. Detachment faulting at ocean core complexes, *Geology*, 27, 983–986.

Reston, T. (2018). Flipping detachments: The kinematics of ultraslow spreading ridges. *Earth and Planetary Science Letters*, 503, 144–157. https://doi.org/10.1016/j.epsl.2018.09.032

Reston, T., & McDermott, K.G. (2011). Successive detachment faults and mantle unroofing at magma-poor rifted margins. *Geology*, 39(11), 1071-1074.

Reston, T. J., & Ranero, C. R. (2011), The 3-D geometry of detachment faulting at mid-ocean ridges, *Geochem. Geophys. Geosyst.,* 12, Q0AG05, doi:10.1029/2011GC003666.

Reston, T. J., Ranero, C. R., Ruoff, O., Perez-Gussinye, M., & Dañobeitia, J. J. (2004). Geometry of extensional faults developed at slow-spreading centres from pre-stack depth migration of seismic reflection data in the Central Atlantic (Canary Basin). *Geophysical Journal International*, 159(2), 591-606.

Rickett, J. E., Van Manen, D. J., Loganathan, P., & Seymour, N. (2014). Slanted-streamer data-adaptive deghosting with local plane waves. In 76th EAGE Conference and Exhibition 2014 (Vol. 2014, No. 1, pp. 1-5). European Association of Geoscientists & Engineers.

Ronen, S. (2022) An Environmentally Friendly Low-Frequency Seismic Source. *Canadian Society of Exploration Geophysicists*, Focus Article. https://cseg.ca/an-environmentally-friendly-low-frequency-seismic-source.

Rouméjon, S. & Cannat, M. (2014). Serpentinization of mantle-derived peridotites at mid-ocean ridges: Mesh texture development in the context of tectonic exhumation. *Geochemistry, Geophysics, Geosystems*, 15(6):2354–2379.

Rouméjon, S., Cannat, M., Agrinier, P., Godard, M., & Andreani, M. (2015). Serpentinization and fluid pathways in tectonically exhumed peridotites from the Southwest Indian Ridge (62–65°E). *Journal of Petrology*, 56(4):703–734.

Sauter, D., & Cannat, M. (2010). The Ultraslow Spreading Southwest Indian Ridge. Diversity of Hydrothermal Systems on Slow Spreading Ocean Ridges, (November), 153–173. https://doi.org/10.1029/2008GM000843

Sauter, D., Cannat, M., & Mendel, V. (2008). Magnetization of 0-26.5 Ma seafloor at the ultraslow spreading Southwest Indian Ridge, 61°-67°E. *Geochemistry, Geophysics, Geosystems*, 9(4), 1–23. https://doi.org/10.1029/2007GC001764

Sauter, D., Cannat, M., Rouméjon, S., Andreani, M., Birot, D., Bronner, A., et al. (2013). Continuous exhumation of mantle-derived rocks at the Southwest Indian Ridge for 11 million years. *Nature Geoscience*, 6(4), 314–320. https://doi.org/10.1038/ngeo1771

Schlindwein, V., & Schmid, F. (2016). Mid-ocean-ridge seismicity reveals extreme types of ocean lithosphere. *Nature*, 535(7611), 276–279. https://doi.org/10.1038/nature18277

Schrenk, M. O., Kelley, D. S., Bolton, S. A., & Baross, J. A. (2004). Low archaeal diversity linked to subseafloor geochemical processes at the Lost City Hydrothermal Field, Mid-Atlantic Ridge. Environmental Microbiology, 6(10), 1086–1095. https://doi.org/10.1111/j.1462-2920.2004.00650.x

Seher, T., et al. (2010). Crustal velocity structure of the Lucky Strike segment of the Mid-Atlantic Ridge at 37 N from seismic refraction measurements. *Journal of Geophysical Research: Solid Earth*, 115(B3).

Sempéré, J. C., G. M. Purdy, & H. Schouten. (1990). Segmentation of the Mid-Atlantic Ridge between 24°N and 30°40'N, *Nature*, 344, 427-431.

Seyler, M., Cannat, M., & Mével, C. (2003). Evidence for major-element heterogeneity in the mantle source of abyssal peridotites from the Southwest Indian Ridge (52° to 68°E). *Geochemistry, Geophysics, Geosystems*, 4(2). https://doi.org/10.1029/2002GC000305

Shapiro, N.M. & Ritzwoller, M.H. Thermodynamic constraints on seismic inversions. *Geophys. J. Int.* 157(3), 1175-1188 (2004).

Shipp, R. M., & S. C. Singh (2002), Two-dimensional full wavefield inversion of wide-aperture marine seismic streamer data, *Geophys. J. Int.,* 151(2), 325–344, doi:10.1046/j.1365-246X.2002.01645.x.

Sinha, M. C., & Louden, K. E. (1983). The Oceanographer fracture zone—I. Crustal structure from seismic refraction studies. *Geophysical Journal International*, 75(3), 713-736.

Singh, S.C., Collins, J.A., Canales, J.P., Tucholke, B.E. & Detrick, R.S. (2004). New insights into serpentinization at Atlantis Massif, Eos Trans. AGU, 85, V23B-0628.

Smith, D. K., Cann, J. R., & Escartín, J. (2006). Widespread active detachment faulting and core complex formation near 13°N on the Mid-Atlantic Ridge. *Nature*, 442(7101), 440–443. https://doi.org/10.1038/nature04950

Soule, S.A., Perfit, M. (2015). Axial Summit Trough. In: Harff, J., Meschede, M., Petersen, S., Thiede, J. (eds) *Encyclopedia of Marine Geosciences*. Springer, Dordrecht. https://doi.org/10.1007/978-94-007-6644-0_3-2

Talwani, M., Le Pichon, X., & Ewing, M. (1965). Crustal structure of the mid-ocean ridges: 2. Computed model from gravity and seismic refraction data. *Journal of Geophysical Research*, 70(2), 341-352.

Talwani, M., Windisch, C.C., & Langseth Jr, M.G. (1971). Reykjanes ridge crest: A detailed geophysical study. *Journal of Geophysical Research*, 76(2), 473-517.

Tarantola, A. (1987). Inversion of travel times and seismic waveforms. Seismic tomography, 135-157.

Toomey, D. R. & Foulger, G. R. (1989). Tomographic inversion of local earthquake data from the Hengill-Grensdalur central volcano complex, Iceland. *J. Geophys. Res.* 94(B12), 17497–17510.

Toomey, D.R., Purdy, G.M., Solomon, S.C., & Wilcock, W.S.D. (1990). The three-dimensional seismic velocity structure of the East Pacific Rise near latitude 9°30′N. *Nature*, 347, pp. 639-645

Tucholke, B. E., & Lin, J. (1994). A geological model for the structure of ridge segments in slow spreading ocean crust. *Journal of Geophysical Research*, 99(B6), 11937–11958. https://doi.org/10.1029/94jb00338

Tucholke, B. E., Lin, J., & Kleinrock, M. C. (1998). Megamullions and mullion structure defining oceanic metamorphic core complexes on the Mid-Atlantic Ridge. *Journal of Geophysical Research*, 103(B5), 9857–9866. https://doi.org/10.1029/98jb00167

Van Avendonk, H. J., Harding, A. J., Orcutt, J. A., & McClain, J. S. (1998). A two-dimensional tomographic study of the Clipperton transform fault. *Journal of Geophysical Research: Solid Earth*, *103*(B8), 17885-17899.

Van Avendonk, H.J.A., et al. (2017). Seismic structure and segmentation of the axial valley of the Mid-Cayman Spreading Center. *Geochemistry, Geophysics, Geosystems*, 1–13. https://doi.org/10.1002/2017GC006873

VanderBeek, B.P., Toomey, D.R., Hooft, E.E.E., & Wilcock, W.S.D. (2016). Segmentation of mid-ocean ridges attributed to oblique mantle divergence. *Nature Geosciences*, 9, 636–642. https://doi.org/10.1038/ngeo2745

Vera, E.E., & Diebold, J.B. (1994). Seismic imaging of oceanic layer 2A between 9°30'N and 10°N on the East Pacific Rise from two-ship wide-aperture profiles. *Journal of Geophysical Research*, 99(B2), 3031–3041. https://doi.org/10.1029/93JB02107

Vine, F.J. and Moores, E.M. (1972). A Model for the Gross Structure, Petrology, and Magnetic Properties of Oceanic Crust, *Studies in Earth and Space Sciences*, R. Shagam, R. B. Hargraves, W. J. Morgan, F. B. Van Houten, C. A. Burk, H. D. Holland, L. C. Hollister

Virieux, J. and Operto, S. (2009). An overview of full-waveform inversion in exploration geophysics. *Geophysics* 74(6): WCC1-WCC26. https://doi.org/10.1190/1.3238367

Wang, H., S. C. Singh, & H. Calandra (2014). Integrated inversion using combined wave-equation tomography and full waveform inversion, *Geophysical Journal International*, 198(1), 430–446.

Watremez, L., Lau, H.K.W., Nedimović, M.R., & Louden, K.E. (2015). Traveltime tomography of a dense wide-angle profile across Orphan Basin. *Geophysics*, 80(3), B69–B82. https://doi.org/10.1190/geo2014-0377.1

Weekly, R.T., Wilcock, W.S.D., Toomey, D.R., Hooft, E.E.E., & Kim, E. (2014). Upper crustal seismic structure of the Endeavour segment, Juan de Fuca Ridge from traveltime tomography: Implications for oceanic crustal accretion. *Geochemistry, Geophysics, Geosystems,* 15(4), 1296–1315. https://doi.org/10.1002/2013GC005159

Wernicke, B. & Axen, G.J. (1988). On the role of isostasy in the evolution of normal fault systems, *Geology*, 16, 848–851.

Wessel, P. & Smith, W. H. F. (1998). New, improved version of Generic Mapping Tools released. Eos, *Transactions American Geophysical Union*, 79(79), 579–579.

Wilcock, W.S.D., Solomon, S.C., Purdy, G.M. & Toomey, D.R. (1992). The seismic attenuation structure of a fast-spreading mid-ocean ridge. *Science*, 258(5087), 1470-1474.

Wilkens, R. H., Fryer, G. J. & Karsten, J. (1991). Evolution of porosity and seismic structure of upper oceanic crust: Importance of aspect ratios. *J. Geophys. Res.* 96(B11), 17981–17995.

Wilson, J. (1965). A New Class of Faults and their Bearing on Continental Drift. *Nature* 207, 343–347. https://doi.org/10.1038/207343a0

White, R. S., Mckenzie, D., & O'Nions, R. K. (1992). Oceanic crustal thickness from seismic measurements and rare earth element inversions. *Journal of Geophysical Research*, 97(B13), 19683–19715. https://doi.org/10.1029/92jb01749

White, R. S., T. A. Minshull, M. J. Bickle, & C. J. Ronbinson (2001), Melt generation at very slow-spreading oceanic ridges: Constraints from geochemical and geophysical data, *J. Petrol.*, 42(6), 1171–1196.

Whitmarsh, R. B., & Calvert, A. J. (1986). Crustal structure of Atlantic fracture zones—I. The Charlie-Gibbs fracture zone. *Geophysical Journal International*, 85(1), 107-138.

Wu, Y., Louden, K. E., Funck, T., Jackson, H. R., & Dehler, S. A. (2006). Crustal structure of the central Nova Scotia margin off Eastern Canada. *Geophysical Journal International*, 166(2), 878–906. https://doi.org/10.1111/j.1365-246X.2006.02991.x.

Xu, M., et al. (2014). Variations in axial magma lens properties along the East Pacific Rise (9°30′N–10°00′N) from swath 3-D seismic imaging and 1-D waveform inversion, *J. Geophys. Res. Solid Earth*, 119, 2721–2744, doi:10.1002/2013JB010730.

Xu, M., Zhao, X., & Canales, J. P. (2020). Structural variability within the Kane oceanic core complex from full waveform inversion and reverse time migration of streamer data. *Geophysical Research Letters*, 47, e2020GL087405 https://doi.org/10.1029/2020GL087405

Zelt, C. A., & Smith, R. B. (1992). Seismic traveltime inversion for 2-D crustal velocity structure. *Geophysical journal international*, *108*(1), 16-34.

Zhang, J., & Toksöz, M.N. (1998). Nonlinear refraction traveltime tomography. *Geophysics,* 63, 1726–1737, doi: https://doi.org/10.1190/1.1444468.

Zhao, M., et al. (2013). Three-dimensional seismic structure of the Dragon Flag oceanic core complex at the ultraslow spreading Southwest Indian Ridge (49°39′E). *Geochemistry, Geophysics, Geosystems*, 14(10), 4544–4563. https://doi.org/10.1002/ggge.20264

Zhou, H., & Dick, H.J.B. (2013). Thin crust as evidence for depleted mantle supporting the Marion Rise. *Nature*, 494(7436), 195-200.

Appendix A

Supporting Information for Chapter 2: Seismic velocity structure along and across the ultraslow-spreading Southwest Indian Ridge at 64°30'E showcases flipping detachment faults

Contents

A.1 Introduction

We provide additional details about the data acquisition, data processing prior to first arrival picking, and P-wave tomographic inversion for the velocity models as follows. In the Data Acquisition section, we give information on the conversion from the OBS names used during the MD 199 -SISMO-SMOOTH Cruise 2014 seismic experiment to the sequential numerical values used in the paper for presentation purposes (Table A.1). In the Data Processing section, we present the static shifts used for OBS 8, 10 and 12 to achieve acceptable fits during the OBSs relocation process (Table A.2). In the Methods and Results section, Figures A.1, A.2, A.3, A.4, A.5, A.6, A.7, A.8 and A.9 are presented to expand on what is shown in the main text body.

A.2 Data acquisition

SMOO33 (NS profile)		SMOO35 (EW profile)	
Original name	Converted name	Original name	Converted name
C37	*Lost*	C26	17
C36	1	C25	18
C35	2	C24	19
C34	3	C23	20
C33	*Bad data*	C22	21
I1	4	T1	22
T5	5	C21	23

I2	6	I6	24
T6	7	T2	25
I3	8	I2	26
T7	9	T3	27
I4	10	I7	28
T8	11	C27	29
I5	12	T4	30
T10	13	C28	31
T9	*Lost*	*C29*	*Noisy data*
C38	14	C30	32
C39	15		
C40	16		

Table A.1. Conversion of the OBS names from the ones used during the seismic experiment (original) to the ones in use in this work (converted). Italic typography indicates the OBSs that were lost or had unusable data.

A.3 Data processing

The raw data were downloaded, corrected for clock drift, converted to SEGY format, and stored on hard disks while at sea. The data were first inspected to make sure that the clock drift was correctly implemented, and that the shot positions were accurate in all the OBS records. Because the OBSs recorded continuously, the next step was to cut the raw SEGY data into common receiver gathers with 60-s-long data traces pertinent to the shooting operations for the two orthogonal profiles analyzed in this work (Fig. A.1a). The hydrophone or vertical channel data, depending on arrival clarity and signal-to-noise ratio, were then used to pick the water arrival up to offsets of ~8 km. To relocate the OBSs to their true positions on the seafloor, one-way traveltimes of the direct water waves were used as input to a least-square regression to fit the optimal latitude, longitude, and depth locations. For most OBS surveys, including depth as a variable in the regression is not necessary. However, given that the seafloor topography in the study area is very rough with steep gradients present (up to ~35° along the NS Profile around the highest topographic feature), including seafloor depth was quite helpful in determining optimal locations of a number of OBSs. The reduced root-mean square (RMS) misfit of arrival times translate to a horizontal position uncertainty of 11–84 m, with the true OBS seafloor locations differing up to ~300 m from the deployment locations, which is

expected considering the great seafloor depth and ocean currents in the study area. The water velocity structure used for OBS relocations was constructed through a combination of: (i) an ARGO Profile located <200 km away from the study area, at longitude 62°42'E and latitude 27°27'S, collected on 03–11–2017 for depths <2.5 km; and (ii) the Echo-sounding Correction Tables (Carter, 1980) for depths >2.5 km. Despite the detailed work on OBS relocations, first arrivals from OBS 8, 10 and 12 of the French contingent needed arbitrary static shifts to achieve acceptable fits, likely due to problems with their internal clocks (Table A.2).

OBS name	Static shift (ms)
8	-186
10	-150
12	-229

Table A.2. Static shift applied to OBSs 8, 10, and 12 (SMOO33, NS profile).

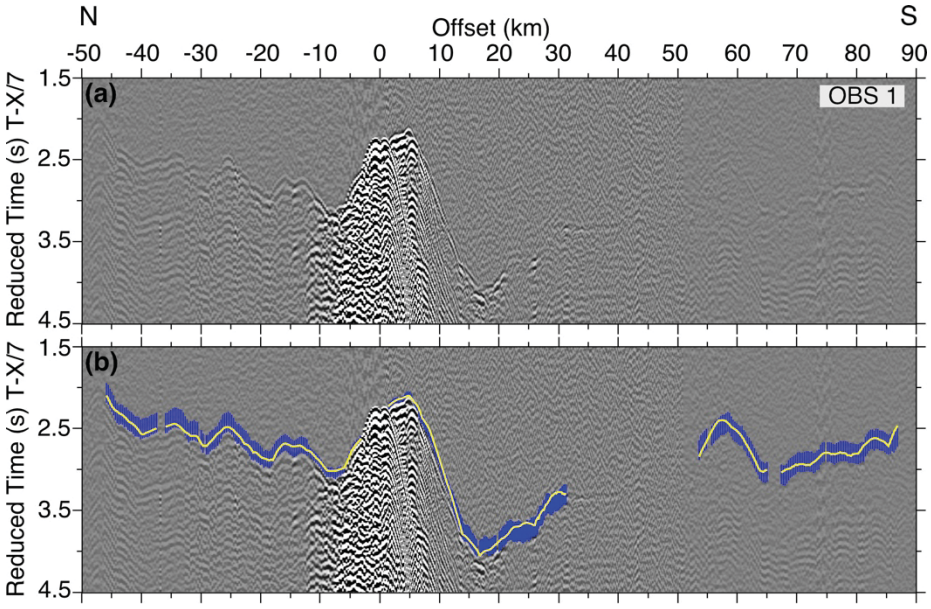

Figure A.1. Example OBS 1 gather for the NS profile. (a and b) Vertical geophone data for OBS 5 after application of a reduction velocity of 7 km/s and band-pass filtering (1-5-18-25 Hz). Picked (centers of blue error bars) and modeled (yellow curves) first arrival traveltimes are shown in (b).

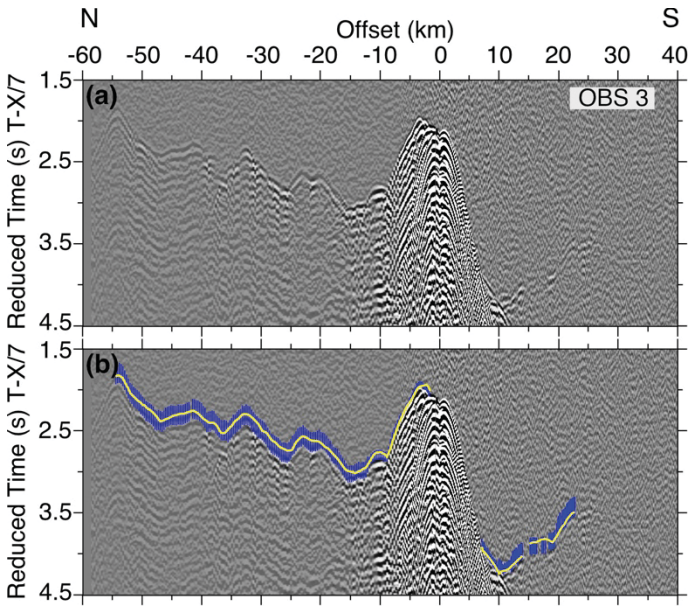

Figure A.2. Example OBS 3 gather for the NS profile. (a and b) Vertical geophone data for OBS 5 after application of a reduction velocity of 7 km/s and band-pass filtering (1-5-18-25 Hz). Blue error bars and yellow curves as in Figure A.1 caption.

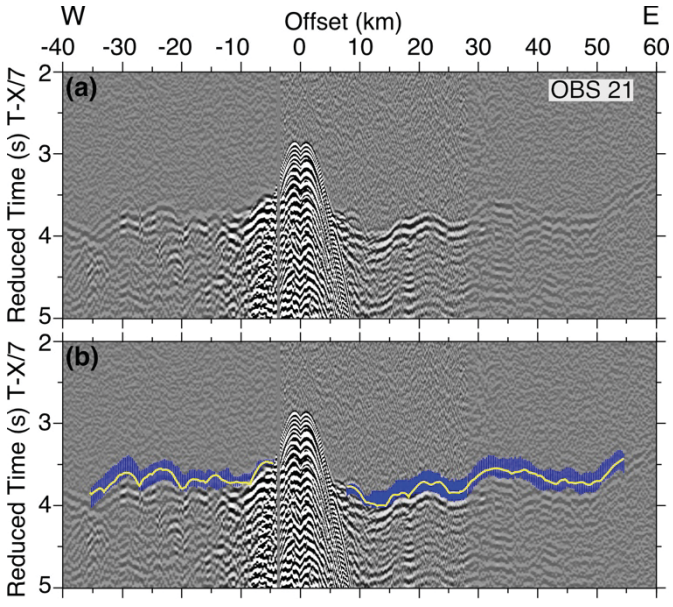

Figure A.3. Example OBS 21 gather for the EW profile. (a and b) Vertical geophone data for OBS 5 after application of a reduction velocity of 7 km/s and band-pass filtering (1-5-18-25 Hz). Blue error bars and yellow curves as in Figure A.1 caption.

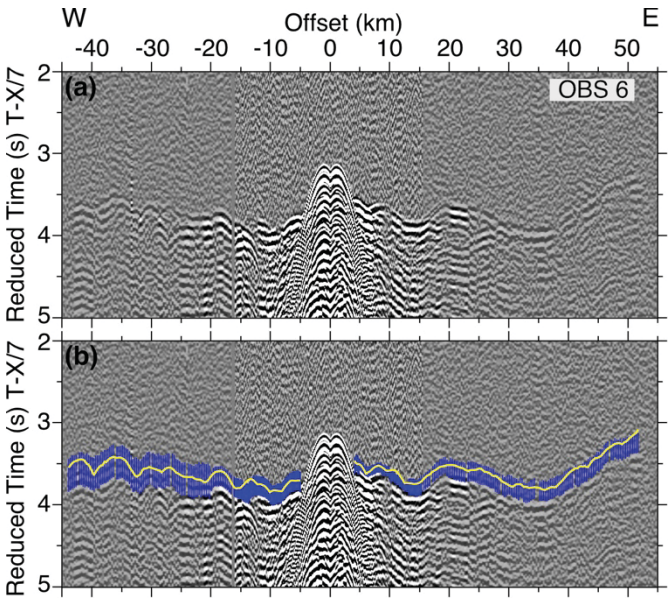

Figure A.4. Example OBS 6 gather for the EW profile. (a and b) Vertical geophone data for OBS 5 after application of a reduction velocity of 7 km/s and band-pass filtering (1-5-18-25 Hz). Blue error bars and yellow curves as in Figure A.1 caption.

A.4 Methods and results

The traveltime tomography method we use, TOMO2D, applies first a hybrid-approach for the forward modeling that combines the graph method with a local ray-bending refinement (Korenaga et al., 2000; Moser, 1991; Moser et al., 1992; Van Avendonk et al., 1998) to find the shortest raypath from the shot to the receiver for each arrival. We use a tenth-order forward star for the horizontal direction and a fifteenth-order for the vertical direction for the graph method (Zhang & Toksöz, 1998), and a minimum segment length of 1 km with 8 interpolation points per segment for the bending method (Papazachos & Nolet, 1997). Tolerances for the conjugate gradient and Brent minimization are $1x10^{-4}$ and $1x10^{-5}$, respectively. The second TOMO2D step is a least-squares regularized inversion, in which the starting velocity model is perturbed and updated until the targeted chi-squared (χ^2) or the set number of maximum iterations is reached (Korenaga et al., 2000). We set our inversion to run 5 iterations and set the least-squares tolerance to 1×10^{-3}. Figure A.5 shows χ^2 as a function of iteration. We tested different values of smoothing and damping to detect the values that result in the best trade-off between data fitting and model smoothness, i.e., a low fitting error concurrent with a low horizontal and

vertical roughness. The damping and smoothing weighting factors used are 30 and 60, respectively. We use a horizontal correlation length that linearly increases from 2 km at the top of the model, at the seafloor, to 6 km at the bottom of the model. Likewise, the vertical correlation length increases from 2 km at the top to 5 km at the bottom of the model.

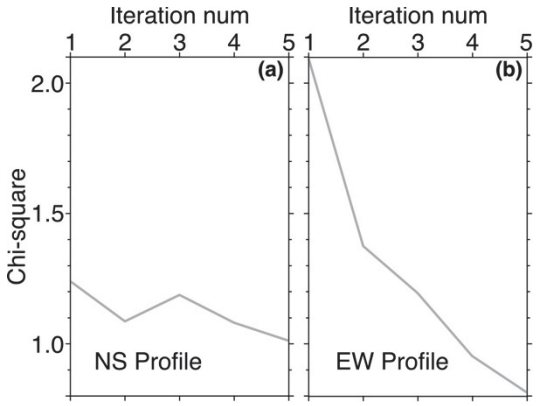

Figure A.5. Scatter plot showing the χ^2 values for each of the 5 iterations during the inversion process.

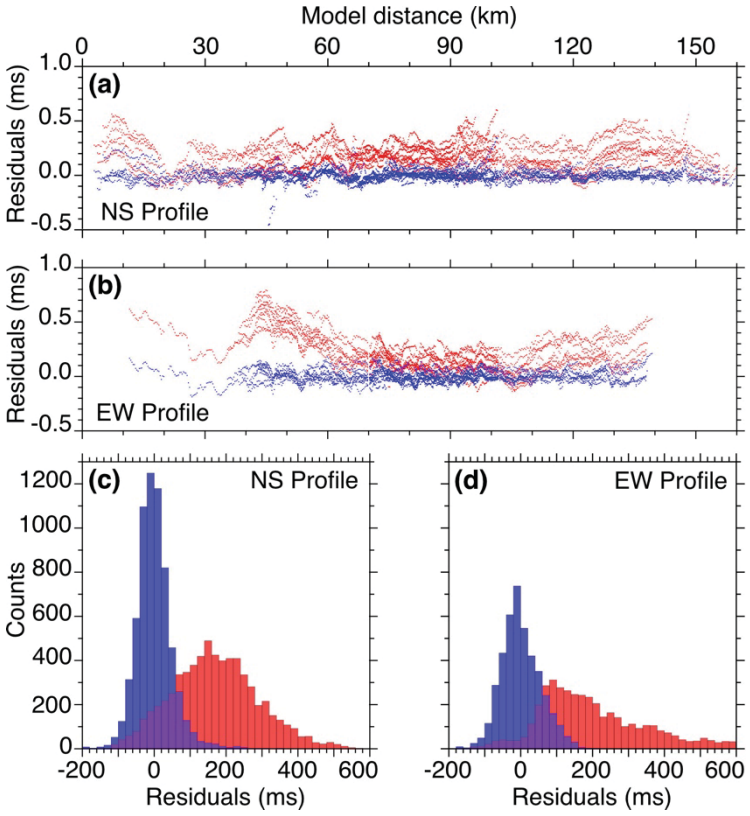

Figure A.6. Traveltime residuals for the starting (red) and final (blue) tomographic velocity models versus model distance for the NS (a) and EW (b) profiles. Histograms of the traveltime

residual distributions for the NS (c) and EW (d) profiles. Bins are 20 ms wide.

Figures A.6a and A.6b show that the travel times are fitted at all distances for the NS and EW profiles. The histograms in Figures A.6c and A.6d show that the traveltime residuals for the starting velocity models are shifted toward positive numbers and centered around zero for the final velocity models, which indicates that the starting velocity models are overall slower than the final velocity models.

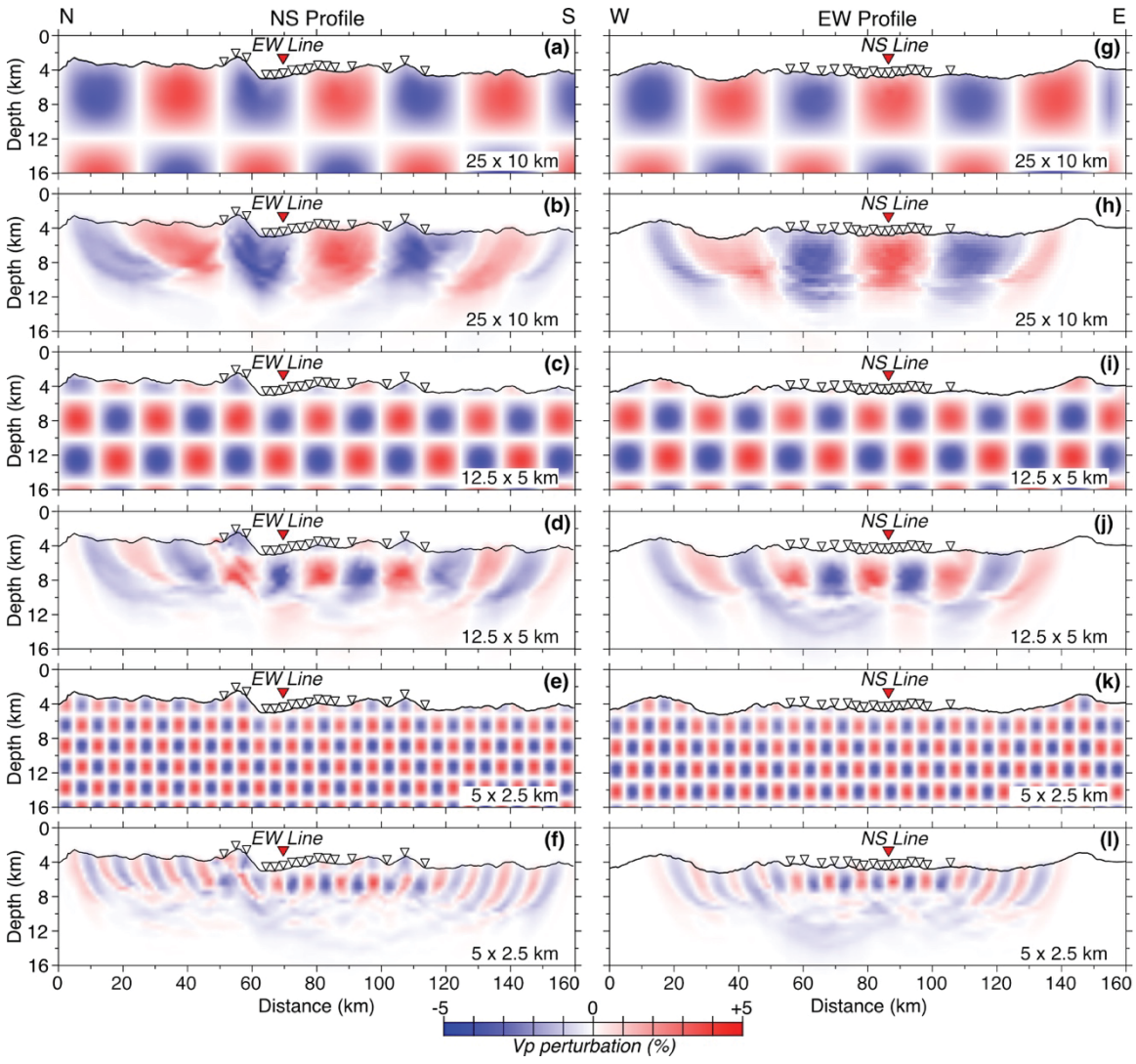

Figure A.7. Full-size checkerboard resolution tests for the NS (left column) and EW (right column) profiles for perturbation cells: 25 km wide x 10 km high (a and d), 12.5 km wide x 5 km high (b and e), 5 km wide x 2.5 km high (c and f). The input perturbed model is shown in the bottom left inset and the recovered perturbed model is the full-size figure. White inverted triangles show the positions of the OBSs on the seafloor. Red triangles show the location at which

the profiles cross each other.

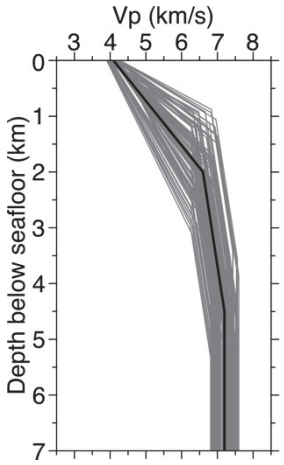

Figure A.8. Starting 1D velocity model (thick black line) hung off the seafloor in Figures 2.6.1.1a and 2.6.1.1d is shown together with 100 of its randomizations (thin grey lines) used for the Monte Carlo analysis.

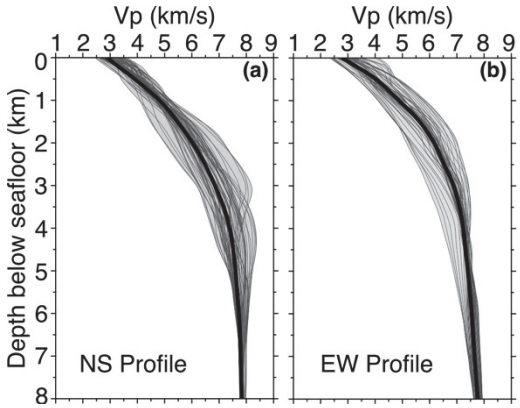

Figure A.9. 1D velocity-depth profiles (dark grey) sampled every 1 km in the section of the NS (a) and EW (b) averaged velocity models within the best resolved areas (Figs. 2.6.2.2.1a,b): (a) 51 km to 114 km and (b) 55 km to 106 km. Average 1D velocity-depth profiles are shown with thick black lines and the velocity envelope in light grey.

Appendix B

Methods for Chapter 3: Evolution of tectonically accreted oceanic lithosphere

B.1 Age estimation Method

Unlike the accretion at faster spreading rates, which is continuous and to the first order symmetric on both flanks, accretion at the SWIR at 64°30' E is discontinuous and asymmetric, resulting in disrupted lithospheric age with increasing distance from the ridge axis. This is a consequence of the flip-flop detachment faulting pattern in which successive detachment faults have an alternating polarity (Sauter et al., 2013). In the flip-flop rolling hinge faulting mode, an initially steep normal fault is rotated and flattened to form a low-angle detachment surface on the seafloor until the fault is abandoned and a new steep normal fault cuts through the footwall and becomes the new master fault. Each new fault has an opposite polarity to the previous fault, whose footwall it is cutting through. Thus, footwall surfaces of abandoned faults are split and migrate in opposite directions, which results in footwall surfaces of abandoned faults located both north and south of the spreading axis (Cannat et al., 2019; Reston, 2018; see also Fig. C.5). As a consequence of this faulting mode, ages are discontinuous as a function of distance from the ridge axis and change between emergence and breakaway of successive faults (Fig. 3.3.2b). Magnetic anomalies available for our study area (Cannat et al., 2006) are not robust due to the overall low magnetization of serpentinized peridotites and the potential overprinting of serpentinization-related magnetic signature of ultramafic rocks by occasional magmatic diking and volcanic eruptions (Bronner et al., 2014; Cannat et al., 2019). Thus, to estimate the seafloor ages we choose to use the point at which the ridge axis, mapped as the emergence of the currently active fault, crosses the SMOO33 profile as the marker for 0 Ma age, and unravel the rest of the ages with a constant spreading rate of 14 mm/year using the tomographic model distance between emergences and breakaways (Table C.3) and two simple conditions:

$$Age(E_{N+1}) = Age(B_N)$$
$$Age(B_N) > Age(E_N),$$

where *E* stands for emergence and *B* stands for breakaway. *N* indicates the fault number. Faults are numbered sequentially from youngest to oldest from 1 (active fault) to 9. Figure 3.3.2b shows the location of the *Bs* and *Es* and the estimated ages for each identified footwall surface. A pattern of ages increasing in an alternating opposite direction can be observed consistently with the flip-flop detachment faulting mode. Although these ages are only based on the spreading rate and not on magnetic anomaly record, they are adequate to carry out a first-order analysis of the changes in the seismic velocities as a function of distance from the ridge axis and lithospheric age.

B.2 Thermal modelling Method

To test if the observed velocity increase is related to changes in the geothermal regime as the lithosphere ages, we carry out a finite-difference (FD) modelling (see Supplementary Methods) to investigate how a 1D geothermal curve evolves in our study area. The initial geotherm is a 3-point curve with a temperature (T) of 750 °C at 15 km dbsf (Chen et al., 2020; Grevemeyer et al., 2019), 1260 °C at 50 km dbsf (Barruol et al., 2019; Bickert et al., 2020), and 1350 °C at 100 km (Kelly et al., 2016). The last point represents the base lithosphere temperature and the bottom of the 1D model (Kelly et al., 2016). FD models to evaluate the thermal evolution are computed for a time span of 10 Myr (Fig. C.3) and 100 Myr (Fig. C.4). Thermal relaxation is achieved in ~60 Myr (Fig. C.4) and the thermal differences in 10 Myr for the upper lithosphere (~6 km dbsf) are very small (Fig. C.3c). These differences imply a maximum cooling rate of ~10 °C/Myr for the lithosphere up to ~6 km dbsf.

In order to better understand the effect of thermal variation on seismic velocity we convert the 1D temperature-depth functions to velocity variation with depth using a factor denominated here as the gamma ratio (γ). Assuming that for a given serpentinization

degree, Young's modulus (Ψ) and Poisson's ratio (μ) are constant and their temperature dependency is nil, the P-wave velocity formula can be rearranged as follows:

$$B \equiv \frac{E(1-\mu)}{(1-2\mu)(1+\mu)}; \qquad V_P = \sqrt{\frac{E(1-\mu)}{\rho(1-2\mu)(1+\mu)}} = \sqrt{\frac{B}{\rho}} = \sqrt{\frac{B}{\rho_0(1-\alpha T)}}$$

In these equations, B is a constant, ρ is density, ρ_0 is the density at standard pressure, α is the thermal expansion coefficient, and T is the temperature. We can then calculate γ as:

$$\gamma \equiv \frac{V_{P2}}{V_{P1}} = \sqrt{\frac{B * \rho_0(1-\alpha T_1)}{B * \rho_0(1-\alpha T_2)}} = \sqrt{\frac{1-\alpha T_1}{1-\alpha T_2}}$$

While there are several studies on how the elastic properties of peridotites change with the degree of serpentinization (Table C.4), there are only a few on how they change with temperature. Laboratory determinations show that μ for variably serpentinized peridotites does not vary significantly with temperature (Christensen, 2004), as is the case with most rocks (Anderson et al., 1968; Christensen 1972; Christensen 1996; Hughes & Maurette, 1956). Similarly, a negligible temperature dependency of Ψ for olivine has been observed (Evan & Goetze, 1979). Considering the lack of experimental studies on how Ψ changes with temperature for peridotites, we assume that the findings for Olivine are applicable to peridotites. Thus, no thermal dependency of the elastic parameters μ and Ψ has been observed for variably serpentinized peridotites.

Appendix C

Supporting Information for Chapter 3: Evolution of tectonically accreted oceanic lithosphere

C.1 Seismic data analysis and inversion

A total of 6,523 first P-wave arrivals are hand-picked on the OBS records to offsets of up to ~90 km after relocating the OBSs to their true positions on the seafloor and applying a minimum phase trapezoidal band-pass filter (1–5–18–25 Hz). The unfiltered data were used as much as possible for the picking, with the filtered data used only to extend the picks to further offsets. In some instances, arrivals of the first water multiple are picked where first arrivals are not clear at long offsets. Water multiple picks were then time-shifted until picks from the multiple for near and/or mid offsets coincide with equivalent picks for the first arrivals. Picking uncertainties are assigned with an offset dependency as follows: 30 ms for high-quality waveforms at offsets <6.5 km; 60 ms for offsets between 6.5 and 12 km; 100 ms for offsets between 12 and 20 km; 120 ms for offsets >20 km; and 150 ms for time-shifted multiple arrival picks.

Travel times of first arriving P-waves were next used to compute a tomographic 2D velocity model shown in Figure 3.3.2a using the TOMO2D software (Korenaga et al., 2000). The method results in a minimum-structure smooth sheared mesh velocity model hung from the seafloor (Fig. 3.3.2a). TOMO2D first combines the graph method with a ray bending conjugate gradient method for a hybrid ray-tracing approach. Next, a least-squares regularized inversion is employed and the starting velocity model is perturbed and updated until the targeted chi-square (χ^2) or the set number of maximum iterations is reached. Smoothing and damping constraints are used to regularize the iterative inversion. After five iterations, the model converged to a χ^2 of 1.10 and a Root Mean Square (RMS) traveltime residual of 53 ms. To estimate the velocity uncertainty across the model we performed a nonlinear Monte Carlo analysis (Fig. C.1). For this purpose, the starting 1D

velocity model is randomly perturbed to create a set of 100 randomized 2D extended starting velocity models. These randomized models were used to run 100 inversions using the same parametrization used for our inversion. The resulting tomographic models are used to calculate the average velocity model (Fig. 3.3.2a and C.1a) and the standard deviations (SD) of the P-wave velocities across the model (Fig. C.1b). The ray density in the model is represented by the derivative weight sum (DWS; Toomey & Foulger, 1989), a nondimensional relative indicator of ray coverage (Fig. C.1c). The checkerboard tests computed for resolution assessment are shown in Figures C.1d, C.1e and C.1f. To carry them out, checkerboard patterns with different horizontal and vertical cycle lengths with a ±5% periodic velocity perturbation were added to our final velocity model and used as starting velocity model for the inversion. Subtracting the input velocity models from the final inverted velocity models gave us the perturbations that our inversion is able to recover (Fig. C.1d-f). Thus, the resolvability of the model can be assessed with the extent of the perturbation recovery.

C.2 Velocity change as a function of ridge axis distance and lithospheric age

We carry out linear and five-degree polynomial regressions in addition to those shown in Figure 3 to evaluate possible effects of 1D velocity-depth function positions along the OBS profile (their distances from the fault emergences and breakaways) and the size of the velocity-depth group ranges. Results from this analysis are shown in Figures C.2a-d with the specifics of the analysis carried out explained in the figure caption. A positive trend relationship between P-wave velocity and age or distance away from the ridge axis, like the one shown in Figure 3, is noted for all the tests carried out.

As would be expected, all the fifth order polynomial curves (Figs. 3.3.2 and C.2a-d) show a better fit than the linear trends, i.e. lower Root Mean Squared Error (RMSE in Tables C.1 and C.2a-d) and higher Adjusted R^2 (Adj R-sq in Table C.1), for each corresponding depth group. Nonetheless, the t-Test and p values (<5% significant level) in Tables C.1 and C.2a-d for the linear regression fits show strong evidence against the null hypothesis, i.e., that there is no linear relationship between P-wave velocity and age or distance and

support the occurrence of a statistically significant positive trend between the studied variables.

C.3 Thermal evolution modeling

The 1D finite-difference (FD) model used to solve for the heat flow equation and to evaluate the thermal evolution expected at the SWIR at 64°30′E employs a Forward Time Centered Space (FTCS) method. FTCS is an FD method normally used to solve parabolic partial differential equations, such as the heat flow equation. It applies an explicit forward difference scheme (first order) in time and a centered difference scheme (second order) in space. We use 500 nodes in our FD model, and we assume the entire model domain consists of mantle-derived rocks, peridotites. The boundary conditions are 0 °C at the model surface and 1350 °C at the depth of 100 km (Kelly et al., 2016), which assumes the asthenosphere is well mixed below. The model time steps satisfy the Von Neumann stability criteria. Values used to calculate the lithospheric heat flow are: $3e^{-8}$ W/m^3 for the mantle heat production (Gholamrezaie et al., 2018); 4 W/m K for the thermal conductivity (Shapiro & Ritzwoller, 2004), 1793 J/Kg K for the specific heat capacity of mantle-derive rocks (Lesher & Spera, 2015), and 3000 kg/m (Christeson et al., 2019) for density (Bickert et al., 2020). Results for the 1D FD thermal modelling are shown in Figures C.3 and C.4.

Figures and Tables

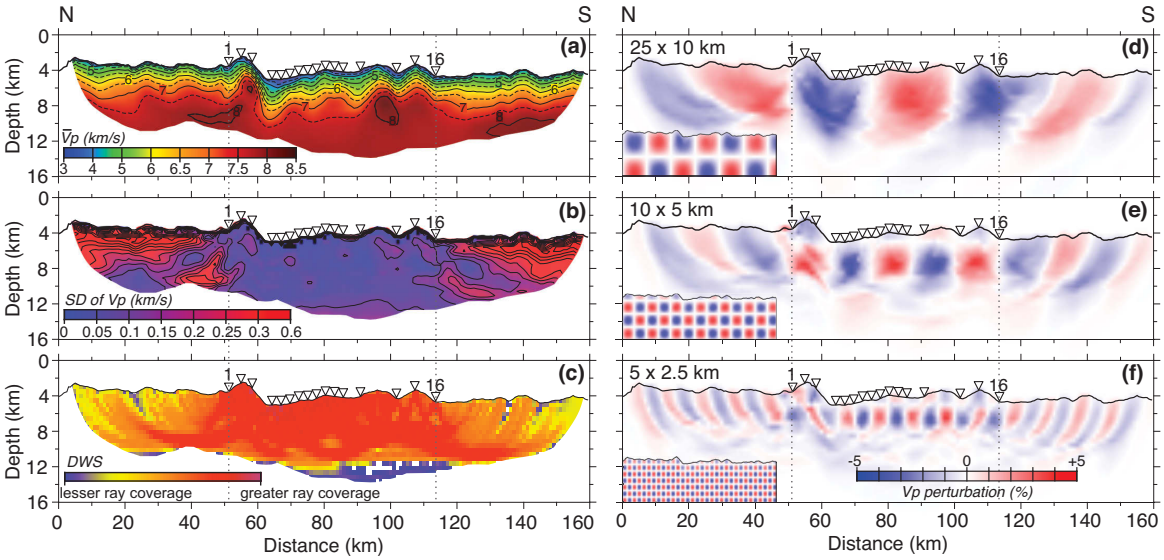

Figure C.1. Uncertainty assessment using Monte Carlo analysis (a, b and c) and checkerboard resolution tests (d, e and f) for the first arrival traveltime tomographic inversion. (a) Averaged final velocity model; (b) Standard deviation of the P-wave velocity; (c) Derivative weight sum (DWS) indicating the ray coverage. Results from checkerboard resolution tests for perturbation cells: 25 km wide x 10 km high (d), 10 km wide x 5 km high (e), and 5 km wide x 2.5 km high (f). In (d, e and f), the input perturbed model is shown in the bottom left inset and the recovered perturbed model is the full-size figure. In all figures, white inverted triangles show the positions of the OBSs on the seafloor thus outlining the best resolved area delimited by the dotted light grey lines. This area is covered with crossing rays and shows a standard deviation (SD) in velocity of <~0.1 km/s.

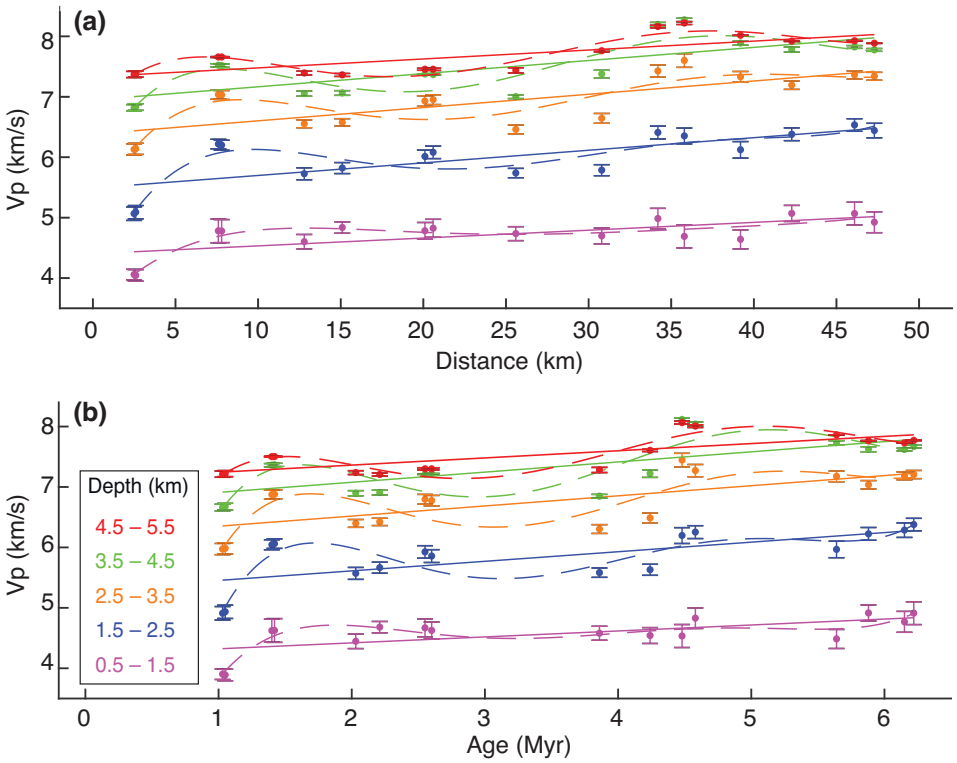

Figure C.2a. Upper lithospheric velocity change at the SWIR as a function of both increasing distance from the ridge axis and increasing age for depth group sizes and 1D velocity-depth function extraction locations other than those shown in Figure 3.3.3. Figure C.2a shows the regression analysis for extraction locations ±2.5 km to the left and right of the emergences (*E*) and breakaways (*B*). Figure C.2b shows the regression analysis for extraction locations at a regular interval of 2.5 km from *E1* to before *E9*. Figures C.2c and C.2d show the regression analysis for the same data points used in Fig. 3 (+2.5 km to the right of *Es* and *Bs*) but with different depth group sizes explored: 2.5 km and 0.5 km, respectively. In all figures (C.2a–C.2d), coloured circles represent the average velocities for the depth groups at each extraction location. 1D velocity-depth functions are extracted with a depth sampling of 0.1 km and then averaged for each depth group. The standard error of the mean pertinent to each average value of each group is shown with thin-coloured vertical lines and horizontal bars using the same colour code as for the circles. Linear regression and five-degree polynomial fits for each depth group are shown as solid and dashed lines, respectively. Depth groups are colour coded as shown in legend in (b).

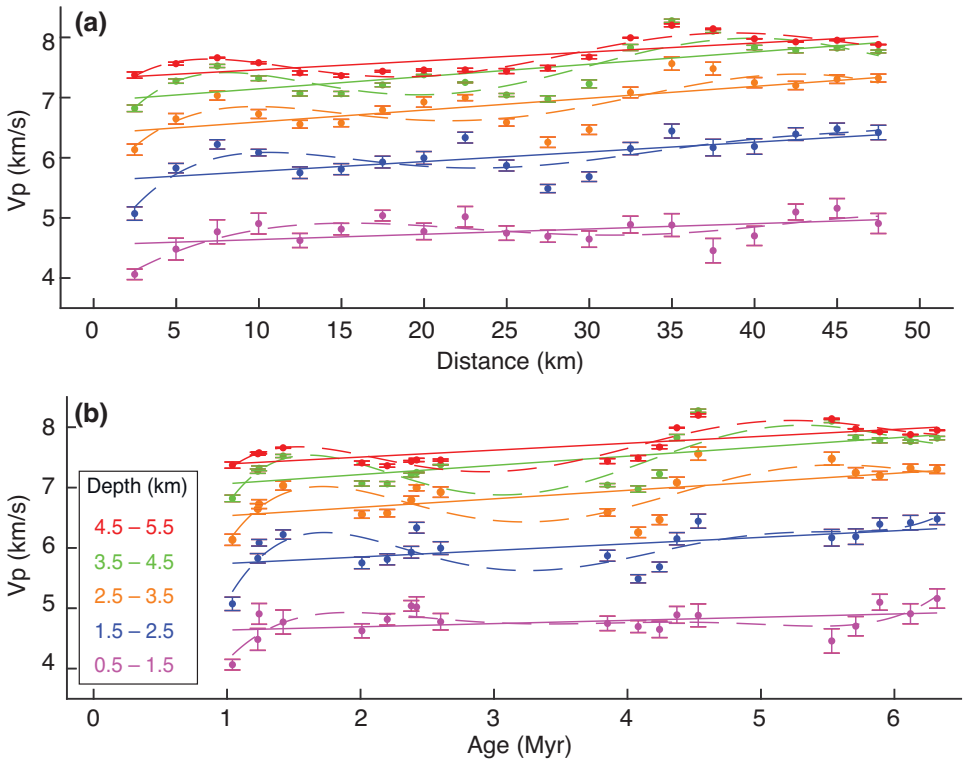

Figure C.2b. Figure C.2 continuation. Please refer to Figure C.2a caption for annotation.

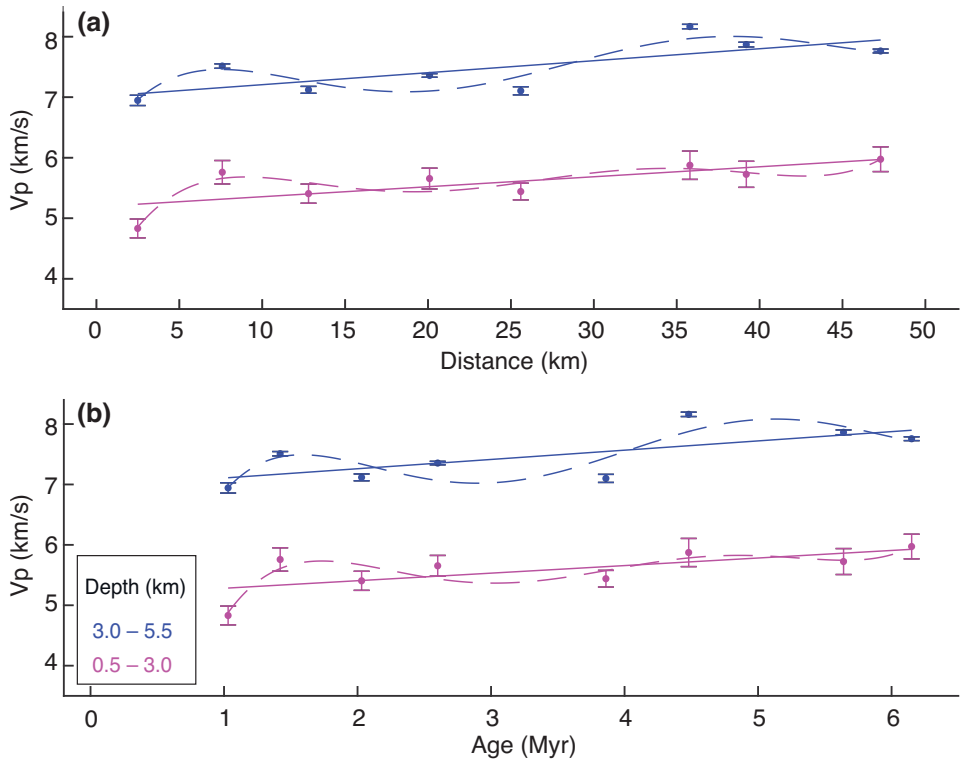

Figure C.2c. Figure C.2 continuation. Please refer to Figure C.2a caption for annotation.

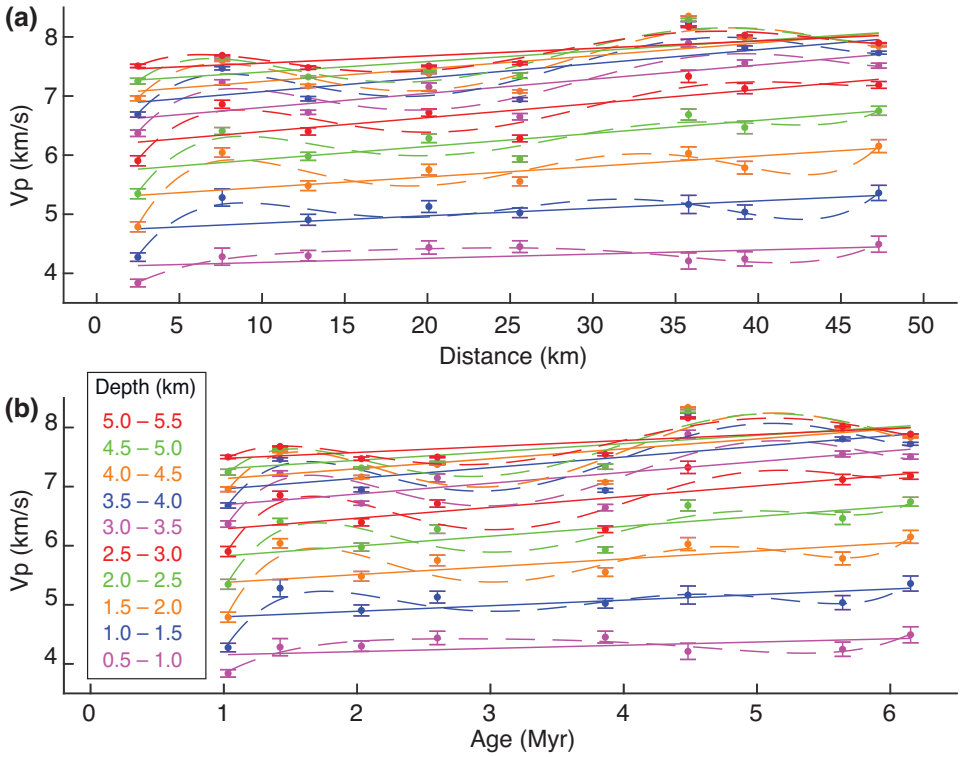

Figure C.2d. Figure C.2 continuation. Please refer to Figure C.2a caption for annotation.

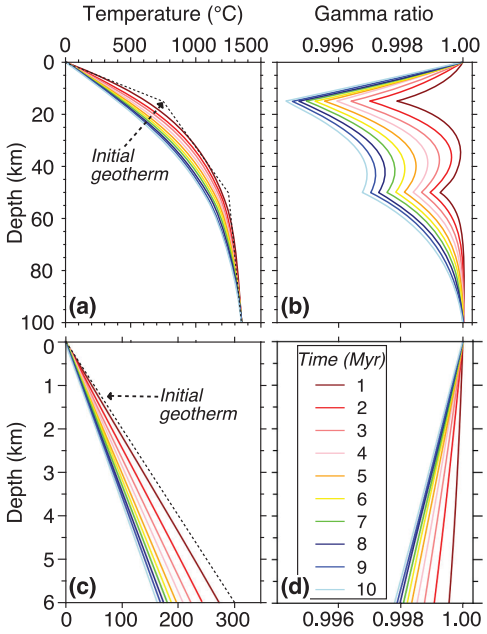

Figure C.3. Results from the thermal analysis with the 1D finite-difference model computed for a time span of 10 Myr. In (a) and (c) the initial geotherm is shown as a dashed black line and the computed geotherms are shown as coloured solid lines corresponding to different ages, from 1 to 10 Myr every 1 Myr. The colour code used is provided in the legend in (d) and it applies to all figures (a-d). Gamma (γ), which is a ratio between the P-wave velocity of the aging lithosphere and the initial P-wave velocity at zero age, is shown in (b) and (d). Top panels (a and b) show the

full depth studied, up to 100 km dbsf, and bottom panels (c and d) show zoom to the depth range of interest, from 0–6 km dbsf.

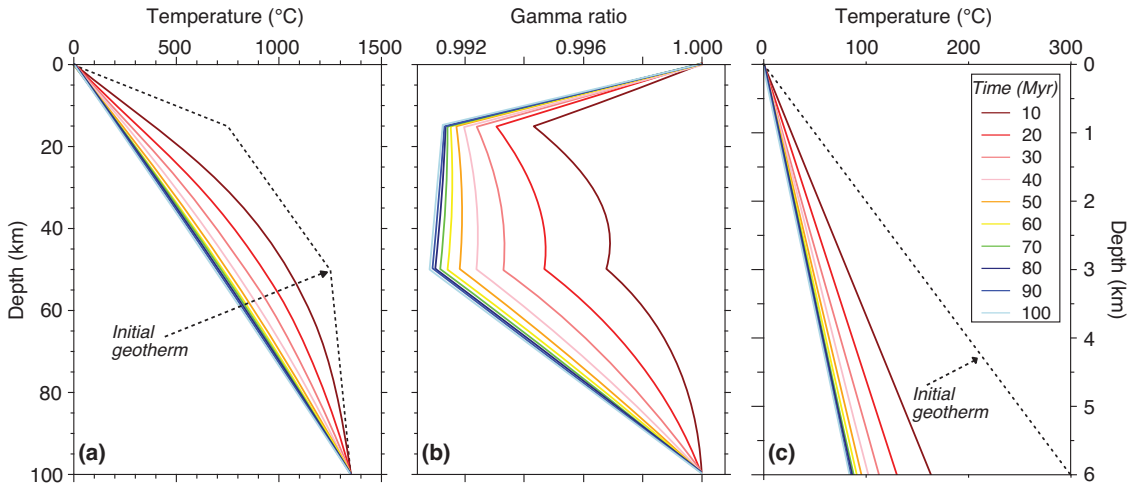

Figure C4. Results from the thermal analysis with the 1D finite-difference model computed for a time span of 100 Myr. In (a) and (c) the initial geotherm is shown as a dashed black line and the computed geotherms are shown as coloured solid lines corresponding to different ages, from 10 to 100 Myr every 10 Myr. The colour code used is provided in the legend shown in (c) and it applies to all figures (a-c). Full depth (100 km dbsf) analysis is shown in (a) and zoom to depth range of interest from 0–6 km dbsf is shown in (c). Gamma (γ) for the full depth is shown in (b).

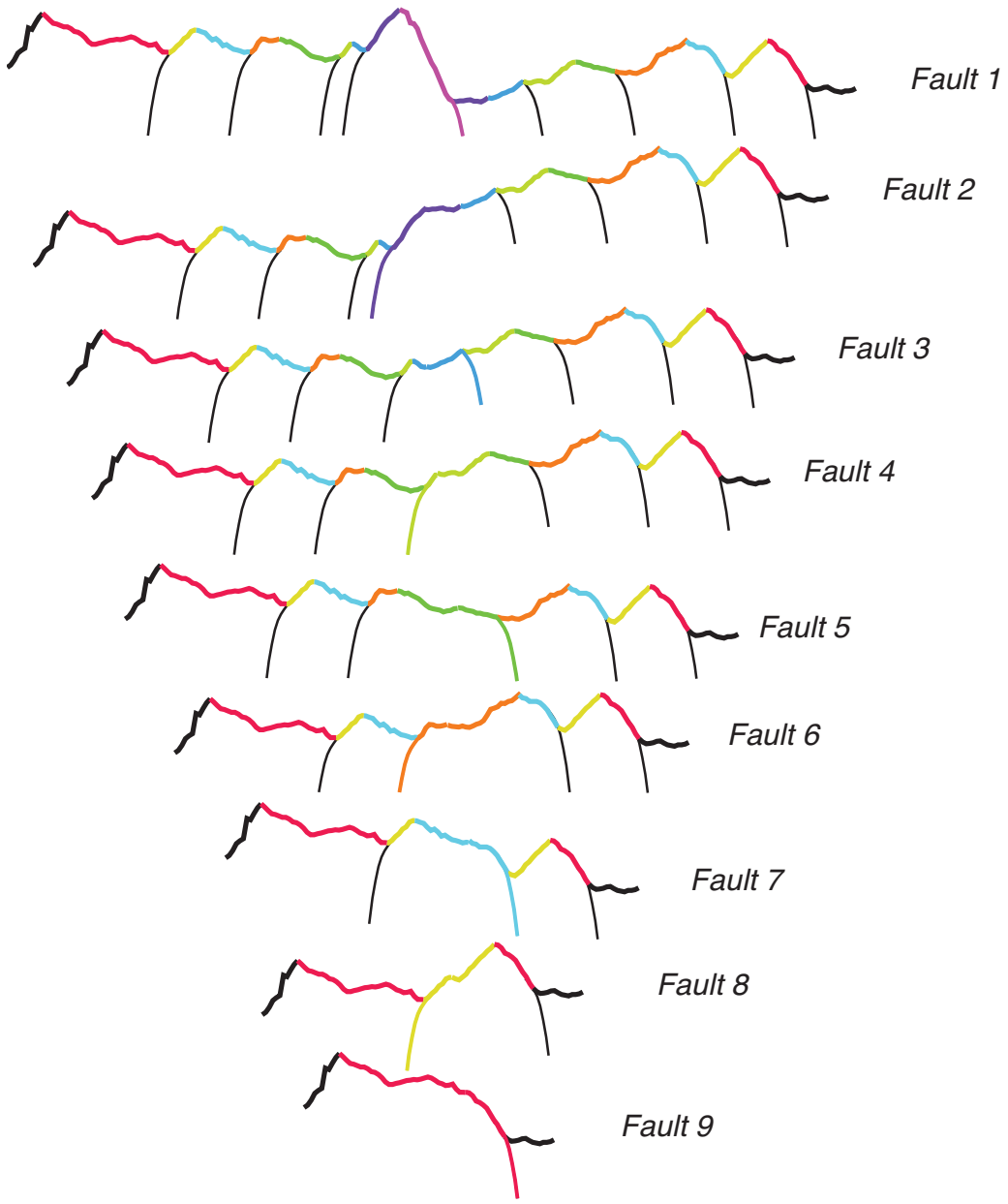

Figure C.5. A series of conceptual sketches showing the flip-flop detachment faulting system evolution from present seafloor topography (top sketch) to the estimated topography exhibited when the oldest identified fault was the active master fault (bottom sketch). The fault surface of each successive flip-flop fault is colour coded as in Figure 3.3.2b. Name on the right of each topographic profile indicates the active fault.

	ID	Depth (mbsf)	Poly. reg. degree	SSE	RMSE	R-sq	Adj. R-sq
VA w/ Distance	1	500-1500	5	0.033	0.129	0.929	0.752
	2	1500-2500	5	0.194	0.311	0.860	0.510
	3	2500-3500	5	0.350	0.418	0.805	0.317
	4	3500-4500	5	0.340	0.412	0.805	0.318
	5	4500-5500	5	0.059	0.171	0.920	0.721
VA with Age	1	500-1500	5	0.065	0.180	0.863	0.519
	2	1500-2500	5	0.282	0.376	0.796	0.2870
	3	2500-3500	5	0.518	0.509	0.711	-0.011
	4	3500-4500	5	0.533	0.516	0.695	-0.007
	5	4500-5500	5	0.130	0.255	0.824	0.384

Velocity analysis (VA) with Distance	ID	Depth (mbsf)	Linear regressions		SE	tStat	pValue	RMSE	R-sq	Adj. R-sq
	1	500-1500	m	0.010	0.005	1.844	0.115	0.224	0.362	0.255
			b	4.419	0.149	29.611	9.84e-08			
	2	1500-2500	m	0.020	0.008	2.474	0.048	0.338	0.505	0.423
			b	5.489	0.225	24.37	3.14e-07			
	3	2500-3500	m	0.024	0.008	2.786	0.032	0.361	0.564	0.491
			b	6.356	0.241	26.419	1.94e-07			
	4	3500-4500	m	0.023	0.009	27.954	1.39e-07	0.372	0.525	0.445
			b	6.925	0.248	2.573	0.042			
	5	4500-5500	m	0.015	0.005	2.738	0.034	0.234	0.555	0.481
			b	7.320	0.156	47.036	6.19e-09			
Velocity analysis (VA) with Age	1	500-1500	m	0.074	0.046	1.605	0.159	0.235	0.300	0.184
			b	4.401	0.177	24.856	2.79e-07			
	2	1500-2500	m	0.15	0.072	2.089	0.082	0.366	0.421	0.325
			b	5.451	0.276 03	19.749	1.09e-06			
	3	2500-3500	m	0.182	0.077	2.361	0.056	0.394	0.482	0.395
			b	6.304	0.297	21.206	7.17e-07			
	4	3500-4500	m	0.174	0.078	2.219	0.068	0.400	0.451	0.359
			b	6.873	0.302	22.778	4.69e-07			
	5	4500-5500	m	0.121	0.045	2.532	0.044	0.244	0.517	0.436
			b	7.270	0.184	39.531	1.75e-08			

Table C.1. Summary of linear and polynomial regression statistics for the data and results shown in Figures 3.3.3b and 3.3.3c. Table annotation is as follows: ID = layer identification; mbsf = meters below sea floor; m = slope of the linear regression; b = intercept of the linear regression; SSE = Sum of Squares Errors; RMSE = Root Mean Squared Error; R-sq = R-squared (coefficient of determination); Adj. R-sq = Adjusted R-squared; SE = Standard error (of the estimate); tStat = t-statistic; pValue = p-value.

	ID	Depth (mbsf)	Poly. reg. degree	SSE	RMSE	R-sq	Adj. R-sq
VA w/ Distance	1	500-1500	5	0.2186	0.1478	0.8329	0.7493
	2	1500-2500	5	0.4858	0.2204	0.8352	0.7529
	3	2500-3500	5	0.7530	0.2744	0.7601	0.6402
	4	3500-4500	5	0.6496	0.2549	0.7897	0.6846
	5	4500-5500	5	0.1095	0.1046	0.9182	0.8772
VA with Age	1	500-1500	5	0.2287	0.1512	0.8252	0.7378
	2	1500-2500	5	0.5830	0.2415	0.8023	0.7034
	3	2500-3500	5	0.9351	0.3058	0.7021	0.5531
	4	3500-4500	5	0.8602	0.2933	0.7216	0.5824
	5	4500-5500	5	0.1886	0.1373	0.8590	0.7885

Velocity analysis (VA) with Distance	ID	Depth (mbsf)	Linear regressions		SE	tStat	pValue	RMSE	R-sq	Adj. R-sq
	1	500-1500	m	0.013	0.004	3.449	0.004	0.225	0.459	0.421
			b	4.404	0.108	40.927	5.65e-16			
	2	1500-2500	m	0.021	0.005	3.946	0.001	0.316	0.527	0.493
			b	5.491	0.151	36.32	2.96e-15			
	3	2500-3500	m	0.022	0.005	4.131	0.001	0.318	0.549	0.517
			b	6.384	0.152	41.948	4.01e-16			
	4	3500-4500	m	0.022	0.005	4.104	0.001	0.316	0.546	0.514
			b	6.950	0.151	45.863	1.16e-16			
	5	4500-5500	m	0.015	0.003	4.423	0.001	0.2	0.583	0.553
			b	7.333	0.096	76.7	8.91e-20			
Velocity analysis (VA) with Age	1	500-1500	m	0.099	0.032	3.056	0.008	0.237	0.4	0.357
			b	4.379	0.126	34.667	5.65e-15			
	2	1500-2500	m	0.158	0.046	3.444	0.004	0.338	0.459	0.42
			b	5.452	0.180	30.257	3.71e-14			
	3	2500-3500	m	0.168	0.046	3.612	0.003	0.341	0.482	0.445
			b	6.340	0.182	34.878	5.20e-15			
	4	3500-4500	m	0.168	0.046	3.6844	0.002	0.335	0.492	0.456
			b	6.899	0.179	38.624	1.26e-15			
	5	4500-5500	m	0.119	0.028	4.2894	0.001	0.203	0.568	0.537
			b	7.282	0.108	67.153	5.70e-19			

Table C.2a. Summary of linear and polynomial regression statistics for other explored 1D velocity-depth profiles extraction locations and depth group sizes (Figures C.2a-d). The rest of the notation as in Table C.1 caption.

	ID	Depth (mbsf)	Poly. reg. degree	SSE	RMSE	R-sq	Adj. R-sq
VA w/ Distance	1	500-1500	5	0.4338	0.1827	0.6348	0.4944
	2	1500-2500	5	0.8395	0.2541	0.6473	0.5116
	3	2500-3500	5	1.1013	0.2911	0.6333	0.4922
	4	3500-4500	5	0.7490	0.2400	0.7534	0.6585
	5	4500-5500	5	0.1362	0.1024	0.9019	0.8641
VA with Age	1	500-1500	5	0.5075	0.1976	0.5728	0.4084
	2	1500-2500	5	0.9803	0.2746	0.5881	0.4297
	3	2500-3500	5	1.1717	0.3002	0.6098	0.4597
	4	3500-4500	5	0.9784	0.2743	0.6778	0.5539
	5	4500-5500	5	0.2375	0.1352	0.8288	0.7630

Velocity analysis (VA) with Distance	ID	Depth (mbsf)	Linear regressions	SE	tStat	pValue	RMSE	R-sq	Adj. R-sq
	1	500-1500	m	0.009	0.004	2.260	0.037	0.232	0.231	0.186
			b	4.552	0.111	41.12	1.84e-18			
	2	1500-2500	m	0.016	0.005	3.294	0.004	0.292	0.39	0.354
			b	5.612	0.134	40.202	2.69e-18			
	3	2500-3500	m	0.020	0.005	3.802	0.001	0.309	0.46	0.428
			b	6.397	0.148	43.351	7.56e-19			
	4	3500-4500	m	0.020	0.005	4.033	0.001	0.302	0.489	0.459
			b	6.939	0.144	48.094	1.31e-19			
	5	4500-5500	m	0.015	0.003	4.657	0.0002	0.189	0.561	0.535
			b	7.312	0.090	80.848	1.99e-23			

Velocity analysis (VA) with Age	ID	Depth (mbsf)							
	1	500-1500	m	0.053	0.031	1.690	0.109	0.245	0.144	0.093
			b	4.583	0.125	36.706	1.24e-17			
	2	1500-2500	m	0.108	0.040	2.677	0.0160	0.314	0.297	0.255
			b	5.632	0.160	35.159	2.56e-17			
	3	2500-3500	m	0.141	0.042	3.342	0.004	0.327	0.396	0.361
			b	6.391	0.167	38.344	5.97e-18			
	4	3500-4500	m	0.152	0.040	3.795	0.001	0.311	0.459	0.427
			b	6.912	0.159	43.542	7.02e-19			
	5	4500-5500	m	0.115	0.024	4.745	0.0002	0.187	0.57	0.545
			b	7.276	0.096	76.062	5.61e-23			

Table C.2b. Table C.2 continuation. Please refer to Table C.2a caption for annotation.

	ID	Depth (mbsf)	Poly. reg. degree	SSE	RMSE	R-sq	Adj. R-sq
VA w/ Dist.	1	500-3000	5	0.1146	0.2394	0.8744	0.5603
	2	3000-5500	5	0.2046	0.3198	0.8391	0.4369
VA w/ Age	1	500-3000	5	0.1679	0.2897	0.8159	0.3556
	2	3000-5500	5	0.3425	0.4138	0.7306	0.0572

	ID	Depth (mbsf)	Linear regressions		SE	tStat	pValue	RMSE	R-sq	Adj. R-sq
VA w/ Distance	1	500-3000	m	0.0165	0.006	2.617	0.040	0.266	0.533	0.455
			b	5.191	0.177	29.257	1.06e-07			
	2	3000-5500	m	0.020	0.007	2.713	0.035	0.308	0.551	0.476
			b	7.009	0.205	34.114	4.22e-08			
VA w/ Age	1	500-3000	m	0.125	0.057	2.210	0.070	0.289	0.449	0.357
			b	5.158	0.218	23.609	3.79e-07			
	2	3000-5500	m	0.154	0.065	2.372	0.055	0.331	0.484	0.398
			b	6.958	0.250	27.875	1.41e-07			

Table C.2c. Table C.2 continuation. Please refer to Table C.2a caption for annotation.

	ID	Depth (mbsf)	Poly. reg. degree	SSE	RMSE	R-sq	Adj. R-sq
VA w/ Distance	1	500-1000	5	0.0126	0.0793	0.9583	0.8540
	2	1000-1500	5	0.0844	0.2054	0.8923	0.6230
	3	1500-2000	5	0.1765	0.2971	0.8679	0.5376
	4	2000-2500	5	0.2184	0.3304	0.8536	0.4877
	5	2500-3000	5	0.2880	0.3795	0.8333	0.4166
	6	3000-3500	5	0.4172	0.4567	0.7795	0.2282
	7	3500-4000	5	0.4175	0.4569	0.7774	0.2208
	8	4000-4500	5	0.2755	0.3711	0.8330	0.4155
	9	4500-5000	5	0.1027	0.2266	0.8995	0.6483
	10	5000-5500	5	0.0261	0.1143	0.9478	0.8172
VA with Age	1	500-1000	5	0.0308	0.1242	0.8977	0.6419
	2	1000-1500	5	0.1427	0.2671	0.8178	0.3624
	3	1500-2000	5	0.2713	0.3683	0.7970	0.2894
	4	2000-2500	5	0.3125	0.3953	0.7905	0.2667
	5	2500-3000	5	0.4324	0.4650	0.7497	0.1241
	6	3000-3500	5	0.6123	0.5533	0.6763	-0.1329
	7	3500-4000	5	0.6226	0.5579	0.6680	-0.1619
	8	4000-4500	5	0.4576	0.4783	0.7226	0.0291
	9	4500-5000	5	0.2058	0.3208	0.7986	0.2952
	10	5000-5500	5	0.0696	0.1865	0.8608	0.5127

Velocity analysis (VA) with Distance										
ID	Depth (mbsf)	Linear regressions		SE	tStat	pValue	RMSE	R-sq	Adj. R-sq
1	500-1000	m	0.007	0.004	1.57	0.167	0.189	0.291	0.173
		b	4.116	0.126	32.752	5.39e-08			
2	1000-1500	m	0.0126	0.007	1.838	0.113	0.289	0.36	0.254
		b	4.722	0.192	0.192	3.01e-07			
3	1500-2000	m	0.018	0.008	2.083	0.082	0.36	0.42	0.323
		b	5.274	0.239	22.027	5.72e-07			
4	2000-2500	m	0.022	0.008	2.856	0.029	0.325	0.576	0.506
		b	5.705	0.216	26.39	1.95e-07			
5	2500-3000	m	0.024	0.008	2.878	0.028	0.348	0.58	0.51
		b	6.156	0.232	26.575	1.87e-07			
6	3000-3500	m	0.024	0.009	2.661	0.037	0.38	0.541	0.465
		b	6.560	0.253	25.9	2.18e-07			
7	3500-4000	m	0.024	0.009	2.608	0.040	0.383	0.531	0.453
		b	6.8308	0.255	26.795	1.78e-07			
8	4000-4500	m	0.022	0.009	2.504	0.046	0.367	0.511	0.43
		b	7.021	0.244	28.754	1.17e-07			
9	4500-5000	m	0.018	0.006	2.716	0.035	0.276	0.551	0.477
		b	7.220	0.184	39.215	1.84e-08			
10	5000-5500	m	0.012	0.004	2.746	0.033	0.192	0.557	0.483
		b	7.423	0.128	58.013	1.76e-09			

Table C.2d. Table C.2 continuation. Please refer to Table C.2a caption for annotation.

Velocity analysis (VA) with Age											
1	500-1000	m	0.054	0.054	1.418	0.206	0.194	0.251	0.126		
		b	4.100	0.146	28.001	1.37e-07					
2	1000-1500	m	0.094	0.059	1.579	0.165	0.304	0.294	0.176		
		b	4.702	0.229	20.516	8.72e-07					
3	1500-2000	m	0.133	0.075	1.773	0.126	0.382	0.344	0.235		
		b	5.245	0.288	18.178	1.78e-06					
4	2000-2500	m	0.167	0.070	2.387	0.054	0.357	0.487	0.402		
		b	5.660	0.269	20.999	7.60e-07					
5	2500-3000	m	0.182	0.074	2.448	0.050	0.38	0.5	0.416		
		b	6.102	0.286	21.295	6.99e-07					
6	3000-3500	m	0.183	0.081	2.255	0.065	0.413	0.459	0.369		
		b	6.510	0.312	20.877	7.86e-07					
7	3500-4000	m	0.180	0.081	2.2178	0.068402	0.414	0.45	0.359		
		b	6.781	0.313	21.678	6.29e-07					
8	4000-4500	m	0.168	0.076	2.1955	0.070541	0.39	0.445	0.353		
		b	6.967	0.295	23.641	3.76e-07					
9	4500-5000	m	0.141	0.057	2.4686	0.048547	0.291	0.504	0.421		
		b	7.165	0.220	32.654	5.49e-08					
10	5000-5500	m	0.101	0.034	2.6138	0.039919	0.197	0.532	0.454		
		b	7.377	0.149	49.519	4.55e-09					

Table C.2d continuation. Table C.2 continuation. Please refer to Table C.2a caption for annotation.

Es and *Bs* locations		2.5 km to the right of the *E*/*B*		
	Distance (km)		Dist. (km)	Age (Ma)
B3	48.8	***B3R***	NU	NU
E2	50.8	***E2R***	53.3	NU
B1	55.7	***B1R***	58.2	NU
E1	62.8	***E1R***	65.3	1.03
B2	67.9	***B2R***	70.4	1.42
E3	73.1	***E3R***	75.6	2.03
B4	80.4	***B4R***	82.9	2.60
E5	85.9	***E5R***	88.4	3.86
B6	96.1	***B6R***	98.6	4.48
E7	99.5	***E7R***	102	5.65
B8	107.6	***B8R***	110.1	6.15
E9	111.4			

Table C.3. Tomographic model distances and corresponding crustal ages for the sample locations of 1D velocity functions used in the analysis shown in Figure 3.3.3, which are annotated with a letter-number-letter patterns (e.g., *E2L*). Also listed are tomographic model distances for locations of emergences (*E*) and breakaways (*B*), which are annotated with a letter-number pattern (e.g., *B3*). NU stands for Not Used in the analysis and it pertains to *Es* and *Bs* located north of the spreading axis.

	Variably serpentinized peridotites			
Elastic Constants	0% serpentinization	50% serpentinization	100% serp. (serpentinite)	
Young's modulus (Mb)	1.76	0.83	0.38	Christensen 1966
Bulk's modulus (Mb)	1.34	0.84	0.47	
Shear's modulus (Mb)	0.68	0.32	0.15	
Elastic Constants	0% serpentinization	50% serpentinization	100% serp. (serpentinite)	
Poisson's ratio	0.28	0.33	0.37	
Young's modulus (Mb)	1.77		0.43	Christensen 1972
Bulk's modulus (Mb)	1.34		0.53	
Shear's modulus (Mb)	0.69		0.16	
Density (g/cm^3)		2.9		
Elastic Constants	0% serpentinization	??% serpentinization	100% serp. (serpentinite)	
Poisson's ratio		0.30-0.31	0.34-0.35 (0.35*)	
Young's modulus (Mb)		0.80-0.81	0.39-0.44	Christensen 1978
Bulk's modulus (Mb)		0.66-0.70	0.42-0.50	*reported in abstract
Shear's modulus (Mb)		0.31	0.15-0.16	
Density (g/cm^3)		2.62-2.87	2.51-2.55 (2.53*)	
Elastic Constants	0% serpentinization	50% serpentinization	100% serp. (serpentinite)	Christensen 1996
Poisson's ratio	0.26	0.33	0.36	
	0% serpentinization	50% serpentinization	100% serp. (serpentinite)	Miller & Christensen 1997
Density (g/cm^3)	3.3	2.9	2.52	
Elastic Constants	0% serpentinization	50% serpentinization	100% serp. (serpentinite)	Christensen 2004
Poisson's ratio	0.265	0.303	0.362	

Averaged values	0% serpentinization	50% serp. (w 1978 data)	50% serp. (w/o 1978 d.)	100% serp. (serpentinite)
Poisson's ration	0.27	0.42	0.32	0.36
Young's modulus (Mb)	1.77	0.82	0.83	0.41
Bulk's modulus (Mb)	1.34	0.76	0.84	0.49
Shear's modulus (Mb)	0.69	0.32	0.32	0.16
Density (g/cm^3)	3.30	2.82	2.90	2.53

Table C.4. Summary of elastic parameters available in the literature for variably serpentinized peridotites. While the variation in the elastic parameters as a function of the degree of serpentinization has been observed and measured in experimental studies, laboratory determinations have shown no such variation with the change in temperature (Christensen, 2004; Evan & Goetze, 1979).

Appendix D

Supporting Information for Chapter 4: Seismic reflection structure across the ultraslow-spreading Southwest Indian Ridge at 64°30′E

Contents

Figures D1 to D2

D.1 Figures

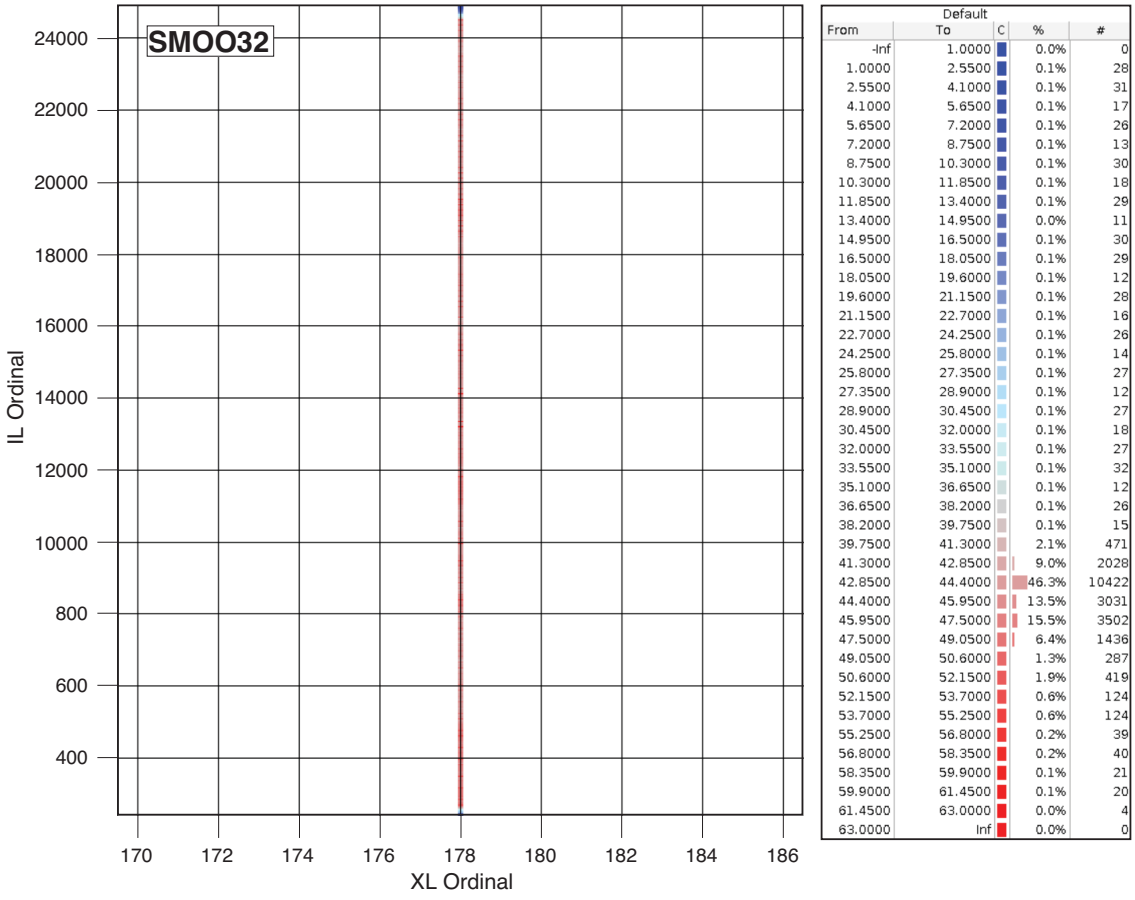

Default

From	To	C	%	#
-Inf	1.0000		0.0%	0
1.0000	2.5500		0.1%	28
2.5500	4.1000		0.1%	31
4.1000	5.6500		0.1%	17
5.6500	7.2000		0.1%	26
7.2000	8.7500		0.1%	13
8.7500	10.3000		0.1%	30
10.3000	11.8500		0.1%	18
11.8500	13.4000		0.1%	29
13.4000	14.9500		0.0%	11
14.9500	16.5000		0.1%	30
16.5000	18.0500		0.1%	29
18.0500	19.6000		0.1%	12
19.6000	21.1500		0.1%	28
21.1500	22.7000		0.1%	16
22.7000	24.2500		0.1%	26
24.2500	25.8000		0.1%	14
25.8000	27.3500		0.1%	27
27.3500	28.9000		0.1%	12
28.9000	30.4500		0.1%	27
30.4500	32.0000		0.1%	18
32.0000	33.5500		0.1%	27
33.5500	35.1000		0.1%	32
35.1000	36.6500		0.1%	12
36.6500	38.2000		0.1%	26
38.2000	39.7500		0.1%	15
39.7500	41.3000		2.1%	471
41.3000	42.8500		9.0%	2028
42.8500	44.4000		46.3%	10422
44.4000	45.9500		13.5%	3031
45.9500	47.5000		15.5%	3502
47.5000	49.0500		6.4%	1436
49.0500	50.6000		1.3%	287
50.6000	52.1500		1.9%	419
52.1500	53.7000		0.6%	124
53.7000	55.2500		0.6%	124
55.2500	56.8000		0.2%	39
56.8000	58.3500		0.2%	40
58.3500	59.9000		0.1%	21
59.9000	61.4500		0.1%	20
61.4500	63.0000		0.0%	4
63.0000	Inf		0.0%	0

Figure D.1a. Fold coverage map for line SMOO32.

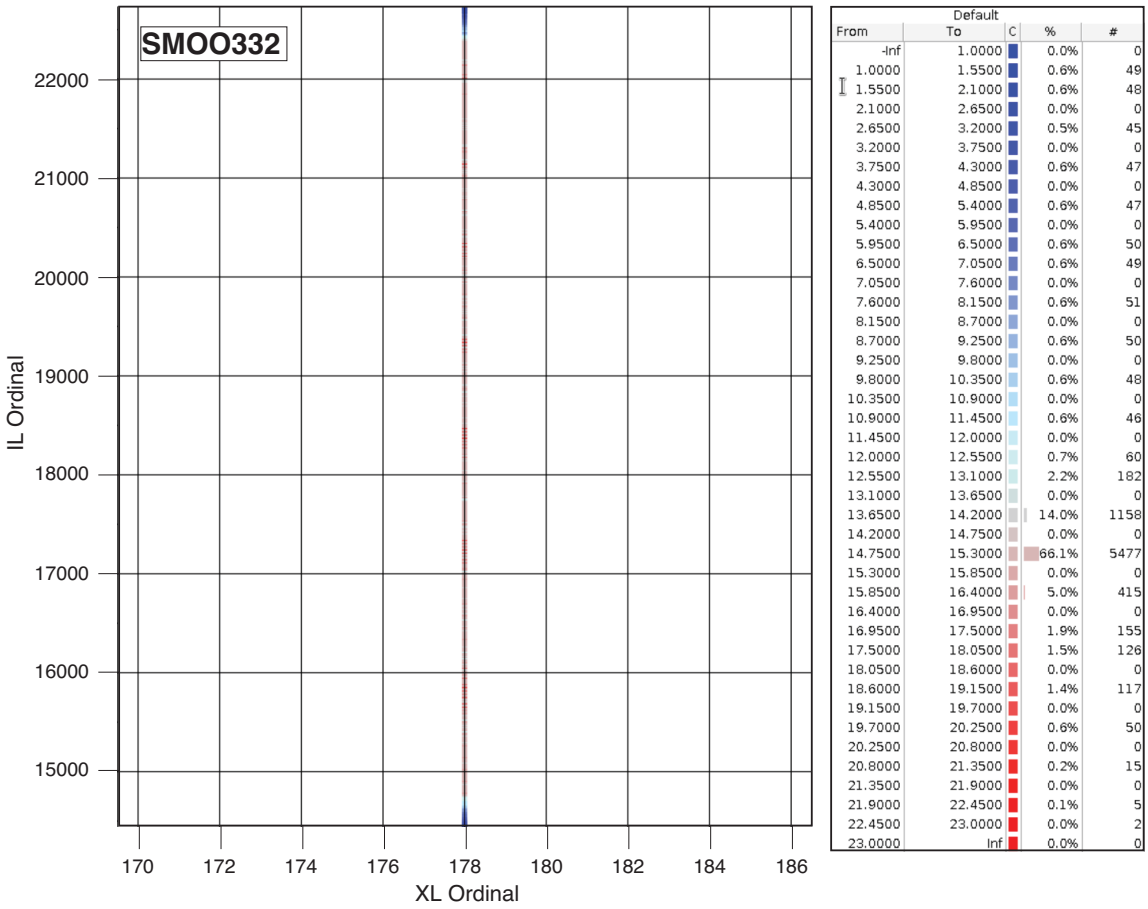

Figure D.1b. Fold coverage map for line SMO332.

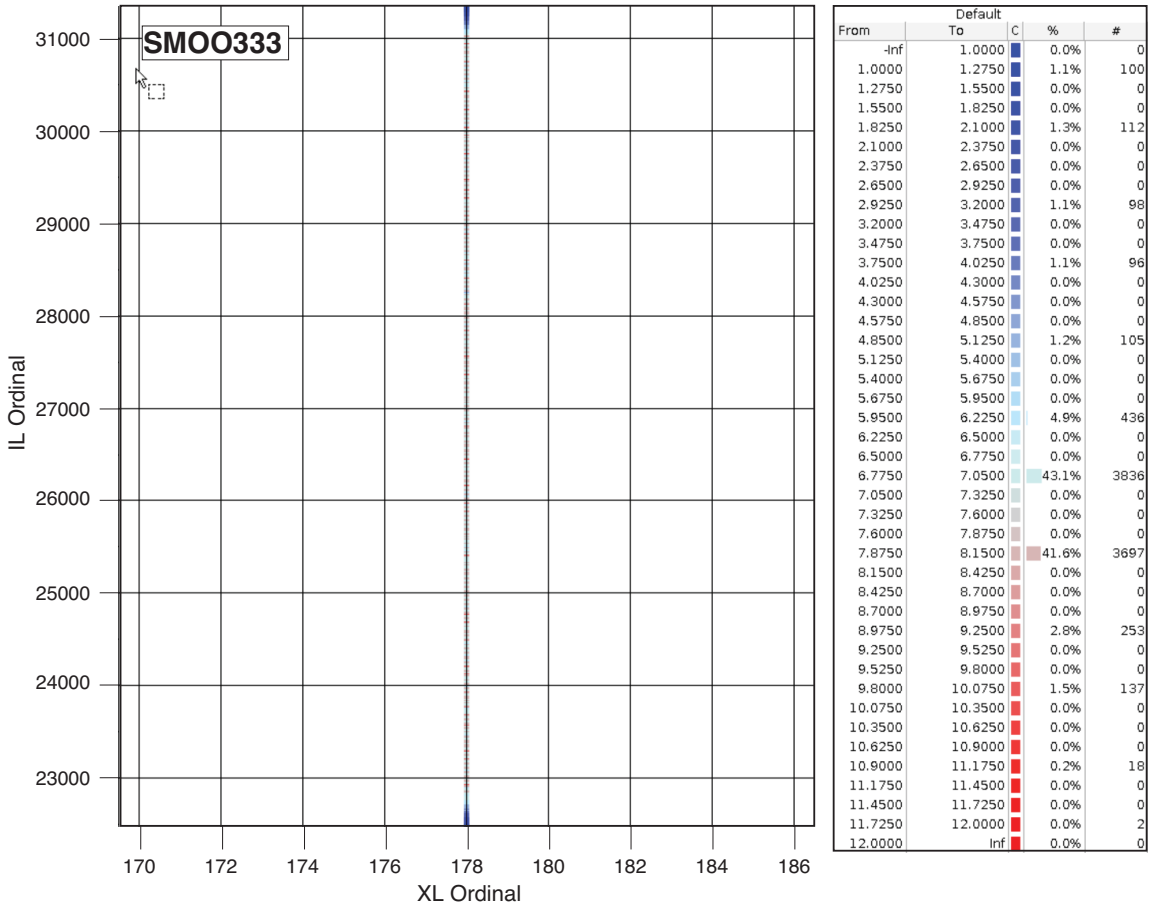

Default

From	To	C	%	#
-Inf	1.0000		0.0%	0
1.0000	1.2750		1.1%	100
1.2750	1.5500		0.0%	0
1.5500	1.8250		0.0%	0
1.8250	2.1000		1.3%	112
2.1000	2.3750		0.0%	0
2.3750	2.6500		0.0%	0
2.6500	2.9250		0.0%	0
2.9250	3.2000		1.1%	98
3.2000	3.4750		0.0%	0
3.4750	3.7500		0.0%	0
3.7500	4.0250		1.1%	96
4.0250	4.3000		0.0%	0
4.3000	4.5750		0.0%	0
4.5750	4.8500		0.0%	0
4.8500	5.1250		1.2%	105
5.1250	5.4000		0.0%	0
5.4000	5.6750		0.0%	0
5.6750	5.9500		0.0%	0
5.9500	6.2250		4.9%	436
6.2250	6.5000		0.0%	0
6.5000	6.7750		0.0%	0
6.7750	7.0500		43.1%	3836
7.0500	7.3250		0.0%	0
7.3250	7.6000		0.0%	0
7.6000	7.8750		0.0%	0
7.8750	8.1500		41.6%	3697
8.1500	8.4250		0.0%	0
8.4250	8.7000		0.0%	0
8.7000	8.9750		0.0%	0
8.9750	9.2500		2.8%	253
9.2500	9.5250		0.0%	0
9.5250	9.8000		0.0%	0
9.8000	10.0750		1.5%	137
10.0750	10.3500		0.0%	0
10.3500	10.6250		0.0%	0
10.6250	10.9000		0.0%	0
10.9000	11.1750		0.2%	18
11.1750	11.4500		0.0%	0
11.4500	11.7250		0.0%	0
11.7250	12.0000		0.0%	2
12.0000	Inf		0.0%	0

Figure D.1c. Fold coverage map for line SMO333.

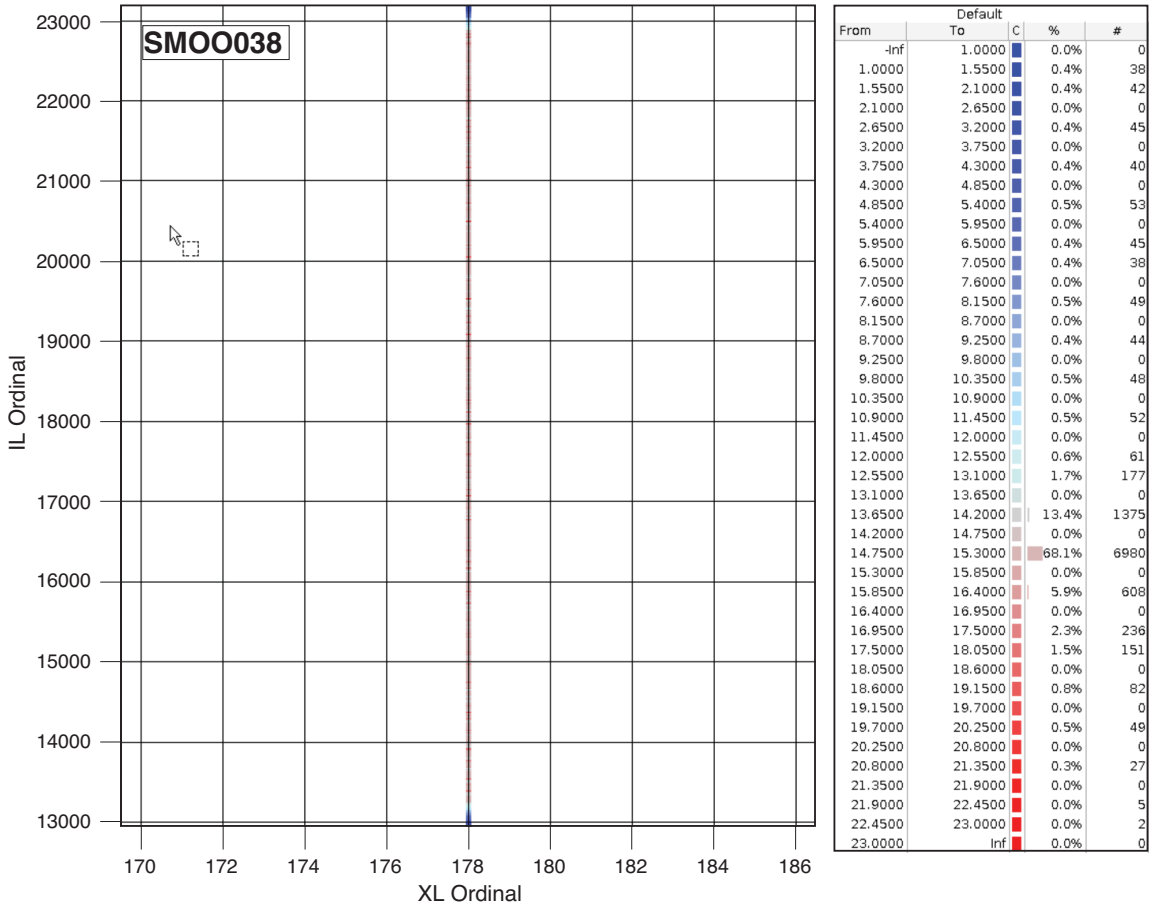

Default

From	To	C	%	#
-Inf	1.0000		0.0%	0
1.0000	1.5500		0.4%	38
1.5500	2.1000		0.4%	42
2.1000	2.6500		0.0%	0
2.6500	3.2000		0.4%	45
3.2000	3.7500		0.0%	0
3.7500	4.3000		0.4%	40
4.3000	4.8500		0.0%	0
4.8500	5.4000		0.5%	53
5.4000	5.9500		0.0%	0
5.9500	6.5000		0.4%	45
6.5000	7.0500		0.4%	38
7.0500	7.6000		0.0%	0
7.6000	8.1500		0.5%	49
8.1500	8.7000		0.0%	0
8.7000	9.2500		0.4%	44
9.2500	9.8000		0.0%	0
9.8000	10.3500		0.5%	48
10.3500	10.9000		0.0%	0
10.9000	11.4500		0.5%	52
11.4500	12.0000		0.0%	0
12.0000	12.5500		0.6%	61
12.5500	13.1000		1.7%	177
13.1000	13.6500		0.0%	0
13.6500	14.2000		13.4%	1375
14.2000	14.7500		0.0%	0
14.7500	15.3000		68.1%	6980
15.3000	15.8500		0.0%	0
15.8500	16.4000		5.9%	608
16.4000	16.9500		0.0%	0
16.9500	17.5000		2.3%	236
17.5000	18.0500		1.5%	151
18.0500	18.6000		0.0%	0
18.6000	19.1500		0.8%	82
19.1500	19.7000		0.0%	0
19.7000	20.2500		0.5%	49
20.2500	20.8000		0.0%	0
20.8000	21.3500		0.3%	27
21.3500	21.9000		0.0%	0
21.9000	22.4500		0.0%	5
22.4500	23.0000		0.0%	2
23.0000	Inf		0.0%	0

Figure D.1d. Fold coverage map for line SMOO38.

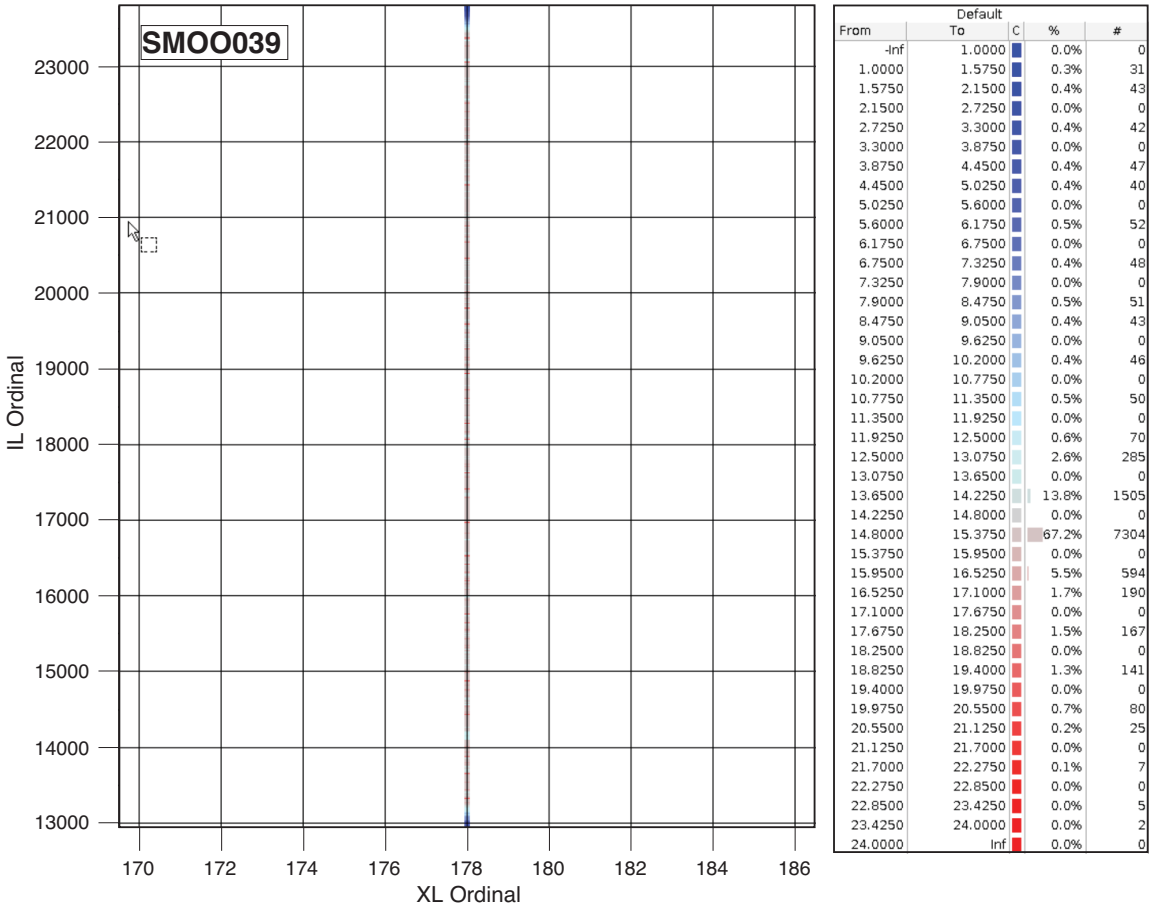

Default

From	To	C	%	#
-Inf	1.0000		0.0%	0
1.0000	1.5750		0.3%	31
1.5750	2.1500		0.4%	43
2.1500	2.7250		0.0%	0
2.7250	3.3000		0.4%	42
3.3000	3.8750		0.0%	0
3.8750	4.4500		0.4%	47
4.4500	5.0250		0.4%	40
5.0250	5.6000		0.0%	0
5.6000	6.1750		0.5%	52
6.1750	6.7500		0.0%	0
6.7500	7.3250		0.4%	48
7.3250	7.9000		0.0%	0
7.9000	8.4750		0.5%	51
8.4750	9.0500		0.4%	43
9.0500	9.6250		0.0%	0
9.6250	10.2000		0.4%	46
10.2000	10.7750		0.0%	0
10.7750	11.3500		0.5%	50
11.3500	11.9250		0.0%	0
11.9250	12.5000		0.6%	70
12.5000	13.0750		2.6%	285
13.0750	13.6500		0.0%	0
13.6500	14.2250		13.8%	1505
14.2250	14.8000		0.0%	0
14.8000	15.3750		67.2%	7304
15.3750	15.9500		0.0%	0
15.9500	16.5250		5.5%	594
16.5250	17.1000		1.7%	190
17.1000	17.6750		0.0%	0
17.6750	18.2500		1.5%	167
18.2500	18.8250		0.0%	0
18.8250	19.4000		1.3%	141
19.4000	19.9750		0.0%	0
19.9750	20.5500		0.7%	80
20.5500	21.1250		0.2%	25
21.1250	21.7000		0.0%	0
21.7000	22.2750		0.1%	7
22.2750	22.8500		0.0%	0
22.8500	23.4250		0.0%	5
23.4250	24.0000		0.0%	2
24.0000	Inf		0.0%	0

Figure D.1e. Fold coverage map for line SMOO39.

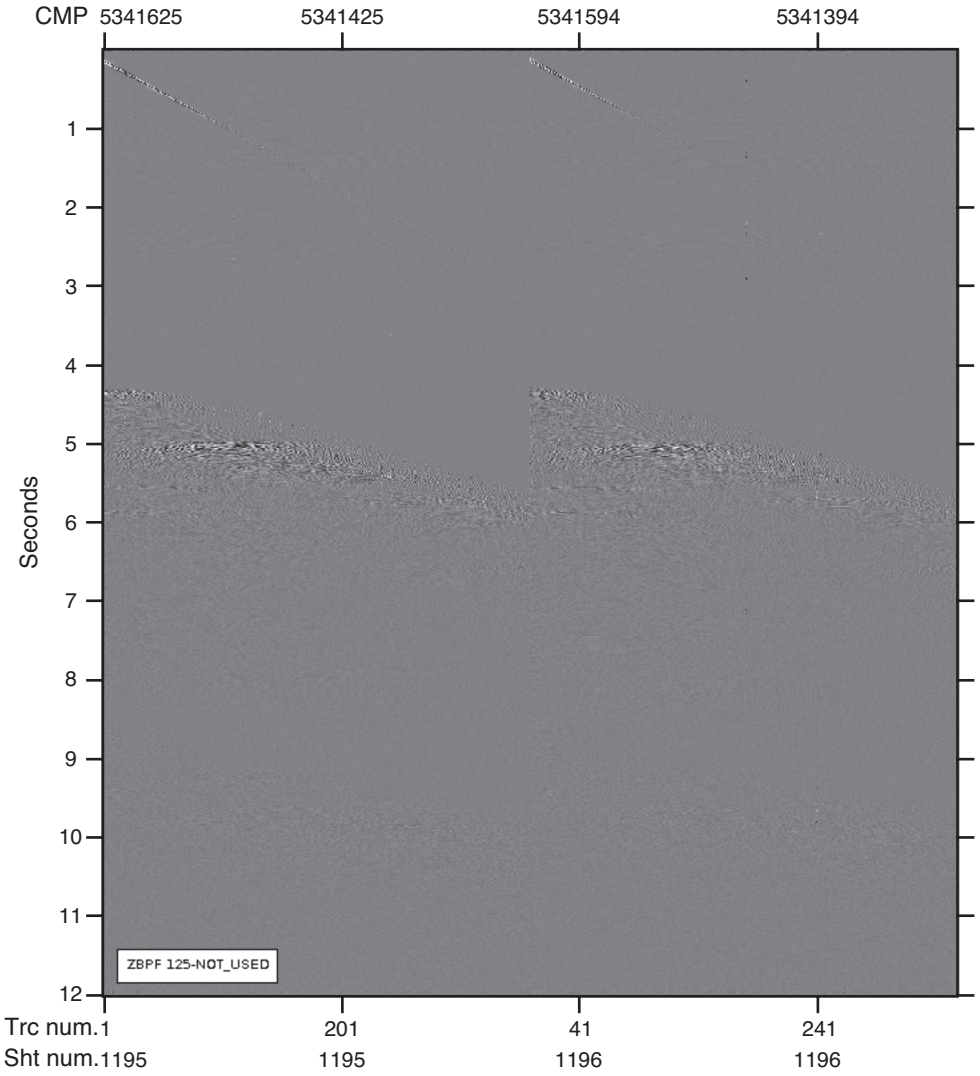

Figure D.2. HP (125–250 Hz) filtered shot gathers 1196 and 1196, Line SMOO32.

Appendix E

Copyright release printable license for Chapter 2: Seismic velocity structure along and across the ultraslow-spreading Southwest Indian Ridge at 64°30'E showcases flipping detachment faults (Journal of Geophysical Research: Solid Earth research article (https://doi.org/10.1029/2021JB022177).

JOHN WILEY AND SONS LICENSE
TERMS AND CONDITIONS

Jul 10, 2023

This Agreement between Dr. Ana Corbalan Castejon ("You") and John Wiley and Sons ("John Wiley and Sons") consists of your license details and the terms and conditions provided by John Wiley and Sons and Copyright Clearance Center.

License Number	5585520124980
License date	Jul 10, 2023
Licensed Content Publisher	John Wiley and Sons
Licensed Content Publication	Journal of Geophysical Research: Solid Earth
Licensed Content Title	Seismic Velocity Structure Along and Across the Ultraslow-Spreading Southwest Indian Ridge at 64°30′E Showcases Flipping Detachment Faults
Licensed Content Author	S. Leroy, L. Watremez, I. Grevemeyer, et al
Licensed Content Date	Sep 29, 2021
Licensed Content Volume	126
Licensed Content Issue	10

Licensed Content Pages	24
Type of use	Dissertation/Thesis
Requestor type	Author of this Wiley article
Format	Electronic
Portion	Full article
Will you be translating?	No
Title	GEOPHYSICAL FINGERPRINTS OF EXHUMED SERPENTINIZED MANTLE DOMAINS AT THE ULTRASLOW-SPREADING SOUTHWEST INDIAN RIDGE
Institution name	DALHOUSIE UNIVERSITY
Expected presentation date	Aug 2023
Requestor Location	Dr. Ana Corbalan Castejon Department of Earth Sciences Dalhousie University 1459 Oxford Street Halifax, NS B3H 4R2 Canada Attn: Dalhousie University
Publisher Tax ID	EU826007151
Total	0.00 CAD

Terms and Conditions

TERMS AND CONDITIONS

This copyrighted material is owned by or exclusively licensed to John Wiley & Sons, Inc. or one of its group companies (each a"Wiley Company") or handled on behalf of a society with which a Wiley Company has exclusive publishing rights in relation to a particular work (collectively "WILEY"). By clicking "accept" in connection with completing this licensing transaction, you agree that the following terms and conditions apply to this transaction (along with the billing and payment terms and conditions established by the Copyright Clearance Center Inc., ("CCC's Billing and Payment terms and conditions"), at the time that you opened your RightsLink account (these are available at any time at http://myaccount.copyright.com).

Terms and Conditions

- The materials you have requested permission to reproduce or reuse (the "Wiley Materials") are protected by copyright.

- You are hereby granted a personal, non-exclusive, non-sub licensable (on a stand-alone basis), non-transferable, worldwide, limited license to reproduce the Wiley Materials for the purpose specified in the licensing process. This license, **and any CONTENT (PDF or image file) purchased as part of your order,** is for a one-time use only and limited to any maximum distribution number specified in the license. The first instance of republication or reuse granted by this license must be completed within two years of the date of the grant of this license (although copies prepared before the end date may be distributed thereafter). The Wiley Materials shall not be used in any other manner or for any other purpose, beyond what is granted in the license. Permission is granted subject to an appropriate acknowledgement given to the author, title of the material/book/journal and the publisher. You shall also duplicate the copyright notice that appears in the Wiley publication in your use of the Wiley Material. Permission is also granted on the understanding that nowhere in the text is a previously published source acknowledged for all or part of this Wiley Material. Any third party content is expressly excluded from this permission.

- With respect to the Wiley Materials, all rights are reserved. Except as expressly granted by the terms of the license, no part of the Wiley Materials may be copied, modified, adapted (except for minor reformatting required by the new Publication), translated, reproduced, transferred or distributed, in any form or by any means, and no derivative works may be made based on the Wiley Materials without the prior permission of the respective copyright owner.**For STM Signatory Publishers clearing permission under the terms of the STM Permissions Guidelines only, the terms of the license are extended to include subsequent editions and for editions in other languages, provided such editions are for the work as a whole in situ and does not involve the separate exploitation of the permitted figures or extracts,** You may not alter, remove or suppress in any manner any copyright, trademark or other notices displayed by the Wiley Materials. You may not license, rent, sell, loan, lease, pledge, offer as security, transfer or assign the Wiley Materials on a stand-alone basis, or any of the rights granted to you hereunder to any other person.

- The Wiley Materials and all of the intellectual property rights therein shall at all times remain the exclusive property of John Wiley & Sons Inc, the Wiley Companies, or their respective licensors, and your interest therein is only that of having possession of and the right to reproduce the Wiley Materials pursuant to Section 2 herein during the continuance of this Agreement. You agree that you own no right, title or interest in or to the Wiley Materials or any of the intellectual property rights therein. You shall have no rights hereunder other than the license as provided for above in Section 2. No right, license or interest to any trademark, trade name, service mark or other branding ("Marks") of WILEY or its licensors is granted hereunder, and you agree that you shall not assert any such right, license or interest with respect thereto

- NEITHER WILEY NOR ITS LICENSORS MAKES ANY WARRANTY OR REPRESENTATION OF ANY KIND TO YOU OR ANY THIRD PARTY, EXPRESS, IMPLIED OR STATUTORY, WITH RESPECT TO THE MATERIALS OR THE ACCURACY OF ANY INFORMATION CONTAINED IN THE MATERIALS, INCLUDING, WITHOUT LIMITATION, ANY IMPLIED WARRANTY OF MERCHANTABILITY, ACCURACY, SATISFACTORY QUALITY, FITNESS FOR A PARTICULAR PURPOSE, USABILITY, INTEGRATION OR NON-INFRINGEMENT AND ALL SUCH WARRANTIES ARE HEREBY EXCLUDED BY WILEY AND ITS LICENSORS AND WAIVED BY YOU.

- WILEY shall have the right to terminate this Agreement immediately upon breach of this Agreement by you.

- You shall indemnify, defend and hold harmless WILEY, its Licensors and their respective directors, officers, agents and employees, from and against any actual or threatened claims, demands, causes of action or proceedings arising from any breach of this Agreement by you.

- IN NO EVENT SHALL WILEY OR ITS LICENSORS BE LIABLE TO YOU OR ANY OTHER PARTY OR ANY OTHER PERSON OR ENTITY FOR ANY SPECIAL, CONSEQUENTIAL, INCIDENTAL, INDIRECT, EXEMPLARY OR PUNITIVE DAMAGES, HOWEVER CAUSED, ARISING OUT OF OR IN CONNECTION WITH THE DOWNLOADING, PROVISIONING, VIEWING OR USE OF THE MATERIALS REGARDLESS OF THE FORM OF ACTION, WHETHER FOR BREACH OF CONTRACT, BREACH OF WARRANTY, TORT, NEGLIGENCE, INFRINGEMENT OR OTHERWISE (INCLUDING, WITHOUT LIMITATION, DAMAGES BASED ON LOSS OF PROFITS, DATA, FILES, USE, BUSINESS OPPORTUNITY OR CLAIMS OF THIRD PARTIES), AND WHETHER OR NOT THE PARTY HAS BEEN ADVISED OF THE POSSIBILITY OF SUCH DAMAGES. THIS LIMITATION SHALL APPLY NOTWITHSTANDING ANY FAILURE OF ESSENTIAL PURPOSE OF ANY LIMITED REMEDY PROVIDED HEREIN.

- Should any provision of this Agreement be held by a court of competent jurisdiction to be illegal, invalid, or unenforceable, that provision shall be deemed amended to achieve as nearly as possible the same economic effect as the original provision, and the legality, validity and enforceability of the remaining provisions of this Agreement

shall not be affected or impaired thereby.

- The failure of either party to enforce any term or condition of this Agreement shall not constitute a waiver of either party's right to enforce each and every term and condition of this Agreement. No breach under this agreement shall be deemed waived or excused by either party unless such waiver or consent is in writing signed by the party granting such waiver or consent. The waiver by or consent of a party to a breach of any provision of this Agreement shall not operate or be construed as a waiver of or consent to any other or subsequent breach by such other party.

- This Agreement may not be assigned (including by operation of law or otherwise) by you without WILEY's prior written consent.

- Any fee required for this permission shall be non-refundable after thirty (30) days from receipt by the CCC.

- These terms and conditions together with CCC's Billing and Payment terms and conditions (which are incorporated herein) form the entire agreement between you and WILEY concerning this licensing transaction and (in the absence of fraud) supersedes all prior agreements and representations of the parties, oral or written. This Agreement may not be amended except in writing signed by both parties. This Agreement shall be binding upon and inure to the benefit of the parties' successors, legal representatives, and authorized assigns.

- In the event of any conflict between your obligations established by these terms and conditions and those established by CCC's Billing and Payment terms and conditions, these terms and conditions shall prevail.

- WILEY expressly reserves all rights not specifically granted in the combination of (i) the license details provided by you and accepted in the course of this licensing transaction, (ii) these terms and conditions and (iii) CCC's Billing and Payment terms and conditions.

- This Agreement will be void if the Type of Use, Format, Circulation, or Requestor Type was misrepresented during the licensing process.

- This Agreement shall be governed by and construed in accordance with the laws of the State of New York, USA, without regards to such state's conflict of law rules. Any legal action, suit or proceeding arising out of or relating to these Terms and Conditions or the breach thereof shall be instituted in a court of competent jurisdiction in New York County in the State of New York in the United States of America and each party hereby consents and submits to the personal jurisdiction of such court, waives any objection to venue in such court and consents to service of process by registered or certified mail, return receipt requested, at the last known address of such party.

WILEY OPEN ACCESS TERMS AND CONDITIONS

Wiley Publishes Open Access Articles in fully Open Access Journals and in Subscription

journals offering Online Open. Although most of the fully Open Access journals publish open access articles under the terms of the Creative Commons Attribution (CC BY) License only, the subscription journals and a few of the Open Access Journals offer a choice of Creative Commons Licenses. The license type is clearly identified on the article.

The Creative Commons Attribution License

The Creative Commons Attribution License (CC-BY) allows users to copy, distribute and transmit an article, adapt the article and make commercial use of the article. The CC-BY license permits commercial and non-

Creative Commons Attribution Non-Commercial License

The Creative Commons Attribution Non-Commercial (CC-BY-NC)License permits use, distribution and reproduction in any medium, provided the original work is properly cited and is not used for commercial purposes.(see below)

Creative Commons Attribution-Non-Commercial-NoDerivs License

The Creative Commons Attribution Non-Commercial-NoDerivs License (CC-BY-NC-ND) permits use, distribution and reproduction in any medium, provided the original work is properly cited, is not used for commercial purposes and no modifications or adaptations are made. (see below)

Use by commercial "for-profit" organizations

Use of Wiley Open Access articles for commercial, promotional, or marketing purposes requires further explicit permission from Wiley and will be subject to a fee.

Further details can be found on Wiley Online Library http://olabout.wiley.com/WileyCDA/Section/id-410895.html

Other Terms and Conditions:

v1.10 Last updated September 2015

Questions? customercare@copyright.com.